Scuola di Dottorato in Ingegneria Civile e Architettura

Dottorato in Ingegneria delle Strutture

BIFURCATION SCENARIOS, DYNAMICAL INTEGRITY AND CONTROL OF NONCONTACT ATOMIC FORCE MICROSCOPES

PHD CANDIDATE

Valeria Settimi

ADVISOR

Prof.Giuseppe Rega

Rome, 07/10/2013

Dipartimento di Ingegneria Strutturale e Geotecnica

Sapienza Università di Roma

Contents

List of Figures

List of symbols

Abbreviations

AFM, AFMs	Atomic Force Microscope, Atomic Force Microscopes
AM-AFM	Amplitude modulated Atomic Force Microscope
bd	bifurcation diagram
c.c.	Complex conjugate terms
DFC	Delayed Feedback Control
FM-AFM	Frequency modulated Atomic Force Microscope
bd	bifurcation diagram
GIM	Global Integrity Measure
IBVP	Initial Boundary Value Problem
i.c.	initial conditions
IF	Integrity Measure
LIM	Local Integrity Measure
MEMs	Micro Electro-Mechanical Systems
ni	numerical integration
OGY	Ott, Grebogi, Yorke
P_n, P'_n, P''_n	Periodic solution of period n
P1H	Periodic solution of period 1 and high amplitude (resonant)
P1L	Periodic solution of period 1 and low amplitude (nonresonant)
PDH	Period doubling bifurcation of the high amplitude periodic solution
$RevSpPD_n$	Reverse supercritical period doubling bifurcation of solution of period n
SN	Saddle-node bifurcation
SN_n	Saddle-node bifurcation of solution of period n
SN1H	Saddle-node bifurcation of solution of period 1 and high amplitude (resonant)
SN1L	Saddle-node bifurcation of solution of period 1 and low amplitude (nonresonant)
$SbPD_n$	Subcritical period doubling bifurcation of solution of period n
$SpPD_n$	Supercritical period doubling bifurcation of solution of period n

SpPD1H	Supercritical period doubling bifurcation of solution of period 1 and high amplitude (resonant)
T	Transcritical bifurcation
TH, TL	Transcritical bifurcation of the high amplitude, low amplitude solution
TR	Torus bifurcation
TRH, TRL	Torus bifurcation of the high amplitude, low amplitude solution

General

$\dot{x}$	First order derivative of x with respect to time
$\ddot{x}$	Second order derivative of x with respect to time
x_y	First order derivative of x with respect to y
x_{yy}	Second order derivative of x with respect to y
x_{yyy}	Third order derivative of x with respect to y
x_{yyyy}	Fourth order derivative of x with respect to y

Roman Letters

a_T	Tip distance from the fixed side of the cantilever
a_{21}, a_{22}, a_{23}	Jacobian matrix elements
A_H	Hamaker constant
A, $\bar{A}$	Complex amplitude, conjugate complex amplitude of the generating solution in the asymptotic analysis
A_{un}, $\bar{A}_{un}$	Complex amplitude, conjugate complex amplitude of the generating reference solution in the asymptotic analysis
B, b	Amplitude of the generating control solution in the asymptotic analysis
C_1, C_2, C_3	Coefficients of the characteristic polynomial of the Jacobian matrix
C_{ij}, C_{ijk}	Coefficients in the order equations of the asymptotic analysis
d	Dimensional viscous damping coefficient
D_i	First order partial derivative with respect to T_i
D_i^2	Second order partial derivative with respect to T_i
E	Young's modulus of the cantilever
F_v^A	Dimensional atomic interaction force
g	Dimensional distance between cantilever fixed side and sample
g_a	Dimensional actual distance between cantilever tip and sample
$\bar{g}_1$, g_1	Dimensional, nondimensional controller's constant corresponding to proportional damping
$\bar{g}_2$, g_2	Dimensional, nondimensional controller's constant corresponding to viscoelastic damping
$\bar{g}_3$, g_3	Dimensional, nondimensional controller's constant corresponding to proportional displacement gain

G, $\bar{G}$	Redefined amplitude variables in the asymptotic analysis
G_{un}, $\bar{G}_{un}$	Redefined reference amplitude variables in the asymptotic analysis
h_T	Dimensional tip height
H	System's Hamiltonian
I	Cantilever moment of inertia with respect to the principal axis orthogonal to the beam plane
I_{ij}	Constants of integration in the single-mode dynamical system
j	Real part of the complex amplitude of the generating solution in the asymptotic analysis
j_{un}	Real part of the complex amplitude of the generating reference solution in the asymptotic analysis
J_z	Principal mass moment of inertia of the cantilever
J_{q^*}	Jacobian matrix at the equilibrium of the system with external feedback control
K_1	Constant from the dispersion equation
$\bar{k}$, k, k_g	Dimensional, nondimensional, normalized feedback control parameter
$\hat{k}_g$	Scaled feedback control parameter in the asymptotic analysis
L	Dimensional cantilever span
m	Cantilever mass per unit reference length
n	Imaginary part of the complex amplitude of the generating solution in the asymptotic analysis
n_{un}	Imaginary part of the complex amplitude of the generating reference solution in the asymptotic analysis
N_{ij}	Coefficients in the order equations of the asymptotic analysis
p	Nondimensional control variable in the asymptotic analysis
p_i	Control variable of the i-th order in the asymptotic solution
$p_{J_{q^*}}$	Characteristic polynomial of the Jacobian matrix at the equilibrium of the system with external feedback control
q_1	Generalized coordinate of the first mode
q_{ref1}	Generalized coordinate of the first mode for the reference solution
q^*	Equilibrium of the system with external feedback control
$\bar{Q}_u$, Q_u	Dimensional, nondimensional generalized forces in the horizontal direction
$\bar{Q}_v$, Q_w	Dimensional, nondimensional generalized forces in the vertical direction
r	Dimensional arc length
R_T	Tip radius
s	Nondimensional arc-length
T	Period
T_i	Time scales
t,t_N	Dimensional, nondimensional time
$\bar{u}$	Dimensional horizontal displacement

U	Amplitude of the parametric excitation
U_g	Nondimensional normalized horizontal scan displacement
$\bar{U}$, $U(\tau)$	Dimensional, nondimensional horizontal scan displacement
$\hat{U}$	Scaled amplitude of the parametric excitation in the asymptotic analysis
$\bar{v}$, v	Dimensional, nondimensional vertical displacement
$\bar{v}_{ref}$	Dimensional reference vertical displacement
V	Amplitude of the external excitation in the asymptotic analysis
V_g	Nondimensional normalized vertical scan displacement
$\bar{V}$, $V(\tau)$	Dimensional, nondimensional vertical scan displacement
$\hat{V}$	Scaled amplitude of the external excitation
w	Nondimensional vertical displacement in a moving reference frame
w_{ref}	Nondimensional reference vertical displacement
$\bar{W}$, W	Dimensional, nondimensional total vertical displacement in the model with external feedback control
W_v^A	Lennard-Jones potential
x	Nondimensional vertical variable
x_{ref}	Nondimensional normalized reference vertical variable, which represents the reference periodic solution in the model with external feedback control
$\bar{x}_{ref}$	Constant mean component of the reference solution vertical variable
$\bar{x}_{ref1}$, $\bar{x}_{ref2}$	Equilibrium positions of the vertical variable for the system with external feedback control
$\tilde{x}_{ref}$	Time-dependent oscillating component of the reference solution vertical variable
$\tilde{x}_{refi}$	Reference solution variable of the i-th order in the asymptotic solution
x_1, x_2	Vertical state-space variables
y	Nondimensional vertical variable in the asymptotic analysis
y_i	Vertical variable of the i-th order in the asymptotic solution
z	Nondimensional control variable
z_1	Root of the dispersion equation
z_s	Nondimensional normalized displacement of the sample surface from the selected reference position

Greek Letters

α	Nondimensional distance between tip and cantilever fixed end
α_1, α_2, α_3	Normalized nondimensional parameters in the equation of motion
β_{ij}	Coefficients in the order equations of the asymptotic analysis
γ	Nondimensional gap distance
γ_{ij},γ_{ijk}	Coefficients in the order equations of the asymptotic analysis
$\bar{\Gamma}_1$, Γ_1	Nondimensional, normalized atomic attractive force constant

$\bar{\Gamma}_2$, Γ_2	Nondimensional, normalized atomic repulsive force constant
δ	Dirac delta
δ_i, δ_{ij}	Coefficients in the order equations of the asymptotic analysis
δ_g	Nondimensional reduction ratio of the tip-sample gap
Δ_2	Coefficient combination of the characteristic polynomial of the Jacobian matrix
ϵ	Small dimensionless ordering parameter in the asymptotic analysis
η_1, η_2	Normalized nondimensional controller's constants
Φ	Frequency combination in the asymptotic analysis
Φ_{un}	Reference frequency combination in the asymptotic analysis
Φ_1	Spatial modal shape of the first mode
Φ_u	Phase of the parametric scan excitation
λ, λ_i	Eigenvalues of the Jacobian matrix
Λ	Dimensional Lagrangian multiplier
μ	Nondimensional beam inertia
μ_1, μ_2	1 Normalized nondimensional parameters in the equation of motion
ν	Nondimensional damping coefficient
ν_1, ν_2	Normalized nondimensional parameters in the equation of motion
$\hat{\nu}_1$, $\hat{\nu}_2$	Scaled parameters in the asymptotic analysis
$\bar{\xi}$, ξ	Dimensional, nondimensional distance of the fixed end of the cantilever from the horizontal reference axis in the model with external feedback control
$\bar{\xi}_s$, ξ_s	Dimensional, nondimensional displacement of the sample surface from the selected reference position
ρ_1, ρ_2	Normalized nondimensional damping parameters in the equation of motion
$\hat{\rho}_1$, $\hat{\rho}_2$	Scaled damping parameters in the asymptotic analysis
σ_a	Typical atomic size
σ_u	Detuning from primary resonance of the parametric excitation in the asymptotic analysis
σ_v	Detuning from primary resonance of the external excitation in the asymptotic analysis
τ	Nondimensional time
ω_H	Coefficient combination of the characteristic polynomial of the Jacobian matrix
ω_s	Frequency scale
ω_u	Nondimensional parametric excitation frequency
ω_v	Nondimensional external excitation frequency
ω_1	Nondimensional natural frequency
Ω_u	Frequency ratio of ω_u with respect to ω_1
Ω_v	Frequency ratio of ω_v with respect to ω_1

Chapter 1

Introduction

1.1 Generalities

Atomic Force Microscopes (AFMs) are powerful devices used for surface analysis in nano-electronics, mechanics of materials and biotechnology, as they permit to topologically characterize surfaces up to micro and nano resolution levels. An AFM consists of a probe, scanner, controller, and a signal processing unit (figure 1.1). AFM works by rastering a sharp probe across the surface to obtain a three-dimensional surface topography. As the probe rasters, it feels the highs and lows of surface topography through complex mechanisms of tip-surface interactions. These signals are sent via a laser reflected back from the probe surface to a photo-detector. The photo-detector, through a feedback control loop, keeps the tip at constant height or constant force from the surface. The feedback signals are sent to a signal processing software, which generates a three-dimensional topograph of the surface.

The operating modes of AFM can be divided into static mode, when the probe does not vibrate during imaging, and dynamic mode, when the cantilever is excited to vibrate at or off its resonant frequency. The dynamic mode AFM can be either an amplitude-modulated AFM (AM-AFM) or a frequency-modulated AFM (FM-AFM), depending on the parameters used as feedback signal, oscillation amplitude in AM-AFM and frequency shift and excitation amplitude in FM-AFM. Usually, AM-AFM is referred to as intermittent contact mode or tapping mode, and is characterized by the close proximity of the probe to the sample surface, which induces both at-

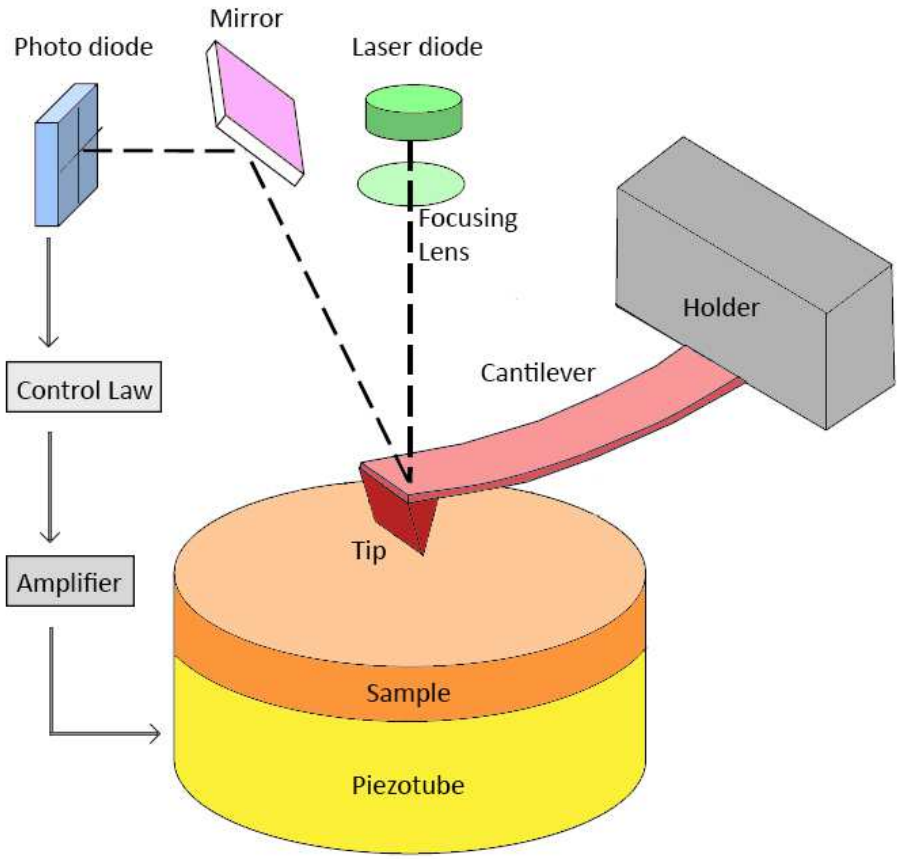

Figure 1.1: Schematic diagram of the main features of an AFM

tractive and repulsive interactions between the probe and the sample atoms depending on their mutual distance. When, on the other hand, the imaging is conducted by manipulating the repulsive interaction between a probe and the surface, AFM is referred to as contact mode AFM, and when the probe images the surface via an attractive interaction, it is usually referred to as noncontact mode, which is also called FM-AFM (figure 1.2).

This study is focused on the latter mode, in which the beam is placed above the sample, and the attractive forces cause the beam to change its stable equilibrium configuration. The new position is a result of the balance between the tip-sample atomic interaction and the stiffness of the beam. When the beam elastic restoring force cannot contrast the attractive atomic force, instability of the equilibrium configuration occurs, with the so called "jump to contact" or escape (in dynamical systems terms) phenomenon.

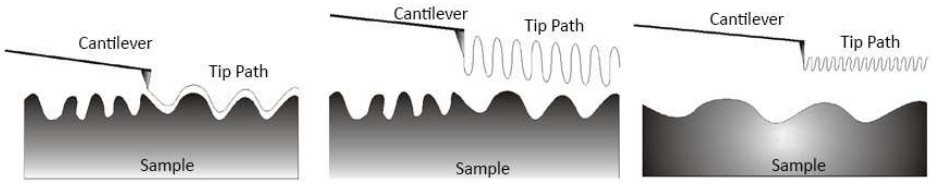

(a) Contact mode (b) Tapping mode (c) Noncontact mode

Figure 1.2: AFM operation modes

In addition, the cantilever motion can be influenced by various perturbations, such as instrumental noise, thermal fluctuations, artifacts created by the AFM tip, contamination of the mineral or tip surface, and tip-induced surface deformations, which cause strong alterations of the dynamical response and lead to possible unstable, aperiodic or even chaotic oscillations. Well-known dynamical events have been experimentally and theoretically documented in responses of atomic force microscopes operating in dynamic mode, so that the crucial importance of investigating the AFM cantilever nonlinear dynamical behavior has been clearly revealed in the last years. Tools of nonlinear dynamics are in fact widely used not only for the purpose of describing and interpreting the dynamical features of several mechanical systems, but also, although still in a marginal way, to obtain useful practical indications to be applied toward design and control. The latter topics, in particular, are of great interest in the field of AFM, and more generally regarding all systems which require a precise calibration of the operating parameters and efficient control techniques aimed at avoiding unwanted responses of the system.

This work intends to deepen both the mentioned instances, on one hand dealing with the detailed analysis of the dynamical behavior of a model of AFM and its dependence on the main system parameters, and on the other hand using the obtained results to provide design indications of practical interest, as well as proposing, in the second part of the thesis, a simple yet effective control technique to prevent dangerous unstable motions.

1.2 Literature review

Starting from the birth of Atomic Force Microscopes (AFMs) in 1986 [11], a considerable number of improvements and developments have been made, and many results have been achieved in measuring topography and physical-chemical properties of organic and inorganic materials at nanometer length scales in a variety of ambient media, together with the manipulation and fabrication of a variety of functional nanostructures. The great success of AFM utilization has produced also a wide variety of experimental and theoretical studies, which have inspired several books [10, 27, 76, 77, 100], surveys and special issues [36, 38, 58, 127] as well as a number of workshops and conferences dedicated to the topic.

In a typical AFM, the topography is imaged by scanning a sharp tip, fixed to the free end of a micro-cantilever vertically bending over the sample surface, and by measuring the tip deflection through a laser technology. The tip-sample interaction modifies the beam dynamics and allows one not only to image surfaces, but also to measure some physical properties of the sample [36, 38, 58]. Thus, referring to a proper mechanical model for the analysis of strongly nonlinear dynamics of these devices, in different operational modalities, is crucial at both the design and in-service phase.

A commonly used model for the AFM microbeam is the lumped-mass model, in which the cantilever beam is modeled as a single spring-mass system [8, 21, 26, 29, 108]. This simple model, however, does not capture the complexity of the spatial-temporal boundary-value problem describing AFM dynamics because of the single-frequency content of the low-order dynamical model. Moreover, its discrete nature does not allow one to account for the effects of the actual geometry and location of the tip in cantilever dynamics, as well as to accurately reproduce the actual control force applied to the continuum structure. On the other hand, the continuum problem of the scanning microbeam is addressed by formulation of the IBVP describing the whole beam's deflection and its boundary conditions. Theoretical investigations that treat the continuum problem include models employing nonlinear boundary conditions and models incorporating nonlinear field forces localized towards the end of the cantilever [17, 44, 45, 85, 94, 110, 117, 118, 120].

As far as the AFM dynamics is concerned, there are three main commonly used techniques for AFM operation, as already mentioned: contact,

tapping and noncontact mode [10]. In contact AFM [4, 38, 107, 117, 118] the tip is brought to a close proximity with the sample, where repulsive forces dominate the tip-sample interaction, and the beam's deflection is measured and compared to the calibrated value. This mode can be operated in constant force mode or constant height mode, depending on whether the feedback loop is turned on or off; the first one is used for non-atomically smooth surfaces, while the second is most suitable for scanning atomically smooth surfaces. This mode permits fast scanning and is used for rough samples and for friction analyses, even if sometimes forces can deform or damage samples. In the intermittent mode (also called tapping or Amplitude Modulation mode (AM-AFM)) [59, 78, 85, 93, 97, 110, 111, 128], the tip operates in the repulsive force region, but touches the surface only for short periods, in order to reduce damage to potentially fragile samples. The cantilever is excited at a setpoint amplitude of cantilever oscillation, which dampens from full oscillation (noncontact) to smaller oscillation when it encounters a structure on the surface (intermittent contact). The change in the amplitude of the probe stores the structural information of the surface, which generates a three-dimensional topography. It is usually conducted on soft samples, such as loosely attached structure on the surface or even more delicate biological samples such as DNA, cells and micro-organisms, and permits high resolution topography, although it becomes more challenging when scanning liquids, for which slower scan speed is needed. In the noncontact mode (also called Frequency Modulation mode (FM-AFM))[1, 21, 29, 38, 86, 120] the tip is excited with a low amplitude (which produces a displacement of a few nm), while vibrating 10-100 nm above the sample surface. In this range, attractive van der Waals forces govern tip-sample interaction and cause a change in its oscillating frequency. Thus, the detection of these forces is performed by measuring the change in the beam's resonance frequency as a function of the tip-surface distance. Thanks to this mode a very low force is exerted on the sample, even if it usually needs ultra high vacuum (UHV) to have best imaging.

For the noncontact AFM the tip has to maintain a design gap from the sample such to ensure that the beam elastic restoring force is stronger than the atomic attraction. Otherwise, an instability of the equilibrium configuration called "jump to contact" or escape (in dynamical systems terms) [115] occurs. As the dynamic excitation tends to strongly reduce the equi-

librium gap, the system stability study as a function of varying excitation amplitude, or other (bifurcation) parameters, is a very important issue for noncontact AFMs, in order to reliably determine the escape threshold separating the region of bounded (i.e., noncontact) solutions from that of unbounded solutions, the latter corresponding to unwanted contacts between tip and sample.

As in all dynamical systems, the existence of possibly transient unbounded solutions is triggered by the occurrence of global bifurcations of the system main saddle, whose analytical approximation is obtained by the Melnikov method [7, 44], whereas in the specific AFM literature the threshold for final jump to contact is determined only via numerical integration of the system equations of motion with fixed initial conditions [44]. In fact to date there are no works that evaluate AFMs escape boundary based on a system bifurcation analysis. Yet, bifurcation diagrams permit to follow the evolution (and eventually the disappearance) of all steady-state solutions of the system (and not only of those related to particular sets of initial conditions) and therefore offer a complete description of the dynamical response as a function of the varying parameter (usually, the forcing amplitude). Examples of systematic numerical simulations based on basins of attraction, bifurcations diagrams and behavior charts which are used to develop a careful interpretation of systems nonlinear dynamical behavior are Rega and Salvatori [91], Rega et al. [92], Szemplinska-Stupnicka [112], Szemplinska-Stupnicka and Tyrkiel [114] for what concerns nonlinear oscillators, Lenci and Ruzziconi [68] for cable-supported beams, Ghayesh et al. [37] for axially moving viscoelastic beams, Orlando et al. [82] for the Augusti's model, Ruzziconi et al. [95],[96] for MEMs and Liu et al. [72] for axially moving plates.

Together with the deep investigation of the dynamical bifurcation behavior, identification of the main kinds of regular response and of their basins of attraction, along with the analysis of the erosion process of the latter up to final escape of the solutions are topics of great theoretical and practical importance, as it is nowadays agreed that the safe operation of a nonlinear system depends not only on the local stability of its solutions but also on the global dynamics associated with the uncorrupted basin surrounding each solution [66, 67]. The issue of safety and integrity of a nonlinear dynamical system was first addressed by Thompson and co-workers [56, 105, 106, 115]

which introduced the concepts of safe basin and erosion profiles. To investigate in an analytical manner how the structure reliability is changed when the parameters of the problem vary, integrity criteria have been proposed in the literature to measure the magnitude of the safe basins [89]; among them the global integrity measure (GIM) and the integrity factor (IF) are capable of providing adequate information without formidable computational efforts. The GIM is defined as the normalized hyper-volume of the safe basin, while the IF is defined as the normalized radius of the largest hyper-sphere entirely belonging to the safe basin. The IF is as computationally easy as GIM, but it succeeds in eliminating the unsafe fractal tongues from the integrity evaluation. It is indeed a measure of the compact part of the safe basin, which is the largest convex set entirely belonging to the basin and the sole region which guarantees the system dynamical integrity. Drawing the integrity measure vs. a selected system parameter which, from a practical point of view, is often the excitation amplitude, provides the so-called "erosion profiles", which are very useful in evaluating the loss of structural safety. Detailed investigations on this topic have been presented by Lenci and Rega [64, 67, 88, 90] who analyzed several definitions of safe basins and different measures for their integrity, and presented also practical applications of dynamical integrity concepts to nonlinear mechanical oscillators [60, 61, 89] and MEMs [63], as well as other authors who applied them to nonlinear oscillators (Lansbury et al. [56], Szemplinska-Stupnicka [112], Soliman and Thompson [106], Souza and Rodrigues [109], Xu et al. [121], Gan et al. [35]), to cylindrical shells (Gonçalves et al. [40], Gonçalves et al. [39], Soliman and Gonçalves [104]), to suspended bridges (de Freitas et al. [24]), to guyed masts (Orlando et al. [83]) and to MEMs (Ruzziconi et al. [95]), just to quote some examples. Integrity tools are here used to theoretically check the robustness of competing attractors [65], [40], [39] and to analyze erosion processes that bring to the escape from bounded regions [60], [67], [114], but they become also practical instruments to validate experimantal results and to furnish valuable information toward engineering design [83], [96], [69]. Conversely, analyses devoted to investigate the solutions robustness and dynamical integrity are to date lacking in AFM literature, despite several numerical analyses have been accomplished to describe the AFM nonlinear dynamical behavior. Moreover, in spite of many studies concerning AFMs operating in tapping mode, such as investigation of their bistable

oscillatory regime [14, 80, 85], detection of subharmonic, quasiperiodic and chaotic motions [7, 23, 50, 122], examination of possible internal resonances [94, 97] and influence of higher modes [3, 53], a handful of results refers to the noncontact AFMs [20, 21, 44, 45, 120].

On the other hand, another topic of crucial importance in the AFM operation study concerns motion control to avoid possible unstable or chaotic responses of the system. It is in fact known that AFM nonlinear dynamics exhibits several nonlinear phenomena, such as bifurcations, in-well instability regions and possibly chaotic motions, that are common to many other dynamical systems and represent an undesirable behavior which restricts the operating range of many electronic and mechanical devices. For this reason, several control techniques have been proposed in the last two decades, mostly devoted to the interesting feature of controlling chaos of whatsoever dynamical system. The starting point of this field is the work published at the beginning of the 90s by Ott et al. [84], who suggested a method (known as OGY method) for stabilizing an unstable periodic orbit by making a small time-dependent perturbation in the form of feedback to an accessible system parameter. Subsequently, an alternative approach has been introduced by Pyragas [87], who proposed two effective control methods for continuous chaotic dynamical systems, the external and the delayed feedback control technique. The first method combines feedback with a periodic external force of a special form, while the second (DFC method) is based on a self-controlling delayed feedback and thus does not require any external force. Starting from these pioneering works, several books [16, 18, 19, 33, 51, 52, 57, 99, 102], surveys [12, 13, 31, 32, 34, 88], journal issues [5, 64], conference symposia and workshops have been devoted to the topic of chaos control, together with various attempts to classify control techniques and goals to be attained with them. Among them, Chen and Dong [19] proposed a classification based on various tools employed in the control process (parameter-dependent approaches, open-loop strategies, engineering feedback control, adaptative control, intelligent control, etc.), while Fradkov [31] proposed also a classification of the various applications in science and engineering. Recent classifications focused on the phenomenological aspects of chaos control distinguish among techniques aimed at stabilizing an unstable zone in parameter space or moving away from previously known chaotic zones (control by system design [12], control through operating conditions,

parametric variation methods [19]), techniques which stabilize a given, erratic solution (classical methods where a properly modified input, periodic or a-periodic, open-loop or feedback, is applied to the system [47, 48, 87, 103], OGY method and its revision and enhancement [28, 42, 84, 125]) and methods able to regularize the overall system dynamics, irrespective of a single solution behavior (method based on either combining parametric and external excitations [71], or applying weak periodic perturbations [16], or modifying the shape of the excitation [62, 90]). Together with the great development of chaos control theory, several experimental realizations have been carried out in the area of science and engineering, such as the physics of turbulence, laser physics and optics, physics of plasma, molecular and quantum physics, chemistry and electrochemistry, biology and ecology, economics and finance, medicine, electrical and chemical engineering, motion control, telecommunication and information systems. Many theoretical and experimental studies have focused also on mechanics and mechanical engineering, an extensively survey of which was presented by Fradkov and Evans [32], who referred to pendulums, beams and plates, stick-slip friction motion, impacting systems, spacecrafts, vibroformers, ship oscillations, robot-manipulator arms, earthquake engineering applications, milling, whirling motion under mechanical resonance and mechanical systems with clearance.

Also in the field of AFMs, chaos control techniques have been applied to improve microscope performances or avoid unwanted behaviors: Ashhab et al. [8] proposed a state feedback control based on the Melnikov function; Humphris et al. [46] used a positive feedback system to improve the AFM force; Zou et al. [129] presented and experimentally applied an inversion-based feedback/feedforward control approach; Merry et al. [74] applied a feedback control to all of 3 d.o.f. of a metrological AFM. Besides, Arjmand et al. [6] used a nonlinear delayed feedback control to control chaos in AFMs, as well as Yamasue and Hikihara [126] and Salarieh and Alasty [98]. Moreover, a feedback control composed by a sliding mode control (SMC) and a backstepping feedback is proposed by Wang et al. [119] to control chaotic motions in a spring-mass model of AFM, while Nozaki et al. [81] applied the State Dependent Riccati Equation (SDRE) together with time-delayed feedback control to a tapping-mode AFM model, and Korayem et al. [54] used a sliding mode controller. Furthermore, Yagasaki [123] has recently applied the external feedback control technique proposed by Pyragas to a

simple tapping AFM model, which works by keeping the cantilever vibration to a selected reference one and allowing to simultaneously measure the sample surface.

1.3 Aims of the work

Considered the above mentioned state of the art, the research focuses on the description of the global dynamical behavior of a reduced-order model of AFM. Different numerical analyses and continuation techniques are employed to investigate the evolution of the main system periodic solutions and relevant basins of attraction under variations of the most significant system parameters. Local bifurcations, stability boundaries and basin erosion processes are studied in presence of the parametric horizontal excitation, as well as of the external one, the former corresponding to horizontal scan excitation of the AFM cantilever, the latter to vertical motion of its support. Similarities and differences on the system outcomes, in the vicinity of both primary and subharmonic resonance regions, are highlighted.

The obtained behavior charts represent a valuable tool not only to compare the results with the literature findings, but also as practical instruments able to characterize the operation ranges in terms of the selected parameters.

Within the same perspective, dynamical integrity concepts, such as basin-of-attraction detection, and quantification of their erosion process via integrity measures, are applied to determine acceptable frequency-dependent thresholds associated with a priori safe design targets.

On the other hand, the mentioned analyses allow one to theoretically discuss similarities and differences between the chosen global approach and the more traditional local one: the first involves the study of the evolution of the periodic solutions and of their basins, while the other one is based on the numerical integration of single trajectories.

Furthermore, an external feedback control is introduced at the outset of the model formulation, with the aim to take the system response to a selected reference one, and thus provide a simple and efficient method to avoid possible unstable motions.

Upon checking the effectiveness of the procedure in the weakly nonlinear regime via a perturbation approach, several numerical analyses in the

strongly nonlinear regime are carried out for the controlled model too, with the aim of achieving a description of its dynamical behavior in terms of the newly inserted control parameters, and to realize a comparison with the previous results related to the uncontrolled system. The latter objective has the practical consequence of permitting the critical evaluation of the effectiveness of the control actuation on the system dynamics, with also a view to the overall response scenario.

1.4 Thesis outline

The first part of this thesis deals with the strongly nonlinear dynamics of a reduced-order model of noncontact AFM formulated by Hornstein and Gottlieb [44], and presents results obtained by the combined use of bifurcation diagrams, behavior charts, attractor-basins phase portraits and erosion profiles. In the second part of the work an external feedback control according to the Yagasaki [123] proposal is applied to the same AFM model, and its effect on the dynamical behavior of the system is analyzed in view of a comparison with the previous results.

More specifically, Chapter 2 includes a brief description of the single-mode model noncontact AFM proposed by Hornstein and Gottlieb [44] which represents the object of further numerical analyses; Chapter 3 is devoted to a systematic detection of bifurcation scenarios, response charts and escape thresholds for the system under horizontal parametric excitation and under vertical external excitation. On the other hand, the issue of dynamical integrity and basins erosion is elaborated in Chapter 4, which presents several erosion profiles and isointegrity curves for both the parametrically and externally forced system. A comparison between theoretical and practical stability boundaries of possible intent for design purposes is finally presented in Chapter 5. The topic of controlling undesirable system dynamical responses is addressed in Chapter 6, with the formulation of a 2-dof system of AFM model with external feedback control (Sect. 6.1) and analysis of existence and stability of its equilibrium solutions (Sect. 6.2). The weakly nonlinear dynamics of the controlled system is analyzed in Chapter 7 by means of the asymptotic technique of multiple scales, together with its validation via comparison with numerical results. A detailed description of the strongly nonlinear dynamical behavior for the system under horizontal

and vertical excitation applied separately is shown in Chapter 8, where the influence of the applied control on the overall dynamical behavior of the AFM system is discussed together with some critical aspects of practical utility summarized in the concluding part of the work.

Chapter 2

Continuum formulation and reduced-order modeling

In AFMs, a small radius tip is connected to a cantilever with a low spring constant and interacts with a surface; in the non-contact mode region, the tip is always in the weak attractive region, so that the sample and tip are not easily damaged. Away from the surface, the cantilever is made to oscillate close to its resonance frequency at a certain oscillation amplitude. When the tip is close to the surface, the gradient of the total force on the tip acts as an additional spring on the cantilever, so that it changes its resonant frequency and, consequently, its amplitude, measured by a lock-in amplifier. The deflection signal is then fed to the lock-in amplifier, and a feedback loop performs topography changing the voltage in a piezoscanner used to control the cantilever oscillation. Thus, imaging of the surface topography in AFM is performed by measurement of the changes of the microbeam properties and the quality of the mathematical model used for the microstructure dynamics influences the force estimation and consequently the final mapping of the measured surface. Among many lumped-mass-spring-dashpot models presented in literature, Hornstein and Gottlieb [44] proposed a general nonlinear continuum model of noncontact AFM which consistently incorporates the generalized forces describing motion control and tip-sample interaction and which the following sections refer to.

2.1 Equations of motion

The physical model at the base of the work is a fixed-free AFM microcantilever, which is assumed to be planar, inextensible and horizontal, with length L and a sharp tip of height h_T close to its free end, and with a distance g between its fixed side and the sample (figure 2.1). The beam material is considered linearly elastic, homogeneous and isotropic, with Young's modulus denoted by E. The general formulation proposed by Hornstein and Gottlieb [44], based on the classical inextensional beam model of Crespo da Silva and Glynn [22], is referred to and is reported here for the sake of completeness. The associated set of two truncated coupled PDEs for the beam

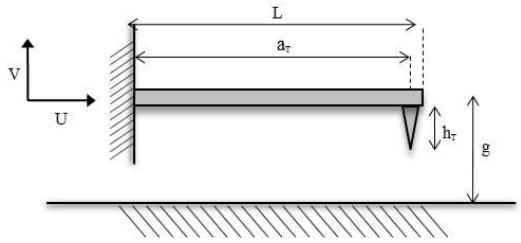

Figure 2.1: Microbeam parameters

horizontal and vertical transverse vibrations is

$$\begin{aligned} &m\bar{u}_{tt} - [EI\bar{v}_{rrr}\bar{v}_r - J_z\bar{v}_{ttr}\bar{v}_r + \Lambda(1+\bar{u}_r)]_r = \bar{Q}_u \\ &m\bar{v}_{tt} - [EI(\bar{v}_{rrr} + \bar{v}_r\bar{v}_{rr}^2) + J_z(\bar{v}_{ttr} + \bar{v}_{tr}^2\bar{v}_r) + \Lambda\bar{v}_r]_r = \bar{Q}_v \end{aligned} \tag{2.1}$$

where $\bar{u}(r,t)$ and $\bar{v}(r,t)$ are the horizontal and vertical displacements and subscript letters denote partial differentiation with respect to the arc-length r and time t. Coefficients EI, J_z and m are the beam flexural stiffness, principal mass moment of inertia about z and mass per unit reference length, respectively, and Λ is a Lagrange multiplier accounting for the inextensibility condition. Generalized forces in the horizontal and vertical directions are represented by $\bar{Q}_u$ and $\bar{Q}_v$, the former corresponding to a feedback control force depending on the horizontal displacement and the latter also accounting for the localized (at $r = a_T$ see figure 2.1) transverse atomic force interaction. They have the following expressions

$$\begin{aligned} \bar{Q}_u &= -\bar{g}_1\bar{u}_t - \bar{g}_2\bar{u}_{trr} - \bar{g}_3\bar{u} \\ \bar{Q}_v &= \delta(r-a_T)F_v^A - d\bar{v}_t \end{aligned} \tag{2.2}$$

where $\bar{g}_1$, $\bar{g}_2$ and $\bar{g}_3$ are coefficients related to linear viscous damping, material viscoelastic damping and a proportional displacement gain, respectively, while d is a viscous damping coefficient and δ is the Dirac delta. F_v^A takes into account the interaction forces between cantilever tip and sample; different intermolecular, surface and macroscopic effects, in fact, give rise to interactions with distinctive distance dependencies. They can involve a variety of forces derived from electric, magnetic, and atomic interactions for the noncontact regime, and from atomic, indentation, adhesion, and capillary interactions for the contact regime. Several approximations to simulate tip-surface forces have been proposed, based on continuum mechanics (Hertz model, JKR model, MD model, Schwarz model), long-range van der Waals force, capillary forces, short-range forces, electrical double-layer force in a liquid, and contamination effects [15, 49, 73]. In absence of external fields and without special environmental conditions, an intermediate approach that represents a good compromise between a realistic description of the tip-surface interaction and reasonable computational times consists in referring to the phenomenological Lennard-Jones potential [49, 101] for a sphere-plane system, which combines the attractive van der Waals and repulsive atomic potentials, yielding

$$W_v^A = \frac{A_H R_T}{6\sigma_a}\left[\frac{1}{210}\left(\frac{\sigma_a}{g_a}\right)^7 - \frac{\sigma_a}{g_a}\right] \tag{2.3}$$

The term out of parenthesis to the right-side is the magnitude of the potential in terms of Hamaker constant A_H and tip radius R_T, while the term in parenthesis describes the shape of the potential in terms of the actual tip-sample distance g_a and a typical atomic distance σ_a. The Lennard-Jones force F_v^A, localized at the tip of the microcantilever (figure 2.1), is obtained by taking the derivative of the potential function with respect to g_a and changing its sign

$$\begin{aligned} F_v^A &= \frac{A_H R_T}{6\sigma_a^2}\left[-\frac{\sigma_a^2}{g_a^2} + \frac{1}{30}\frac{\sigma_a^8}{g_a^8}\right] \\ &= \frac{A_H R_T}{6\sigma_a^2}\left[-\left(\frac{\sigma_a}{g+\bar{v}-h_T}\right)^2 + \frac{1}{30}\left(\frac{\sigma_a}{g+\bar{v}-h_T}\right)^8\right] \end{aligned} \tag{2.4}$$

where $s = g + \bar{v} - h_T$ and h_T is the tip height.

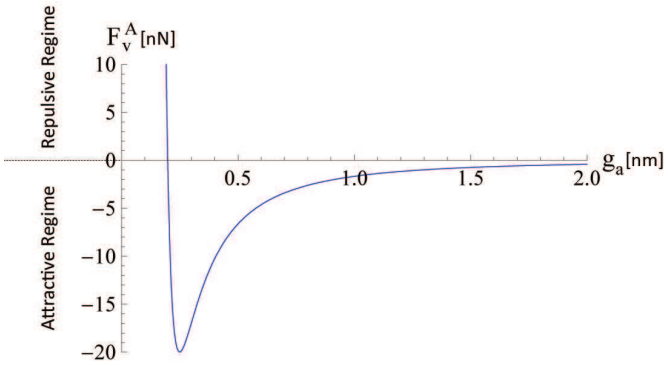

Figure 2.2: Lennard-Jones force as a function of the tip-sample distance s, for $R_T = 10$ nm, $\sigma_a = 0.35$ nm, $A_H = 1$ aJ

The set of non-homogeneous boundary conditions

$$\begin{aligned} &\bar{v}(0,t) = \bar{V}(t), \quad \bar{v}_r(0,t) = 0, \qquad \bar{u}(0,t) = \bar{U}(t), \\ &\bar{v}_{rr}(L,t) = 0, \qquad \bar{v}_{rrr}(L,t) = 0, \quad \bar{u}_r(L,t) = 0. \end{aligned} \tag{2.5}$$

completes the formulation of the problem, with $\bar{V}(t)$ and $\bar{U}(t)$ the vertical transverse and horizontal scan displacement, respectively. The holonomic inextensibility constraint ($(1+\bar{u}_r)^2 + \bar{v}_r^2 = 1$) integration and incorporation in the horizontal boundary conditions yields

$$\bar{u}(r) = \bar{U}(t) - \int_0^r \bar{v}_r^2 \mathrm{d}r \tag{2.6}$$

Its substitution in the first equation of (2.1) and the subsequent integration of the partial integro-differential equation, allows one to isolate the Lagrangian multiplier:

$$\begin{aligned} \Lambda = \left(1 - \frac{1}{2}\bar{v}_r^2\right)^{-1} \Bigg[& J_z \bar{v}_{ttr} \bar{v}_r - EI \bar{v}_{rrr} \bar{v}_r \\ & + m \int_L^r \bar{U}_{tt} \mathrm{d}r - \frac{m}{2} \int_L^r \frac{\mathrm{d}^2}{\mathrm{d}t^2} \left(\int_0^r \bar{v}_r^2 \mathrm{d}r \right) \mathrm{d}r - \int_L^r \bar{Q}_u \mathrm{d}r \Bigg] \end{aligned} \tag{2.7}$$

Rescaling the boundary problem by its length L ($s = r/L$) and time ($\tau = \omega_s t$) by a standard characteristic frequency $\omega_s = \sqrt{EI/mL^4}$, expanding the multiplier up to the cubic order and substituting into the nondimensional

form of the second of (2.1) yields

$$\begin{aligned} v_{\tau\tau} + v_{ssss} - \mu v_{\tau\tau ss} - Q_v = \Bigg[& -v_s \left(v_{ss} v_s\right)_s + \mu v_s \left(v_{\tau s} v_s\right)_\tau \\ & - v_s \frac{1}{2} \int_1^s \left(\int_0^s v_s^2 \mathrm{d}s \right)_{\tau\tau} \mathrm{d}s + v_s \left(1 + \frac{1}{2} v_s^2\right) \\ & \left(\int_1^s U_{\tau\tau} \mathrm{d}s - \int_1^s Q_u \mathrm{d}s \right) \Bigg]_s \end{aligned} \tag{2.8}$$

where

$$\begin{aligned} v = \bar{v}/L, \qquad & v_s = \bar{v}_r, \qquad & v_{ss} = \bar{v}_{rr}/L, \\ v_{sss} = \bar{v}_{rrr}/L^2, \qquad & Q_u = L^3 \bar{Q}_u / EI, \qquad & Q_v = L^3 \bar{Q}_v / EI, \\ \mu = J_z / mL^2, \quad & U(\tau) = \bar{U}/L, \qquad & V(\tau) = \bar{V}/L. \end{aligned} \tag{2.9}$$

Equation 2.8, expressed in an inertial reference system, has nonhomogeneous boundary conditions; it is thus convenient to transform the nondimensional system in equation 2.8 to a moving reference frame:

$$v(s,\tau) = w(s,\tau) + V(\tau) \tag{2.10}$$

It results

$$\begin{aligned} w_{\tau\tau} + V_{\tau\tau} + w_{ssss} - \mu w_{\tau\tau ss} - Q_w = \Bigg[& -w_s \left(w_{ss} w_s\right)_s + \mu w_s \left(w_{\tau s} w_s\right)_\tau \\ & + w_s \left(\left(1 + \frac{1}{2} w_s^2\right) \left(U_{\tau\tau} - \int_1^s Q_u \mathrm{d}s \right) \right. \\ & \left. - \frac{1}{2} \int_1^s \left(\int_0^s w_s^2 \mathrm{d}s \right)_{\tau\tau} \mathrm{d}s \right) \Bigg]_s \end{aligned} \tag{2.11}$$

where

$$\begin{aligned} Q_u = & -g_1 \left[U_\tau(\tau) - \frac{1}{2} \frac{\partial}{\partial \tau} \left(\int_0^s w_s^2 \mathrm{d}s \right) \right] \\ & + \frac{1}{2} g_2 \left[\frac{\partial^3}{\partial \tau \partial s^2} \left(\int_0^s w_s^2 \mathrm{d}s \right) \right] - g_3 \left[U(\tau) - \frac{1}{2} \int_0^s w_s^2 \mathrm{d}s \right] \\ Q_w = & \, \delta(s-\alpha) \bar{\Gamma}_1 \left[- \frac{1}{(\gamma + w + V(\tau))^2} + \frac{\bar{\Gamma}_2}{(\gamma + w + V(\tau))^8} \right] \\ & - \nu (w_\tau V \tau(\tau)) \end{aligned} \tag{2.12}$$

and

$$\begin{aligned} g_1 &= \bar{g}_1 L^4 \omega_s / EI, \quad g_2 = \bar{g}_2 L^2 \omega_s / EI, \quad g_3 = \bar{g}_3 L^4 \omega_s / EI, \\ \bar{\Gamma}_1 &= A_H R_T / 6EI, \quad \bar{\Gamma}_2 = (\sigma_a L)^6 / 30, \quad \nu = d\omega_s L, \\ \alpha &= a_T / L, \quad \gamma = (g - h_T)/L. \end{aligned} \tag{2.13}$$

g_1, g_2 and g_3 are controller's constants, $\bar{\Gamma}_1$ and $\bar{\Gamma}_2$ are nondimensional atomic force constants, α is the nondimensional distance between tip and microbeam fixed end, γ is the nondimensional gap distance and ν is the nondimensional damping coefficient. A set of homogeneous boundary conditions completes the problem formulation:

$$w(0,\tau) = 0, \quad w_s(0,\tau) = 0, \quad w_{ss}(1,\tau) = 0, \quad w_{sss}(1,\tau) = 0. \tag{2.14}$$

2.2 Single-mode model

To study the main aspects of the nonlinear dynamics of AFMs, reduced-order models can be satisfactorily used by considering the first-order approximation of the generalized force of transverse interaction. In this perspective, it has been shown that for tapping AFMs a multimode Galerkin approximation allows to detect nonlinear phenomena (e.g. grazing bifurcations) which a single-mode analysis cannot describe [3, 9], thus highlighting the importance of employing higher-order modes to avoid qualitative and quantitative errors. However, in the noncontact operation range, a multimode discretization does not enrich the system response, and a single-mode approximation is thus sufficient to detect the main nonlinear aspects [9]. Moreover, the frequency range of the analyses reported in this paper spans around the primary and subharmonic resonance of the first mode, where the contribution of the higher modes is substantially negligible [45]. For these reasons, a single-degree-of-freedom model is used for the purposes of this work, as it allows feasible analyses and computations aimed at highlighting the main response aspects in the absence of internal resonances, which are instead considered in [43]. Thus, a single-mode assumption and a Galerkin procedure are employed to reduce the IBVP to a set of ordinary differential

equations:

$$w(s,\tau) = q_1(\tau)\Phi_1(s) \tag{2.15}$$

where the basis function is that of a clamped-spring beam:

$$\begin{aligned} &\Phi_1(s) = \cosh(z_1 s) - \cos(z_1 s) - K_1\left(\sinh(z_1 s) - \sin(z_1 s)\right), \\ &K_1 = \frac{\cos(z_1 s) + \cosh(z_1)}{\sin(z_1) + \sinh(z_1)} \end{aligned} \tag{2.16}$$

and the frequencies are obtained form the dispersion equation:

$$\begin{aligned} \omega_1 = z_1^2 : \\ z_1^3\left[\cosh(z_1 s)\cos(z_1 s)\right] - f_1\left[\sin(z_1 s)\cosh(z_1 s)\right. \\ \left. - \cos(z_1 s)\sinh(z_1 s)\right] \end{aligned} \tag{2.17}$$

Substitution of (2.15) into (2.11)-(2.12), multiplication by $\Phi_1(s)$ and integration over the domain yields

$$\begin{aligned} &I_1 q_{1\tau\tau} + I_{11}(\nu q_{1\tau} + \omega_1^2 q_1) + I_2(V_{\tau\tau}(\tau) + \nu V_\tau(\tau)) + I_3 q_1^3 \\ &\quad + I_4 q_1\left(q_{1\tau}^2 + q_{1\tau\tau} q_1\right) = q_1^2 q_{1\tau}\left(g_1 I_{41} + g_2 I_7\right) + \frac{1}{2} q_1^3 I_{41} g_3 \\ &\quad + \bar{\Gamma}_1 \Phi_1(\alpha)\left(-\frac{1}{\left(\gamma + q_1\Phi_1(\alpha) + V(\tau)\right)^2}\right) \\ &\quad + \left(q_1 I_5 + \frac{1}{2} q_1^3 I_6\right)\left(U_{\tau\tau}(\tau) + g_1 U_\tau(\tau) + g_3 U(\tau)\right) \end{aligned} \tag{2.18}$$

where expressions of the I_{ij} integrals are reported in Appendix A. Here the repulsion interaction ($\bar{\Gamma}_2$) has been neglected, since the work focuses on noncontact mode, for which the most important atomic force interaction is the attractive one, associated with the Γ_1 parameter. A new variable $x(\tau) = q_1(\tau)\Phi_1(\alpha)/\gamma$ is defined, and a new time scale $t_N = \omega_1\tau$ is introduced

to obtain

$$\begin{aligned}\left(1+\alpha_2 x^2\right)\ddot{x}+\left(\alpha_1+\alpha_2\dot{x}^2+\alpha_3 x^2\right)x=\\ -\frac{\Gamma_1}{\left(1+x+V_g\right)^2}-\left(\rho_1+\rho_2 x^2\right)\dot{x}\\ -\left(\ddot{V}_g+\nu_1\dot{V}_g\right)\nu_2\\ +\left(\mu_1 x+\mu_2 x^3\right)\left(\ddot{U}_g+\eta_1\dot{U}_g+\eta_2 U_g\right)\end{aligned} \tag{2.19}$$

where

$$\begin{aligned}&\alpha_1=\frac{I_{11}}{I_1},\quad \alpha_2=\frac{\gamma^2 I_4}{\Phi_1(\alpha)I_1},\quad \alpha_3=\frac{\gamma^2}{\Phi_1^2(\alpha)\omega_1^2}\left(\frac{I_3}{I_1}+\frac{g_3 I_{41}}{2I_1}\right),\\ &\Gamma_1=\bar{\Gamma}-1\frac{\Phi_1^2(\alpha)}{\gamma^3\omega_1^2 I_1},\quad \mu_1=\frac{I_5\gamma}{I_1},\quad \mu_2=\frac{I_6\gamma^3}{2\Phi_1^2(\alpha)I_1},\\ &\rho_1=\frac{\nu I_{11}}{\omega_1 I_1},\quad \rho_2=\frac{\gamma^2}{\Phi-1^2(\alpha)}\left(\frac{g_1 I_{41}}{\omega_1 I_1}\frac{g_2 I_7}{\omega_1 I_1}\right),\quad \eta_1=\frac{g_1}{\omega_1},\\ &\eta_2=\frac{g_3}{\omega_1},\quad \nu_1=\frac{\nu}{\omega_1},\quad \nu_2=\frac{I_2\Phi_1(\alpha)}{I_1},\quad V_g=\frac{V(\tau)}{\gamma},\quad U_g=\frac{U(\tau)}{\gamma}.\end{aligned} \tag{2.20}$$

ρ_1 is the damping coefficient; U_g and V_g are horizontal and vertical excitations, respectively, that are supposed to be harmonic ($U_g = U\sin(\omega_u t)$, $V_g = V\sin(\omega_v t)$); η_1, η_2 and ρ_2 are feedback control parameters related to the time-dependent horizontal scan and the cubic damping term, respectively; the coefficient α_3 of the cubic stiffness term is also affected by the horizontal control gain. Looking at the various orders of magnitudes of the parameters in (2.20) with respect to the nondimensional distance between the tip and the sample γ, it results that α_1 is of order 1, whereas both α_2 and α_3 are a function of γ^2. Choosing a dimensional gap (between the tip and the sample) of $g - h_T = 100$ nm, and a microbeam length of $L = 200$ μm, it turns out to be $\gamma = O(10^{-4})$ and $\gamma^2 = O(10^{-8})$, so that both $\alpha_2, \alpha_3 \ll \alpha_1$, and for the other parameters, $\mu_2 \ll \mu_1$ and $\rho_2 \ll \rho_1$. Accounting for the orders of magnitude of various coefficients in commercial AFMs [44], and in view of obtaining a simplified model for the numerical analyses reported hereafter, terms related to feedback controls and the nonlinear term related to α_2 can thus be neglected, while the curvature nonlinearity, which is related to the coefficient α_3, is considered different from zero. The latter also depends on the neglected proportional displacement gain of the controller in the horizontal direction; yet, even consistently considering only small varia-

tions of α_3, it is possible to observe nontrivial modifications of the position and amplitude of the system response, as shown, e.g., in the following figure 2.3, where the almost negligible contribution of α_2 is also highlighted.

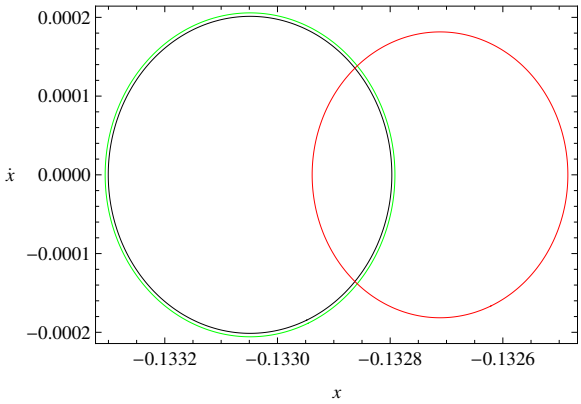

Figure 2.3: System periodic response in the state plane for $\alpha_2 = 0$, $\alpha_3 = 0$ (black orbit), $\alpha_2 = 0$, $\alpha_3 = 0.1$ (red orbit) and $\alpha_2 = 0.1$, $\alpha_3 = 0$ (green orbit)

The simplified dynamical system becomes

$$\begin{aligned} \ddot{x} + \alpha_1 x + \alpha_3 x^3 = &-\frac{\Gamma_1}{(1+x+V_g)^2} - \rho_1 \dot{x} \\ &- \left(\ddot{V}_g + \nu_1 \dot{V}_g\right) \nu_2 + \mu_1 x \ddot{U}_g \end{aligned} \tag{2.21}$$

which describes the single-mode dynamics of a nonlinear microcantilever with a localized atomic interaction, subject to both parametric and external excitation. Note that the vertical excitation V_g appears also in the nonlinear atomic interaction term, thus generating a parametric excitation which adds to the sole external ones, after a series expansion. However, since the ensuing relation with the variable x is of order -3, it is reasonable to liken the effects of the vertical excitation V_g to those of the sole externally forced problem.

2.3 Equilibrium analysis

The operation domain of noncontact AFMs must be such to avoid jump to contact with the scanned sample. In dynamical system terms, this is ascertained by considering the undamped, unforced version of (2.21)

$$\alpha_1 x + \alpha_3 x^3 + \frac{\Gamma_1}{(1+x)^2} = 0 \tag{2.22}$$

whose Hamiltonian version reads

$$\begin{cases} x_1 = x, \quad \dot{x}_1 = \dfrac{\partial H}{\partial x_2} \\ x_2 = \dot{x}, \quad \dot{x}_2 = -\dfrac{\partial H}{\partial x_1} \end{cases} \tag{2.23}$$

$$H(x_1, x_2) = \frac{\alpha_1 x_1^2}{2} + \frac{\alpha_3 x_1^4}{4} - \frac{\Gamma_1}{1 + x_1} + \frac{x_2^2}{2}$$

with the associated single potential well with left (i.e. , towards the sample position $x = -1$) contact direction. The unperturbed state space is depicted in figure 2.4(a), where the two fixed points of the time-independent problem, the stable equilibrium (E) of the cantilever tip under elastic (α_1, α_3) and atomic interaction (Γ_1) forces and the corresponding hilltop saddle (S), are reported for a given set of values of the governing parameters. The homoclinic orbit of the saddle is also plotted in figure 2.4(a): it separates the inner region of bounded periodic solutions from the outer region of unbounded solutions, the former representing the safe domain for noncontact AFM operation.

The study of the fixed points as a function of the atomic interaction coefficient Γ_1 is reported in figure 2.4(b) for $\alpha_1 = 1$ and $\alpha_3 = 0.1$, and fixes the upper boundary for the stable equilibrium E existence at the limit value $\Gamma_1 = 4/27$ where a saddle-node bifurcation leads to the birth of the unstable branch S. Beyond this point, the microbeam "jump to contact" with the sampled surface. Note that the fixed points and the extent of the safe domain

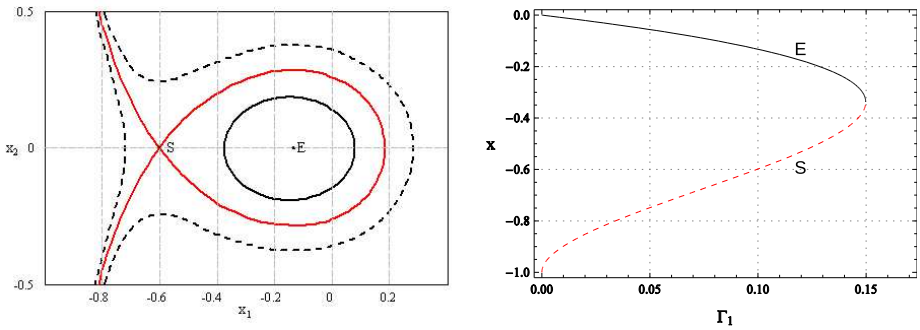

(a) (b)

Figure 2.4: Unperturbed phase space for $\Gamma_1 = 0.1$ (a) and fixed points as a function of Γ_1 (b) for $\alpha_1 = 1, \alpha_3 = 0.1$. Homoclinic orbit (solid red), periodic orbit (solid black), unbounded orbit (dashed black), equilibrium point (E), saddle point (S)

depend not only on the balance between atomic interaction force and nonlinear elastic force of the microbeam but also on the horizontal control gain taken into account by the α_3 coefficient [44]. Apart from the distinct physical framework, the bounded/unbounded nature of the AFM Hamiltonian phase space is analogous to that of a number of archetypal softening systems [60, 112, 115], also occurring in micromechanics (see, e.g. , [2, 63, 95, 96]), which possibly undergo escape of the response from the single potential well in one direction. In the AFM physical context, this phenomenon corresponds to jump of the microbeam tip to contact with the sampled surface. This operation mode is precluded in noncontact AFMs: so, there is a great interest in analyzing the conditions for its impending occurrence in different ranges of frequency around parametric and/or external resonance, along with the features through which they are realized when varying a control parameter, typically an excitation amplitude characteristic of the system.

In this last respect, the AFM scan process is performed by means of both vertical and horizontal excitations, the former allowing to quantify the interaction forces and the latter being necessary to obtain the three-dimensional map of the sample. Yet, in existing commercial AFMs the horizontal scan frequency is much smaller than the vertical one (which is on the order of 100 kHz and above) [44, 101]. Thus, in view of a systematic bifurcation analysis of the response, it appears reasonable to study the two forced cases in the neighborhood of resonances separately, as their weak interaction does not meaningfully modify the qualitative and quantitative behavior of the system. Following [44], most of the results presented in the subsequent sections will refer to the sole horizontal scan (i.e. , $V_g = 0$), which entails only parametric excitation, with the equation (2.21) reading

$$\ddot{x} + \alpha_1 x + \alpha_3 x^3 = -\frac{\Gamma_1}{(1 + x + V_g)^2} - \rho_1 \dot{x} - \mu_1 x U \omega_u^2 \sin(\omega_u t) \tag{2.24}$$

However, considering the major role played by the sole vertical external excitation (i.e. , $U_g = 0$) in the AFM resonant dynamics [36, 77], it will be addressed in the Sect. 3.2, as well.

Chapter 3

Local bifurcations and response scenarios

The nonlinear response of the AFM single-mode model described in the previous chapter has been analyzed via continuation techniques (using Dynamics software and AUTO software) and numerical simulations, taking into account the presence of the horizontal parametric excitation and of the vertical external one, separately.

Several bifurcation diagrams have been obtained in a large range of forcing frequencies which includes the fundamental (primary) ($\omega_u(\omega_v) \cong \omega_1$) and principal (subharmonic) ($\omega_u(\omega_v) \cong 2\omega_1$) parametric (external) resonances, whereby the main periodic solutions and local bifurcations have been detected (for a description of such bifurcations in terms of Floquet multipliers, see Appendix D). These diagrams, produced by increasing slowly the forcing amplitude while holding the frequency constant, exhibit a variety of response scenarios. The local bifurcation loci in the excitation parameter control space (forcing frequency vs. forcing amplitude) are summarized in semi-logarithmic charts, which report also the system escape threshold obtained as the envelope of local bifurcation escape thresholds in different parameter ranges. The escape excitation amplitude corresponds to total annihilation of all basins of attraction (see Chapter 4 forward) and, from a physical viewpoint, it represents the (unacceptable) amplitude value that would bring the beam tip oscillation beyond the location of the sample (at $x = -1$).

3.1 AFM system under parametric excitation

The parametrically excited single-mode model (2.24) has been analyzed for the following set of parameter values

$$\alpha_1 = 1, \quad \alpha_3 = 0.1, \quad \rho_1 = 0.001, \quad \mu_1 = 1.5708, \quad \Gamma_1 = 0.1$$

corresponding to those chosen in [44]. The calculated natural frequency for these values is $\omega_1 = 0.8358$. For the sake of completeness, it is useful to report here that analyses concerning the effect of the damping ratio variation on the system escape threshold have been presented by Hornstein and Gottlieb [44]; the results show that increasing the damping by two orders of magnitude (corresponding to low damping (10^{-4}) in ultra-high vacuum and larger damping (10^{-2}) in air) does not modify the fundamental structure of the escape region. As a consequence, the following numerical analyses have been carried out setting the damping parameter at a fix intermediate value of 10^{-3}.

The local bifurcation loci in the ω_u-U plane, obtained as result of a series of bifurcation diagrams, are summarized in the semi-logarithmic chart of figure 3.1. The system escape threshold (black curve) separates the bounded solutions (below the curve) from the unbounded solutions (above the curve); changes in its slope correspond to changes in the kind of bifurcation event leading to escape and, apart from a localized exchange of the governing one in the frequency range between 0.2 and 0.5 (which will be analyzed hereinafter), four main different regions can be identified in the parameter control space (figure 3.1), from the escape viewpoint. The corresponding response scenarios are reported in figures 3.2-3.7 in terms of bifurcation diagrams, time histories, phase portraits and frequency power spectra.

Region I includes low frequencies set to the left ($\omega_u = 0.5 - 0.72$) of the downward vertex A of the overall escape threshold corresponding to nonlinear fundamental resonance. Here, the system displays coexistence, for low values of the forcing amplitude, of two stable period-1 solutions, with the initial Low-amplitude (non-resonant) P1L solution being connected to the (resonant) P1H solution of High-amplitude through the classical unstable branch in between a couple of saddle-node bifurcations (figure 3.2(a)). The upper one (SN1L), related to the low-amplitude solution, is responsible for the system escape from bounded response (green line in figure 3.1). The

disappearance of P1H is caused by a supercritical period doubling bifurcation (SpPD1H), which occurs at growing amplitude values as the frequency increases close to the A-vertex ($\omega_u \cong 0.72$), and is followed by a sequence of period doublings. Note that, for the sake of readability, in figure 3.2(a) and in the following bifurcation diagrams only one branch of the period-doubled solutions is reported.

In the right neighborhood of the nonlinear fundamental resonance this bifurcation becomes the local event (red line in figure 3.1) triggering global escape, and it plays this role in the whole region II ($\omega_u = 0.72 - 1.12$), as reported in figures 3.3(a), 3.4(a), where coexisting solutions with higher periodicity are also seen to occur in some ranges of forcing amplitude.

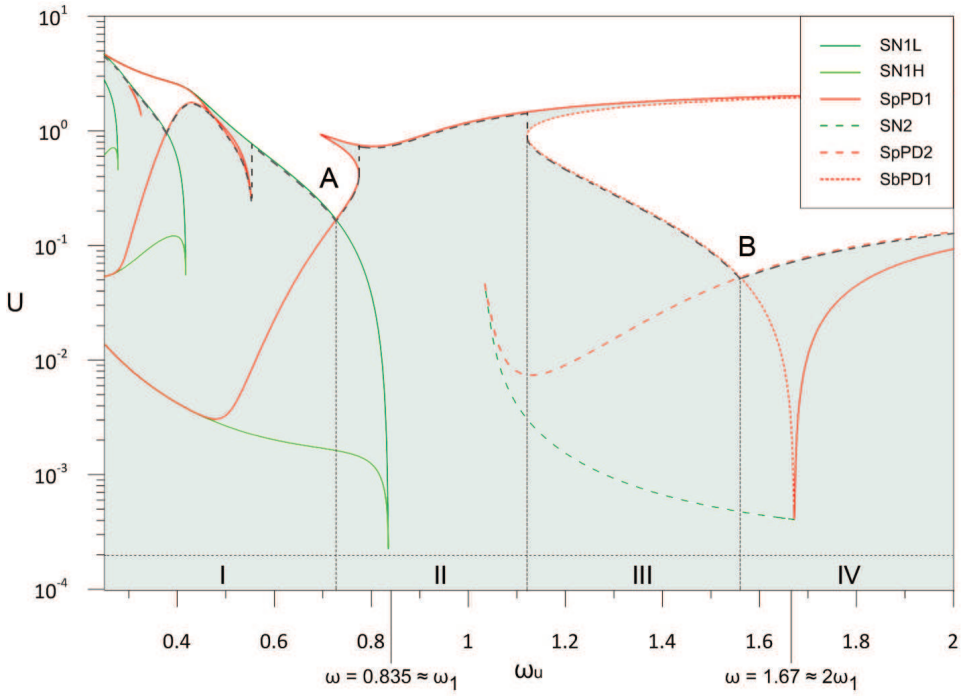

Figure 3.1: Local bifurcations map and overall escape threshold in the frequency-amplitude space of parametric excitation. Gray area: region of stable reference response of the controlled system; dotted gray line: overall escape boundary; SN1H: saddle-node bifurcation of the P1H solution; SN1L: saddle-node bifurcation of the P1L solution; SN2: saddle-node bifurcation of the P2 solution; SpPD1: supercritical period doubling of the P1 solution; SpPD2: supercritical period doubling of the P2 solution; SbPD1: subcritical period doubling of the P1 solution. Numbers I to IV correspond to four main regions of distinct response scenarios

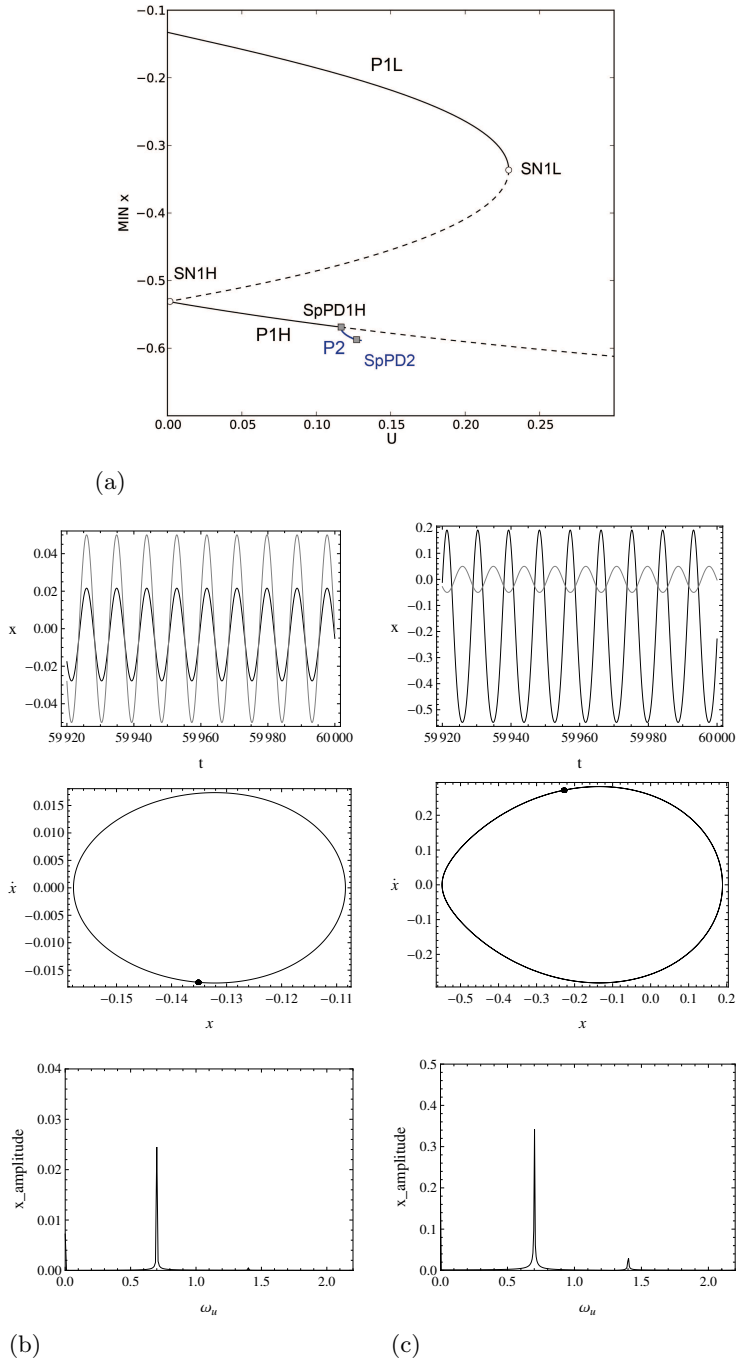

Figure 3.2: Bifurcation diagram at $\omega_u = 0.7$ (region I)(a); time histories, trajectories in the state plane and Fourier transform of P1L solution (b) and P1H solution (c) at $U = 0.05$. Gray lines on time history diagrams represent the parametric excitation

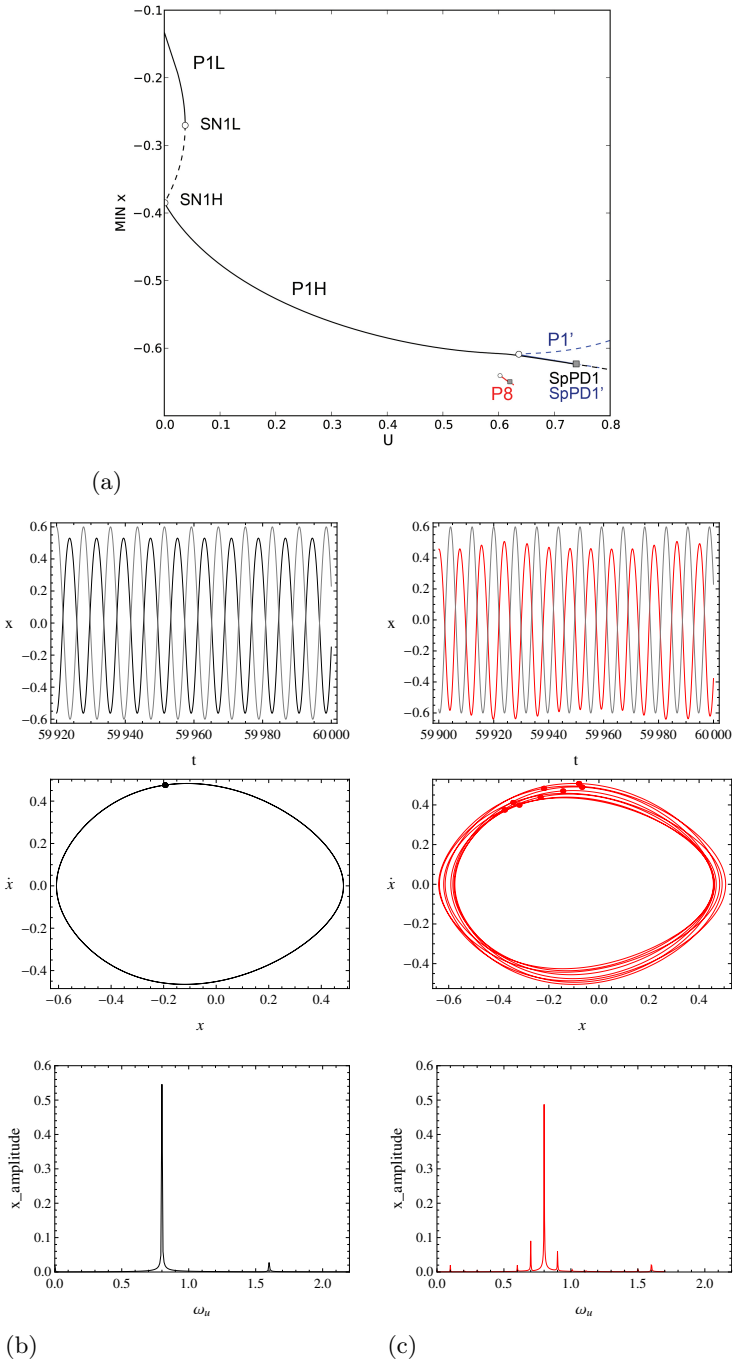

Figure 3.3: Bifurcation diagram at $\omega_u = 0.8$ (around fundamental resonance)(a); time histories, trajectories in the state plane and Fourier transform of P1 solution (b) and P8 solution (c) at $U = 0.6$. Gray lines on time history diagrams represent the parametric excitation

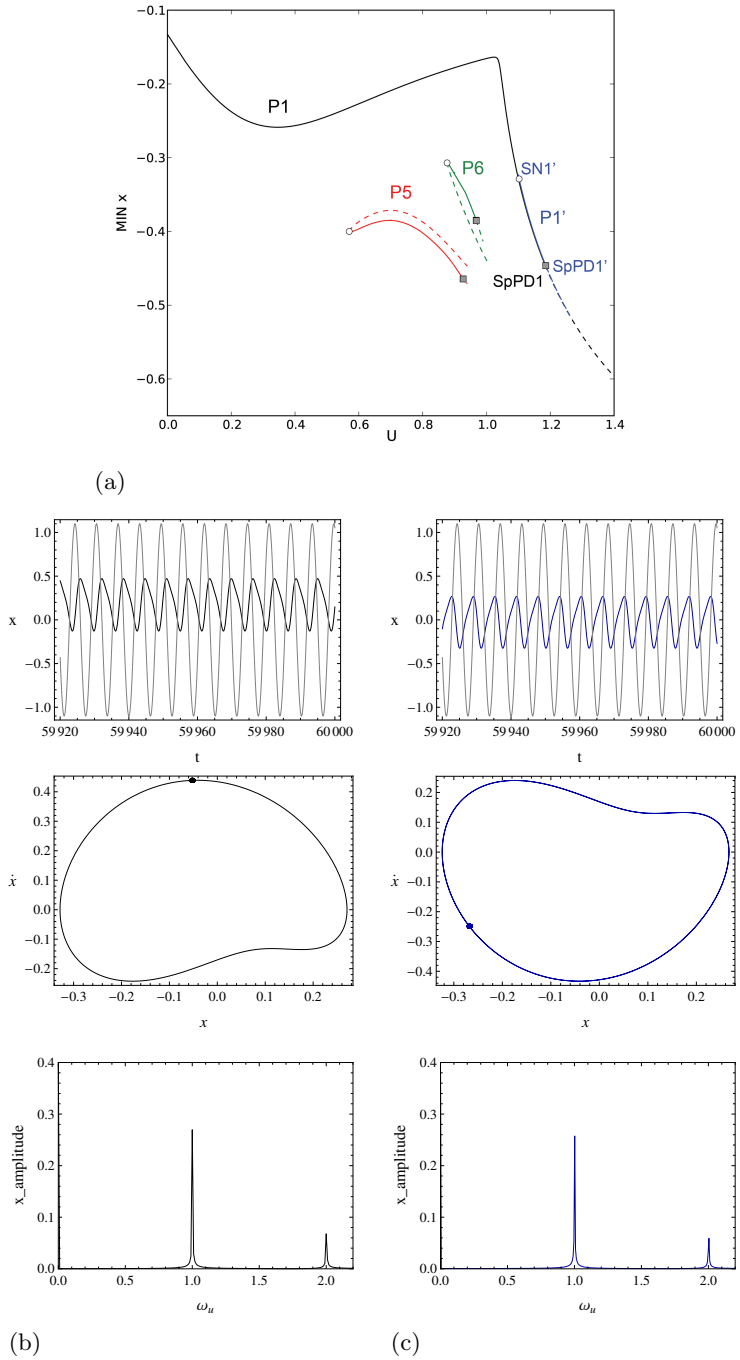

Figure 3.4: Bifurcation diagram at $\omega_u = 1$ (region II)(a); time histories, trajectories in the state plane and Fourier transform of P1 solution (b) and P1' solution (c) at $U = 1.1$. Gray lines on time history diagrams represent the parametric excitation

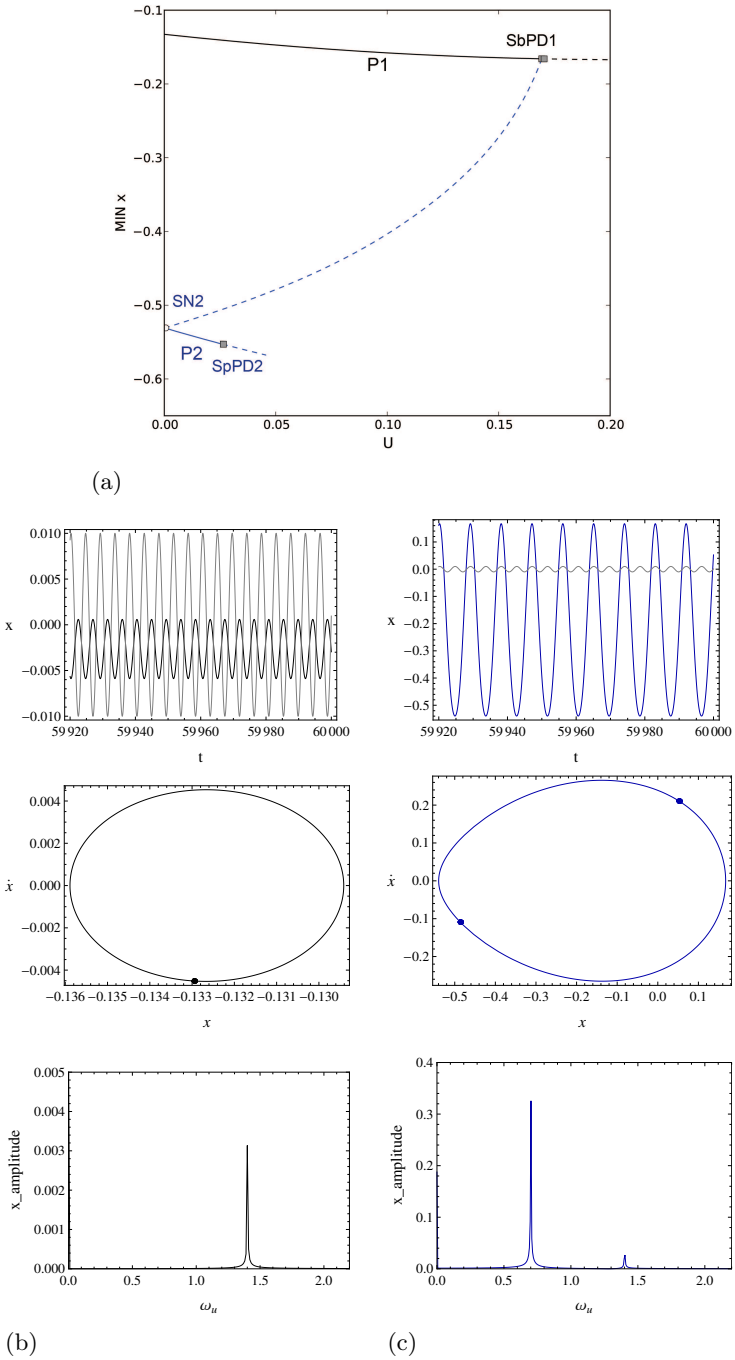

Figure 3.5: Bifurcation diagram at $\omega_u = 1.4$ (region III)(a); time histories, trajectories in the state plane and Fourier transform of P1 solution (b) and P2 solution (c) at $U = 0.01$. Gray lines on time history diagrams represent the parametric excitation

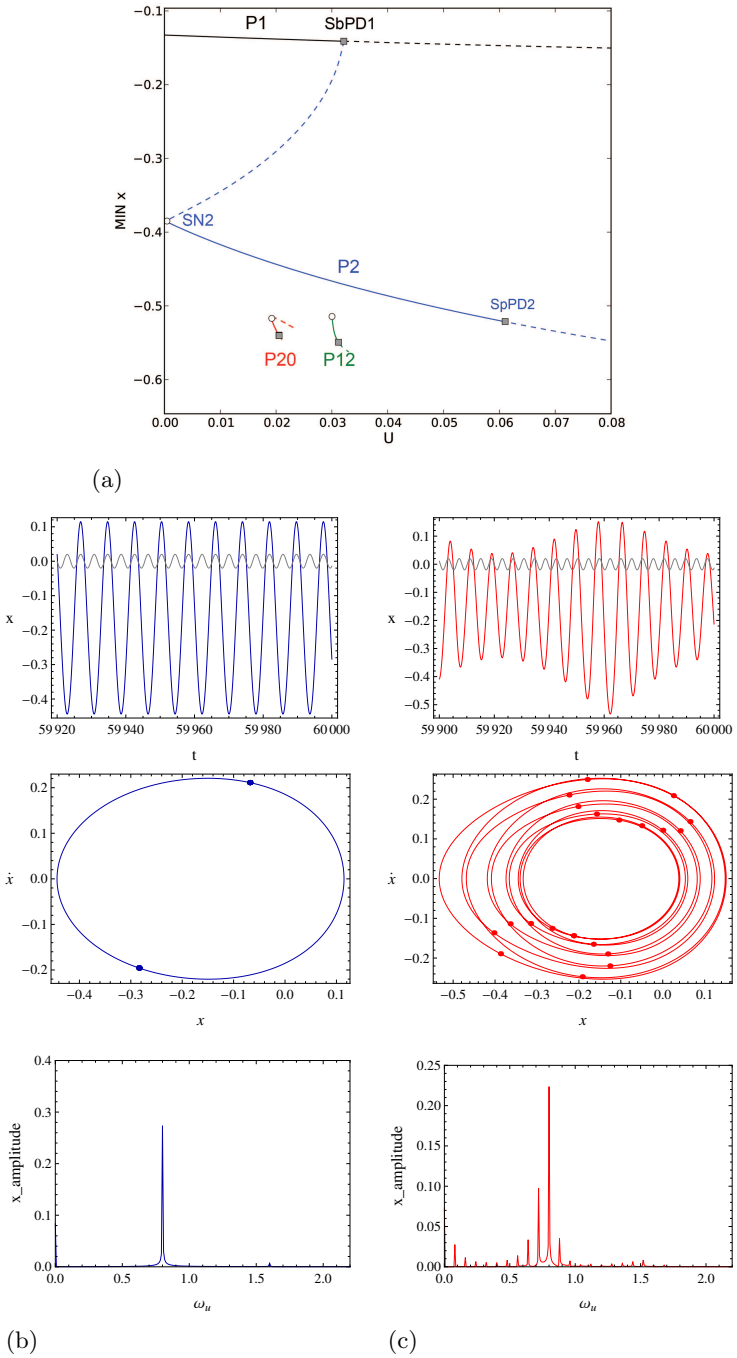

Figure 3.6: Bifurcation diagram at $\omega_u = 1.6$ (around principal resonance)(a); time histories, trajectories in the state plane and Fourier transform of P2 solution (b) and P20 solution (c) at $U = 0.02$. Gray lines on time history diagrams represent the parametric excitation

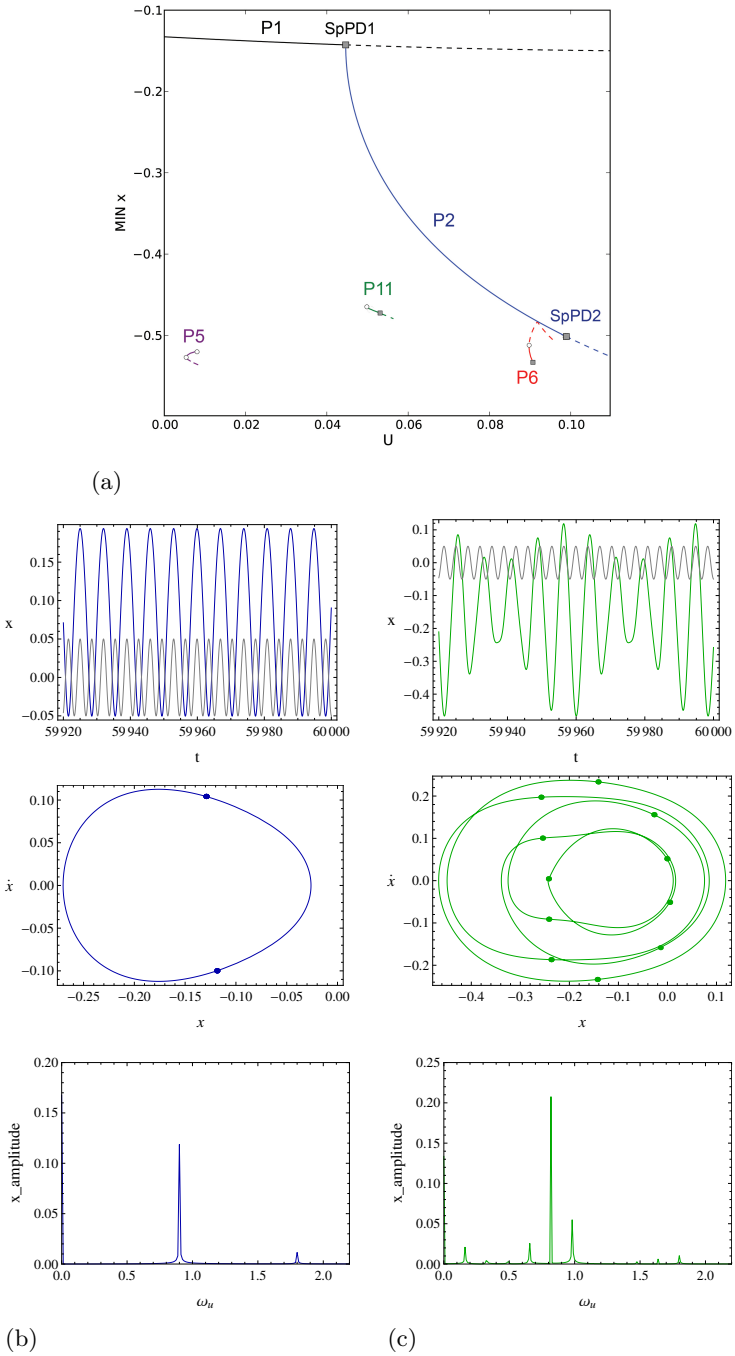

(a)

(b) (c)

Figure 3.7: Bifurcation diagram at $\omega_u = 1.8$ (region IV)(a); time histories, trajectories in the state plane and Fourier transform of P2 solution (b) and P11 solution (c) at $U = 0.05$. Gray lines on time history diagrams represent the parametric excitation

At the same time, the region of coexistence of P1L and P1H solutions is progressively reduced as the forcing frequency approaches the fundamental resonance ($\omega_u = \omega_1 = 0.835$), as evident in figure 3.1 and also from the comparison between figures 3.2(a) and 3.3(a); after this value, the P1H solution becomes the main periodic solution for the system (figure 3.4(a)).

Figure 3.5(a) shows a sample bifurcation diagram for frequencies ranging in between 1.12 and 1.56 (region III), to the left of the downward vertex B of the nonlinear principal resonance. Here a subcritical period doubling bifurcation (SbPD1) of the sole stable period-1 solution P1 entails its disappearance and onset of an unstable period-2 solution, thus marking the occurrence of escape (dotted red line in figure 3.1). In this last respect, the role played by the saddle-node bifurcation (SN1L) of the low-amplitude period-1 solution to the left of the A-vertex is herein replaced by this subcritical period doubling bifurcation.

In figure 3.5(a), the period-2 solution becomes stable via saddle-node (SN2) bifurcation at low values of forcing amplitude and is characterized by a highly prevailing amplitude of the subharmonic component (see the frequency spectrum in figure 3.5(b)); the response pattern is now similar to the one in region I (figure 3.2), apart from replacing P1H with P2. As in that case, the range of coexistence of stable P1 and P2 solutions grows up with increasing forcing frequency, up to entailing (at $\omega_u \cong 1.56$, B-vertex) the exchange of the local event triggering overall escape from SbPD1 to the supercritical period doubling bifurcation (SpPD2) of P2 (dashed red line in figure 3.1). This is substantially the same pattern as the one occurring to the right of the nonlinear fundamental resonance and, indeed, the cascade of period doubling bifurcations arising from SpPD2 (figures 3.6(a), 3.7(a)) keeps governing the system escape in the whole region IV (figure 3.1), which includes the principal resonance range ($\omega_u = 1.56$-1.8). Also in this case, the P1-P2 coexistence region reduces after the B-vertex, up to its disappearance at the principal frequency value $\omega_u = 2\omega_1 = 1.67$, after which the subcritical period doubling bifurcation (SbPD1) responsible for the instability of the P1 solution is replaced by a supercritical period doubling event (SpPD1) (see comparison between figures 3.6(a) and 3.7(a)).

As already mentioned, the reported examples also show the coexistence with the main periodic solutions of variable solutions of higher periodicity, which arise from saddle-node bifurcations and end up with local chaotic

responses via series of period doublings occurring in very narrow ranges of amplitude values. This is the case of the period-5 and -6 solutions (P5 and P6) in figure 3.4, for $\omega_u = 1$ and amplitudes in between 0.5 and 0.9, or of the period-5 and -11 solutions in figure 3.7, for $\omega_u = 1.8$, at low forcing amplitudes and around SpPD1, respectively.

3.1.1 Bifurcation/response charts at fundamental and principal resonances

It is worth focusing on the fundamental and principal resonance zones to highlight similarities and differences in the local bifurcation/response scenarios prior to escape. Two charts summarizing the relevant outcomes are reported in figures 3.8 and 3.9, respectively, with the identification of the local bifurcation loci and of the main periodic solutions in the various regions. In the left neighborhood of fundamental resonance ($\omega_u = 0.835$, figure 3.8), the system shows the same qualitative behavior of a number of softening oscillators subjected to primary external excitation, such as the Helmholtz oscillator [112] and single-mode models of MEMs [2, 63], especially for what concerns the V-shaped region of escape, its limiting boundaries, and the underlying triangle region with the two coexisting period-1 solutions. Figure 3.8 shows that such a coexistence in the region in between the two SN loci occurs up to $\omega_u = 0.835 = \omega_1$, where they collapse with each other. To the right of this value, and above the corresponding value of forcing amplitude, the sole period-1 solution previously associated with P1H occurs and its annihilation through SpPD1H (and the following series of period doublings) characterizes the smooth transition to escape for increasing amplitude (see also figure 16a in the following). Note that no loci of supercritical period doubling of higher periodicity solutions are reported in figure 3.8, to the left of the SpPD1H threshold, nor the ensuing locus of boundary crisis leading to escape (as the one in, e.g., figure 3.8 of [63]), since these events occur in a very narrow range of control parameter values. Note also that, in contrast, transition to escape from the left side occurs via the typical sudden SN bifurcation.

The chart of bifurcation/response scenarios in the neighborhood of principal resonance ($\omega_u = 1.67 = 2\omega_1$, figure 3.9) shows some similarities with the previous one, along with some meaningful differences. To grasp the latter, it is worth looking at the bifurcation diagram in figure 3.6(a), just to the

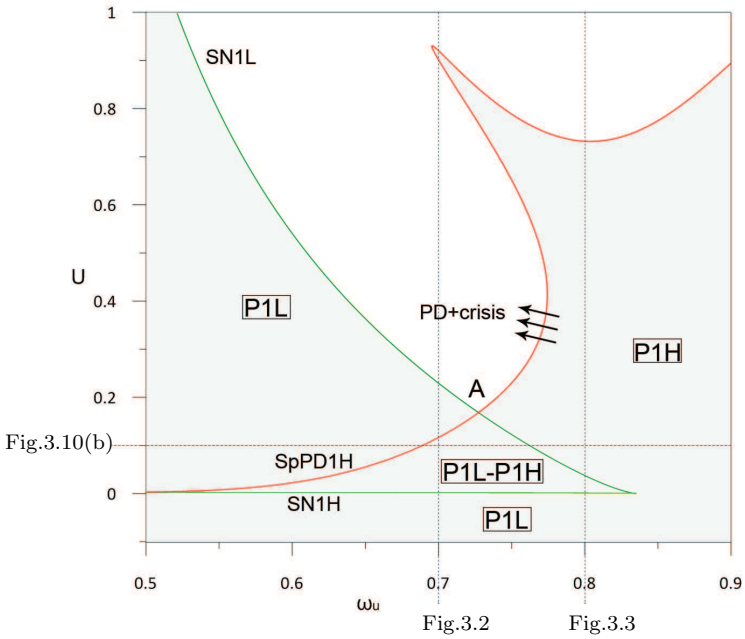

Figure 3.8: Frequency-amplitude response chart and bifurcation loci of AFM system with parametric scan excitation close to fundamental resonance $\omega_u = \omega_1 = 0.835$

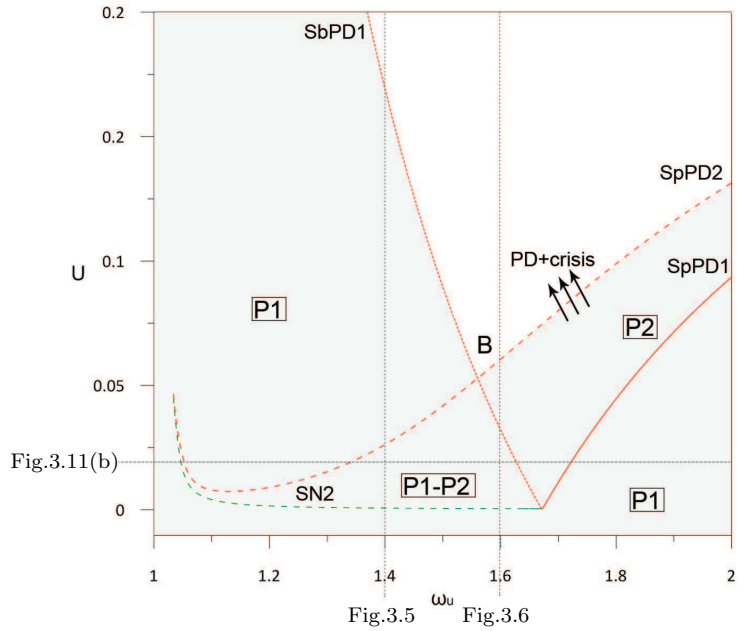

Figure 3.9: Frequency-amplitude response chart and bifurcation loci of AFM system with parametric scan excitation close to principal resonance $\omega_u = 2\omega_1 = 1.67$

left of $\omega_u = 1.67$. Here, the main periodic solutions are P1 and P2, with the

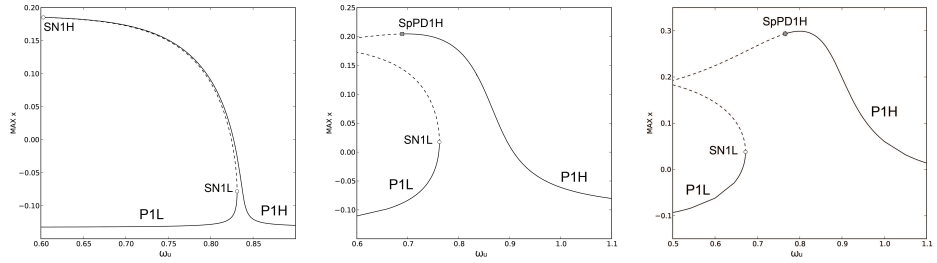

(a) (b) (c)

Figure 3.10: Frequency-response curves at $U = 0.002$ (a), $U = 0.1$ (b), $U = 0.3$ (c) near the fundamental resonance frequency $\omega_u = 0.835$

latter playing a major role according to closeness to the $2\omega_1$ frequency; the end of the region of their coexistence is due to collision between the SbPD1 locus (responsible for onset of the unstable P2 solution from P1) and the SN2 locus (which stabilizes the unstable P2 solution) at $\omega_u = 1.67$. At this highly degenerate cusp point, the subcritical period doubling of period-1 solution (SbPD1) changes to supercritical (SpPD1). The regions of occurrence of the main periodic solutions are clearly detected also in this case, and a common feature with the previous chart (figure 3.8) consists of the main coexisting solutions being confined within the triangle region, with the P1H of figure 3.8 being now replaced by P2. To the right of principal resonance, the P2 solution persists in the quite large region in between the two supercritical period doubling thresholds now governing the response scenario. As regards transition to escape, it still occurs suddenly (via SbPD1) from the left and smoothly (via the complete period doubling sequence originated at SpPD1) from the right.

The frequency-response curves of figures 3.10 and 3.11 complete the description of system response around the two resonance frequencies. In both regions, softening behavior is observed, with the typical features of primary and subharmonic response [79]. At fundamental resonance, with low values of forcing amplitude, the classical frequency-response curve occurs (figure 3.10(a)). At values of forcing amplitude within the triangle region and sweeping the frequency down (figure 3.10(b)), the P1H branch of period-1 solution becomes unstable via the supercritical period doubling SpPD1H; finally, within the V-shaped region (figure 3.10(c)), zones of unbounded solutions appear.

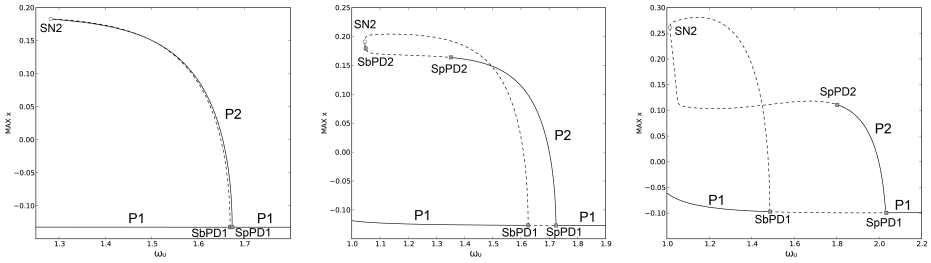

(a) (b) (c)

Figure 3.11: Frequency-response curves at $U = 0.001$ (a), $U = 0.02$ (b), $U = 0.1$ (c) near the principal resonance frequency $\omega_u = 1.67$

At principal resonance, with decreasing frequency, the stable and unstable branches of the dominant P2 response originate from P1 via supercritical (SpPD1) and subcritical (SbPD1) period doublings, respectively. Just above the lower degenerate cusp (figure 3.11(a)), the two branches disappear via saddle-node (SN2); for higher forcing amplitude still within the triangle region (figure 3.11(b)), the stable P2 solution becomes unstable via SpPD2; finally, within the V-shaped region (figure 3.11(c)), zones of unbounded solutions appear. It is worth noting that the results at principal resonance qualitatively match those obtained for different systems. In particular, the outcomes of figures 3.9 and 3.11(b) are similar to those of figures 1 and 3 of [113], relevant to a driven nonlinear oscillator at 2T-subharmonic resonance, and confirm the possibility [60, 113] to analyze a parametrically driven system via the equivalent externally forced one. As regards distributed parameter systems, the occurrence of the two different, subcritical and supercritical, bifurcation scenarios, respectively to the left and right of principal resonance, can be found, e.g., in [40].

3.1.2 Bifurcation/response charts at low frequencies

Furthermore, the inspection of the chart of bifurcation/response scenarios at low values of the forcing frequency reported in figure 3.12 points out some interesting features of the system dynamical behavior. The global escape threshold, in fact, displays local minima at frequencies values corresponding to superharmonic resonances $\omega_u \cong 0.41 = \omega_1/2$, $\omega_u \cong 0.27 = \omega_1/3$ and $\omega_u \cong 0.21 = \omega_1/4$, where, as already seen at fundamental resonance, the dynamical response is characterized by a recurrent triangle region of

coexistence of nonresonant P1L and resonant P1H solutions. Their dynamical evolution at increasing values of the forcing amplitude U reproduces what already described for $\omega_u = \omega_1$, with the two solutions connected to an unstable branch via a couple of saddle-node bifurcations and the P1H solution which dies through a supercritical period doubling. According to the resonance frequency value, such solutions are now periodic responses with 2 harmonics of frequency ω and 2ω (3ω, 4ω) respectively, as shown in temporary evolutions and power spectra of figures 3.13-3.14, where the superharmonic components are seen to exhibit the highest amplitudes for the P1H solution.

Soon after and to the right of these triangle regions, the behavior chart highlights the presence of two thresholds of period doubling which delimit a narrow region around ultrasuperharmonic frequencies at $\omega_u = 0.218 - 0.229 \cong 2\omega_1/7$, $\omega_u = 0.301 - 0.326 \cong 2\omega_1/5$ and $\omega_u = 0.47 - 0.55 \cong 2\omega_1/3$. Inside these ranges, the sole P1 solution becomes unstable via a subcritical period doubling SbPD which leads to the birth of an unstable P2 solution (see bifurcation diagrams of figures 3.15(a), 3.16(a)); a saddle-node bifurcation SN2 provides it stability, just as it occurs to the right of the principal resonance (e.g., at $\omega_u = 1.4$, in figure 3.5). Also in this

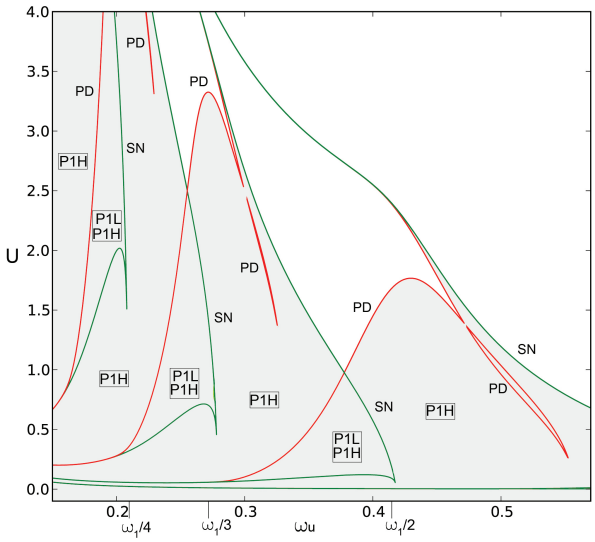

Figure 3.12: Frequency-amplitude response chart of the parametrically forced system at low frequency values. Red lines: period doubling bifurcation loci (PD); green lines: saddle-node bifurcation loci (SN)

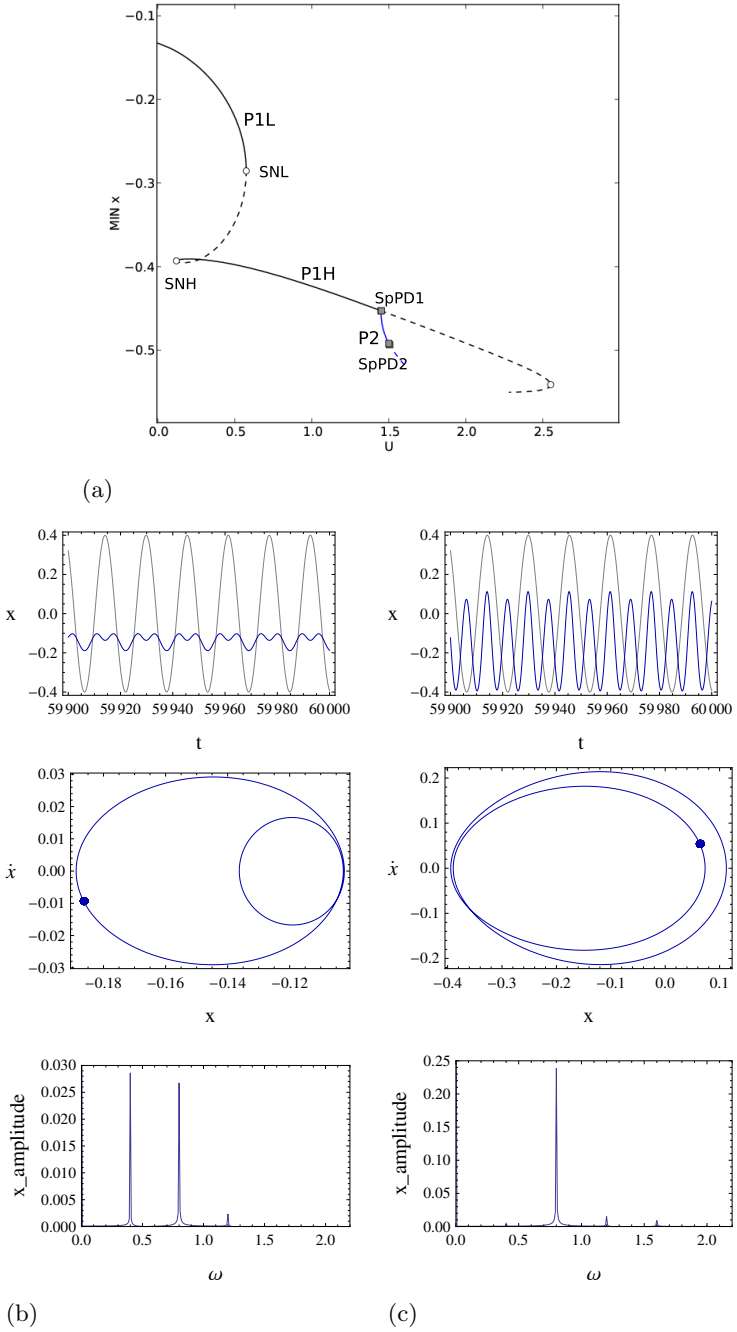

Figure 3.13: Bifurcation diagram at $\omega_u = 0.4 \cong \omega_1/2$ (a). Time histories, trajectories in the phase plane and Fourier transform of P1L solution (b) and P1H solution (c) at $U = 0.4$. Gray lines on time history diagrams represent the parametric excitation

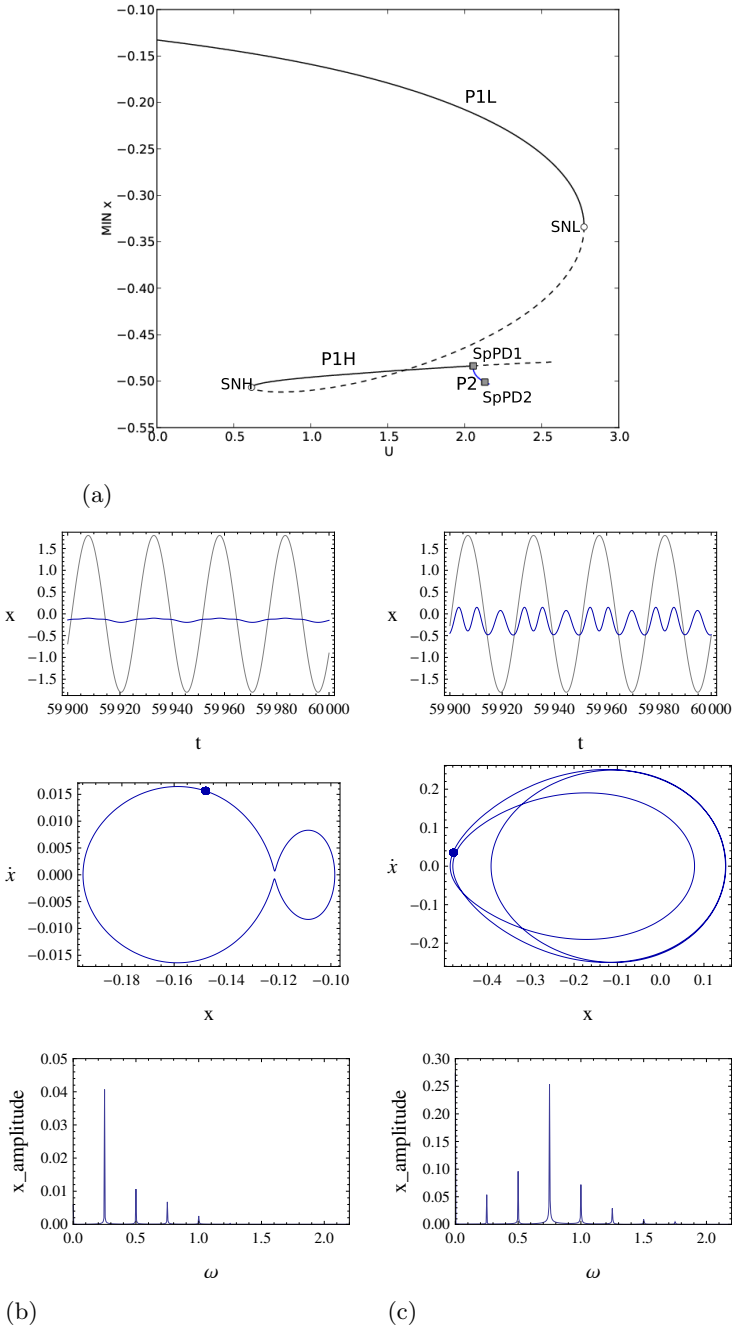

Figure 3.14: Bifurcation diagram at $\omega_u = 0.25 \cong \omega_1/3$ (a). Time histories, trajectories in the phase plane and Fourier transform of P1L solution (b) and P1H solution (c) at $U = 1.8$. Gray lines on time history diagrams represent the parametric excitation

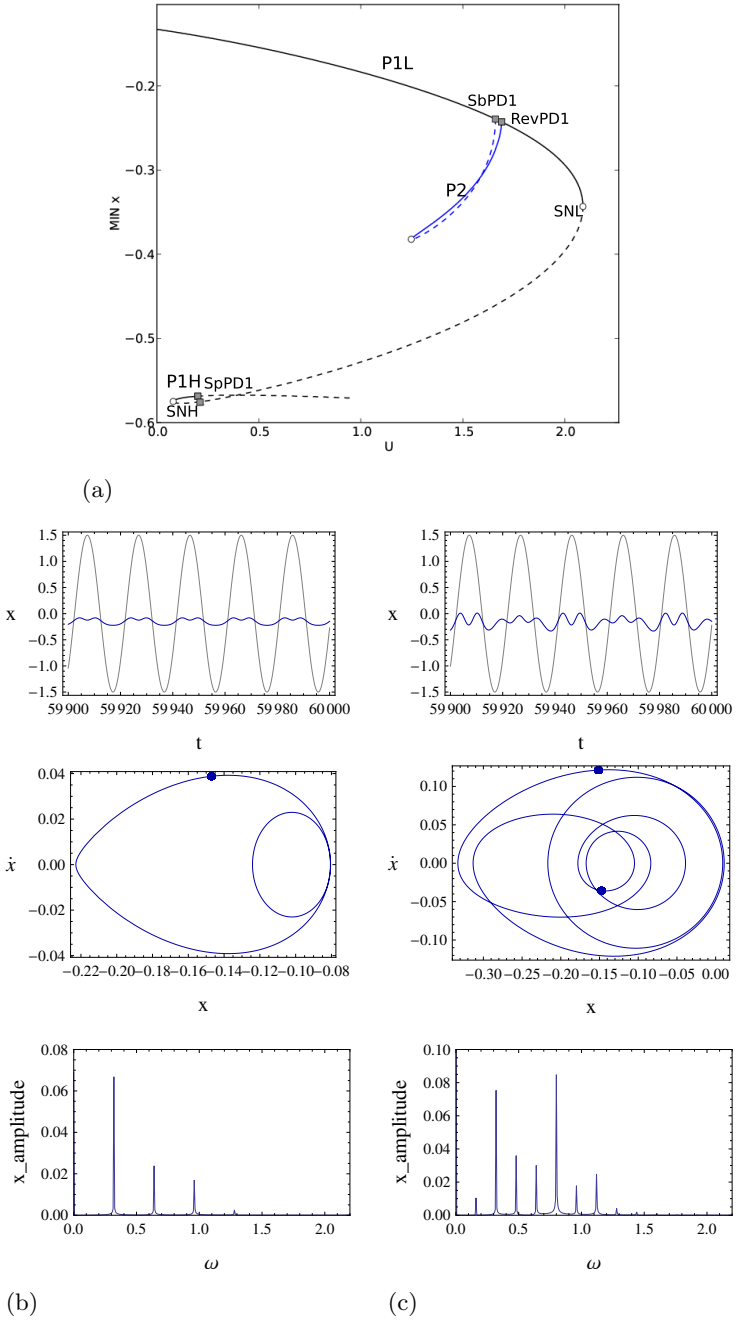

Figure 3.15: Bifurcation diagram at $\omega_u = 0.32 \cong 2\omega_1/5$ (a). Time histories, trajectories in the phase plane and Fourier transform of P1 solution (b) and P2 solution (c) at $U = 1.5$. Gray lines on time history diagrams represent the parametric excitation

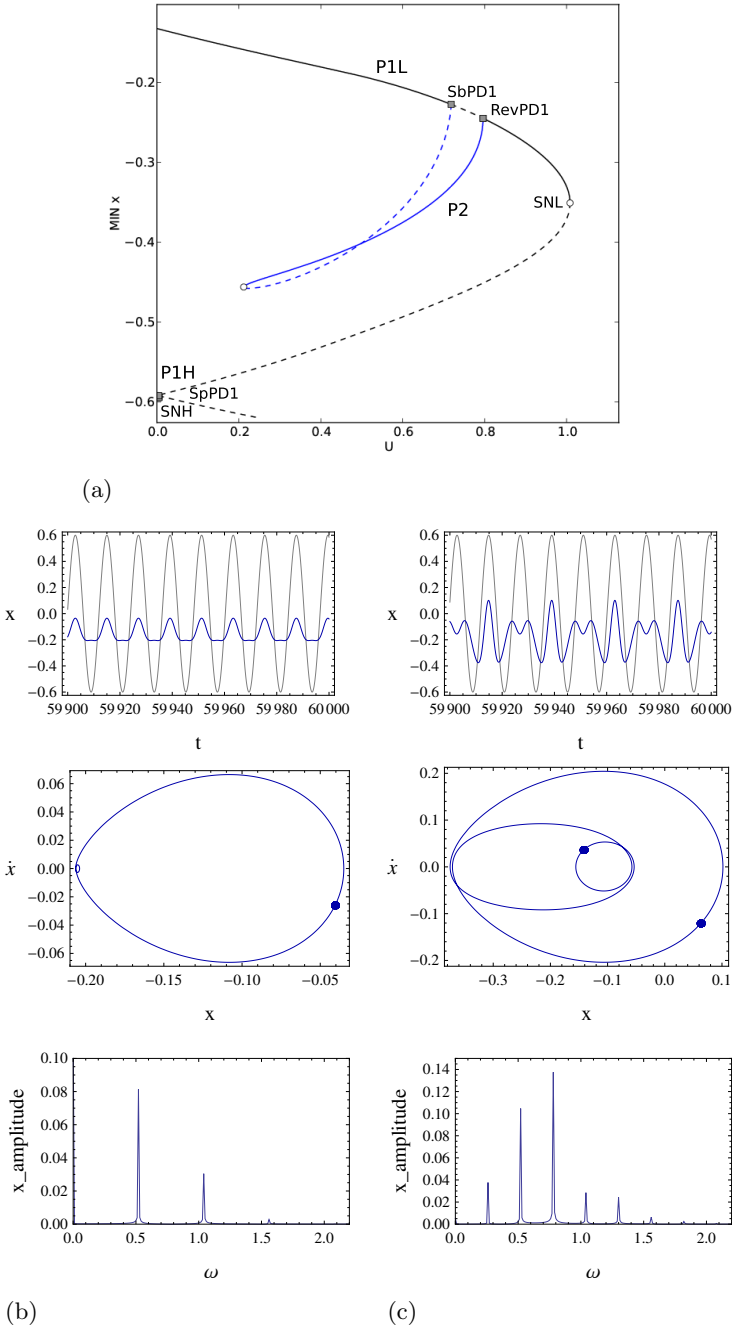

Figure 3.16: Bifurcation diagram at $\omega_u = 0.52 \cong 2\omega_1/3$ (a). Time histories, trajectories in the phase plane and Fourier transform of P1 solution (b) and P2 solution (c) at $U = 0.6$. Gray lines on time history diagrams represent the parametric excitation

case the P2 solution fails to become the dominant solution, but now it disappears through a reverse period doubling RevPD (and not via a series of supercritical perdiod doublings as in the principal resonance case) which gives back stability to the initial P1 solution.

Bifurcation diagrams with analysis of P1 and P2 solutions are reported in figures 3.15-3.16, where the close proximity to the ultrasuperharmonic resonances is highlighted by the power spectra of the P2 solutions, which include, besides the $\omega/2$ frequency characterizing the period-doubled solutions, the superharmonic frequency and its higher harmonics. The described results allow to detect two different dynamical behaviors the system displays, depending on the kind of resonance frequency the parametric excitation interacts with. At fundamental resonance and superharmonic resonance frequencies (i.e. $\omega_u = \omega_1/n$, $n = 1, 2, 3, 4...$) the system response is characterized by coexistence of resonant and nonresonant 1-period solutions, while at principal resonance and ultrasuperharmonic resonance frequencies (i.e. $\omega_u = 2\omega_1/n$, $n = 1, 3, 5, 7...$) the main periodic responses are 1-period and 2-period solutions.

3.1.3 Influence of the nonlinear atomic interaction

Finally, it is of interest to analyze the influence of the nonlinear interaction parameter variation Γ_1 on the system dynamical response; such parameter, which depends on the kind of tip and sample materials and their distance at nanoscale level, is in fact the characterizing ingredient of an AFM model, and introduces a nonlinear term of order -2 into the system.

The result of the influence of the interaction parameter Γ_1 on the forcing amplitude escape value U is reported in the behavior chart of figure 3.17 for a frequency value of $\omega_u = 0.7$ close to the fundamental resonance, with bifurcation diagrams of figure 3.18 as a support for the description. As the nonlinear interaction increases, with respect ot the reference value $\Gamma_1 = 0.1$ used for the previous numerical analyses, the amplitude escape value for the P1L solution rapidly decreases, up to the disappearance of such periodic solution and consequently of the region of coexistence of resonant P1H and nonresonant P1L solutions (at $\Gamma_1 \cong 0.13$); after that, for higher values of the interaction parameter the sole P1H solution remains as system stable periodic solution, and its escape boundary represented by the supercritical period doubling threshold PD1H moves to higher values of the forcing am-

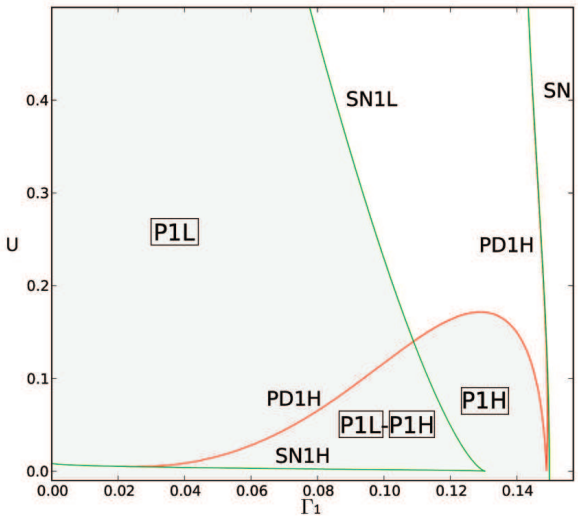

Figure 3.17: Bahavior chart in the Γ_1-U plane at $\omega_u = 0.7$

plitude U, enlarging the stability region up to $\Gamma_1 \cong 0.14$, when it drastically falls down causing the annihilation of the P1H stability region.

Conversely, the behavior chart of figure 3.17 can be analyzed considering the effect of the forcing amplitude presence on the system equilibria as a function of the interaction parameter; as already described in the previous section 2.3, for the chosen set of parameters values the limiting value of the nonlinear interaction parameter Γ_1 in the unperturbed case is about 0.15, and corresponds to the stability loss via a saddle-node bifurcation of the sole acceptable equilibrium solution (see figure 2.4(b)). The parametric excitation insertion into the model, together with the damping term, obviously modifies the system nonlinear dynamics changing the stability of the periodic solutions derived from the equilibria, leading to the birth of a softening resonance peak on the original equilibrium stable branch, which is now composed of two periodic nonresonant and resonant solutions (P1L and P1H), and also to the occurrence of a narrow instability region, close to the original saddle-node bifurcation, which is confined by two (direct and reverse) period doubling bifurcations PD1H (see figure 3.18(b) at $U = 0.0005$). As the amplitude increases, the resonance peak moves to lower values of the atomic interaction parameter, and accentuates its softening behavior, while the unstable region between the two period doublings enlarges reducing the escape value of Γ_1 (figures 3.18(c), 3.18(d)). The described behavior occurs

at all the frequencies around the principal resonance, as reported in figure 3.19.

This dual reading key in interpreting the outcomes of figure 3.17 can also be exploited for design purposes; on the one hand, in fact, it points out the crucial role played by the tip-sample nonlinear interaction on the response of the AFM cantilever, furnishing practical informations about the limiting values of forcing amplitude to be used depending on the sample constitutive properties, while on the other hand it can be used to calibrate the tip-sample interaction (e.g., tip material choice, or material of the sample to be possibly scanned) depending on the AFM operation settings.

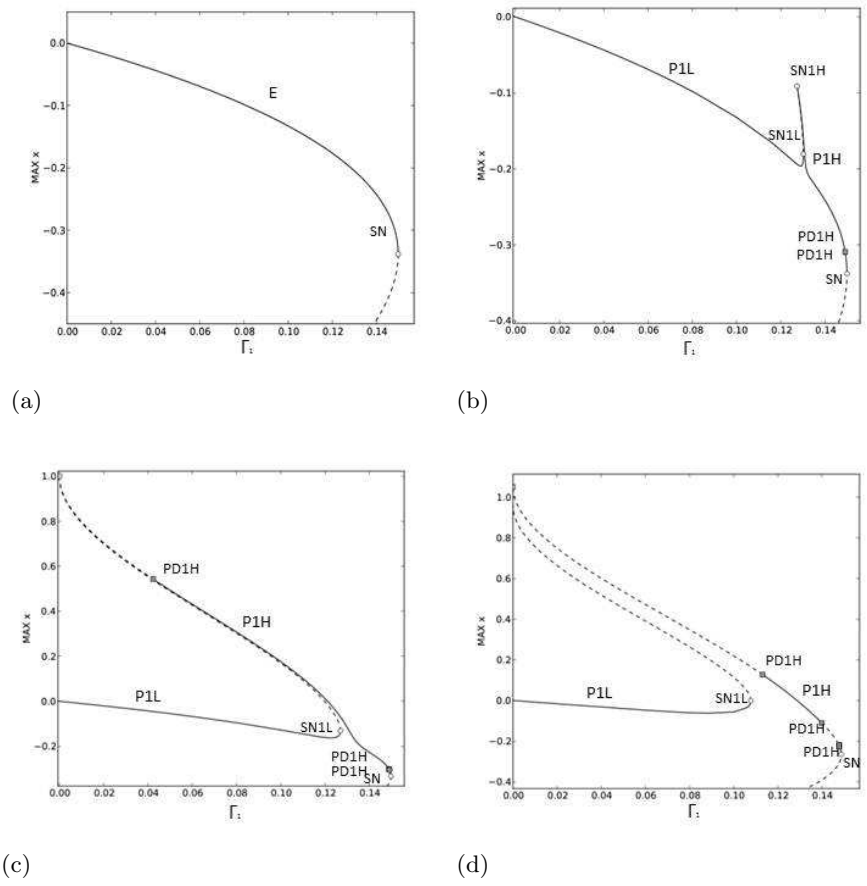

(a) (b)

(c) (d)

Figure 3.18: Bifurcation diagrams as a function of the atomic interaction Γ_1 at $\omega_u = 0.7$ for $U = 0$ (a), $U = 0.0005$ (b), $U = 0.01$ (c) and $U = 0.15$ (d). E in (a) represents the equilibrium position of the unforced system

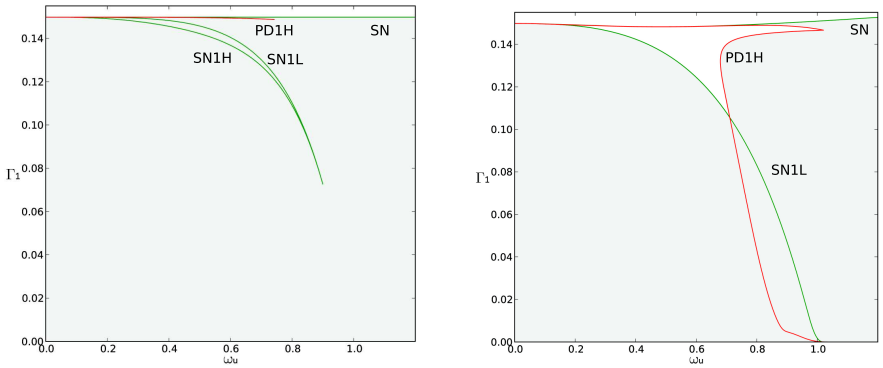

(a) (b)

Figure 3.19: Behavior chart in the ω_u-Γ_1 plane at $U = 0.0005$ (a), and $U = 0.15$ (b)

3.2 AFM system under external excitation

To complete the nonlinear analysis of the system in terms of bifurcation scenarios, it is interesting to study the response under the sole vertical excitation V_g, which, as in the case of the horizontal excitation, is supposed to be harmonic ($V_g = V\sin(\omega_v t)$). The system equation (2.21) hence becomes:

$$\begin{aligned}\ddot{x} + \alpha_1 x + \alpha_3 x^3 = &-\frac{\Gamma_1}{(1 + x + V\sin(\omega_v t))^2} - \rho_1 \dot{x} \\ &- \nu_2 \left(\nu_1 \omega_v V \cos(\omega_v t) - \omega_v^2 V \sin(\omega_v t)\right)\end{aligned} \tag{3.1}$$

and the parameter values used in the numerical analyses are

$$\alpha_1 = 1, \quad \alpha_3 = 0.1, \quad \rho_1 = 0.001, \quad \Gamma_1 = 0.1, \quad \nu_1 = 0.01, \quad \nu_2 = 0.01.$$

This case can be referred to as of a (largely dominant) external excitation.

The results concerning the local escape thresholds exhibit the same qualitative behavior as the one obtained under parametric excitation, even though some differences can be pointed out. Analyzing the local bifurcation map of figure 3.20, it is evident how the application of an external force shifts the absolute minimum of the total escape threshold (continuous gray line) from the subharmonic resonance range to the primary one, consistent with the well-known higher response amplitudes occurring at the latter for a given excitation amplitude. Therein, the figure shows the same local bifurcation scenario as the one previously analyzed at fundamental parametric reso-

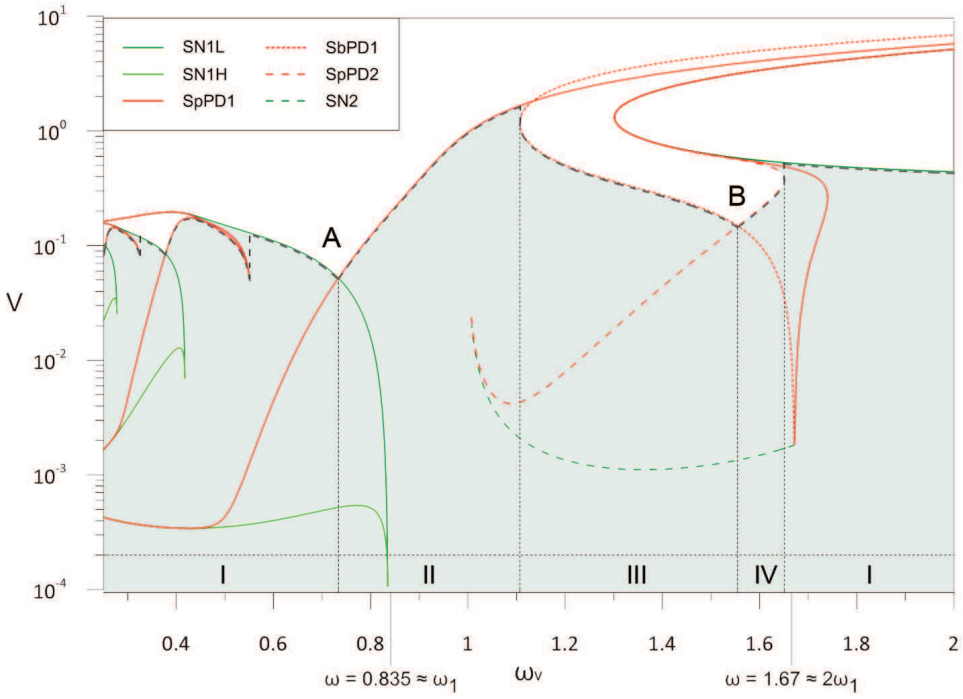

Figure 3.20: Local bifurcations map and overall escape threshold in the frequency-amplitude space of external excitation. Gray area: region of stable reference response of the controlled system; dotted gray line: overall escape boundary; SN1H: saddle-node bifurcation of the P1H solution; SN1L: saddle-node bifurcation of the P1L solution; SN2: saddle-node bifurcation of the P2 solution; SpPD1: supercritical period doubling of the P1 solution; SpPD2: supercritical period doubling of the P2 solution; SbPD1: subcritical period doubling of the P1 solution. Numbers I to IV correspond to four main regions of distinct response scenarios

nance, while the system behavior is slightly different in the subharmonic region (see figure 3.1 for comparison). Figure 3.21 is a zoom around the latter and, for high values of the forcing amplitude, displays the birth, at $\omega_v \cong 1.31$, of a narrow region of stable solutions which does not exist in the parametrically driven case.

Such a new stability region involves the same periodic solutions as the main stable one (i.e. P1 and P2 solutions), which have former become unstable through a subcritical and supercritical period doubling, respectively. In the bifurcation diagram (figure 3.22), the latter gives rise to an unstable bubble characterized by a period doubling transition to in-well chaos. For frequency values of about 1.30 a couple of reverse supercritical period doublings (RevSpPD2 and RevSpPD1) make those solutions again stable, and finally a saddle-node bifurcation (SN1) causes the disappearance of P1 (fig-

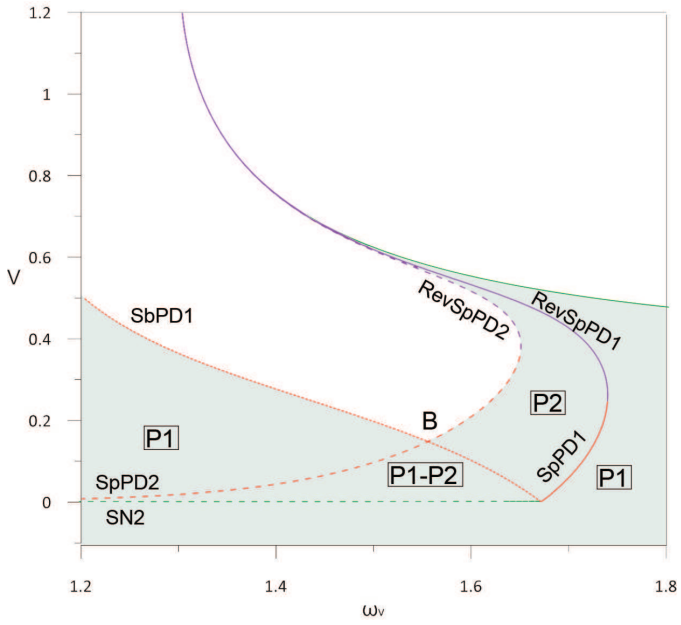

Figure 3.21: Frequency-amplitude response chart and bifurcation loci of AFM system with external beam excitation close to subharmonic resonance $\omega_v = 2\omega_1 = 1.67$

ure 3.22(a)). The new stability region grows up as the frequency increases up to about $\omega_v = 1.648$ where it connects with the main stable one, owing to the collapse of the two bifurcation loci (RevSpPD2 and SpPD2) limiting the unstable bubble (figure 3.22(b)). At the same frequency value, the escape threshold shifts from the series of supercritical period doublings originated from P2 (SpPD2), typical of the companion region under parametric excitation (figure 3.9), to the saddle-node of P1 (SN1).

Moving to higher forcing frequencies, the lower right vertex of the P2 triangle region (at $\omega_v = 1.672$) corresponds to collision between the SN2 and SbPD1 thresholds (figure 3.22(c)), and to the concurrent change of the latter to supercritical (SpPD1), just as in figure 3.9. Finally, at $\omega_v = 1.745$ the collapse of the SpPD1 threshold with the RevSpPD1 one marks the disappearance of P2 and the existence of the sole P1 solution (figure 3.22(d)). It is thus worth noting how, to the right of subharmonic resonance, the characterizing P2 solution is definitely less robust than the companion one at principal parametric resonance. As regards actual escape to contact between beam tip and sample, it only occurs above the SN1 threshold, which is indeed identified as the stability threshold in figure 3.21. However, from a system effectiveness viewpoint the highly periodic or chaotic solutions occurring

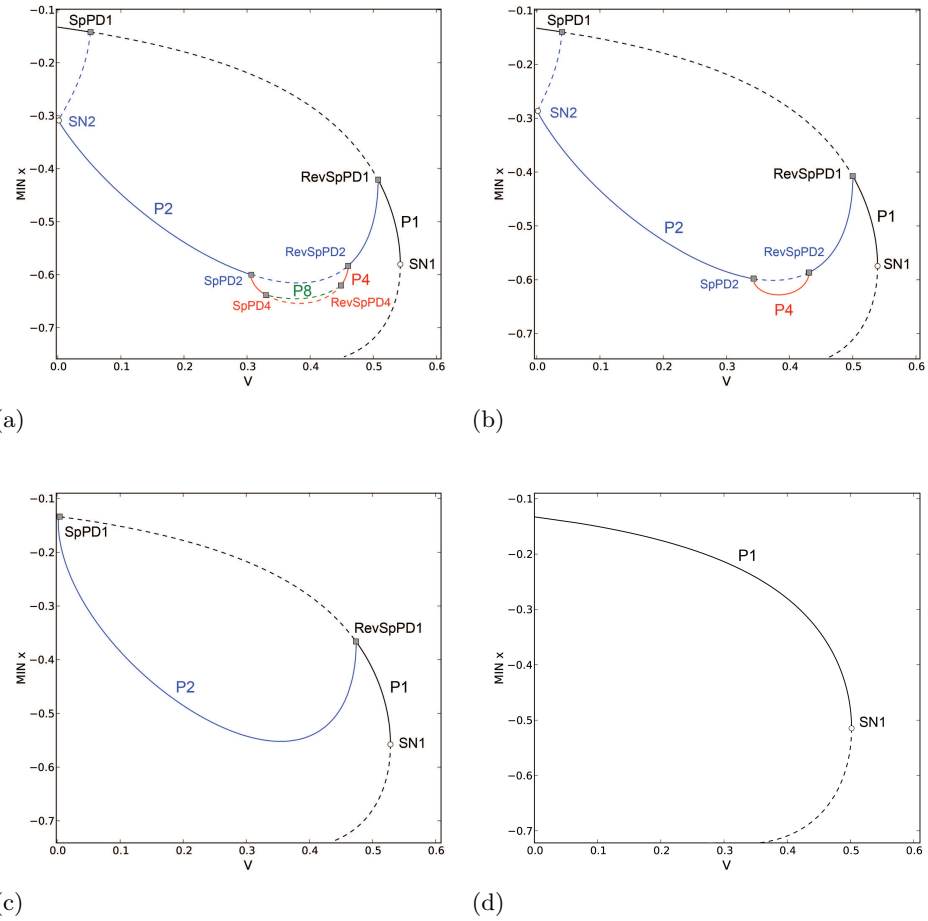

Figure 3.22: Bifurcation diagrams for $\omega_v = 1.64$ (a), $\omega_v = 1.648$ (b), $\omega_v = 1.672$ (c), $\omega_v = 1.745$ (d)

within the unstable bubble region, though confined, may meaningfully affect the quality of the AFM dynamics expected in practical applications.

It's interesting to note that such behavior characterized by a confined unstable region is present also at the fundamental resonance of the parametrically forced system, in correspondence of the tongue of period doubling just above the triangle region on figure 3.1,at values of the forcing frequency around $U = 0.8$. Here, as in the above described case, an unstable bubble affects the P1H solution delimited by the period doubling thresholds, up to $\omega_u \cong 0.775$ when it disappears leaving the P1H solution return the only one for the system.

Such behavior can be explained by referring to what said about the

system behavior at low frequency values: since primary (subharmonic) resonance is the dominant one for an externally (parametrically) forced system, the dynamical behavior in this region is of the typical type described in literature [112, 113] and previously analyzed; on the other hand, in the region of subharmonic (primary) resonance, the system results to be slightly affected by the influence of the ultrasuperharmonic behavior seen in the previous section, which leads to the birth of a period doubled superharmonic solution. As a result, even if the P1 and P2 (P1L and P1H) solutions remain the dominant ones, in a limited range of amplitude V (U) values a new period doubled solution P4 (P2) occurs, with the frequency content typical of the subharmonic resonance condition.

The same motivation can explain also the strong decrease, at low frequencies, of the stability region boundary with respect to the parametrically forced case (see figure 3.1 or figure 3.12 for a comparison), with a reduction of the amplitude escape value up to 97%. At $\omega_{u,v} = 0.25$, in fact, the escape value of the parametric excitation amplitude is $U \cong 4$, in spite of an amplitude value of $V \cong 0.1$ of the vertical excitation. Also in this case, the dominant role of the primary resonance in the externally forced system ensures that it significantly influences the frequencies at its left-side, causing a considerable reduction of the stability region, while in the system under parametric excitation its reduced importance entails no lowering of the neighboring escape threshold.

Chapter 4

Global dynamics and integrity

The previous investigations highlight that the lowest escape values of forcing amplitude occur at the two resonance regions, and provide the escape profile as the envelope of forcing amplitude values at which bounded solutions disappear. Yet, such a global stability boundary does not furnish any information about the erosion process of the basins of attraction of the various solutions, which is indeed a critical issue corresponding to system impending jump to contact; therefore, it has no practical utility from the viewpoint of AFM safe operation mode.

Within this context, the fundamental guiding concept is the dynamical integrity of the system, which depends on the extent of the erosion of its so-called safe basin [90, 115]. Tools for investigating the complete basin evolution under a control parameter variation up to escape are the so-called erosion profiles, which permit to quantify the varying level of basin erosion. Their construction is carried out by means of specific computational tools, based on the safe basin definition and the integrity measure concept [89, 90, 105].

In this chapter the evolution of basins of attraction is examined for increasing parametric (and external, separately) excitation amplitude, spanning the whole range of forcing frequencies which includes fundamental (primary) and principal (subharmonic) resonances. The rich erosion patterns underlying escape which occur in the two resonance regions are then quantifyied using selected integrity measures, and several erosion profiles are

constructed at different forcing frequencies. The outcomes are interpreted from a theoretical viewpoint to highlight similarities and differences between the chosen integrity measures and to judge the robustness of periodic solutions, while from a design perspective they will be used to obtain thesholds of residual integrity able to ensure acceptable safety targets established a priori according to required system performances.

4.1 Dynamical integrity concepts

The investigation of the dynamical integrity of a system when varying some of the control parameters is strictly related to the definition and choice of specific tools, namely the safe basin concept and the integrity measure detection.

The safe basin is the union, in phase space, of all initial conditions guaranteeing some specific response performances, which are usually the convergence in time toward one or more attractors, or the non-escape from a potential well. It can be the safe basin of a specific attractor, in this case coinciding with a classical basin of attraction or it can be related to a potential well, in this case being the union of the basins of all attractors belonging to the considered well [89]. The safe basin can be built either by considering only the steady-state dynamics, if the interest is only in the system stationary regime, or by paying attention also to the transient dynamics, in instances in which the short-term dynamics is the most important part of the response or some unsafe phenomena, such as a temporary escape from the potential well, may occur during the transient phase. The former basins are bounded by the stable manifolds of some relevant saddles, thus having a clear dynamical meaning, whereas the latter do not possess this property. Moreover, in many practical situations it can actually be important to take into account the phase of the excitation; in this respect, the true safe basin is defined as the intersection of the previously defined safe basins when the excitation phase ranges over a time interval of interest (e.g., the period for periodic excitations, or the period of free vibration for impulsive excitation). The true safe basin is the smallest phase-independent set of initial conditions leading to safe dynamics [89].

In this work the transient dynamics of the system as well as the phase of the excitation are ignored and, in view of final escape, the safe basin is

considered as the union of all classical basins of attraction of the bounded solutions belonging to the system potential well represented by the region of the phase space bounded by the homoclinic orbit in the underlying unperturbed system of figure 2.4(a). This means that, in the case of coexistence of more in-well attractors, the safe basin may comprise two, or more, competing basins. However, safe basins in the more classical meaning of basins of attraction of given solutions will also be considered when being interested in evaluating the robustness of competing attractors, too, along with the respective roles in the erosion process.

To measure the magnitude of the safe basins many different integrity measures have been proposed [89, 90, 105], with different meaning, relevance and properties.

The Global Integrity Measure (GIM) is the normalized hyper-volume (area in 2D cases) of the safe basin. It is the most intuitive and easy integrity measure, but it is not satisfactory in all cases in which the safe basin is strongly fractal.

The Local Integrity Measure (LIM) is the minimum distance, in the Poincar section, from the attractor to the transient basin boundary [105]. This definition is good in ruling out the fractality of the basins and in focusing on the compact part of the safe basin surrounding the attractor, even if it becomes unclear in the recurrent case of coexisting in-well attractors and is numerically cumbersome, especially when the in-well attractor is chaotic.

The Integrity Factor (IF) is the normalized radius of the largest hypersphere (circle in 2D cases) entirely belonging to the safe basin. As it represents a measure of the sole compact part of the safe basin, it succeeds in eliminating the unsafe fractal tongues from the integrity evaluation and deals with the solely region which guarantees the dynamical integrity of the system.

In the following numerical analyses, the integrity indicators used to build the erosion profiles are the global integrity measure (GIM), and the integrity factor (IF), considering the phase space window $x \in [-0.3, 0.3], \dot{x} \in [-0.65, 0.25]$, since it contains the compact part of the basin of each of the main attractors involved in the erosion/escape process. Normalization has been performed with respect to the integrity measure calculated for the reference safe basin of the unforced system (i.e. for $U(V) = 0$), so that GIM and IF are dimensionless numbers.

4.2 Basins of attraction and erosion

In this section, the evolution of basins of attraction is examined for increasing excitation amplitude at the same frequency values of figures 3.2, 3.4, 3.5 and 3.7; the results, reported in figures 4.1-4.4, are thus examples of the erosion process which characterizes each one of the previously distinguished four regions (figure 3.1). In all four cases, the erosion of the dominant (period-1) in-well solution is seen to begin at quite low values of forcing amplitude, just above the threshold of homoclinic bifurcation of the hilltop saddle (see figure 4.9(b) forward) which represents its triggering global event. However, the erosion progression features up to final escape are possibly different. The global scenarios at the two considered frequencies to the left of the two V-escape regions, $\omega_u = 0.7$ (figure 4.1) and $\omega_u = 1.4$ (figure 4.3), exhibit strong similarities. In both cases, a competing red basin corresponding to the newly SN-originated periodic solution, P1H in figure 4.1(b) and P2 in figure 4.3(b), appears within the in-well safe basin initially coinciding with the blue basin of attraction of the P1L solution, close to its boundary. In both cases, the red basin corresponds to a weak competing solution (see figures 3.2 and 3.5). Nearly after this event (in the considered large range of forcing amplitude values), erosion tongues of the unbounded solution (surrounding white area) enter the boundary between the two basins (figures 4.1(c) and 4.3(c)). This behavior is likely due to a heteroclinic connection between the hilltop saddle in figure 2.4(a) and the saddle on the inner basin boundary corresponding to the unstable solution in figure 3.2 or 3.5.

This entails fast disappearance of the small basin of the weak solution, which has meanwhile evolved to a localized chaos (not shown in the bifurcation diagrams) through the sequence of period doublings originated at SpPD1 (figure 3.2) and SpPD2 (figure 3.5), respectively. Upon disappearance of the small basin, the erosion of the main (blue) one progresses up to escape with smooth, i.e. uncorrupted, basin boundary (figures 4.1(d),(e) and 4.3(d),(e)), since it is protected by the stable manifold of the corresponding saddle. Overall, apart from the change of competing basin from P1H to P2, in connection with staying to left of fundamental and principal resonance, respectively, there are no meaningful global differences between the two cases.

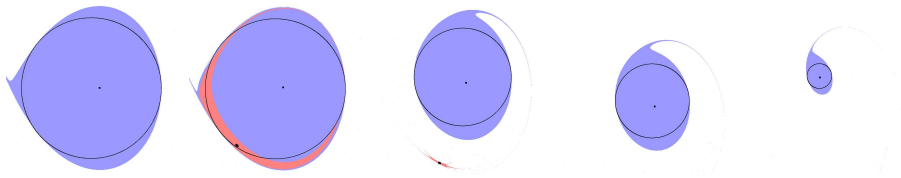

(a) (b) (c) (d) (e)

Figure 4.1: Basin evolution at $\omega_u = 0.7$ for $U = 0$ (a), $U = 0.005$ (b), $U = 0.05$ (c), $U = 0.1$ (d), $U = 0.2$ (e). Black circles are the safe basin IF measure

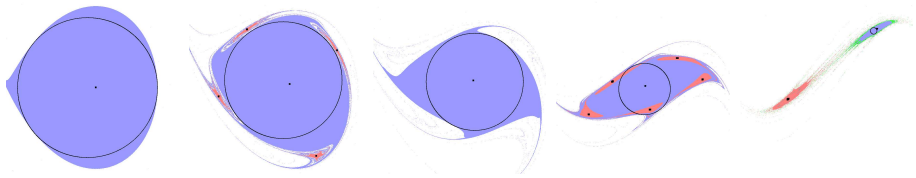

(a) (b) (c) (d) (e)

Figure 4.2: Basin evolution at $\omega_u = 1$ for $U = 0$ (a), $U = 0.3$ (b), $U = 0.5$ (c), $U = 0.8$ (d), $U = 1.1$ (e). Black circles are the safe basin IF measure

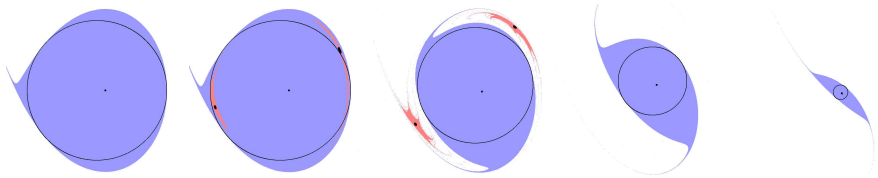

(a) (b) (c) (d) (e)

Figure 4.3: Basin evolution at $\omega_u = 1.4$ for $U = 0$ (a), $U = 0.001$ (b), $U = 0.01$ (c), $U = 0.07$ (d), $U = 0.15$ (e). Black circles are the safe basin IF measure

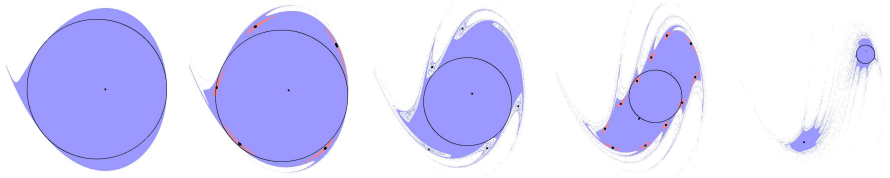

(a) (b) (c) (d) (e)

Figure 4.4: Basin evolution at $\omega_u = 1.8$ for $U = 0$ (a), $U = 0.007$ (b), $U = 0.03$ (c), $U = 0.05$ (d), $U = 0.07$ (e). Black circles are the safe basin IF measure

The frequency value $\omega_u = 1$ (figure 4.2) corresponds to an intermediate region in between the two resonances, where there is no meaningful effect from any of them. The associated erosion scenario exhibits a sequence of competing basins corresponding to higher periodicity solutions (figures 4.2(b), 4.2(d)), each one of them lasting for a limited forcing amplitude range. Their distributed small sub-basins are located close to the boundary of the main (blue) basin, a circumstance that entails an overall ragged aspect of the latter along the erosion process. The subsequent onset of the new competing period-1 solution P1L (figure 3.4) brings to the separation of the residual in-well safe basin in two parts (figure 4.2(e)), with strongly fractal edges in between them.

In the fourth case ($\omega_u = 1.8$, figure 4.4), which corresponds to a frequency range relatively high but still affected by the presence of the P2 solution (see figure 3.7), the period-1 initial basin turns into the period-2 basin (in between $U = 0.03$ and $U = 0.05$) thanks to the supercritical period doubling bifurcation; then, its erosion through fractal tongues from the surrounding unbounded solution brings to the separation in two sub-basins, as before, just prior to total annihilation. The occurrence (for small amplitude intervals) of small basins of higher periodicity solutions also in this case highlights how we are relatively far away from the governing resonance condition. Overall, such a circumstance entails, from the global viewpoint, the ragged aspect of the boundary of the disappearing main basin.

It is worth completing the analysis by looking also at the basins evolution closer to the resonance conditions, and in between linear and nonlinear resonances. This is interesting mostly to ascertain the global effect entailed by the presence of a stronger competing solution, with respect to the dominant one. In fact, the analysis is aimed not only at identifying features of overall erosion of the in-well safe basin but also at evaluating the relative robustness of competing solutions and the role they play in the erosion process. The relevant sequence of basins of attraction is reported in figures 4.5 and 4.6, respectively, for the cases $\omega_u = 0.8$ and $\omega_u = 1.6$, along with the relevant bifurcation diagrams, which have been already addressed in Sect. 3 (figures 3.3(a), 3.6(a)). Here, the common feature is represented just by the competition between the basin of the original period-1 solution and that of another, comparably robust, solution, i.e. the P1H (P2) around fundamental (principal) resonance. In the former case (figure 4.5), the newly born P1H

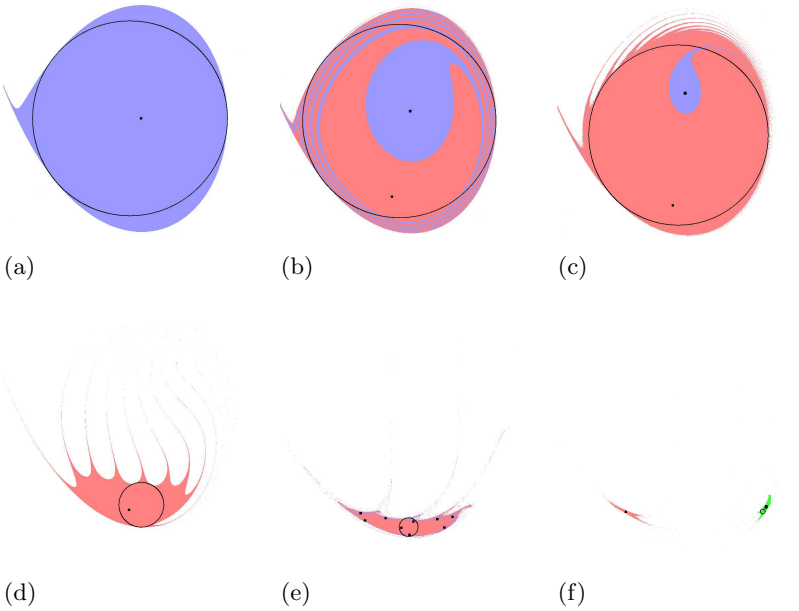

Figure 4.5: Basin evolution at $\omega_u = 0.8$, for $U = 0$ (a), $U = 0.01$ (b), $U = 0.03$ (c), $U = 0.1$ (d), $U = 0.6$ (e), $U = 0.7$ (f). Black circles are the safe basin IF measure

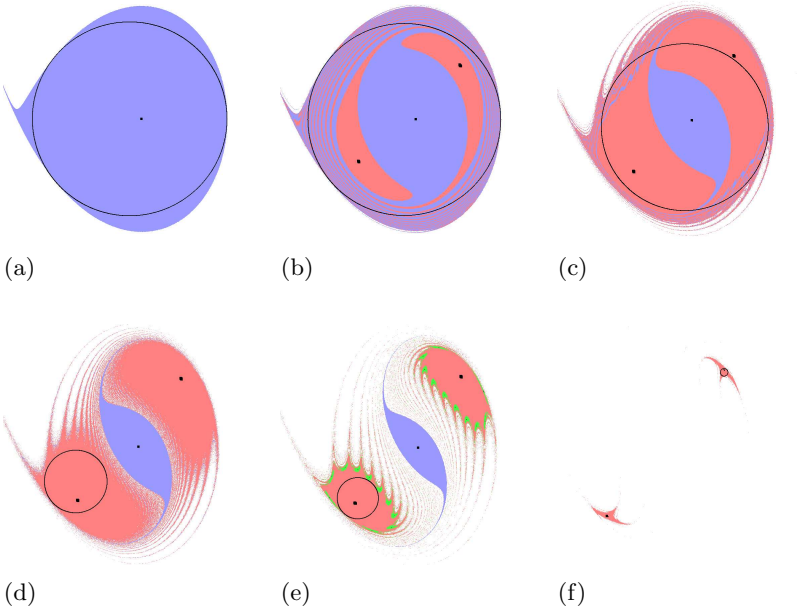

Figure 4.6: Basin evolution at $\omega_u = 1.6$, for $U = 0$ (a), $U = 0.002$ (b), $U = 0.01$ (c), $U = 0.015$ (d), $U = 0.02$ (e), $U = 0.05$ (f). Black circles are the safe basin IF measure

basin grows up swiftly, and with smooth boundary, within the in-well safe basin (see the value $U = 0.01$), up to fully replacing the original P1L basin and being then raggedly eroded from the outside. This global scenario is indeed very common when the newly born solution is a strong one (see, e g., [63]). In the latter case (figure 4.6), according to the major closeness to the reference (principal) resonance, there is a larger forcing amplitude range of coexistence of the two basins, the original P1 (blue) and the new-born P2 (red), which are of comparable robustness. Again, the erosion from the outside meaningfully affects the boundary in between the two basins, as in figures 4.1 and 4.3; here, however, it is much more apparent. As in figure 4.3, the blue basin decreases up to its subcritical period doubling disappearance with a smooth boundary, which is the stable manifold of the relevant saddle. Here, however, the final erosion involves only the split red basin of the formerly stronger P2 solution, which plays the definitely major role, as in figure 4.4.

4.3 Erosion profiles and dynamical integrity

The previous investigation highlights how the richest erosion patterns underlying escape occur in the two resonance regions. Accordingly, in this section the dynamical integrity analysis aimed at quantifying the extent and development of these phenomena is restricted to those regions. GIM and IF integrity measures have been calculated from the basins evolution to the left and right of the fundamental and principal resonances, within the triangle regions; the ensuing erosion profiles are reported in figures 4.7 and 4.8. Reference is made both to the individual basins of main periodic solutions (red and blue lines) and to the total in-well safe basin (black lines). GIM and IF profiles are plotted in solid and dashed lines, respectively.

In each figure, the left-side profiles (a) refer to frequencies before the vertex of V-shaped escape region, the right-side profiles (b) to frequencies after the vertex. A comparison between them shows that, before the peak, the safe basin erosion of the in-well safe basin, which coincides with the basin of the dominant periodic solution, starts at lower values of the forcing amplitude, but develops with a substantially smooth profile. In contrast, after the escape peak, the erosion profiles undergo a sudden, i.e., more dangerous, decrease, corresponding to a strong reduction of safe basin size, with

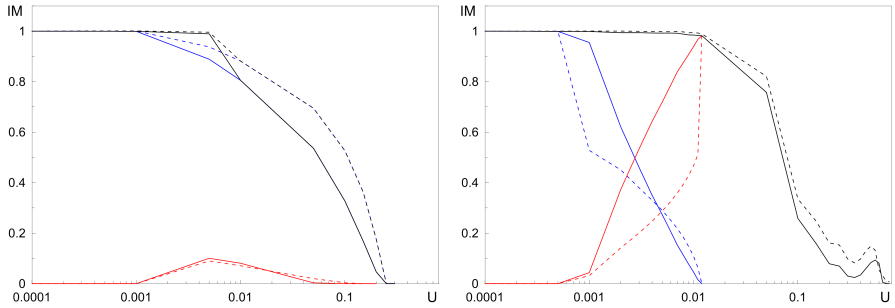

(a) (b)

Figure 4.7: Erosion profiles inside the triangle region of fundamental resonance, before and after the A vertex, for $\omega_u = 0.7$ (a) and $\omega_u = 0.8$ (b). Solid lines: GIM measure; dashed lines: IF measure; blue lines: P1L basin; red lines: P1H basin; black lines: total safe basin

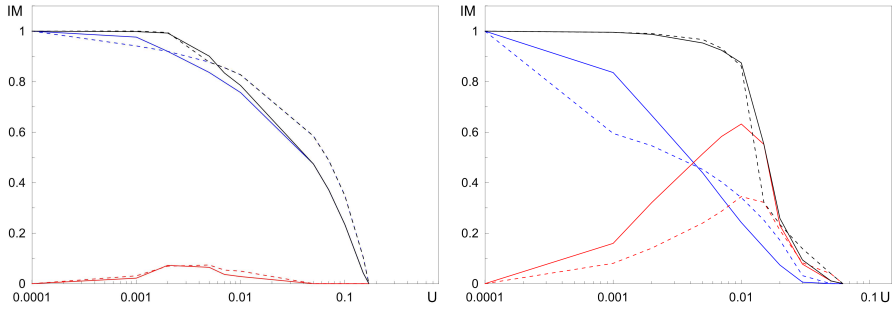

(a) (b)

Figure 4.8: Erosion profiles inside the triangle region of principal resonance, before and after the B vertex, for $\omega_u = 1.4$ (a) and $\omega_u = 16$ (b). Solid lines: GIM measure; dashed lines: IF measure; blue lines: P1L basin; red lines: P1H basin; black lines: total safe basin

only the very final part of the erosion process evolving in a smooth way.

Thus, analysis of the integrity process to the right of the two resonances (figures 4.7(b) and 4.8(b)) is carried on with the aim of highlighting common and distinct features of the basin erosion process. Firstly, it is interesting to consider the mutual role of the two competing periodic solutions, whose integrity is described by the single component profiles, with the crossing between the decreasing one of the initial P1 solution and the increasing one, related to the new growing up P1H (P2) solution in the fundamental (principal) resonance case. The two groups of profiles quantify the robustness of the competing solutions with the varying parameter, and some differences occur in the two resonance cases. At fundamental resonance (figure 4.7(b)),

the internal competition occurs up to nearly complete substitution of the original P1L basin with the new P1H one, which is immediately followed by an ever sharper erosion (red profiles) of the in-well safe basin (now coinciding with the P1H one), due to the surrounding escape tongues. Instead, at principal resonance (figure 4.8(b)), the erosion of the in-well safe basin (red profile, initially relevant to the P1, P2 union) smoothly progresses as the P2 profile is still increasing, up to becoming very sharp when the latter starts to decrease: this occurs at the separation of the two competing basins (for $U = 0.012$, see figure 4.6(c)-4.6(d)), which also entails drastic reduction of the compact part of the in-well safe basin.

The integrity curves of the two different basins also highlight a different behavior of the two integrity measures, ensuing from their respective definitions. At both resonances, since the basin of the new periodic solution, P1H (P2) in figure 4.7(b) (4.8(b)), is born inside the compact one of the original solution, its onset causes a meaningful initial reduction of the circle measuring the integrity (IF, dashed blue profile) of the former (P1) safe basin, while affecting its volume decrease (GIM, solid blue profile) to a minor extent. So, initially, the IF measure is definitely more conservative than the GIM one, from the safety viewpoint. This is a rather general behavior, also found for other systems [90]. However, after a while, the decrease of the circle radius (IF) of the disappearing solution becomes smoother than the decrease of the corresponding basin volume (GIM), which entails crossing of the two blue curves and major conservativeness of GIM in the residual part of the profiles. Overall, the different behavior of the two measures is less apparent in the (black) profiles of the in-well safe basin. This is evident in figure 4.7(b), where the erosion is due to a penetration of fractal tongues localized in the overall basin boundary (see figures 4.5(c)), thus poorly affecting the different integrity evaluation of the anyway compact in-well basin. In the second part of the profile, this coincides with the basin of the dominant P1H solution, which is rapidly eroded. In contrast, the effect of the different integrity evaluations is somehow higher in figure 4.8(b), since the fractal tongues affect now not only the outer boundary of the in-well safe basin, but also the inner boundary in between the two component basins. From about $U = 0.012$, the reduction of the basin of the now dominant P2 solution (and of the corresponding (solid red) GIM profile) corresponds to a sharp reduction also of the (solid black) GIM profile of the in-well safe basin, since

the latter substantially coincides with the former. But the reduction of the (dashed black) IF profile of the in-well safe basin is even sharper because of the separation of the two component basins (see figures 4.6(c)-4.6(d)), which entails the mentioned drastic reduction of the compact part of the in-well basin, i.e. of the circle of the P2 basin now governing the IF evaluation. In the residual part of the IF profiles, although the (dashed blue and red) ones of the two component solutions are comparable almost up to complete erosion, the (dashed black) profile of the in-well basin coincides with the sole (dashed red) one of the dominant P2.

It is worth looking at a summary diagram of GIM profiles of the in-well safe basin for different forcing frequencies: figures 4.9(a), 4.9(b) show an erosion surface in the range $\omega_u = 0.5 - 1.8$, with several iso-integrity curves obtained by expressing the erosion profiles in terms of remaining safe basin percentage. The profiles have the classical qualitative behavior of the so-called Dover cliff erosion curve [116], which is characterized by a slow decrease of the un-eroded volume of the safe compact region, followed by a sudden fall down to zero. Near the two resonance frequencies, the surface shows two evident depressions, with the lowest percentage values of residual integrity before the V peak and the sharpest decrease of the profiles after the peak, thus confirming what already noticed about the differences between figure 4.7(4.8)(a) and figure 4.7(4.8)(b). A matter of interest consists of investigating the safe basin evolution around the peaks, this time fixing the forcing amplitude U and using the forcing frequency ω_u as control parameter. Focusing, for example, around the fundamental resonance frequency, at an amplitude value of $U = 0.01$, a strong residual integrity variability is evident in the frequency range $0.6 - 0.8$ (dashed blue line in figure 4.9b), with differences up to nearly 20% of residual integrity. This behavior can be explained by analyzing the basin evolution at the selected excitation amplitude (figure 4.9(c)): at $\omega_u = 0.65$ two disconnected competing attractors (P1H and P1L solutions) are present in the same well, with the external one (P1H solution) which arises and gradually reduces the existent P1L basin (and consequently its residual integrity) as the frequency increases up to $\omega_u = 0.73$, where the interpenetration of the two basins occurs, thus enlarging the safe basin. After this frequency value, the penetration of fractal tongues of the surrounding infinity attractor starts for higher values of the forcing amplitude, and therefore the residual integrity at the reference ampli-

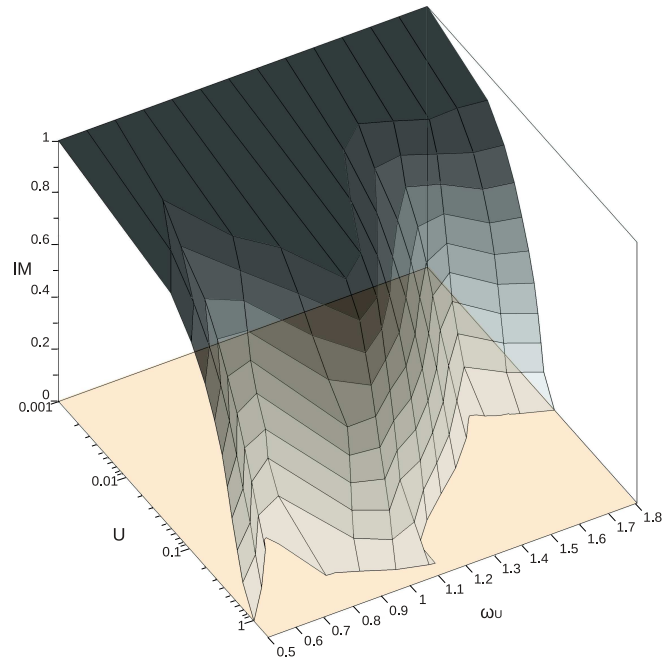

(a)

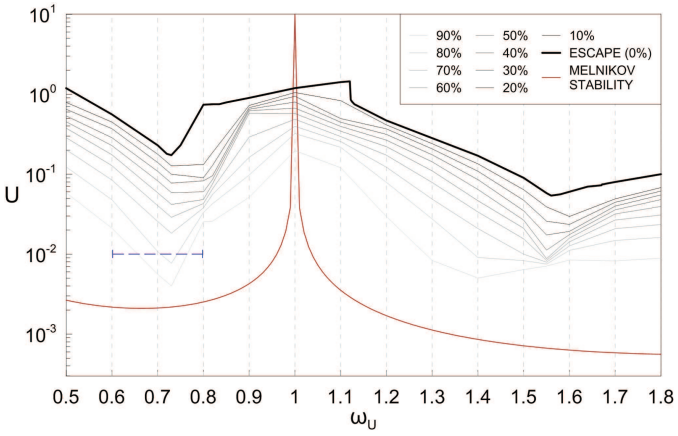

(b)

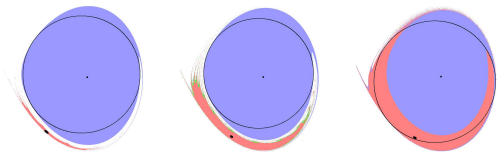

(c)

Figure 4.9: Erosion surface (a) with isointegrity curves (a,b) and basin evolution at $U = 0.01$ in the $0.6 - 0.8$ frequency range(dashed blue line in (b))(c)

tude ($U = 0.01$) increases. These results confirm, from another perspective, the observations of Sect. 4.2 about the increasing robustness of the new P1H basin as the frequency increases. In fact, before the frequency peak (see figure 4.1(b), 4.1(c), whose U values include the present one), the newly born basin of the weak P1H solution is disconnected from the dominant one of the strong P1L solution and reduces the in-well safe basin, which coincides with the latter. Instead, after the frequency peak (figure 4.5(b)), the robustness of the two solutions becomes comparable and the competition of the two connected basins occurs inside the in-well basin, which is now the sum of the two. A similar process happens in the principal region, where the new growing basin corresponds to the solution P2. It is important to highlight that, even if the two regions exhibit a qualitatively similar behavior, the escape amplitude values differ by an order of magnitude, being around 1 in the fundamental resonance range and around 0.1 in the principal resonance one. For the sake of comparison with the iso-integrity curves, the Melnikov curve of homoclinic bifurcation [44], corresponding to the threshold of transverse interaction of stable and unstable manifolds of the perturbed saddle of figure 2.4(a), is also reported in figure 4.9(b). It provides an estimate for the existence of solutions with long transverse transients that may lead to unbounded response. Possible occurrence of these transients is not taken into account in the integrity evaluation and, accordingly, the curve of nearly maximal (90%) iso-integrity is non-trivially higher than the Melnikov one.

Finally, the erosion processes of the total safe basin and of the main periodic solutions basins have been analyzed also for the externally driven system. The obtained results match very well those described in the previous section, as regards both the features of basins erosion and the slope of the corresponding profiles. In spite of the different sequence of bifurcations leading to escape, such a good agreement also holds in the high-frequency range, to the right of the subharmonic resonance vertex, due to the advanced erosion level at which the new bifurcations occur. Figure 4.10 represents the basin evolution and the erosion profiles at $\omega_v = 1.648$. Here, indeed, the supercritical flip bifurcation of P2, which marks the escape event in the parametrically driven system (see figure 4.8(a)), occurs when the erosion process has reduced the safe basin size of about 99% (figure 4.10(b)4), confining the subsequent bifurcations to the very last part of the profiles, with no meaningful effects.

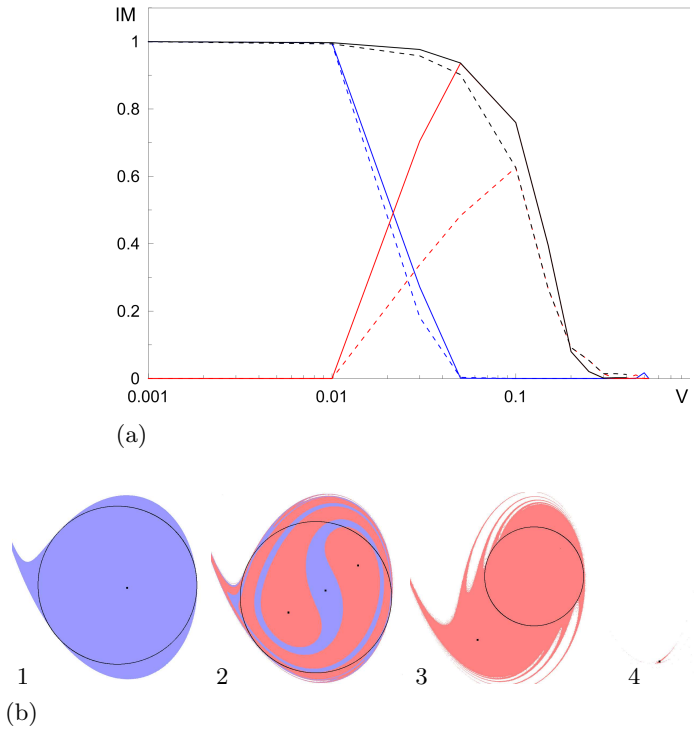

Figure 4.10: Erosion profiles (a) and basin evolution (b) for $\omega_v = 1.648$ and for $V = 0$ (P1 solution, (b1)), $V = 0.03$ (P1-P2 solutions, (b2)), $V = 0.1$ (P2 solution, (b3)), $V = 0.35$ (P4 solution, (b4))

Chapter 5

Exploiting dynamical integrity for engineering design

The potential of nonlinear dynamics to enhance performance, effectiveness, reliability and safety of systems is crucial to the aim of developing novel design criteria. In particular, dynamical integrity associated with global behavior meaningfully affects the actual practical stability of systems, and their capability to effectively withstand excitations in a dynamic environment.

The increasing interest towards such aspects for designing engineering systems is reflected in different works related to the topic, which have applied the dynamical integrity tools and concepts to different mechanical systems with the aim of highlighting their relevance and further investigating other mechanical/integrity issues that arise in practical cases [39, 40, 66, 70, 82, 95]. The quoted works highlight the great advantages of the integrity concept use with regard to the validation of experimental results, the verification of theoretical outcomes and a design perspective, the latter two being addressed in this chapter.

For what concerns the checking of theoretical results, attention is devoted to the critical comparison between stability boundaries obtained with a global approach, based on the study of the evolution of the periodic solutions and of their basins, and the ones obtained via the more traditional local methods based on the numerical integration of single trajectories. Fur-

thermore, integrity measures are applied to determine frequency-dependent thresholds able to ensure a priori established safety targets, in view of avoiding the escape from bounded region, which for noncontact AFMs corresponds to the unwanted "jump to contact" phenomenon, responsible for the alteration of the scanning results.

5.1 Theoretical and practical stability boundaries

From the viewpoint of AFM safe operation mode, some matters are of considerable interest regarding the evaluation of the system theoretical and practical stability. The first one is concerned with the comparison of the stability boundary carried out by mapping the bifurcation diagrams (bd), to be considered as a global boundary, with the escape threshold obtained by looking at the response under numerical integration (ni) with fixed initial conditions (i.c.) [44], to be considered as a local boundary. The comparison is reported in figure 5.1 for both parametric (blue) and external (red) excitations, where the dashed thresholds, related to numerical simulation, represent the forcing amplitude values U or V, for several forcing frequencies, at which divergence of system response does occur. Of course, the ni escape values strongly depend on the particular selection of the i.c. pair; here, values corresponding to the equilibrium position of the unperturbed system have been chosen. With respect to all of the local ni boundaries to be possibly constructed by considering divergence from different pairs of i.c. inside the safe basin, the global bd boundary represents the upper bound, since it corresponds to safe basin annihilation. For the considered selection of i.c. , the figure highlights significant differences between the two boundaries, the local one lying below the global, with a gap of up to 25 times the ni absolute value. Moreover, ni local minima occur at primary and subharmonic resonance frequencies, while bd minima are shifted towards left (i.e. , to nonlinear resonances) due to the softening behavior of the system. The apparent underestimation of system stability with ni ensues from the particular selection of the i.c. pair against the basin erosion scenario. Focusing on parametric excitation and looking for example at $\omega_u = 0.8$, a slight increase of the excitation amplitude (around the escape value $U = 0.03$) is seen to cause a basin boundary erosion which swiftly expands up to including the initial position (black point in figures 5.1(b),5.1(c)), while leaving

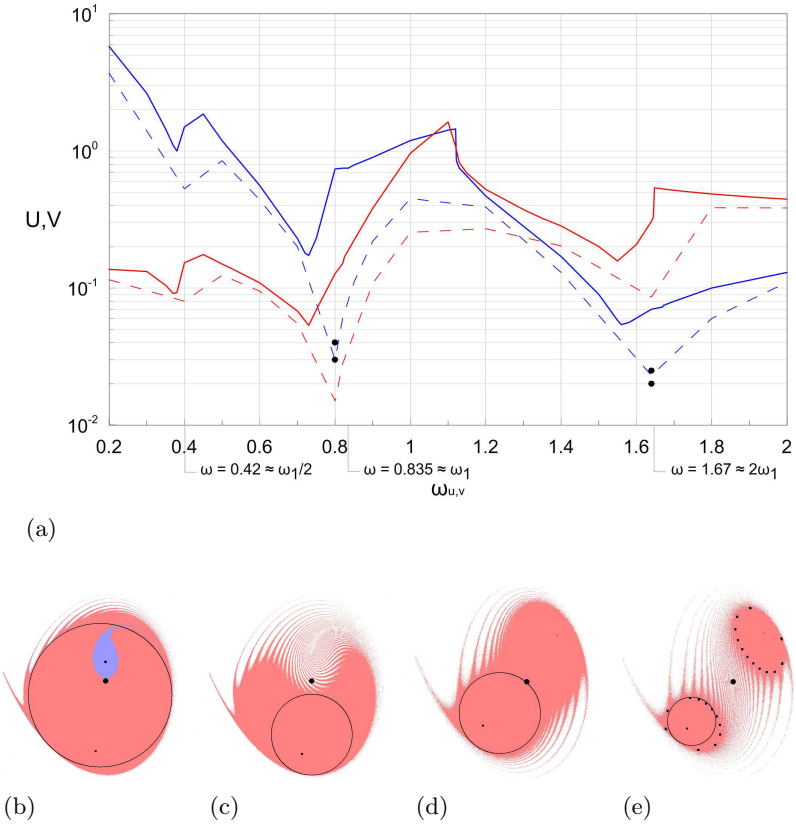

Figure 5.1: Comparison between *ni* (dashed) and *bd* (solid) escape thresholds for the parametrically (blue) (externally (red)) driven system (a): for parametric excitation, state-space basin evolution at $\omega_u = 0.8$, for $U = 0.03$ (b) and $U = 0.04$ (c), and at $\omega_u = 1.64$ for $U = 0.023$ (d) and $U = 0.025$ (e). The black point is the equilibrium position

more than 50% of residual integrity of the (red) safe basin. In contrast, the actual basin annihilation (*bd* threshold) occurs only at $U = 0.74$. In turn, figures 5.1(d), 5.1(e) show the similar topological process responsible for the marked difference between *ni* and *bd* thresholds at principal resonance: in fact, here, the selected i.c. lie just in the region of the in-well safe basin separation, so that the divergence of the trajectory occurs for a residual integrity of more than 40%. This clearly highlights how, in terms of overall system safety with respect to escape, consideration of the outcome of a single trajectory may furnish misleading and too conservative information, unless being specifically interested in the response ensuing from that particular set of i.c. Anyway, even correctly referring to the global stability boundary in terms of escape, the major problem in a safety assessment perspective ensues from

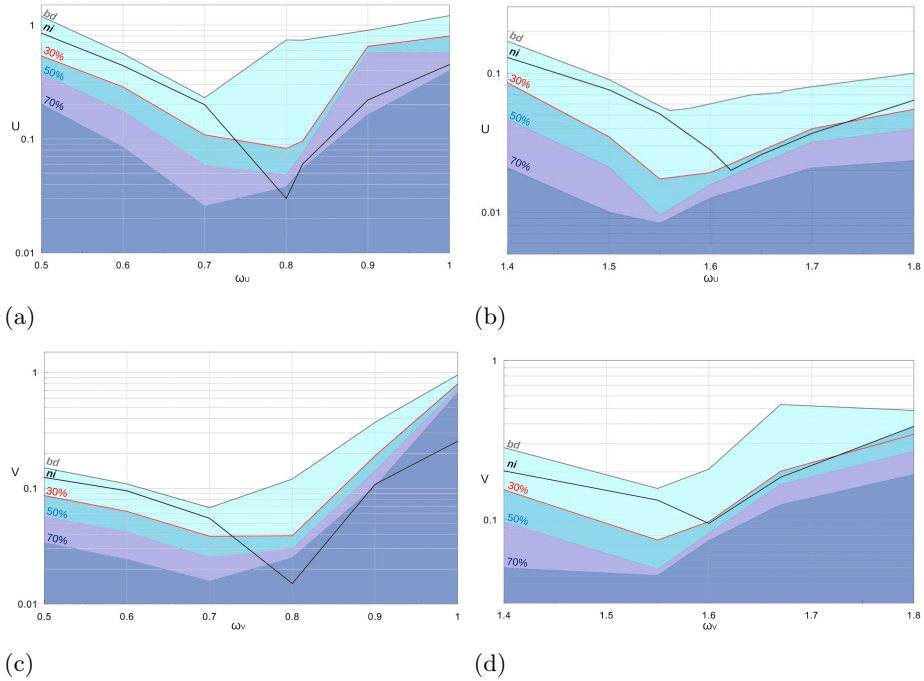

Figure 5.2: Comparison between theoretical (*ni* and *bd*) and practical (residual integrity) stability boundaries with the detection of some residual isointegrity curves. (a) and (b) refer to fundamental and principal resonance region for the parametrically forced system, respectively, while (c) and (d) refer to the externally forced system, respectively

the associated total lack of information about the features of basin erosion. Hence, in practical applications, it is particularly important to refer to integrity evaluations in order to determine acceptable frequency-dependent thresholds associated with a priori safe design targets [2, 66]. Figure 5.2 shows four iso-integrity curves corresponding to increasing target values in the two resonance regions under scan parametric excitation. Selecting for instance the 30% residual safety target, the corresponding red threshold allows us to critically discuss the results furnished by numerical simulations (black threshold). Away from the two nonlinear resonances (left of them), though the *ni* thresholds underestimate system safety with respect to the *bd* threshold, they are definitely unacceptable because of corresponding to very low values of residual integrity (0-30%). Yet, the most questionable point is that *ni* thresholds correspond to a residual integrity strongly variable over the control parameter range (see for example the frequency range in between 0.7 and 0.8 in figure 5.2(a)), even though the associated threshold tends to become more and more over conservative (thus corresponding to a higher

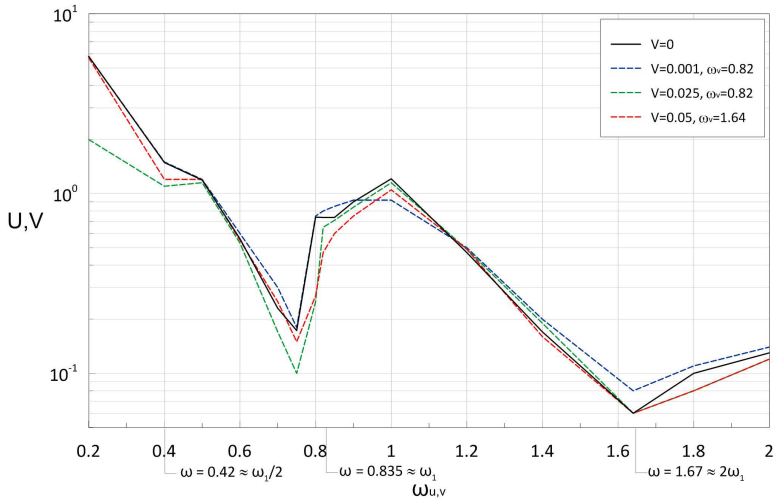

Figure 5.3: *bd* stability boundaries of the system under combination of varying horizontal U and fixed V excitations, for $V = 0$ (parametrically forced system)(solid black line), $V = 0.001$ and $\omega_v = 0.8325$ (dashed blue line), $V = 0.025$ and $\omega_v = 0.82$ (dashed green line), $V = 0.05$ and $\omega_v = 1.64$ (dashed red line)

residual integrity) just where this is more needed. At principal resonance (figure 5.2(b)), a minor variability of the *ni* threshold with respect to the residual integrity occurs. However, the threshold corresponds again to a very poor safety reserve, and this occurs where it is more needed, owing to the lower values of escape excitation. Behaviors similar to those in figure 5.2(a), 5.2(b) have been obtained also for the externally forced problem, whose results are reported in figures 5.2(c), 5.2(d).

A final point has to be made as regards the influence of combined horizontal scan excitation and vertical beam excitation, which coexist in the noncontact AFM operation mode, on the overall dynamics. Using the numerical integration approach, Hornstein and Gottlieb [44] compared the local escape thresholds in the $\omega_u - U$ control plane as obtained either with the sole (parametrical) horizontal scan or by adding an (external) vertical excitation with constant amplitude ($V = 0.001$) and a frequency at primary resonance ($\omega_v = 0.8325$). They found that the effect of dual frequency excitation on the escape regions is negligible, apart from a substantially minor decrease of the allowed forcing amplitude of the scan process in the low frequency area, with respect to that obtained without base excitation (see also [45]). The same behavior is obtained constructing the global escape threshold with the same $\omega_v - V$ values of [44]: the results highlight a neg-

ligible difference with those obtained from the bifurcation diagrams of the sole parametric excitation case, therefore confirming that, for the chosen set of parameters values, the dual excitation analysis is not even necessary in the primary resonance region in which the vertical excitation produces the major effects. To complete the analysis, higher values of the vertical excitation amplitude have been also considered, corresponding to 50% of residual integrity of the externally forced problem both at primary ($V = 0.025$ at $\omega_v = 0.82$) and subharmonic ($V = 0.05$ at $\omega_v = 1.64$) resonance frequencies, whose results are reported in figure 5.3. Also in these cases the escape profile remains substantially unchanged, with a slight decrease of the forcing amplitude at the fundamental resonance vertex and a small increase (reduction) of the one at the principal resonance vertex for $\omega_v = 0.82$ ($\omega_v = 1.64$). The negligible differences between the dual excitation problem and the sole scan process make the previous results not worth to be reported.

Chapter 6

Noncontact AFM with external feedback control

The AFM dynamical behavior is strongly related to the distance between the cantilever tip and the sample to be scanned, which modifies the nonlinear atomic force interaction and is used to perform the topography. During the scan operations, the sample roughness can thus induce unstable motions to the cantilever and eventually chaotic responses, which have been numerically and experimentally observed [9, 20, 58, 75, 122]. Referring to the AFM model presented in the previous section, it is therefore of interest to investigate the changes in the system response as a function of the varying tip-sample gap. To this end, a new nondimensional parameter is introduced in the atomic interaction term of (2.19), which represents the possible changes in the tip-sample distance:

$$\begin{aligned}\left(1+\alpha_2 x^2\right)\ddot{x}+\left(\alpha_1+\alpha_2\dot{x}^2+\alpha_3 x^2\right)x = \\ -\frac{\Gamma_1}{\left(1-\delta_g+x+V_g\right)^2}-\left(\rho_1+\rho_2 x^2\right)\dot{x}-\left(\ddot{V}_g+\nu_1\dot{V}_g\right)\nu_2 \\ +\left(\mu_1 x+\mu_2 x^3\right)\left(\ddot{U}_g+\eta_1\dot{U}_g+\eta_2 U_g\right)\end{aligned} \tag{6.1}$$

where $\delta_g = \bar{\delta_g}/\gamma$ is the nondimensional reduction ratio of the tip-sample gap. Remember that the nondimensional equation (2.19) has been scaled with respect to the dimensional gap γ to set it equal to 1. Some behavior charts as a function of the varying δ_g are reported in figure 6.1, for the

parametrically excited AFM model near the fundamental resonance and for the following set of parameters values:

$$\alpha_1 = 1, \quad \alpha_3 = 0.1, \quad \rho_1 = 0.001, \quad \Gamma_1 = 0.1, \quad \mu_1 = 1.5708.$$

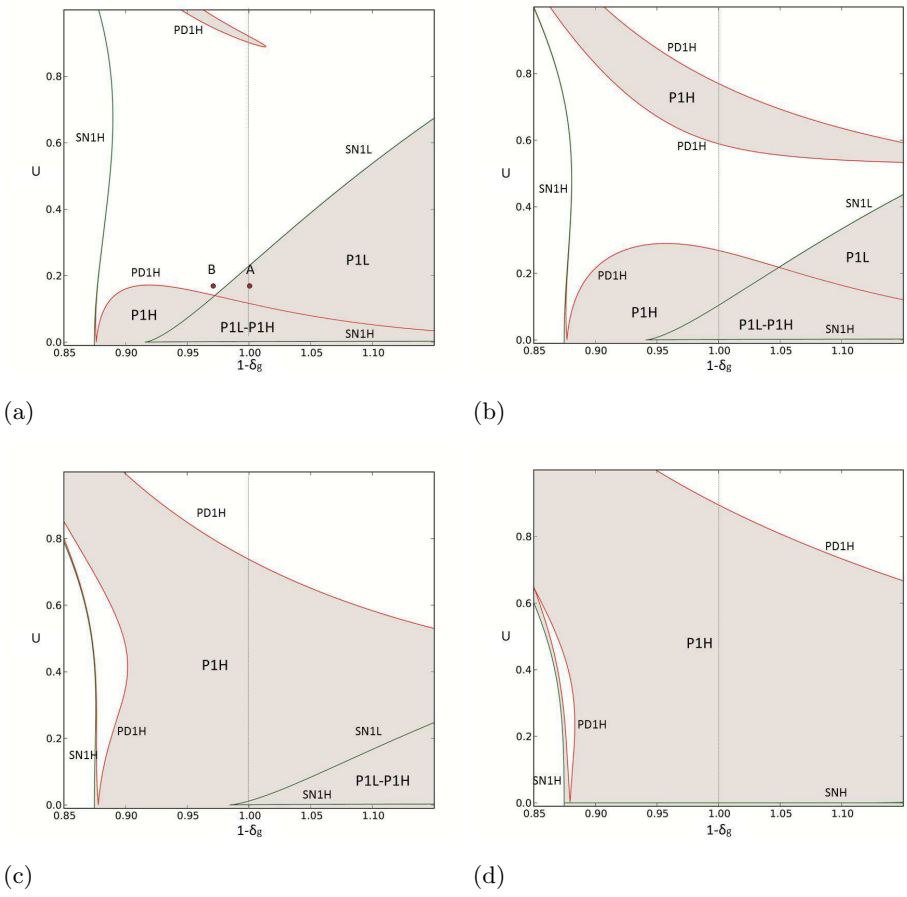

Figure 6.1: Behavior charts at $\omega_u = 0.7$ (a), $\omega_u = 0.76$ (b), $\omega_u = 0.82$ (c), $\omega_u = 0.9$ (d). PDH = period doubling threshold of the high-amplitude P1 solution; SNH = saddle-node threshold of the high-amplitude P1 solution; SNL = saddle-node threshold of the low-amplitude P1 solution

The reported charts point out that the tip-sample gap strongly modifies the dynamical behavior of the AFM cantilever, changing the regions of existence of the main periodic solutions (i.e. low-amplitude P1L solution and high-amplitude P1H solution) together with their stability thresholds. This means that during the scan operations, which lead to changes in the tip-

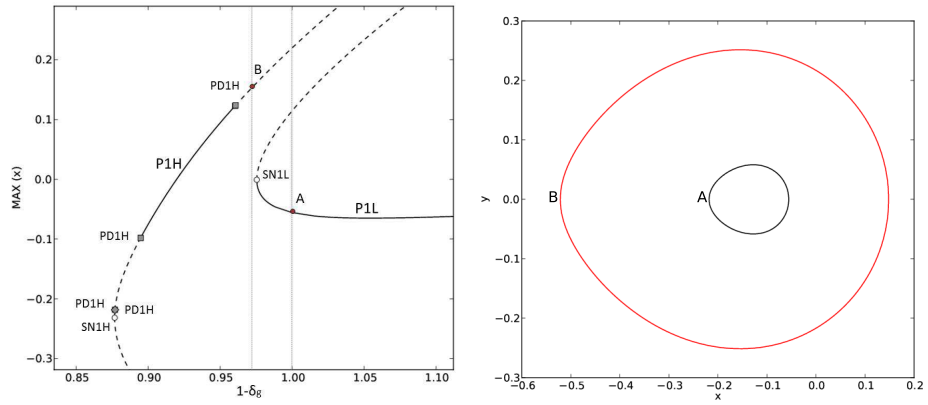

(a) (b)

Figure 6.2: Bifurcation diagram (a) and trajectories in the state plane for $\delta_g = 0.03$ (red orbit B) and $\delta_g = 0$ (black orbit A) (b) at $\omega_u = 0.7$ and $U = 0.15$

sample distance, the dynamical response of the cantilever can suddenly pass from low-amplitude oscillations to high-amplitude motions and eventually bring to unstable periodic solutions. Such undesirable behavior is shown, as example, in figures 6.1(a) and 6.2 which are referred to a frequency of $\omega_u = 0.7$ and a forcing amplitude of $U = 0.15$. Here, point (orbit) A represents the stable low-amplitude 1-period solution for the system which maintains an unitary distance from the sample. As the tip-sample gap decreases, P1L solution loses stability through a saddle-node bifurcation and the system displays a narrow region of instability between $\delta_g = 0.025$ and $\delta_g = 0.039$, which corresponds to the white area just above the V vertex of the behavior chart 6.1(a), characterized by the presence of the unstable high-amplitude solution (point(orbit) B). For higher values of the gap ratio δ_g the P1H solution becomes the only stable solution. It is therefore clear that even slight variations of tip-sample distance can produce critical changes in the system dynamics and thus bring to erroneous results on the sample topography.

To avoid possible unstable periodic responses of the system, an external feedback control is applied to the AFM model, following the method proposed by Yagasaki [123], whose objective is not to stabilize a specific unstable periodic orbit (as, e.g., in the OGY method [84]), but to keep the cantilever vibration to the one chosen as reference and simultaneously measure the sample surface. The periodic reference response is obtained when

the center of the cantilever base oscillation and the sample surface are at the reference position. The control implementation into the model leads to the introduction of a new variable $\bar{\xi}(t)$ which represents the distance of the fixed side of the cantilever from the horizontal reference axis, and of a new parameter $\bar{\xi}_s$ which is the displacement of the sample surface from the selected reference position (figure 6.3).

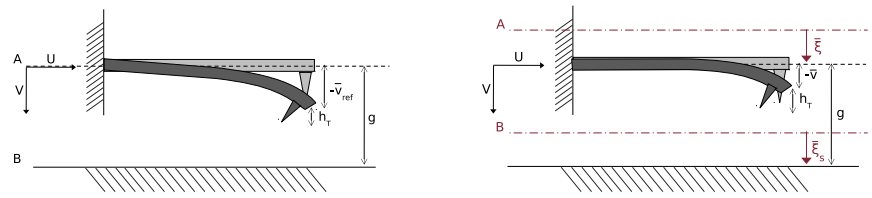

(a) (b)

Figure 6.3: Cantilever at reference position (a) and in a generic configuration (b); lines A and B represent the reference positions of the microcantilever and the sample surface, respectively.

6.1 Model formulation

Differently from the procedure followed by Yagasaki, who inserted the control into the reduced single-mode model of tapping AFM, in this work the control insertion occurs at the very beginning of the model formulation; accordingly, a new d.o.f. is added to the general relations of the uncontrolled system (2.1) deduced from the extended Hamilton's principle:

$$\begin{aligned} &m\bar{u}_{tt} - [EI\bar{v}_{rrr}\bar{v}_r - J_z\bar{v}_{ttr}\bar{v}_r + \Lambda(1+\bar{u}_r)]_r = \bar{Q}_u \\ &m\bar{v}_{tt} - [EI(\bar{v}_{rrr} + \bar{v}_r\bar{v}_{rr}^2) + J_z(\bar{v}_{ttr} + \bar{v}_{tr}^2\bar{v}_r) + \Lambda\bar{v}_r]_r = \bar{Q}_v \\ &\bar{\xi}_t = \bar{k}(\bar{v}_{ref} - \bar{v}) \end{aligned} \tag{6.2}$$

where $\bar{Q}_u$ and $\bar{Q}_v$ are the same of (2.2) and

$$F_v^A = \frac{A_H R_T}{6\sigma_a^2}\left[-\left(\frac{\sigma_a}{g+\bar{v}-h_T-\bar{\xi}_s}\right)^2 + \frac{1}{30}\left(\frac{\sigma_a}{g+\bar{v}-h_T-\bar{\xi}_s}\right)^8\right] \tag{6.3}$$

$\bar{u}(r,t)$ and $\bar{v}(r,t)$ are now the horizontal ad vertical displacements of the controlled system, $\bar{v}_{ref}(r,t)$ represents the reference vertical displacement, obtained from the uncontrolled system ($\bar{\xi} = 0$, i.e. $\bar{v}(r,t)$ of (2.1)), and $\bar{k}$ is

a feedback constant. The new variable $\bar{\xi}(t)$ modifies the boundary conditions as follows:

$$\begin{aligned} &\bar{v}(0,t) = \bar{V}(t) + \bar{\xi}(t) = \bar{W}(t), \quad \bar{v}_r(0,t) = 0, \qquad \bar{u}(0,t) = \bar{U}(t), \\ &\bar{v}_{rr}(L,t) = 0, \qquad\qquad\qquad\quad \bar{v}_{rrr}(L,t) = 0, \quad \bar{u}_r(L,t) = 0. \end{aligned} \tag{6.4}$$

so that the nondimensional homogeneous boundary system (2.11) (2.14) becomes

$$\begin{aligned} w_{\tau\tau} + W_{\tau\tau} + w_{ssss} - \mu w_{\tau\tau ss} - Q_w = \Bigg[& -w_s \left(w_{ss} w_s\right)_s + \mu w_s \left(w_{\tau s} w_s\right)_\tau \\ & + w_s \left(\left(1 + \frac{1}{2} w_s^2\right) \int_1^s U_{\tau\tau} \mathrm{d}s - \frac{1}{2} \int_1^s \left(\int_0^s w_s^2 \mathrm{d}s \right)_{\tau\tau} \mathrm{d}s \right. \\ & \left. - \left(1 + \frac{1}{2} w_s^2\right) \int_1^s Q_u \mathrm{d}s \right) \Bigg]_s \\ \xi_\tau = k(w_{ref} - w) & \end{aligned} \tag{6.5}$$

where Q_u has the same form of (2.12), while the generalized force in vertical direction Q_v is modified by the boundary conditions (6.4) as follows

$$\begin{aligned} Q_w = \delta(s-\alpha)\bar{\Gamma}_1 & \left[-\frac{1}{(\gamma + w + W - \xi_s)^2} + \frac{\bar{\Gamma}_2}{(\gamma + w + W - \xi_s)^8} \right] \\ & - v(w_\tau + B_\tau) \end{aligned} \tag{6.6}$$

with $\xi = \bar{\xi}/L$, $\xi_s = \bar{\xi}_s/L$, $k = \bar{k}/L$, $W = \bar{W}/L$, $w_{ref} = \bar{v}_{ref}/L$. As proposed for the uncontrolled case, a single-mode reduction is applied to the controlled vertical displacement variable $w(s,\tau)$ and to the reference vertical displacement $w_{ref}(s,\tau)$:

$$\begin{aligned} w(s,\tau) &= q_1(\tau)\Phi_1(s) \\ w_{ref}(s,\tau) &= q_{ref1}(\tau)\Phi_1(s) \end{aligned} \tag{6.7}$$

Remember that $w_{ref}(s,\tau)$ corresponds to $w(s,\tau)$ of equation (2.15). The Galerkin procedure leads to the following governing equations:

$$\begin{aligned} &I_1 q_{1\tau\tau} + I_{11}(\nu q_{1\tau} + \omega_1^2 q_1) + I_2(W_{\tau\tau} + \nu W_\tau) + I_3 q_1^3 \\ &\quad + I_4 q_1 \left(q_{1\tau}^2 + q_{1\tau\tau} q_1\right) = q_1^2 q_{1\tau} \left(g_1 I_{41} + g_2 I_7\right) + \frac{1}{2} q_1^3 I_{41} g_3 \\ &\quad + \bar{\Gamma}_1 \Phi_1(\alpha) \left(-\frac{1}{\left(\gamma + q_1 \Phi_1(\alpha) + B - \xi_s\right)^2}\right) \\ &\quad + \left(q_1 I_5 + \frac{1}{2} q_1^3 I_6\right) \left(U_{\tau\tau} + g_1 U_\tau + g_3 U\right) \\ &I_2 \xi_\tau = I_{11} k \left(q_{ref1} - q_1\right) \end{aligned} \tag{6.8}$$

where $I_{i,j}$ are the same of the uncontrolled case reported in Appendix A. Compared with equation (2.18), note that, as expected, the feedback control acts on the system by modifying the terms related to the tip-sample distance, which are the nonlinear atomic interaction term and the vertical vibration V.

New variables $x(\tau) = q_1(\tau)\Phi_1(\alpha)/\gamma$, $x_{ref}(\tau) = q_{ref1}(\tau)\Phi_1(\alpha)/\gamma$ and $z = \xi/\gamma$ are defined, which are rescaled by the time scale $t_N = \omega_1 \tau$, to obtain the final form of the controlled system equations:

$$\begin{aligned} &\left(1 + \alpha_2 x^2\right) \ddot{x} + \left(\alpha_1 + \alpha_2 \dot{x}^2 + \alpha_3 x^2\right) x = \\ &\qquad - \frac{\Gamma_1}{\left(1 + x + V_g + z - z_s\right)^2} - \left(\rho_1 + \rho_2 x^2\right) \dot{x} \\ &\qquad - \left(\ddot{V}_g + k_g \left(\dot{x}_{ref} - \dot{x}\right) + \nu_1 \left(\dot{V}_g + k_g \left(x_{ref} - x\right)\right)\right) \nu_2 \\ &\qquad + \left(\mu_1 x + \mu_2 x^3\right) \left(\ddot{U}_g + \eta_1 \dot{U}_g + \eta_2 U_g\right) \\ &\dot{z} = k_g \left(x_{ref} - x\right) \end{aligned} \tag{6.9}$$

where coefficients have the same definition of (2.20) and

$$z_s = \frac{\xi_s}{\gamma}, \quad V_g = \frac{W}{\gamma}, \quad k_g = \frac{I_{11} k}{\Phi_1(\alpha) I_2 \omega_1}.$$

Note that x_{ref} represents the periodic reference response of the uncontrolled system, and thus can be expressed as the sum of a mean $\bar{x}_{ref}$ and a time-dependent oscillating component $\tilde{x}_{ref}(t)$

$$x_{ref} = \bar{x}_{ref} + \tilde{x}_{ref}(t) \tag{6.10}$$

6.2 Equilibrium analysis and stability of fixed points

The equilibrium analysis of the controlled system involves the elimination of the explicit time-dependent excitations $U_g = V_g = 0$ together with the oscillating reference position $\tilde{x}_{ref}(t) = 0$ so that $x_{ref} = \bar{x}_{ref}$:

$$\begin{aligned}
\dot{x} =& y \\
\dot{y} =& -\frac{1}{1+\alpha_2 x^2}\left(\left(\alpha_1+\alpha_2 y^2+\alpha_3 x^2\right)x + \frac{\Gamma_1}{\left(1+x+z-z_s\right)^2}\right. \\
& \left. +\left(\rho_1+\rho_2 x^2\right)y + \left(-y+\nu_1\left(\bar{x}_{ref}-x\right)\right)k_g\nu_2\right) \\
\dot{z} =& k_g\left(\bar{x}_{ref}-x\right)
\end{aligned} \tag{6.11}$$

To obtain the system fixed points, the velocities are set equal to zero ($\dot{x} = \ddot{x} = \dot{z} = 0$); consequently $x = \bar{x}_{ref}$, and $z = z_s$ is the arbitrary displacement from the reference position. The controlled system becomes

$$\left(1+x\right)^2\left(\alpha_1+\alpha_3 x^2\right)x + \Gamma_1 = 0 \tag{6.12}$$

whose solution $q^*\left(\bar{x}_{ref}, z_s\right)$ points out that the system equilibria are not influenced by the feedback control parameter k_g.

For a general choice of the parameters, the five solutions are obtained from a quintic polynomial which is the same as that of the uncontrolled system; among them, only two solutions are acceptable, and correspond to the upper stable fixed point and to the unstable one of the uncontrolled system (see figure 2.4(b) in Sect. 2.3).

The stability of the system fixed points involves the study of the Jacobian matrix at the equilibrium $q^*\left(\bar{x}_{ref}, z_s\right)$:

$$J_{q^*} = \begin{bmatrix} 0 & 1 & 0 \\ a_{21} & a_{22} & a_{23} \\ -k_g & 0 & 0 \end{bmatrix} \tag{6.13}$$

where

$$\begin{aligned} a_{21} =& \left(1+\alpha_2\bar{x}_{ref}^2\right)^{-2}\left(\left(1+\alpha_2\bar{x}_{ref}^2\right)\alpha_1 - \bar{x}_{ref}^2\left(3+\alpha_2\bar{x}_{ref}^2\right)\alpha_3\right. \\ & +2\Gamma_1\left(1+\bar{x}_{ref}\right)^{-3}\left(1+\alpha_2\bar{x}_{ref}\left(1+2\bar{x}_{ref}\right)\right) \\ & \left.+\nu_1\nu_2 k_g\left(1+\alpha_2\bar{x}_{ref}^2\right)\right) \\ a_{22} =& \left(1+\alpha_2\bar{x}_{ref}^2\right)^{-1}\left(\rho_1+\rho_2\bar{x}_{ref}^2-\nu_2 k_g\right) \\ a_{23} =& 2\Gamma_1\left(1+\alpha_2\bar{x}_{ref}^2\right)^{-1}\left(1+\bar{x}_{ref}\right)^{-3} \end{aligned} \tag{6.14}$$

The coefficients of its characteristic polynomial $p_{J_{q^*}}(\lambda) = \lambda^3 + C_1\lambda^2 + C_2\lambda + C_3 = 0$ are

$$\begin{aligned} C_1 &= -\mathrm{tr}\left(p_{Jq*}\right) = -a_{22} \\ C_2 &= \mathrm{Z}\left(p_{Jq*}\right) = -a_{21} \\ C_3 &= -\det\left(p_{Jq*}\right) = -a_{23}k_g \\ \Delta_2 &= C_1C_2 - C_3 \end{aligned} \tag{6.15}$$

The equilibrium solutions are asymptotically stable if and only if

$$\begin{cases} C_j > 0, \quad j = 1,2,3 \\ \Delta_2 > 0 \end{cases} \tag{6.16}$$

Due to the dependence on the feedback parameter k_g, the stability analysis of the two fixed points has been carried out in function of both Γ_1 and k_g for the following set of parameters values:

$$\begin{array}{lllll} \alpha_1 = 1, & \alpha_2 = 0, & \alpha_3 = 0.1, & \rho_1 = 0.001, & \rho_2 = 0, \\ \nu_1 = 0.01, & \nu_2 = 0.01, & \mu_1 = 1.5708, & \mu_2 = 0, & \eta_1 = 0, \\ \eta_2 = 0, & z_s = 0.01. & & & \end{array} \tag{6.17}$$

The reported results are evaluated numerically, with the values of the equilibrium position $q^*\left(\bar{x}_{ref}, z_s\right)$ obtained as solution of the corresponding uncontrolled system. Figure 6.4 shows the influence of the coefficients of the characteristic polynomial (6.15) on the stability of the system stable equilibrium solution; their contributions are summarized, together with the ones related to the unstable equilibrium branch, in figure 6.5. It is evident that the Δ_2 coefficient governs the fixed point stability, reducing it as the value of the feedback control parameter increases, up to the upper boundary of

$k_g = 0.1$ for which both Δ_2 and C_1 change their sign making the fixed point unstable. As regards the equilibrium that corresponds to the unstable equilibrium of the uncontrolled system, it remains unstable over the whole domain even after the control introduction.

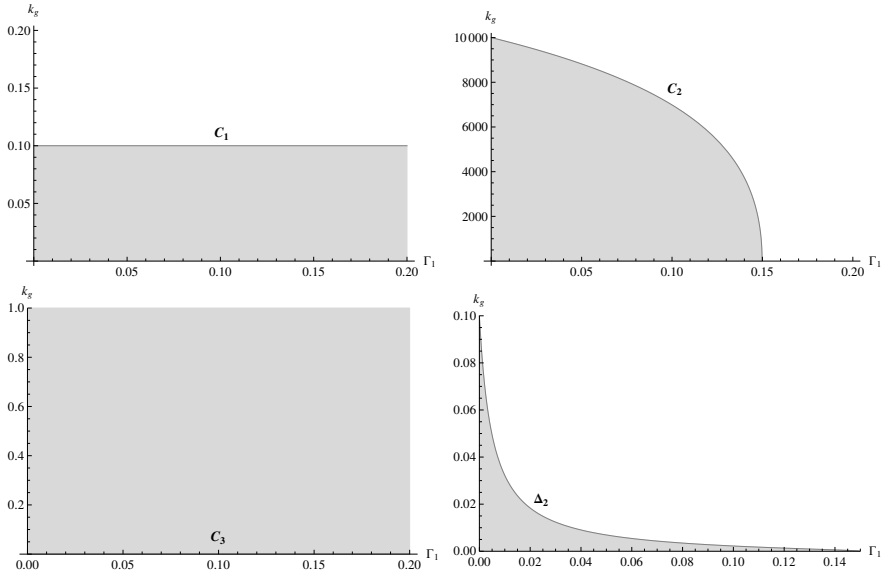

Figure 6.4: Stability thresholds of the fixed point that corresponds to the stable equilibrium of the uncontrolled system, determined by studying the characteristic polynomial coefficients: gray regions represent the loci where $C(\Delta)_j > 0$, gray curves are the loci where $C(\Delta)_j = 0$

For the parameters choice (6.17) and for $\Gamma_1 = 0.1$, the coefficients values as function of k_g are:

$$\begin{aligned}
\bar{x}_{ref1}: \quad & C_1 = 0.001 - 0.01k_g, \quad C_2 = 1.978 - 0.0001k_g, \quad C_3 = 3.085k_g, \\
& \Delta_2 = 10^{-6}k_g^2 - 3.066k_g - 0.002 \\
\bar{x}_{ref2}: \quad & C_1 = 0.001 - 0.01k_g, \quad C_2 = 0.699 - 0.0001k_g, \quad C_3 = 3.07k_g, \\
& \Delta_2 = 10^{-6}k_g^2 - 3.314k_g + 0.0007
\end{aligned}$$

Therefore, for the chosen value of the nonlinear interaction parameter, $\bar{x}_{ref1}$ is always unstable while the asymptotic stability of the equilibrium solution $\bar{x}_{ref2}$ occurs for $0 < k_g < 0.00223$. The three eigenvalues which are solution of the characteristic polynomial $p_{J_{q^*}}$ can be studied to point out the possible bifurcation scenarios of the system fixed points; as they turn out to be $\lambda_{1,2} = \mathrm{Re}_{1,2} \pm i\mathrm{Im}_{1,2}$, $\lambda_3 = \mathrm{Re}_3$, the possible kinds of bifurcations the system

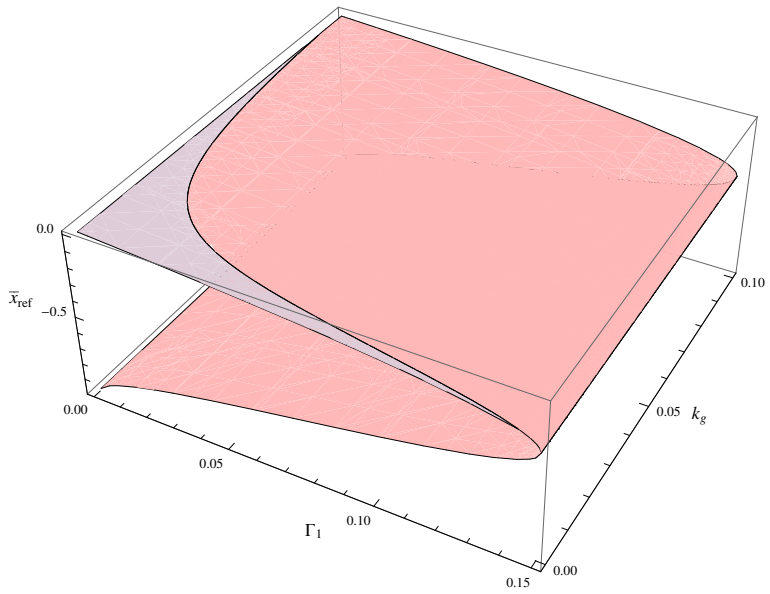

Figure 6.5: Stability regions of the controlled fixed points as a function of the feedback control parameter k_g and the atomic interaction parameter Γ_1. Gray area = stable region, red area = unstable region.

can display are:

- Divergence bifurcation: $\text{Re}_3 = 0 \Rightarrow C_3 = 0$
- Hopf bifurcation: $\text{Re}_{1,2} = 0$, $\text{Im}_{1,2} = \omega_H > 0 \Rightarrow \Delta_2 = 0$, $\omega_H = \sqrt{C_3/C_1} > 0$ with $C_3 = C_1 C_2$
- Divergence-Hopf bifurcation: $\text{Re}_3 = \text{Re}_{1,2} = 0$, $\omega_H > 0 \Rightarrow C_1 = C_3 = 0$, $\sqrt{C_2} > 0$

The bifurcation loci for the system with parameters values (6.17) are reported in figure 6.6(a). Here, blue curve depicts the Hopf bifurcation locus, and comparison with figure 6.4 highlights that it corresponds to the case $\Delta_2 = 0$ and represents the stability boundary for the system equilibrium solutions. Note that positive region of ω_H reported in figure 6.6(b) guarantees the existence of the imaginary parts of $\lambda_{1,2}$ eigenvalues. On the contrary, the green line which represents the divergence bifurcation locus ($C_3 = 0$) and the red point referring to the Hopf-divergence bifurcation ($C_3 = 0$ and $\Delta_2 = 0$) occur for $k_g = 0$, that is when the control is not activated and thus become meaningless scenarios. The red point, in particular, is located at $\Gamma_1 \cong 1.5$

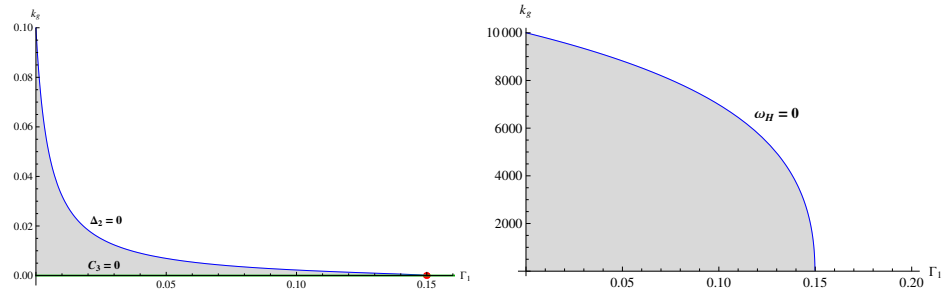

Figure 6.6: Bifurcation chart of the equilibrium solution (a): Hopf bifurcation locus (blue line), Divergence bifurcation locus (green line) and Divergence-Hopf bifurcation locus (red point). $\omega_H > 0$ region is reported in gray in (b)

which is the limit value non only for the stability of the uncontrolled equilibrium, but also for its existence: it corresponds, in fact, to the position of the saddle-node bifurcation which connects the stable equilibrium branch with the unstable one.

Chapter 7

Weakly nonlinear dynamics of the controlled system

In this section, attention is devoted to study the system nonlinear dynamics around the previously obtained fixed point, close to primary resonance; for this purpose, the method of multiple scales is applied. This method, as other perturbation techniques, is useful to separate the slow and fast dynamics of the system. In particular, after the introduction of different time scales, namely the fast one, t_0, and the slower ones, $t_1, t_2, \ldots$, and an asymptotic expansion of the dependent variables, the application of the method of multiple scales provides an approximate expression of the solution of the weakly nonlinear system, as well as a reduced set of differential equations which rule the slow-time amplitudes of motion. While the solution is obtained through the chain-solving of non-homogeneous linear differential systems, the reduced set is obtained through the imposition of solvability conditions at each perturbation step, entailing the neglection of secular terms in the solution, which is actually expected to be bounded.

7.1 Multiple scale analysis

The equations of motions (6.9) are analyzed around the reference position (x_{ref}, z_s), that is $y = x - x_{ref} = x - \bar{x}_{ref} - \tilde{x}_{ref}$ and $p = z - z_s$:

$$\begin{aligned}
&\ddot{y} = -\frac{1}{(1+\alpha_2(y+\bar{x}_{ref}+\tilde{x}_{ref})^2)}\left(\alpha_1+\alpha_2\dot{y}^2+\alpha_3(y+\bar{x}_{ref}+\tilde{x}_{ref})^2\right)\\
&(y+\bar{x}_{ref}+\tilde{x}_{ref}) + \frac{\Gamma_1}{\left(1+(y+\bar{x}_{ref}+\tilde{x}_{ref})+V_g+p\right)^2}\\
&+\left(\rho_1+\rho_2(y+\bar{x}_{ref}+\tilde{x}_{ref})^2\right)\left(\dot{y}+\dot{\tilde{x}}_{ref}\right)\\
&+\left(\ddot{V}_g - k_g\dot{y} + \nu_1\left(\dot{V}_g - k_g y\right)\right)\nu_2\\
&-\left(\mu_1(y+\bar{x}_{ref}+\tilde{x}_{ref})+\mu_2(y+\bar{x}_{ref}+\tilde{x}_{ref})^3\right)\left(\ddot{U}_g+\eta_1\dot{U}_g+\eta_2 U_g\right)\\
&\dot{p} = -k_g y
\end{aligned} \tag{7.1}$$

with $V_g = V\sin(\omega_v t)$, $U_g = U\sin(\omega_u t + \phi_u)$ and accounting for (6.10). The multiple scales method [79] is employed by introducing 4 independent time scales

$$T_0 = t, \quad T_1 = \epsilon t, \quad T_2 = \epsilon^2 t, \quad T_3 = \epsilon^3 t \tag{7.2}$$

where ϵ is a small dimensionless ordering parameter and, consistently, expressing the time derivatives as

$$\begin{aligned}
&\mathrm{d}/\mathrm{d}t = D_0 + \epsilon D_1 + \epsilon^2 D_2\\
&\mathrm{d}^2/\mathrm{d}t^2 = D_0^2 + 2\epsilon D_0 D_1 + \epsilon^2 D_1^2 + 2\epsilon^2 D_0 D_2 + 2\epsilon^3 D_1 D_2
\end{aligned} \tag{7.3}$$

Both displacement y and target distance p are scaled as small perturbations of the reference position:

$$\begin{aligned}
y(t) =& \epsilon y_1(T_0,T_1,T_2,T_3) + \epsilon^2 y_2(T_0,T_1,T_2,T_3)\\
&+ \epsilon^3 y_3(T_0,T_1,T_2,T_3) + \epsilon^4 y_4(T_0,T_1,T_2,T_3)\\
p(t) =& \epsilon p_1(T_0,T_1,T_2,T_3) + \epsilon^2 p_2(T_0,T_1,T_2,T_3)\\
&+ \epsilon^3 p_3(T_0,T_1,T_2,T_3) + \epsilon^4 p_4(T_0,T_1,T_2,T_3)
\end{aligned} \tag{7.4}$$

The system parameters are rescaled to describe small base excitation amplitude ($V \to \epsilon^3 \hat{V}$), small scan amplitude ($U \to \epsilon^3 \hat{U}$), small damping ($\rho_1 \to \epsilon^2 \hat{\rho}_1, \quad \rho_2 \to \epsilon^2 \hat{\rho}_2, \quad \nu_1 \to \epsilon^2 \hat{\nu}_1, \quad \nu_2 \to \epsilon^2 \hat{\nu}_2$) and small control ($k_g \to \epsilon^2 \hat{k}_g$). Two detuning terms are also defined to express the nearness of exciting frequencies to primary resonance:

$$\epsilon^2 \sigma_u = \omega_u - \omega_1 = \omega_1(\Omega_u - 1), \quad \epsilon^2 \sigma_v = \omega_v - \omega_1 = \omega_1(\Omega_v - 1)$$

where ω_1 is the natural system frequency and $\Omega_i = \omega_i/\omega_1, \quad i = u, v$.

Note that the feedback control parameter k_g is ordered in such a way to come into play within the perturbation scheme as the same order as the one where the other system nonlinearities appear, i.e. the third order. To evaluate the effect of control on the system asymptotic response, therefore, the perturbation analysis is carried out up to the fourth order.

It is worth underlining here that the reference solution $\tilde{x}_{ref}$ in (7.1) is the modulated response of the uncontrolled system, and in view of a perturbation analysis, it can be seen as solution of the perturbed uncontrolled system which has been analyzed, up to the third order, by Hornstein and Gottlieb [44] with the same choice of variables and parameters scaling. Here, however, a further perturbation equation at the fourth order has been added, and the system obtained is reported and developed in Appendix B.

Hence, $\tilde{x}_{ref}(t)$ can be considered, and thus scaled, as a further variable:

$$\begin{aligned} \tilde{x}_{ref}(t) =& \epsilon \tilde{x}_{ref1}(T_0, T_1, T_2, T_3) + \epsilon^2 \tilde{x}_{ref2}(T_0, T_1, T_2, T_3) \\ &+ \epsilon^3 \tilde{x}_{ref3}(T_0, T_1, T_2, T_3) + \epsilon^4 \tilde{x}_{ref4}(T_0, T_1, T_2, T_3) \end{aligned} \tag{7.5}$$

For the controlled system, after pre-multiplication by denominator, the following set of perturbation equations is obtained:

order ϵ^0 :

$$\Gamma_1 + \bar{x}_{ref}(1+\bar{x}_{ref})^2(\alpha_3\bar{x}_{ref}^2 + \alpha_1) = 0 \tag{7.6a}$$

order ϵ^1 :

$$D_0^2 y_1 + \omega_1^2 y_1 + D_0^2\tilde{x}_{ref1} + \omega_1^2\tilde{x}_{ref1} + C_{11}p_1 = 0 \tag{7.6b}$$
$$D_0 p_1 = 0$$

order ϵ^2 :

$$\begin{aligned} D_0^2 y_2 + \omega_1^2 y_2 + D_0^2\tilde{x}_{ref2} + \omega_1^2\tilde{x}_{ref2} + C_{11}p_2 &= N_{21}(y_1) \\ + N_{22}(\tilde{x}_{ref1}) + N_{23}(p_1) &+ N_{24}(y_1, \tilde{x}_{ref1}) \\ + N_{25}(y_1, p_1) &+ N_{26}(p_1, \tilde{x}_{ref1}) \end{aligned} \tag{7.6c}$$
$$D_0 p_2 = -D_1 p_1$$

order ϵ^3 :

$$\begin{aligned} D_0^2 y_3 + \omega_1^2 y_3 + D_0^2\tilde{x}_{ref3} + \omega_1^2\tilde{x}_{ref3} + C_{11}p_3 &= N_{31}(y_1, y_2) \\ + N_{32}(\tilde{x}_{ref1}, \tilde{x}_{ref2}) + N_{33}(p_1, p_2) &+ N_{34}(y_1, y_2, \tilde{x}_{ref1}, \tilde{x}_{ref2}) \\ + N_{35}(y_1, y_2, p_1, p_2) + N_{36}(p_1, p_2, \tilde{x}_{ref1}, \tilde{x}_{ref2}) &\\ + N_{37}(y_1, \tilde{x}_{ref1}, p_1) - C_{cu}\cos(\omega_1 T_0 + \sigma_u T_2 + \phi_u) &\\ - C_{sv}\sin(\omega_1 T_0 + \sigma_v T_2) - C_{su}\sin(\omega_1 T_0 + \sigma_u T_2 + \phi_u) & \end{aligned} \tag{7.6d}$$
$$D_0 p_3 = -D_1 p_2 - D_2 p_1 - \hat{k}_g y_1$$

order ϵ^4 :

$$\begin{aligned} D_0^2 y_4 + \omega_1^2 y_4 + D_0^2\tilde{x}_{ref4} + \omega_1^2\tilde{x}_{ref4} + C_{11}p_4 &= N_{41}(y_1, y_2, y_3) \\ + N_{42}(\tilde{x}_{ref1}, \tilde{x}_{ref2}, \tilde{x}_{ref3}) + N_{43}(p_1, p_2, p_3) &\\ + N_{44}(y_1, y_2, y_3, \tilde{x}_{ref1}, \tilde{x}_{ref2}, \tilde{x}_{ref3}) &\\ + N_{45}(y_1, y_2, y_3, p_1, p_2, p_3) &\\ + N_{46}(p_1, p_2, p_3, \tilde{x}_{ref1}, \tilde{x}_{ref2}, \tilde{x}_{ref3}) &\\ + N_{47}(y_1, y_2, \tilde{x}_{ref1}, \tilde{x}_{ref2}, p_1, p_2) & \end{aligned} \tag{7.6e}$$
$$D_0 p_4 = -D_1 p_3 - D_2 p_2 - D_3 p_1 - \hat{k}_g y_2$$

where expressions of the N_{ij} terms are reported in Sect. C.1 of Appendix C. It is worth noting that $N_{21}(y_1)$ and $N_{22}(\tilde{x}_{ref1})$ terms have the same structure, as well as $N_{31}(y_1, y_2)$ and $N_{32}(\tilde{x}_{ref1}, \tilde{x}_{ref2})$ terms, $N_{41}(y_1, y_2, y_3)$ and $N_{42}(\tilde{x}_{ref1}, \tilde{x}_{ref2}, \tilde{x}_{ref3})$ terms, $N_{35}(y_1, y_2, p_1, p_2)$ and $N_{36}(\tilde{x}_{ref1}, \tilde{x}_{ref2}, p_1, p_2)$

terms and $N_{45}(y_1, y_2, y_3, p_1, p_2, p_3)$ and $N_{46}(\tilde{x}_{ref1}, \tilde{x}_{ref2}, \tilde{x}_{ref3}, p_1, p_2, p_3)$ terms. This is due to the fact that the y and $\tilde{x}_{ref}$ variables appear in all of the terms of (7.1) simultaneously, apart from some terms related to the forcing V_g which, in any case, are scaled at higher orders. It is also important to observe that, at each order, all the terms of the uncontrolled system (B.2) can be detected in the controlled system (7.6), as functions of $\tilde{x}_{ref}$ and y; the ones related to $\tilde{x}_{ref}$ vanish identically considering that $\tilde{x}_{ref}$ is solution for the uncontrolled system.

The system hence becomes:

$$
\begin{aligned}
&\text{order } \epsilon^1 : \\
&\quad D_0^2 y_1 + \omega_1^2 y_1 + C_{11} p_1 = 0 \qquad (7.7a)\\
&\quad D_0 p_1 = 0 \\
&\text{order } \epsilon^2 : \\
&\quad D_0^2 y_2 + \omega_1^2 y_2 + C_{11} p_2 = N_{21}(y_1) \\
&\qquad + N_{23}(p_1) + N_{24}(y_1, \tilde{x}_{ref1}) \qquad (7.7b)\\
&\qquad + N_{25}(y_1, p_1) + N_{26}(p_1, \tilde{x}_{ref1}) \\
&\quad D_0 p_2 = -D_1 p_1 \\
&\text{order } \epsilon^3 : \\
&\quad D_0^2 y_3 + \omega_1^2 y_3 + C_{11} p_3 = N_{31}(y_1, y_2) \\
&\qquad + N_{33}(p_1, p_2) + N_{34}(y_1, y_2, \tilde{x}_{ref1}, \tilde{x}_{ref2}) \\
&\qquad + N_{35}(y_1, y_2, p_1, p_2) + N_{36}(p_1, p_2, \tilde{x}_{ref1}, \tilde{x}_{ref2}) \qquad (7.7c)\\
&\qquad + N_{37}(y_1, \tilde{x}_{ref1}, p_1) \\
&\quad D_0 p_3 = -D_1 p_2 - D_2 p_1 - \hat{k}_g y_1 \\
&\text{order } \epsilon^4 : \\
&\quad D_0^2 y_4 + \omega_1^2 y_4 + C_{11} p_4 = N_{41}(y_1, y_2, y_3) \\
&\qquad + N_{43}(p_1, p_2, p_3) \\
&\qquad + N_{44}(y_1, y_2, y_3, \tilde{x}_{ref1}, \tilde{x}_{ref2}, \tilde{x}_{ref3}) \\
&\qquad + N_{45}(y_1, y_2, y_3, p_1, p_2, p_3) \qquad (7.7d)\\
&\qquad + N_{46}(p_1, p_2, p_3, \tilde{x}_{ref1}, \tilde{x}_{ref2}, \tilde{x}_{ref3}) \\
&\qquad + N_{47}(y_1, y_2, \tilde{x}_{ref1}, \tilde{x}_{ref2}, p_1, p_2) \\
&\quad D_0 p_4 = -D_1 p_3 - D_2 p_2 - D_3 p_1 - \hat{k}_g y_2
\end{aligned}
$$

whose first equation, at each order, has the same structure as that in (B.2), apart from replacing $\tilde{x}_{ref}$ with y, including the $\tilde{x}_{ref}y$ coupling terms, and exhibiting terms ensuing from the target distance variable p. Solutions of system (7.7a) are

$$\begin{aligned} p_1 &= B(T_1, T_2, T_3) \\ y_1 &= A(T_1, T_2, T_3)e^{i\omega_1 T_0} - C_{11}/\omega_1^2 B(T_1, T_2, T_3) + c.c. \end{aligned} \tag{7.8}$$

with $A(T_1, T_2, T_3)$ and $B(T_1, T_2, T_3)$ which are undetermined functions of the slow time scales and *c.c.* which are the complex conjugate of terms containing the complex amplitude A (the overbar denotes the complex conjugate and i the imaginary unit). Solutions (7.8) highlight that $p_1(T_1, T_2, T_3)$ is a modulated nontrivial equilibrium solution, while $y_1(T_1, T_2, T_3)$ is a harmonic solution modified by the equilibrium position of p_1. Substitution of p_1 in the second equation of (7.7b) yields

$$D_0 p_2 = -D_1 B \tag{7.9}$$

where the dependence on the time scales has been omitted. Elimination of secular terms requires

$$D_1 B = 0 \tag{7.10}$$

so that $B = B(T_2, T_3)$, and solution of (7.9) is

$$p_2 = 0 \tag{7.11}$$

Using (7.8) and (7.11), and remembering equation (B.3)

$$\tilde{x}_{ref1} = A_{un}(T_1, T_2, T_3)e^{i\omega_1 T_0} + c.c.$$

is solution of amplitude $A_{un}(T_1, T_2, T_3)$ of the first order uncontrolled system, the first equation of (7.7b) becomes

$$\begin{aligned} D_0^2 y_2 + \omega_1^2 y_2 = &-2C_{214}\left(A\bar{A} + A\bar{A}_{un}\right) - C_{212}B^2 \\ &- e^{i\omega_1 T_0}\left(C_{213}\left(A + A_{un}\right)B + 2i\omega_1 D_1 A\right) \\ &- C_{211}e^{2i\omega_1 T_0}\left(A^2 + 2AA_{un}\right) + c.c. \end{aligned} \tag{7.12}$$

and the solvability condition implies that

$$D_1 A = \frac{iC_{213}}{2\omega_1} \left(A + A_{un}\right) B \tag{7.13}$$

For the uncontrolled system, it is (B.5)

$$D_1 A_{un} = 0 \quad \text{thus} \quad A_{un} = A_{un}(T_2, T_3)$$

The particular solution at this order is

$$\begin{aligned} y_2 =& \frac{C_{211}}{3\omega_1^2} \left(A^2 + 2AA_{un}\right) e^{2i\omega_1 T_0} - \frac{2C_{214}}{\omega_1^2} \left(A\bar{A} + A\bar{A}_{un}\right) \\ & - \frac{C_{212}}{\omega_1^2} B^2 + c.c. \end{aligned} \tag{7.14}$$

while the solution of the uncontrolled system (B.2) is (B.6)

$$\tilde{x}_{ref2} = \frac{C_{211}}{3\omega_1^2} A_{un}^2 e^{2i\omega_1 T_0} - \frac{2C_{214}}{\omega_1^2} A_{un}\bar{A}_{un} + c.c.$$

For the expression of the C_{ijk} coefficients, see Sect. C.2 of Appendix C.

At the third order, by means of the obtained results the second of (7.7c) becomes

$$D_0 p_3 = - D_2 B + \hat{k}_g C_{11} B/\omega_1^2 - \hat{k}_g A e^{i\omega_1 T_0} + c.c. \tag{7.15}$$

and the secular terms elimination, providing

$$D_2 B = \hat{k}_g C_{11} B/\omega_1^2 \tag{7.16}$$

permits to obtain

$$p_3 = \frac{i\hat{k}_g A e^{i\omega_1 T_0}}{\omega_1} + c.c. \tag{7.17}$$

Using (7.8), (B.3), (7.10),(7.11),(7.13),(7.14),(7.16),(7.17), the first equation of (7.7c) becomes

$$\begin{aligned} D_0^2 y_3 + \omega_1^2 y_3 =& \gamma_{31} e^{i\omega_1 T_0} + \gamma_{32} e^{2i\omega_1 T_0} + \gamma_{33} e^{3i\omega_1 T_0} + \gamma_{35} B^3 \\ &+ \gamma_{36} \left(A\bar{A} + \bar{A} A_{un} + A\bar{A}_{un} + A_{un}\bar{A}_{un} \right) B \\ &+ \gamma_{37} \left(\bar{A} + \bar{A}_{un} \right) D_1 A + \gamma_{37} \bar{A} D_1 A_{un} \\ &- C_{11}/\omega_1^2 D_1^2 B + c.c. \end{aligned} \tag{7.18}$$

with γ_{ijk} defined in Sect. C.2 of Appendix C.

The solvability condition is, using the definition of γ_{31},

$$\begin{aligned} & 2i\omega_1 D_2 A + C_{301} \left(A^2 \bar{A} + 2A\bar{A}A_{un} + \bar{A}A_{un}^2 + A^2 \bar{A}_{un} + 2AA_{un}\bar{A}_{un} \right) \\ & + C_{302} \left(AB^2 + A_{un}B^2 \right) \\ & + i \left(C_{35}\omega_1 + \frac{C_{11}\hat{k}_g}{\omega_1} \right) A = 0 \end{aligned} \tag{7.19}$$

from which

$$\begin{aligned} D_2 A =& -\frac{C_{35}\omega_1^2 + C_{11}\hat{k}_g}{2\omega_1^2} A \\ &+ i\frac{C_{301} \left(A^2 \bar{A} + 2A\bar{A}A_{un} + \bar{A}A_{un}^2 + A^2 \bar{A}_{un} + 2AA_{un}\bar{A}_{un} \right)}{2\omega_1} \\ &+ i\frac{C_{302} \left(AB^2 + A_{un}B^2 \right)}{2\omega_1} \end{aligned} \tag{7.20}$$

By eliminating the secular terms in (7.18), the particular solution at the third order for the controlled system results

$$\begin{aligned} y_3 =& C_{306} B^3 + C_{303} \left(A^3 + 3A^2 A_{un} + 3A_{un}^2 \right) e^{3i\omega_1 T_0} \\ &+ C_{304} \left(A^2 B + 2AA_{un}B + A_{un}^2 B \right) e^{2i\omega_1 T_0} \\ &+ C_{305} \left(A\bar{A}B + A_{un}\bar{A}B + AB\bar{A}_{un} + A_{un}B\bar{A}_{un} \right) + c.c. \end{aligned} \tag{7.21}$$

For what concerns the uncontrolled system, the solvability condition at the third order yields (B.8)

$$\begin{aligned} D_2 A_{un} =& -\frac{C_{35}}{2} A_{un} + i\frac{C_{301}}{2\omega_1} \left(A_{un}^2 \bar{A}_{un} \right) \\ &+ \frac{C_{sv}}{4\omega_1} e^{i\sigma_v T_2} + \frac{C_{su}}{4\omega_1} e^{i(\sigma_u T_2 + \phi_u)} + i\frac{C_{cu}}{4\omega_1} e^{i(\sigma_u T_2 + \phi_u)} \end{aligned}$$

and the particular solution results (B.9)

$$\tilde{x}_{ref3} = C_{303} A_{un}^3 e^{3i\omega_1 T_0} + c.c.$$

Such results allow one to rewrite the second equation of (7.7d) as

$$\begin{aligned} D_0 p_4 = &- D_3 B - i\frac{\hat{k}_g}{\omega_1} D_1 A e^{i\omega_1 T_0} \\ &+ \frac{2C_{214}\hat{k}_g}{\omega_1^2}\left(A\bar{A} + A_{un}\bar{A} + A\bar{A}_{un}\right) + \frac{C_{212}\hat{k}_g}{\omega_1^2} B^2 \\ &- \frac{C_{211}\hat{k}_g}{2\omega_1^2}\left(A^2 + 2AA_{un}\right) e^{2i\omega_1 T_0} + c.c. \end{aligned} \tag{7.22}$$

with the secular term being

$$D_3 B = + \frac{2C_{214}\hat{k}_g}{\omega_1^2}\left(A\bar{A} + A_{un}\bar{A} + A\bar{A}_{un}\right) + \frac{C_{212}\hat{k}_g}{\omega_1^2} B^2 \tag{7.23}$$

and the particular solution resulting

$$\begin{aligned} p_4 = &- \frac{iC_{213}\hat{k}_g}{2\omega_1^3}\left(AB + A_{un}B\right) e^{i\omega_1 T_0} \\ &+ \frac{iC_{211}\hat{k}_g}{3\omega_1^3}\left(A^3 + 2AA_{un}\right) e^{2i\omega_1 T_0} + c.c. \end{aligned} \tag{7.24}$$

The first equation (7.7d) at the fourth order hence becomes

$$\begin{aligned}
D_0^2 y_4 + \omega_1^2 y_4 = &- A^2\left(\gamma_{47}\bar{A}^2 + 2\gamma_{47}\bar{A}\bar{A}_{un} + \gamma_{47}\bar{A}_{un}^2\right) \\
&- 4\gamma_{47}AA_{un}\bar{A}\bar{A}_{un} - A\left(B^2\left(\gamma_{45}\bar{A} + \gamma_{45}\bar{A}_{un}\right)\right. \\
&\left.+\gamma_{49}\bar{A}_{un} + \gamma_{54}e^{-i\sigma_v T_2} + \gamma_{55}e^{-i\sigma_u T_2 - i\phi_u}\right) \\
&- 2\gamma_{47}A_{un}^2\bar{A}\bar{A}_{un} - \gamma_{45}A_{un}B^2\bar{A}_{un} \\
&- B\left(\gamma_{48}\bar{A}D_1A + \gamma_{48}\bar{A}D_1A_{un}\right. \\
&\left.+\gamma_{48}\bar{A}_{un}D_1A + \gamma_{48}\bar{A}_{un}D_1A_{un} + \gamma_{58}D_1^2B\right) \\
&- \gamma_{57}\bar{A}D_1^2A - \gamma_{57}\bar{A}D_1^2A_{un} - \gamma_{56}\bar{A}D_2A \\
&- \gamma_{56}\bar{A}D_2A_{un} - \gamma_{57}\bar{A}_{un}D_1^2A \\
&- \gamma_{56}\bar{A}_{un}D_2A - \gamma_{50}D_1AD_1\bar{A} \\
&- \gamma_{50}D_1\bar{A}D_1A_{un} - \gamma_{51}D_1B^2 \\
&- \gamma_{46}B^4 - \gamma_{52}D_1D_2B \\
&- \gamma_{53}D_1B - \gamma_{41}e^{i\omega_1 T_0} - \gamma_{42}e^{2i\omega_1 T_0} \\
&- \gamma_{43}e^{3i\omega_1 T_0} - \gamma_{44}e^{4i\omega_1 T_0} + c.c.
\end{aligned} \tag{7.25}$$

The secular terms elimination requires that $\gamma_{41} = 0$. Using equations (7.10),(7.13),(B.5),(7.16),(7.20),(B.8), and assuming that

$$2D_1D_2A = \frac{\mathrm{d}D_1A}{\mathrm{d}T_2} + \frac{\mathrm{d}D_2A}{\mathrm{d}T_1}$$

it results

$$\begin{aligned}
D_3A = &B^3\left(\gamma_{402}A + \gamma_{402}A_{un}\right) \\
&+ B\left(\gamma_{401}A^2\bar{A} + \gamma_{401}A^2\bar{A}_{un}\right. \\
&+2\gamma_{401}A\bar{A}A_{un} + 2\gamma_{401}AA_{un}\bar{A}_{un} \\
&+\gamma_{404}A + \gamma_{403}A_{un} \\
&+\gamma_{401}\bar{A}A_{un}^2 + \gamma_{401}A_{un}^2\bar{A}_{un} \\
&\left.+\gamma_{405}e^{i\sigma_u T_2 + i\phi_u} + \gamma_{406}e^{i\sigma_v T_2}\right)
\end{aligned} \tag{7.26}$$

According to the usual reconstitution procedure [79], the amplitudes derivatives with respect to time t are obtained from (7.3)

$$\begin{aligned}\dot{A} &= \epsilon D_1 A + \epsilon^2 D_2 A + \epsilon^3 D_3 A \\ \dot{B} &= \epsilon D_1 B + \epsilon^2 D_2 B + \epsilon^3 D_3 B\end{aligned} \tag{7.27}$$

in which $D_1B, D_1A, D_2B, D_2A, D_3B, D_3A$ are defined in (7.10), (7.13), (7.16), (7.20), (7.23) and (7.26). Finally, considering that $C_{35}, C_{405}, C_{423} = f(\hat{\rho}_1, \hat{\rho}_2)$, $C_{cu}, C_{su}, C_{cuu}, C_{suu}, C_{411}, C_{413} = f(\hat{U})$, $C_{sv}, C_{svv}, C_{svvv}, C_{412} = f(\hat{V})$, the ϵ parameter is completely reabsorbed through the backward rescaling

$$\begin{aligned}&\epsilon A \to A, \quad \epsilon B \to B, \quad \epsilon A_{un} \to A_{un}, \quad \epsilon^2 \hat{k}_g \to k_g, \quad \epsilon^2 C_{35} \to C_{35}, \\ &\epsilon^2 C_{405} \to C_{405}, \quad \epsilon^2 C_{423} \to C_{423}, \quad \epsilon^3 C_{cu} \to C_{cu}, \quad \epsilon^3 C_{su} \to C_{su}, \\ &\epsilon^3 C_{cuu} \to C_{cuu}, \quad \epsilon^3 C_{suu} \to C_{suu}, \quad \epsilon^3 C_{sv} \to C_{sv}, \quad \epsilon^3 C_{svv} \to C_{svv}, \\ &\epsilon^3 C_{svvv} \to C_{svvv}, \quad \epsilon^3 C_{411} \to C_{411}, \quad \epsilon^3 C_{412} \to C_{412}, \\ &\epsilon^3 C_{413} \to C_{413}, \quad \epsilon^2 \sigma_u \to \sigma_u, \quad \epsilon^2 \sigma_v \to \sigma_v.\end{aligned} \tag{7.28}$$

The obtained modulation equations (or bifurcation equations) are

$$\begin{aligned}\dot{A} =& + \beta_6 AB + \beta_9 A + \beta_5 A_{un} B + \beta_8 B \cos(\sigma_u t + \phi_u) \\ & - \beta_{10} B \sin(\sigma_u t + \phi_u) + \beta_{11} B \cos(\sigma_v t) \\ & + i\left(\bar{A}_{un}\left(A^2(\beta_1 B + \beta_4) + 2AA_{un}(\beta_1 B + \beta_4) + \beta_1 A_{un}^2 B\right)\right. \\ & + A^2 \bar{A}(\beta_1 B + \beta_4) + 2\beta_4 A \bar{A} A_{un} \\ & + AB\left(2\beta_1 \bar{A} A_{un} + B(\beta_2 B + \beta_3) + \beta_7\right) \\ & + A_{un}\left(B\left(\beta_1 \bar{A} A_{un} + B(\beta_2 B + \beta_3) + \beta_7\right) + \beta_4 \bar{A} A_{un}\right) \\ & \left. + B(\beta_8 \sin(\sigma_u t + \phi_u) + \beta_{10} \cos(\sigma_u t + \phi_u) + \beta_{11} \sin(\sigma_v t))\right) \\ \dot{B} =& \frac{2C_{214} k_g}{\omega_1^2}\left(A\bar{A}_{un} + A\bar{A} + \bar{A}A_{un}\right) \\ & + \frac{C_{212} k_g}{\omega_1^2} B^2 + \frac{C_{11} k_g}{\omega_1^2} B\end{aligned} \tag{7.29}$$

Note that the complex amplitudes A and B are of order ϵ ($A = \epsilon A, B = \epsilon B$), as they refer to the displacement y and the target distance p, respectively.

To conveniently express the system (7.29) in Cartesian coordinates, it has to be transformed in an autonomous form, and so the presence of resonant external vertical excitation V_g or resonant parametric horizontal excitation

U_g has to be taken into account separately. For the horizontally forced case ($V_g = 0$), and remembering that $\sigma_u = (\Omega_u - 1)\,\omega_1$, system (7.29) reduces to

$$\begin{aligned}
\dot{A} =& + \beta_6 AB + \beta_9 A + \beta_5 A_{un} B + \beta_8 B e^{i\phi_u + (\Omega_u - 1)\omega_1 t} \\
& + i\left(\bar{A}_{un}\left(A^2\left(\beta_1 B + \beta_4\right) + 2AA_{un}\left(\beta_1 B + \beta_4\right) + \beta_1 A_{un}^2 B\right)\right. \\
& + A^2\bar{A}\left(\beta_1 B + \beta_4\right) + 2\beta_4 A\bar{A}A_{un} \\
& + AB\left(2\beta_1\bar{A}A_{un} + B\left(\beta_2 B + \beta_3\right) + \beta_7\right) \\
& + A_{un}\left(B\left(\beta_1\bar{A}A_{un} + B\left(\beta_2 B + \beta_3\right) + \beta_7\right) + \beta_4\bar{A}A_{un}\right) \\
& \left. + \beta_{10} e^{i\phi_u + (\Omega_u - 1)\omega_1 t}\right) \\
\dot{B} =& \frac{2C_{214}k_g}{\omega_1^2}\left(A\bar{A}_{un} + A\bar{A} + \bar{A}A_{un}\right) \\
& + \frac{C_{212}k_g}{\omega_1^2}B^2 + \frac{C_{11}k_g}{\omega_1^2}B
\end{aligned} \tag{7.30}$$

Pre-multiplication of both sides of equation (7.30) by $e^{-i\phi_u - (\Omega_u - 1)\omega_1 t}$ yields

$$\begin{aligned}
\dot{G} =& + \beta_6 BG + \beta_8 B + \beta_5 BG_{un} + \beta_9 G \\
& + i\left(\bar{G}_{un}\left(G^2(\beta_1 B + \beta_4) + \beta_1 BG_{un}^2 + 2GG_{un}(\beta_1 B + \beta_4)\right)\right. \\
& + \bar{G}\left(G^2(\beta_1 B + \beta_4) + G_{un}^2(\beta_1 B + \beta_4) + 2GG_{un}(\beta_1 B + \beta_4)\right) \\
& + \beta_2 B^3(G + G_{un}) + \beta_3 B^2(G + G_{un}) \\
& \left. + B(\beta_7(G + G_{un}) + \beta_{10}) - \omega_1(\Omega_u - 1)G\right)
\end{aligned} \tag{7.31}$$

where transformations

$$\begin{aligned}
& G = Ae^{-i\phi_u - (\Omega_u - 1)\omega_1 t}, \quad \bar{G} = \bar{A}e^{-i\phi_u - (\Omega_u - 1)\omega_1 t}, \\
& G_{un} = A_{un}e^{-i\phi_u - (\Omega_u - 1)\omega_1 t}, \quad \bar{G}_{un} = \bar{A}_{un}e^{-i\phi_u - (\Omega_u - 1)\omega_1 t}
\end{aligned}$$

have been applied. Finally, using the following coordinates transformations

$$\begin{aligned}
& G = \frac{1}{2}(j(t) + i\,n(t)), \quad \bar{G} = \frac{1}{2}(j(t) - i\,n(t)), \quad B = b(t), \\
& G_{un} = \frac{1}{2}(j_{un}(t) + i\,n_{un}(t)), \quad \bar{G}_{un} = \frac{1}{2}(j_{un}(t) - i\,n_{un}(t))
\end{aligned}$$

system (7.30) results

$$
\begin{aligned}
\dot{j}(t) = &- \beta_2 n(t) b(t)^3 - \beta_2 n_{un}(t) b(t)^3 - \beta_3 n(t) b(t)^2 - \beta_3 n_{un}(t) b(t)^2 \\
&- \frac{\beta_1}{3} j_{un}(t)^2 n_{un}(t) b(t) - \frac{\beta_1}{3} n_{un}(t)^3 b(t) + \beta_5 j_{un}(t) b(t) \\
&+ \beta_6 j(t) b(t) - \beta_7 n(t) b(t) - \beta_7 n_{un}(t) b(t) + 2\beta_8 b(t) \\
&- \frac{\beta_1}{4} j(t)^2 n_{un}(t) b(t) - \frac{3\beta_1}{4} n(t)^2 n_{un}(t) b(t) \\
&- \frac{\beta_1}{2} j(t) j_{un}(t) n(t) b(t) - \frac{\beta_1}{4} j_{un}(t)^2 n(t) b(t) \\
&- \frac{3\beta_1}{4} n(t) n_{un}(t)^2 b(t) - \frac{\beta_1}{4} j(t)^2 n(t) b(t) \\
&- \frac{\beta_1}{2} j(t) j_{un}(t) n_{un}(t) b(t) \\
&- \frac{\beta_1}{4} n(t)^3 b(t) + \beta_9 j(t) - \frac{\beta_4}{4} j(t)^2 n_{un}(t) \\
&- \frac{\beta_4}{4} j_{un}(t)^2 n(t) - 3\frac{\beta_4}{4} n(t)^2 n_{un}(t) \\
&- 3\frac{\beta_4}{4} n(t) n_{un}(t)^2 - \frac{\beta_4}{4} j(t)^2 n(t) \\
&- \frac{\beta_4}{2} j(t) j_{un}(t) n(t) - \frac{\beta_4}{2} j(t) j_{un}(t) n_{un}(t) \\
&- \frac{\beta_4}{4} n(t)^3 + (\omega_1 \Omega_u - \omega_1) n(t)
\end{aligned}
\tag{7.32}
$$

$$
\begin{aligned}
\dot{n}(t) =&\beta_2 j(t)b(t)^3 + \beta_2 j_{un}(t)b(t)^3 + \beta_3 j(t)b(t)^2 + \beta_3 j_{un}(t)b(t)^2 \\
&+ \frac{\beta_1}{4} j_{un}(t)^3 b(t) + \frac{\beta_1}{4} j_{un}(t) n_{un}(t)^2 b(t) + \beta_5 n_{un}(t)b(t) \\
&+ \beta_6 n(t)b(t) + \beta_7 j(t)b(t) + \beta_7 j_{un}(t)b(t) + 2\beta_{10} b(t) \\
&+ 3\frac{\beta_1}{4} j(t)^2 j_{un}(t)b(t) + \frac{\beta_1}{4} j_{un}(t) n(t)^2 b(t) \\
&+ \frac{\beta_1}{2} j(t) n(t) n_{un}(t) b(t) + 3\frac{\beta_1}{4} j(t) j_{un}(t)^2 b(t) \\
&+ \frac{\beta_1}{4} j(t) n_{un}(t)^2 b(t) + \frac{\beta_1}{4} j(t)^3 b(t) \\
&+ \frac{\beta_1}{4} j(t) n(t)^2 b(t) + \frac{\beta_1}{2} j_{un}(t) n(t) n_{un}(t) b(t) + \beta_9 n \\
&+ 3\frac{\beta_4}{4} j(t)^2 j_{un}(t) + 3\frac{\beta_4}{4} j(t) j_{un}(t)^2 \\
&+ \frac{\beta_4}{4} j(t) n_{un}(t)^2 + \frac{\beta_4}{4} j_{un}(t) n(t)^2 \\
&+ \frac{\beta_4}{4} j(t)^3 + \frac{\beta_4}{4} j(t) n(t)^2 + \frac{\beta_4}{2} j(t) n(t) n_{un}(t) \\
&+ \frac{\beta_4}{2} j_{un}(t) n(t) n_{un}(t) + (\omega_1 - \omega_1 \Omega_u) j(t) \\
\dot{b}(t) =&\frac{C_{212} k_g}{\omega_1^2} b(t)^2 + \frac{C_{11} k_g}{\omega_1^2} b(t) + \frac{C_{214} k_g}{2\omega_1^2} j(t)^2 \\
&+ \frac{C_{214} k_g}{\omega_1^2} j(t) j_{un}(t) + \frac{C_{214} k_g}{2\omega_1^2} n(t)^2 + \frac{C_{214} k_g}{\omega_1^2} n(t) n_{un}(t)
\end{aligned}
\tag{7.33}
$$

where $j(t)$ and $n(t)$ are the real and imaginary parts of the complex amplitude A, respectively, and $j_{un}(t)$ and $n_{un}(t)$ are the real and imaginary parts of the reference complex amplitude A_{un}, respectively. The asymptotic system is completed by the 2 Cartesian perturbation equations furnished by the analysis of the uncontrolled system (B.17)

$$
\begin{aligned}
\dot{j}_{un}(t) =& + \frac{C_{su}}{4\omega_1} - \frac{C_{35}}{4} j_{un}(t) - \frac{C_{301}}{16\omega_1} \left(j_{un}(t)^2 n_{un}(t) + n_{un}(t)^3 \right) \\
&+ \frac{\omega_1}{2} n_{un}(t) \left(\Omega_u - 1 \right) \\
\dot{n}_{un}(t) =& + \frac{C_{cu}}{4\omega_1} - \frac{C_{35}}{4} n_{un}(t) + \frac{C_{301}}{16\omega_1} \left(n_{un}(t)^2 j_{un}(t) + j_{un}(t)^3 \right) \\
&- \frac{\omega_1}{2} j_{un}(t) \left(\Omega_u - 1 \right)
\end{aligned}
$$

7.2 Validity of the asymptotic solution

To check the validity of the asymptotic solution, AMEs of the uncontrolled system (B.17) have been added to the controlled ones (7.32), so that the amplitudes reported in figure 7.1, obtained through the relation $a = \sqrt{j^2 + n^2}$, furnish not only the trivial solution $(j, n, b) = (0, 0, 0)$, which confirms the validity of the control application, but also the couple (j_{un}, n_{un}) which corresponds to the asymptotic reference response.

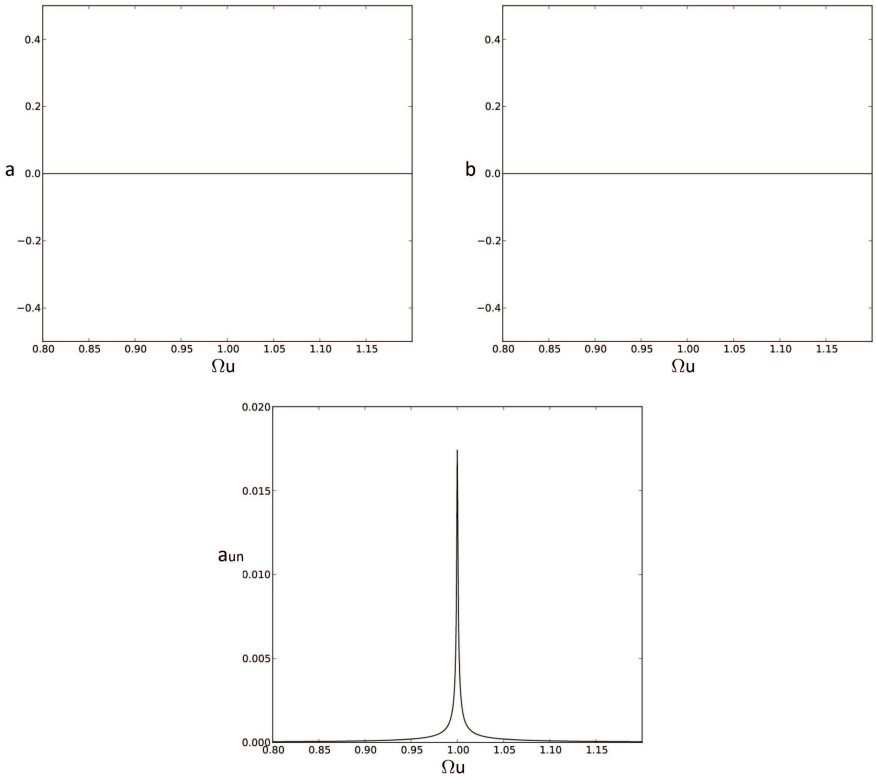

Figure 7.1: Asymptotic solutions for the parametrically forced system at $U_g = 0.0001$: controlled amplitudes a, b (a) and uncontrolled amplitude a_{un} (b)

Once verified the validity of the controlled asymptotic solution, an additional check is developed comparing the reference asymptotic solution – as obtained with the enlarged (i.e., controlled) system – with the results obtained via numerical integration of the system equations, for the vertically and horizontally forced system, separately. Here, the amplitude of the numerical solution is evaluated from $(x_{max} - x_{min})/2$ and the chosen parameters values are the same already considered in (6.17) with $k_g = 0.001$.

Figures 7.2, 7.3 demonstrate that the obtained asymptotic solutions (red lines) are in good agreement with the behavior of the original ODEs (black lines). It is interesting to point out that the amplitude of the system response under horizontal excitation is half the one obtained with the vertical force; this is due to the fact that the primary resonance is the principal one for an externally driven system, while the parametric excitation affects mainly the subharmonic resonance.

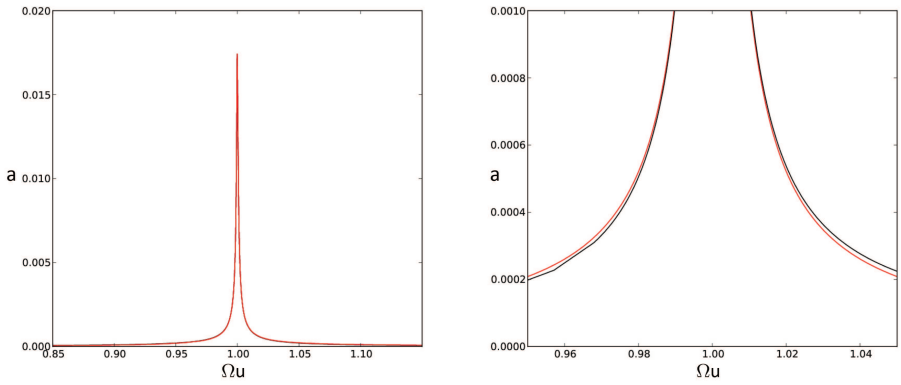

Figure 7.2: Asymptotic (red line) and numerical (black line) solutions for the parametrically forced system at $U_g = 0.0001$

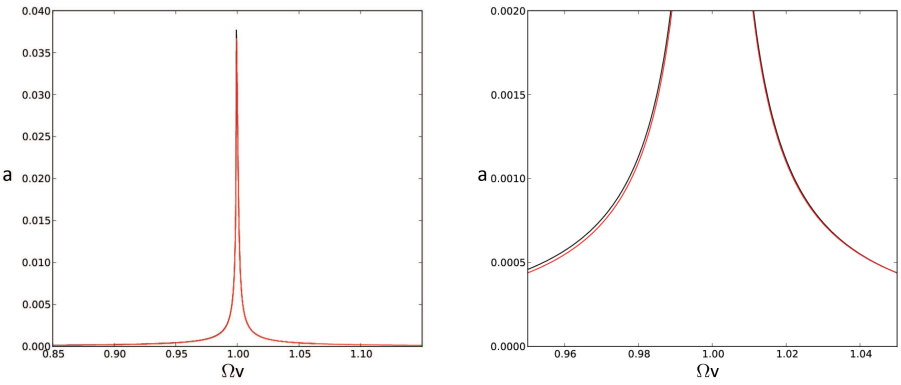

Figure 7.3: Asymptotic (red line) and numerical (black line) solutions for the externally forced system at $V_g = 0.0001$

Stability of the asymptotic solution has been also verified by studying the response of the bifurcation equations as a function of the feedback control parameter k_g. On the basis of what said about figures 7.2-7.3, analyses are referred to the horizontally forced system.

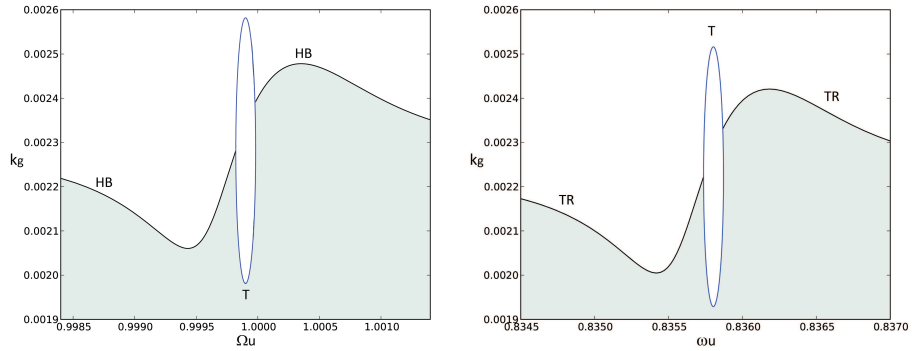

(a) (b)

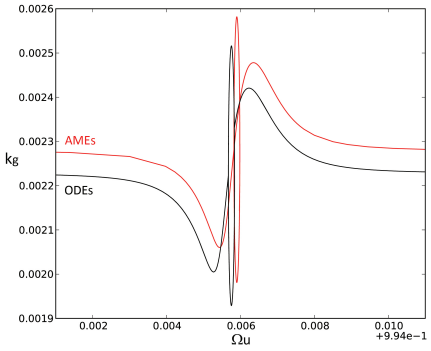

(c)

Figure 7.4: Behavior charts in the Ω_u-k_g plane around primary resonance at $U = 0.0001$ for the asymptotic system (a) and for the original ODEs system (b). Comparison between the asymptotic result (red curve) and the original system result (black curve) (c). TR: torus bifurcation, HB: Hopf bifurcation, T: transcritical bifurcation, gray region: stable region

The behavior chart reported in figure 7.4(a) shows the escape threshold of the asymptotic system in the Ω_u-k_g plane. The results show that the asymptotic system loses its stability through a Hopf bifurcation, except for a confined region around the resonance peak, for which the instability arises via a transcritical bifurcation.

It is evident the similarity between the qualitative behavior of the analyzed system and the same results obtained for the original system of ODEs

reported in figure 7.4(b), which will be described in detail in Sect. 8.1, just considering that a torus bifurcation of a periodic solution corresponds to a Hopf bifurcation of the relevant amplitude asymptotic solution. The good agreement of the results concerns also the quantitative aspect, as shown in figure 7.4(c), with an error on the amplitude of about 2%.

To confirm the accuracy of the asymptotic system, additional bifurcation diagrams, for increasing values of the feedback control parameter k_g, are reported in figure 7.5, together with the corresponding results obtained for the original ODEs system.

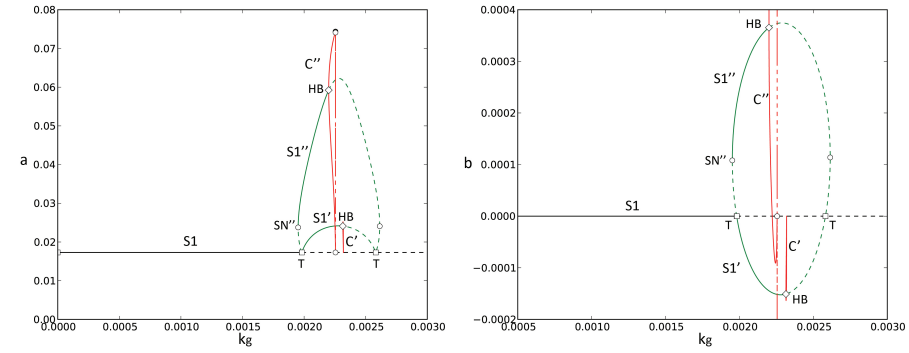

(a)

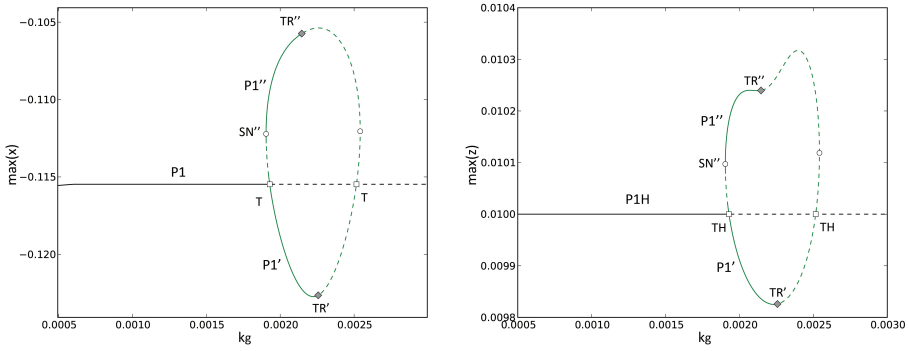

(b)

Figure 7.5: Bifurcation diagram at $U = 0.0001$ for varying k_g at $\Omega_u = 0.9999$ for the asymptotic system (a) and at $\omega_u = 0.8358$ ($\cong \Omega_u = 1$) for the ODEs system (b). S1,S1′,S1″: equilibrium solutions in the AMEs which correspond to P1,P1′,P1″ periodic solutions in the ODEs; C′,C″: limit cicles in the AMEs which correspond to quasiperiodic solutions in the ODEs; HB: Hopf bifurcation in the AMEs which correspond to torus bifurcation (TR) in the ODEs; T: transcritical bifurcation; SN: saddle-node bifurcation

Figure 7.5(a) shows the evolution of the system response as a function of

k_g, at a forcing frequency value close to the primary resonance $\Omega_u = 0.9999$, to be compared with figure 7.5(b) (deeply analyzed in Sect. 8.1). Both the asymptotic system and the original one exhibit the presence of two periodic solutions P1′ and P1″ which arise from the transcritical bifurcation responsible for the loss of stability of the controlled main periodic solution P1. Such solutions, anyway, are not properly controlled by the system, as highlighted by the non-zero value of the control variable z (with amplitude b) reported on the right side of figures 7.5(a),7.5(b). Also in this case an excellent agreement between the results of the two systems can be observed, not only about the qualitative behavior of the response but also about the detection of the bifurcation events responsible for changes in stability. Also the quantitative results are satisfactory, with an error on the amplitude of the controlled solution P1 of about 5% (see spectra of the P1, P1′ and P1″ solution reported in figures 8.13,8.14 of Sect. 8.1). It is worth underlining that the asymptotic system allows one to select and follow also the evolution of the system quasiperiodic responses, which in such system appear as periodic solution arisen from the Hopf bifurcations (red curves C′ and C″ on figures 7.5(a)).

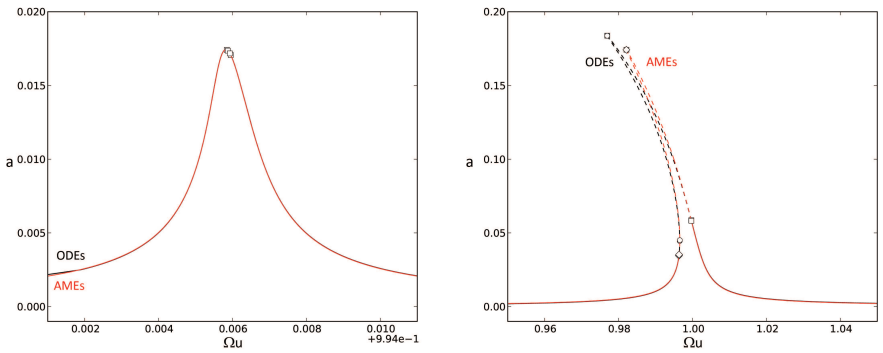

(a) (b)

Figure 7.6: Comparison between results obtained from ODEs system (black) and from AMEs system (red) for $U = 0.0001$ and $k_g = 0.002$ (a) and for $U = 0.001$ and $k_g = 0.001$ (b)

Finally, the good concordance of results is confirmed by the comparison between frequency-amplitude curves obtained for the AMEs system and for the ODEs system at feedback control value close to the escape $k_g = 0.002$ (figure 7.6(a)). The reported response curves almost overlap, as well as the

region of instability confined by a couple of transcritical bifurcations which correspond to the crossing of the resonance loop of figure 7.4. Also for an increased forcing amplitude value $U = 0.001$ (figure 7.6(b)) the asymptotic system provides good results, even if slight differences can be highlighted around the top of the resonance curve, where the high value of the response amplitude does not fulfill the ordering of the asymptotic system (i.e. $a = \epsilon a$).

Chapter 8

Strongly nonlinear dynamics of the controlled system

The previous chapter has pointed out that the external feedback control introduced into the AFM model is a simple but powerful technique able to avoid possible unstable responses of the AFM cantilever and thus to contribute to guarantee the accuracy of the scanning operations. As already explained, this method can be defined as a "local" control, as its aim is not to overall regularize the global system dynamics [62, 90], but to keep the cantilever response to the reference one thus reliably measuring the sample surface. Yet, a matter of considerable theoretical and practical interest is also the study of the global nonlinear dynamics of the controlled system, in order to investigate and a posteriori verify possible undesirable effects of the control introduction on the system behavior.

For this purpose, a comprehensive analysis of the system dynamical response has been carried out and the influence of selected parameters variation has been examined, for both the cases of parametrically and externally forced system. Behavior charts around primary and subharmonic resonances are reported together with several bifurcation diagrams to detect the main local bifurcation thresholds as a function of the forcing amplitude, the feedback control parameter and the nonlinear interaction. Here, the increased number of dofs and parameters produces an enriched dynamical scenario which can be compared with the results presented in Chapter 3 for the uncontrolled system. Overall, the analysis of strongly nonlinear dynamics allows one to highlight the influence of the external feedback control on the

dynamical behavior of the system up to the undesired "jump-to-contact".

8.1 Controlled AFM system under parametric excitation

The dynamical response of the controlled system under the horizontal parametric scan excitation has been studied for a wide range of forcing frequencies that include the principal and the fundamental resonances. By again neglecting the following parameters

$$\alpha_2 = 0, \quad \rho_2 = 0, \quad \mu_2 = 0, \quad \eta_1 = 0, \quad \eta_2 = 0$$

as in the uncontrolled case, the system equation becomes

$$\begin{aligned} \ddot{x} + \alpha_1 x + \alpha_3 x^3 &= -\frac{\Gamma_1}{(1 + x + z - z_s)^2} - \rho_1 \dot{x} + \mu_1 x \ddot{U}_g \\ \dot{z} &= k_g \left(x_{ref} - x\right) \end{aligned} \tag{8.1}$$

with $U_g = U \sin(\omega_u t)$. Parameter values used for the reported analyses are the same considered previously, namely,

$$\begin{aligned} &\alpha_1 = 1, \qquad \alpha_3 = 0.1, \quad \rho_1 = 0.001, \quad \nu_1 = 0.01, \quad \nu_2 = 0.01 \\ &\mu_1 = 1.5708, \quad \Gamma_1 = 0.1, \quad z_s = 0.01. \end{aligned} \tag{8.2}$$

Numerical analyses have been carried out by means of the continuation software AUTO [25], which permits to obtain bifurcation diagrams and behavior charts in terms of selected parameters. Here, most attention is devoted to study the system nonlinear response under changes in the forcing amplitude U and the feedback control parameter k_g, although the influence of the nonlinear interaction term is also investigated. It is worth noting here that some graphical devices are used in the next figures to distinguish among bifurcation loci and simplify their interpretation: considering the charts of bifurcation/response scenarios, green lines correspond to saddle-node thresholds (SN), red lines are associated to period doubling bifurcations (PD), blue lines represent transcritical bifurcations (T) and black lines identify torus loci (TR).

For what concerns the analysis of the system dynamics under variation

of the forcing amplitude U, several bifurcation diagrams have been realized to detect the main kinds of local bifurcations responsible for the stability loss, and local bifurcation thresholds have been numerically obtained, whose results are summarized in figure 8.1. The local bifurcation loci which represent the escape thresholds for the uncontrolled system are present also in the controlled case, even if they do not correspond to the actual stability boundaries anymore: Nevertheless, they are reported in figure 8.1 together with the escape thresholds of the controlled system, as they are useful tools for an immediate comparison of results. In the low-frequency range range up to the fundamental resonance ($\omega_u = 0.835 = \omega_1$), the system escape threshold is governed by the torus bifurcation of the nonresonant P1 solution (apart from confined thresholds of period doublings) which occurs before the saddle-node formerly governing the onset of escape in the uncon-

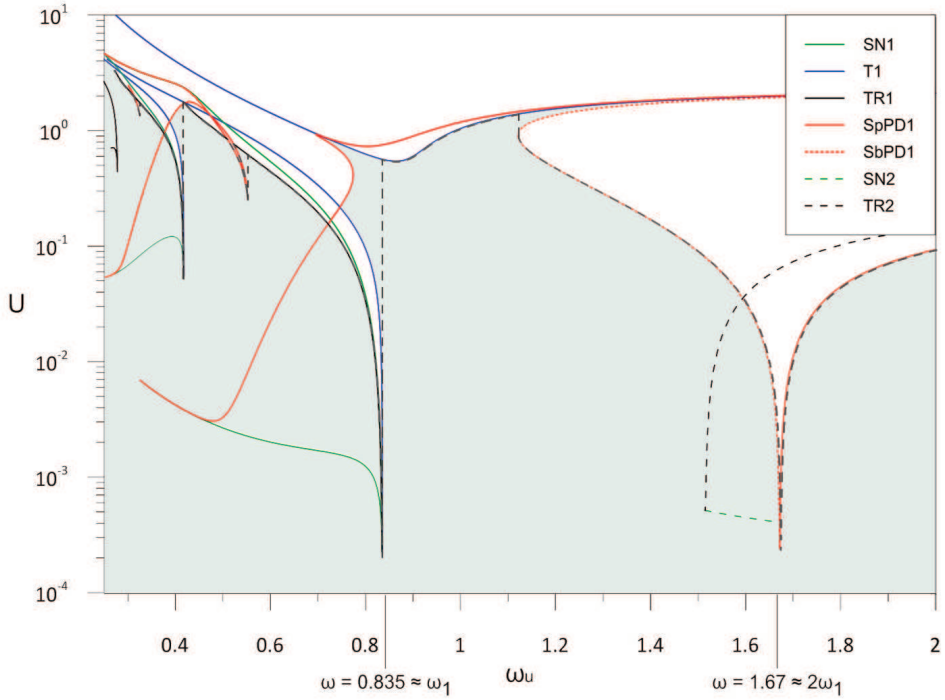

Figure 8.1: Local bifurcations map and overall escape threshold in the frequency-amplitude plane of parametric scan excitation and for $k_g = 0.001$. Gray area: region of stable reference response of the controlled system; dotted gray line: overall escape boundary; SN1: saddle-node bifurcation of P1 solution; T1: trascritical bifurcation of P1 solution; TR1: torus bifurcation of P1 solution; SpPD1: supercritical period doubling of P1 solution; SbPD1: subcritical period doubling of P1 bifurcation; SN2: saddle-node of P2 solution; TR2: torus bifurcation of P2 solution

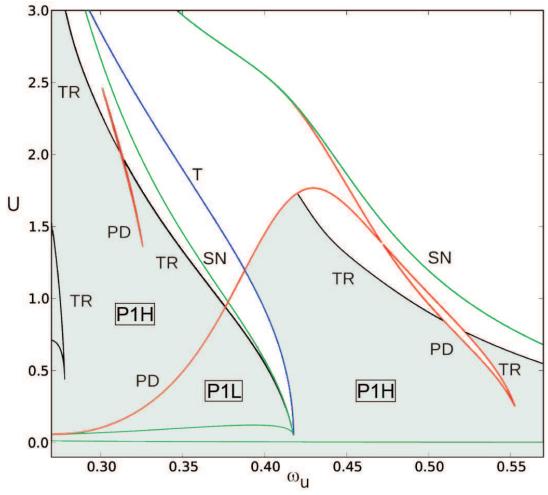

Figure 8.2: Behavior chart at low frequencies in the ω_u-U plane and for $k_g = 0.001$

trolled case (see figure 8.2), while the transcritical bifurcation of the resonant P1 solution occurs before the period doubling, thus leading to system instability for frequencies to the right of the fundamental resonance instead of the period doubling sequence. For higher frequencies which include the principal resonance ($\omega_u = 1.67 = 2\omega_1$), the system shows the coexistence of 1-period and 2-period solutions, which become unstable via a couple of period doublings and a torus bifurcation which replaces the period doubling, respectively.

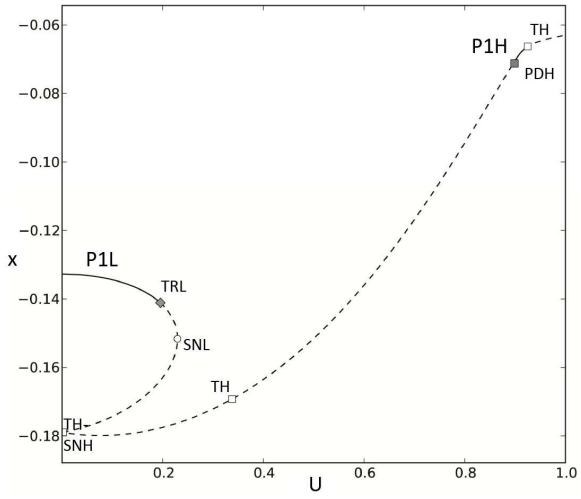

Figure 8.3: Bifurcation diagram at $\omega_u = 0.7$ with detection of the torus bifurcation at $U = 0.1867$ and the saddle-node bifurcation at $U = 0.2293$

It is worth underlining that the stable region of figure 8.1 refers to solutions for which the feedback control works properly, i.e. stable responses of the type (x_{ref}, z_s). Accordingly, stable motions exhibited by the system that do not settle onto the reference one are considered as unwanted outcomes and thus out of the stability range. This is the case, for example, of stable quasi-periodic solutions born out of the torus bifurcations, an example of which is reported in figures 8.3 and 8.4 for a forcing frequency of $\omega_u = 0.7$. Here, the bifurcation diagram as function of the forcing amplitude shows the occurrence of a torus bifurcation at $U = 0.1867$ which makes the nonresonant P1 solution unstable. After that, the birth of a stable quasi-periodic motion can be numerically detected in the controlled system, while it does not exist in the reference uncontrolled one (see figure 3.2). Note that in this case the control variable z does not reach the expected position $z_s = 0.01$ (see the temporal evolution of figure 8.4(b) against the one in figure 8.4(a)). The quasi-periodic solution exists up to the amplitude value $U = 0.2293$, when a saddle-node bifurcation makes the reference solution disappear; since it represents the input for the numerical solution of the controlled system, this local bifurcation signs also the death of the stable quasi-periodic response.

To analyze more in details the system dynamical response, several charts of bifurcation/response scenarios have been realized around fundamental and principal resonances, as function of the most relevant dynamical parameters, i.e. the forcing frequency ω_u, the forcing amplitude U and the feedback control parameter $k - g$. To achieve an exhaustive description of their mutual influence of the system behavior, these charts are produced in the ω_u-U, ω_u-k_g and k_g-U planes, to be considered as planar sections of a more general three-dimensional plot. Moreover, the effect of the nonlinear atomic interaction on the system response is analyzed in view of a comparison with the uncontrolled case, and a series of bifurcation diagrams is presented to complete the results. In the latter, local bifurcations that do not modify the solutions stability are also reported for the sake of completeness, as they belong to thresholds which are plotted in the behavior charts, and they contribute to increase/decrease the number of stable Floquet multipliers. A special behavior concerns the period doubling loci which actually correspond to a couple of local bifurcations occurring consecutively; each of them causes the passage of one Floquet multiplier through -1 but only one signs the arise of a 2-period solution. To improve the figures readability,

only one period doubling is thus reported.

8.1.1 Nonlinear dynamics around the fundamental resonance

The system dynamical behavior around the fundamental resonance in the three-dimensional space (ω_u, U, k_g) is reported in figures 8.5, 8.6, 8.18, 8.19 and 8.11. In the $\boldsymbol{\omega_u}$-$\boldsymbol{U}$ **plane**, it is interesting to investigate the influence of the increasing feedback control parameter on the stability of the main periodic solutions, and compare the results with the ones obtained for the uncontrolled system (i.e. $k_g = 0$ in figure 8.5(a)). For frequencies up to $\omega_u = 0.835 = \omega_1$, the system shows the presence of two 1-period solutions (low-amplitude/nonresonant P1 (P1L) and high-amplitude/resonant P1 (P1H)) connected through a couple of saddle-node bifurcations, just as in the uncontrolled case. However, the control introduction in the model causes the birth of a new threshold of torus bifurcation (TRL) related to the P1L solution and of two thresholds of transcritical bifurcation (TH) of the P1H solution, which considerably modify the system stability region. Figure 8.5(b), in fact, shows the appearance of an unstable tongue delimited by the new bifurcation thresholds which occurs for low values of the forcing amplitude U, and even for weakly controlled systems. Bifurcation diagrams of figures 8.7-8.10 help to clarify the point: due to the control, the nonresonant solution becomes unstable with a torus bifurcation TRL which occurs before the saddle-node SNL, while the resonant one, nearly always unstable in the low-frequency range, regains stability thanks to the transcritical bifurcation TH, which happens always for amplitude values considerably higher than the ones corresponding to both the saddle-nodes and the torus too. The main consequence of these new thresholds is that the triangle region below the V vertex detected in the uncontrolled system with the existence of both P1L and P1H solutions tends to be reduced by the torus curve, with the two periodic solutions not coexisting anymore, up to its complete disappearance for higher k_g values. Furthermore, P1H solution loses stability through another transcritical bifurcation before the period doubling PDH which marked the escape from the boundary region in the uncontrolled system. As a result, the total escape boundary for the controlled system settles on to reduced values of the forcing amplitude. The reported bifurcation diagrams highlight also the presence of other P1 solutions born out of the transcritical bifurcations (represented with green lines in figures 8.7-8.10),

which coexist with the main ones and which display a rich scenario of local bifurcations; however, bifurcation diagrams with respect to the control variable z show that for these additional solutions the system fails to reach the reference position (i.e. $z = z_s = 0.01$) actually making the z response periodic, so that they appear as unwanted responses. As for the discussed case of the quasi-periodic orbits, this is due to the fact that such responses are peculiar to the controlled system, while do not exist in the reference one.

For higher values of the feedback control parameter, (figure 8.6(a)), an unstable region confined by a torus bifurcation (TRH) arises below the upper transcritical threshold, and expands as the control increases. Simultaneously, the torus bifurcation which instabilizes the P1L solution occurs for decreasing values of U, up to the critical value of $k_g = 0.00223$ when the P1L solution becomes entirely unstable. After that, stability regions reduce to narrow strips of existence of stable P1H solution, associated with limited ranges of forcing amplitude U (see behavior charts at $k_g = 0.01$ of figure 8.6(b)).

It is worth underlining that the limit value of the feedback control parameter k_g is the same obtained studying the stability of the equilibrium solution in Sect. 6.2, which was related to the occurrence of a Hopf bifurcation. The comparison with the obtained numerical results shows a good agreement in terms of both the numerical value and the kind of associated local bifurcation (the Hopf bifurcation of the asymptotic equilibrium corresponds to the torus on the ODEs problem), and thus confirms that it represents the upper boundary for the existence of the main stable periodic solution P1L of the system, for increasing k_g.

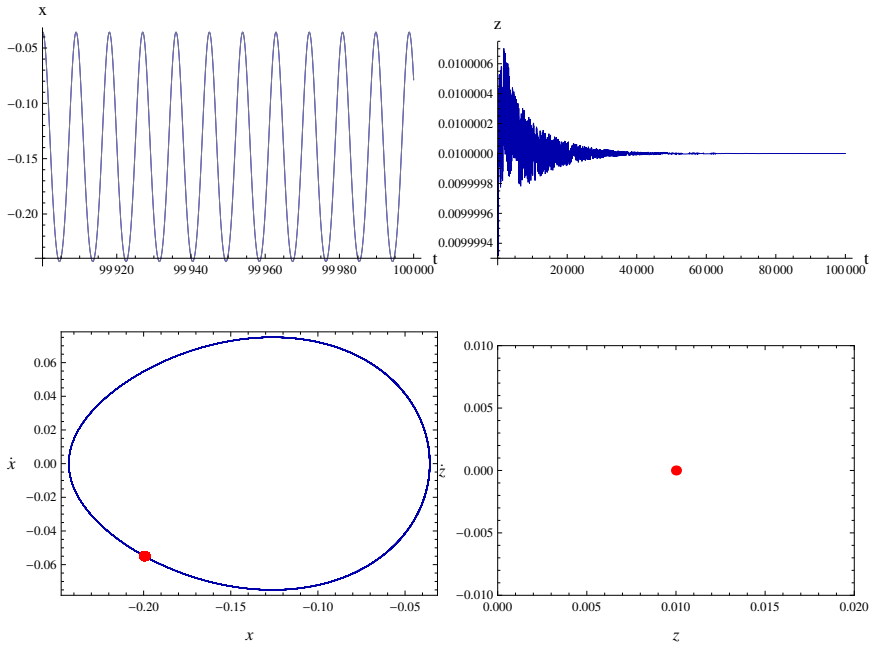

(a)

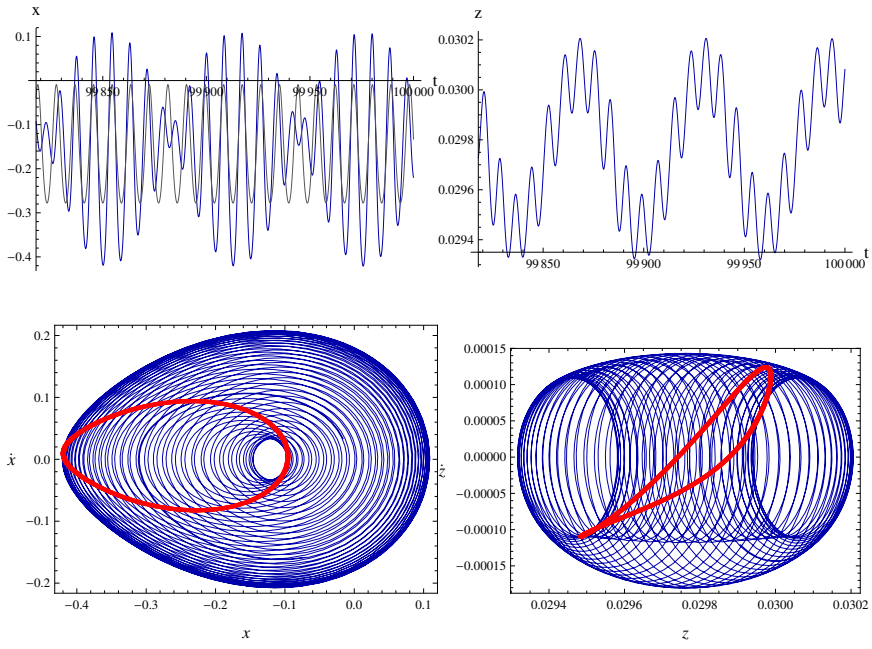

(b)

Figure 8.4: Time histories, phase portraits and Poincaré maps of stable solutions at $\omega_u = 0.7$ before and after the torus bifurcation: periodic solution at $U = 0.18$ (a) and quasi-periodic solution at $U = 0.21$ (b)

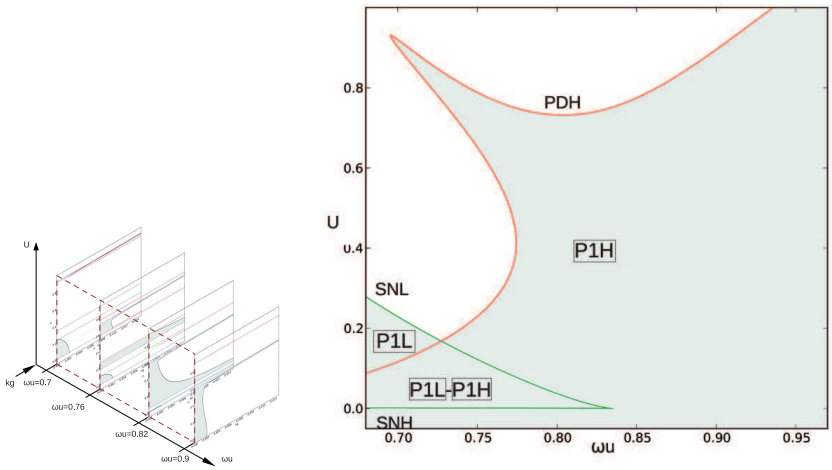

(a)

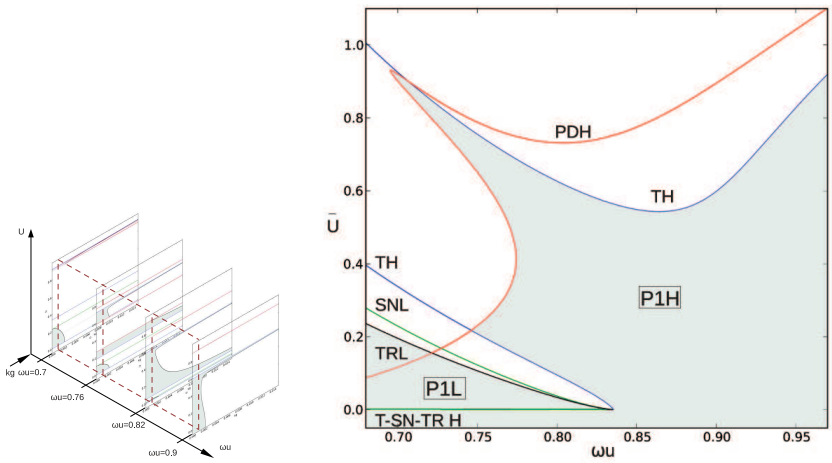

(b)

Figure 8.5: Behavior charts in the ω_u-U plane around primary resonance for $k_g = 0$ (a) and $k_g = 0.001$ (b)

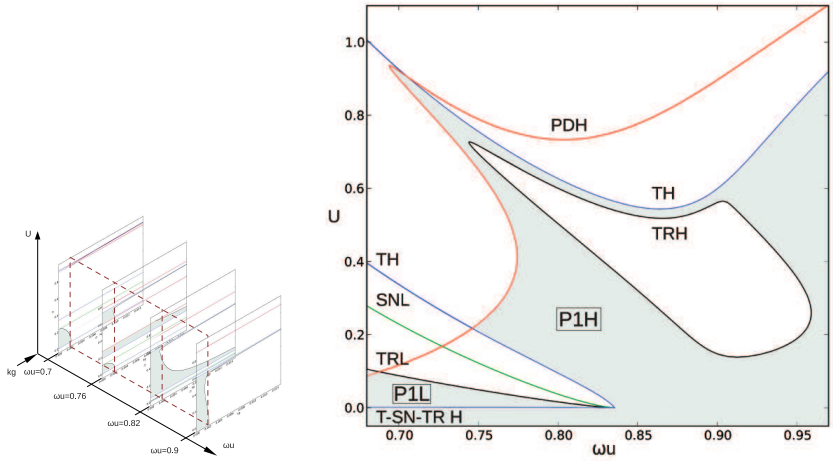

(a)

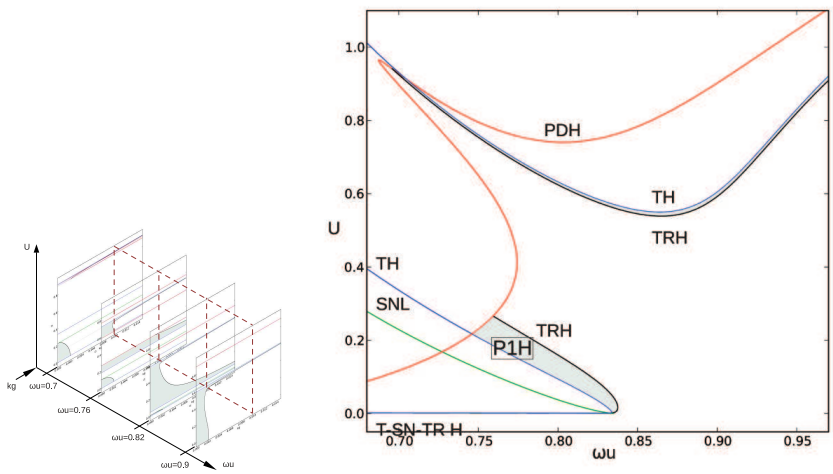

(b)

Figure 8.6: Behavior charts in the ω_u-U plane around primary resonance for $k_g = 0.002$ (c) and $k_g = 0.01$ (d)

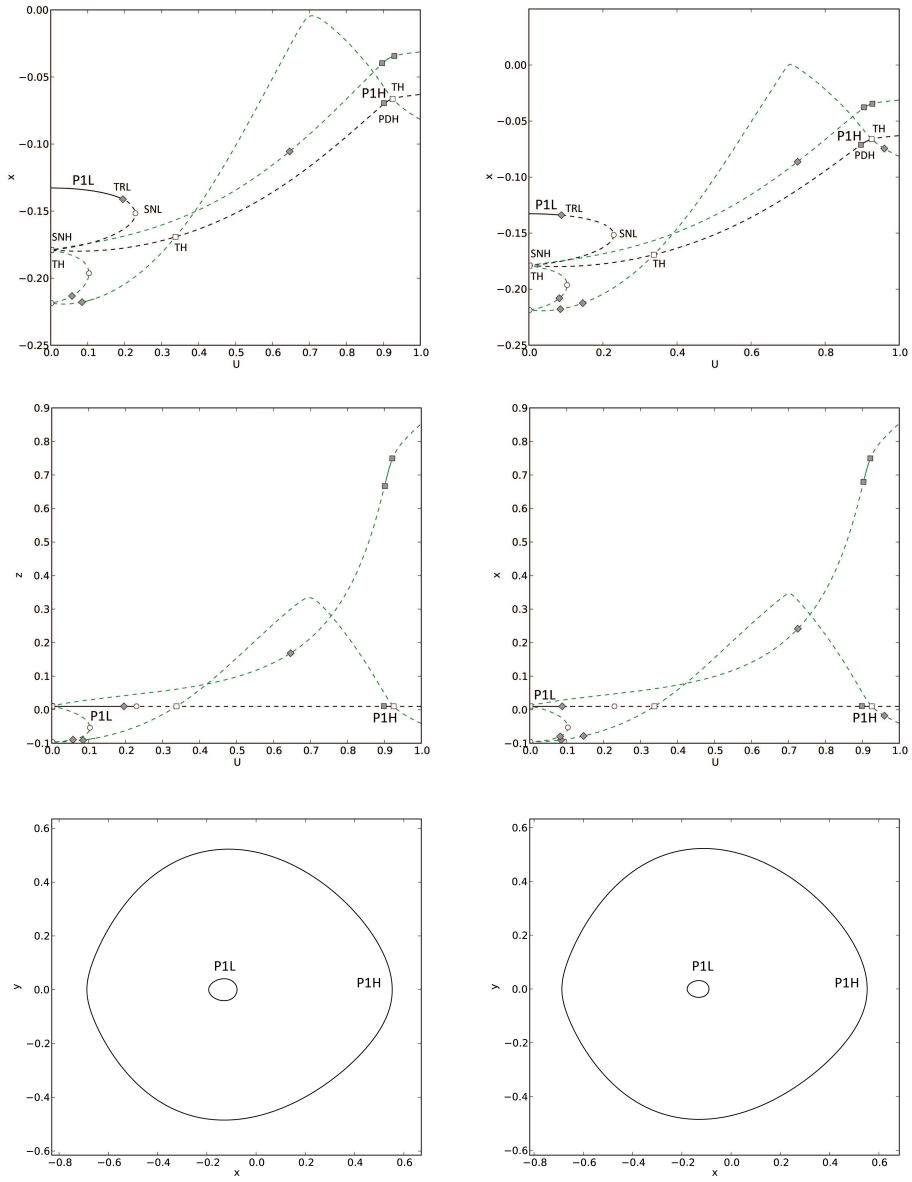

(a) (b)

Figure 8.7: Bifurcation diagrams at $\omega_u = 0.7$ for $k_g = 0.001$ (a) and $k_g = 0.002$ (b). Periodic orbits on the phase plane refer to solutions at $U = 0.1$ (P1L orbit) and $U = 0.91$ (P1H orbit)

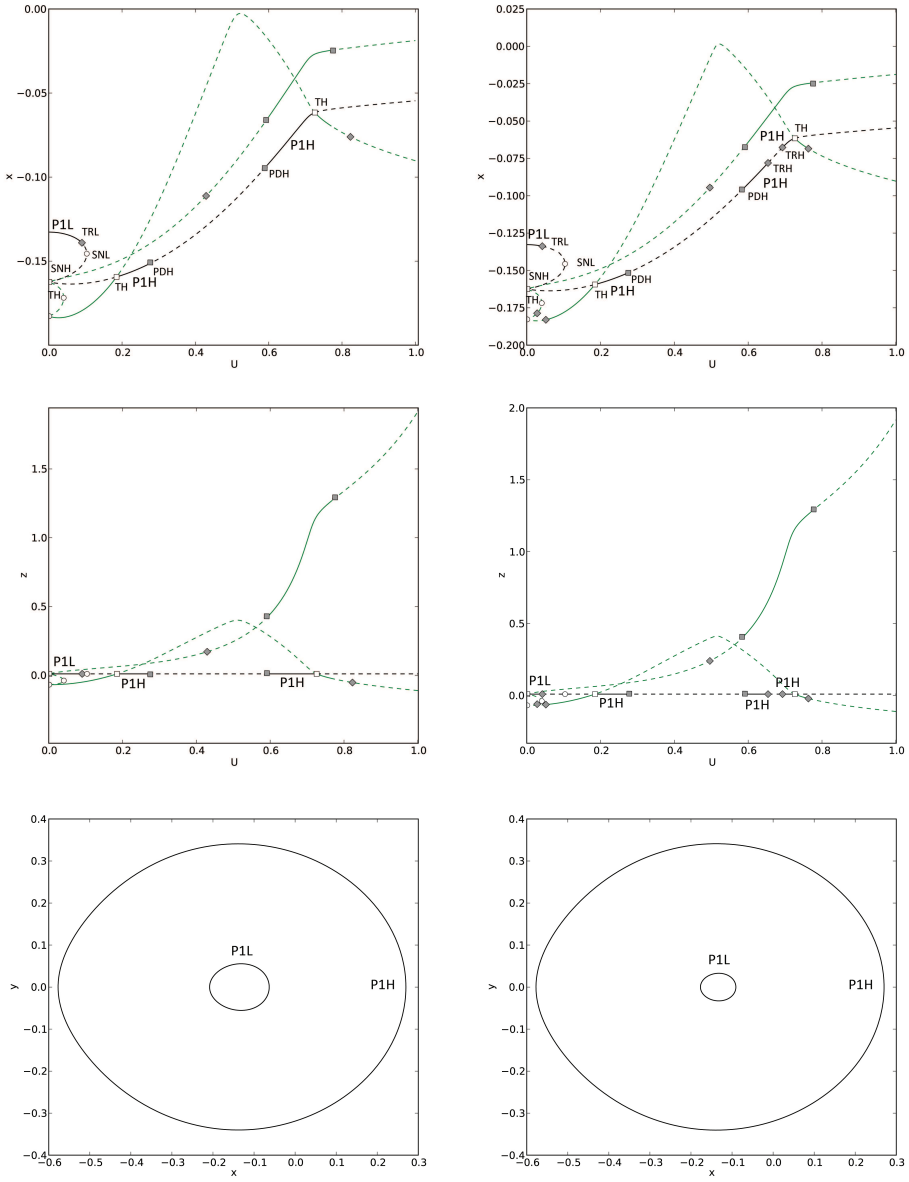

(a) (b)

Figure 8.8: Bifurcation diagrams at $\omega_u = 0.76$ for $k_g = 0.001$ (a) and $k_g = 0.002$ (b). Periodic orbits on the phase plane refer to solutions at $U = 0.05$ (P1L orbit) and $U = 0.25$ (P1H orbit)

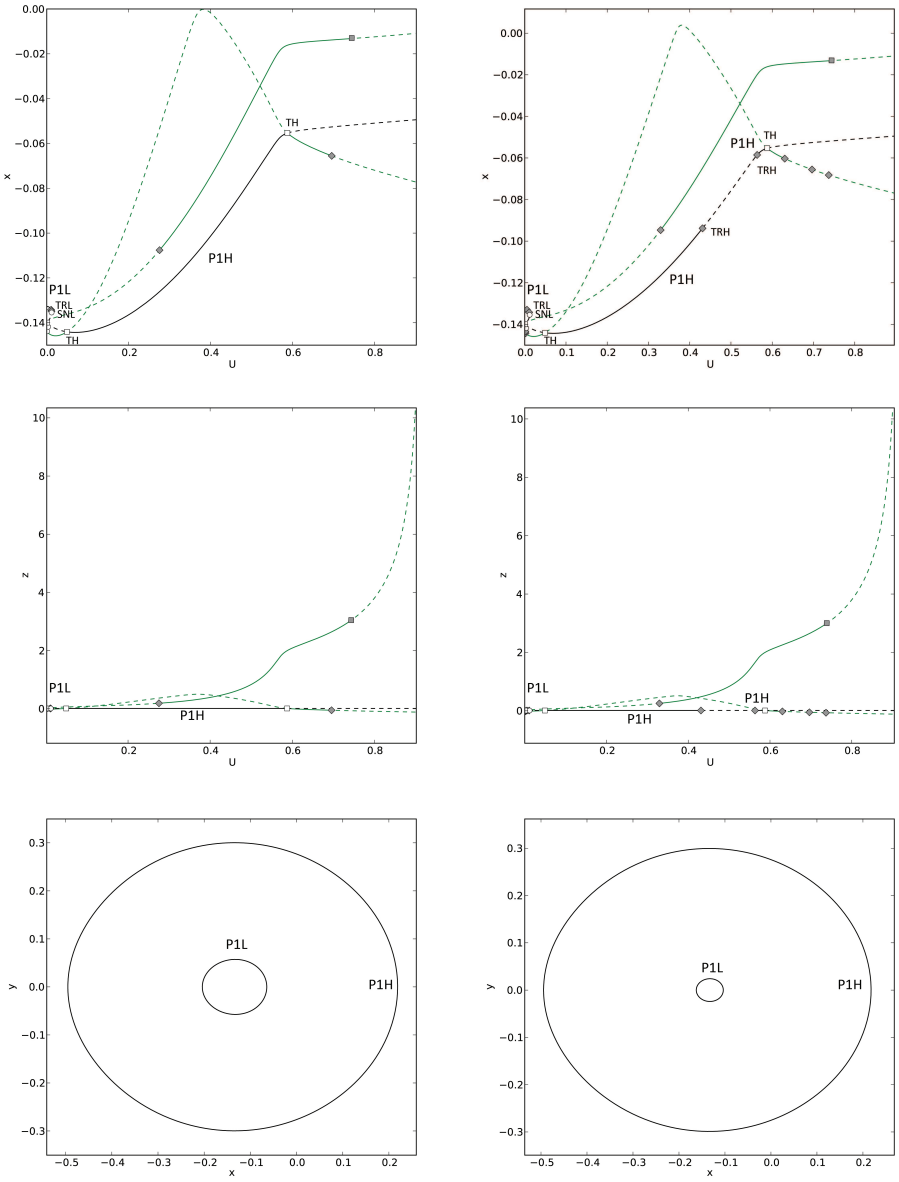

(a) (b)

Figure 8.9: Bifurcation diagrams at $\omega_u = 0.82$ for $k_g = 0.001$ (a) and $k_g = 0.002$ (b). Periodic orbits on the phase plane refer to solutions at $U = 0.005$ (P1L orbit) and $U = 0.2$ (P1H orbit)

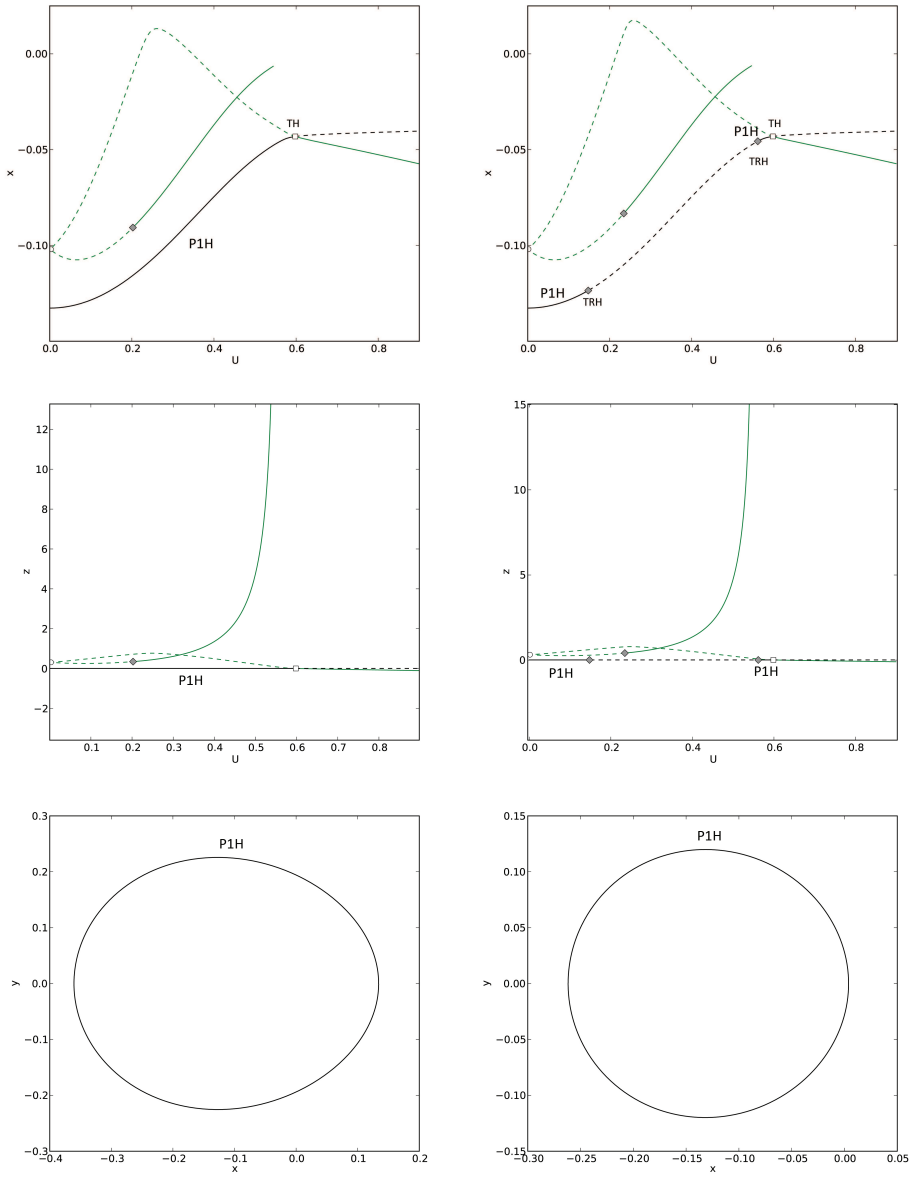

(a) (b)

Figure 8.10: Bifurcation diagrams at $\omega_u = 0.9$ for $k_g = 0.001$ (a) and $k_g = 0.002$ (b). Periodic orbits on the phase plane refer to solutions at $U = 0.2$ and $U = 0.08$

Additional informations are given by figure 8.11 which refers to the bifurcation/response scenario in the $\boldsymbol{\omega_u}$-$\boldsymbol{k_g}$ **plane**.

Figure 8.11(a) is obtained at a forcing amplitude value of $U = 0.0001$, and shows that such torus threshold is approximately valid in the whole frequency range analyzed, with the exception of a narrow range around the fundamental resonance frequency $\omega_u = \omega_1 = 0.8358$ where a loop of transcritical bifurcation breaks the torus curve and let the escape bound-

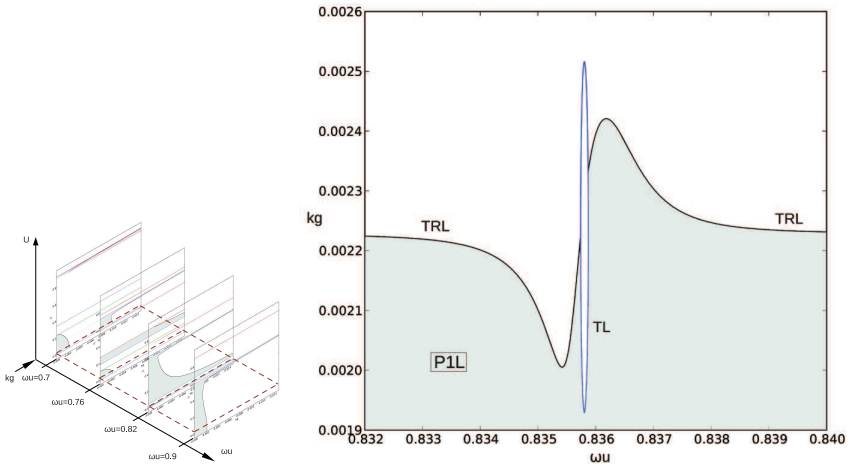

(a)

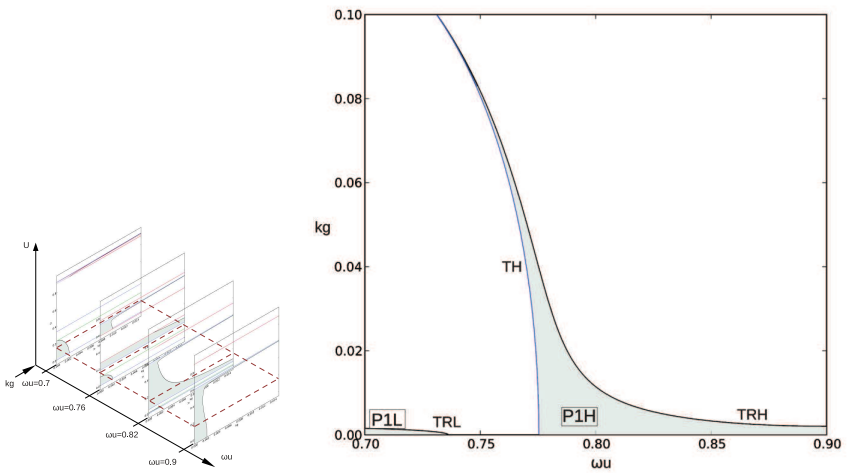

(b)

Figure 8.11: Behavior charts in the $\omega_u - k_g$ plane around primary resonance for different values of the forcing amplitude: $U = 0.0001$ (a), $U = 0.15$ (b)

ary decrease. The bifurcation diagram at this forcing frequency against the k_g parameter is reported in figure 8.12(a). Here, the transcritical event at $k_g = 0.00193$ leads to the birth of a stable switched P1 solution (P1$'$), while from the unstable switched branch another P1 solution (P1$''$) arises through a saddle-node bifurcation at $k_g = 0.0019$. Both the new P1$'$ and P1$''$ responses are periodic in x and z variables, and thus show an improper control operation. Finally, two different torus bifurcations make them unstable at $k_g = 0.00226$ and $k_g = 0.00214$, respectively, and become starting points for quasiperiodic solutions which exist as the feedback control parameter increases. Looking at temporary evolutions and fft diagrams of P1, P1$'$ and P1$''$ solutions reported in figures 8.13-8.14 for increasing k_g values, it is interesting to note that the z variable moves from constant response (figure 8.13) to quasiperiodic motion (figure 8.17(b)) in a narrow range of feedback control values ($\Delta k_g = 4 \times 10^{-4}$), while the x variable remains almost unchanged, becoming quasiperiodic after the torus bifurcation with a frequency modulation which tends to zero. It can be conjectured that at the considered forcing frequency the close proximity to the natural system frequency ($\omega_u \cong \omega_1$) leads to a substantial increase of the response amplitude that the feedback control barely dominates and that is manifested in the decrease of the escape threshold. Outside the resonance loop, on the contrary, the P1 solution becomes quasiperiodic via a torus event for an almost constant value of the feedback control parameter $k_g = 0.00223$, with the x variable which has a modulation considerably faster than the z one, as reported in figure 8.15 for $\omega_u = 0.7$. In this case, thus, it is the x which governs the passage from periodicity to quansiperiodical behavior. Lastly, it is worth focusing on the quasiperiodic response evolution as the forcing frequency approaches the fundamental resonance, referring thus to figure 8.16 at a feedback control parameter value of $k_g = 0.00228$. The reported results highlight that the x variable exhibits the known phenomenon of phase locking, due to the synchronization of the response frequency to the forcing one, which produces the passage from quasiperiodic behavior to periodic oscillations. Its modulation frequency, in fact, passes from fast to almost zero, even if the system variable coupling does not allow it to become periodic. Simultaneously, it is evident a substantial increase of the response amplitude, which is reflected on the increasingly marked quasiperiodic response of the z variable.

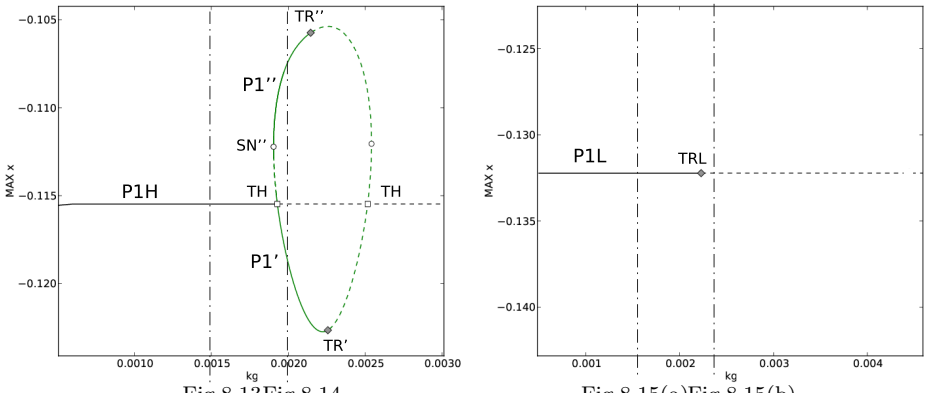

Fig.8.13Fig.8.14 Fig.8.15(a)Fig.8.15(b)

(a) (b)

Figure 8.12: Bifurcation diagram at $U = 0.0001$ for varying k_g at $\omega_u = 0.8358$ (a) and $\omega_u = 0.7$ (b)

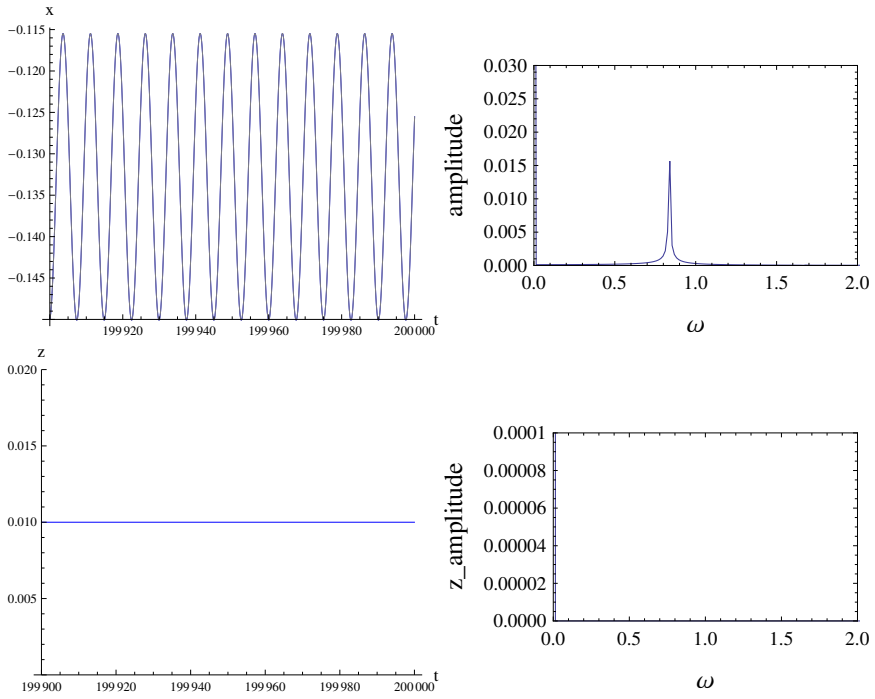

Figure 8.13: Temporary evolution of P1 solution ($k_g = 0.0015$) at $\omega_u = 0.8358$. Gray line represents the reference response evolution

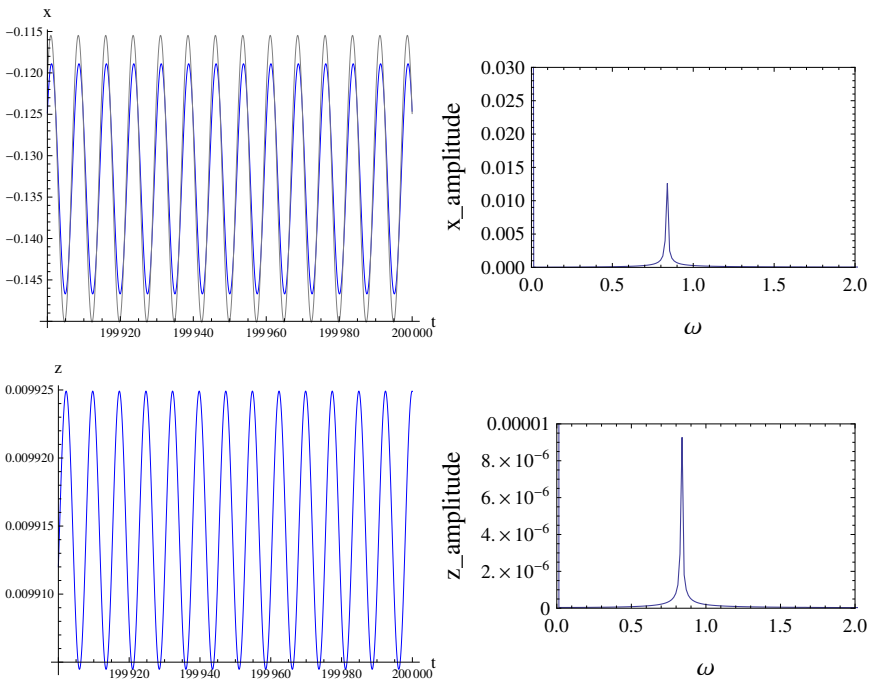

(a)

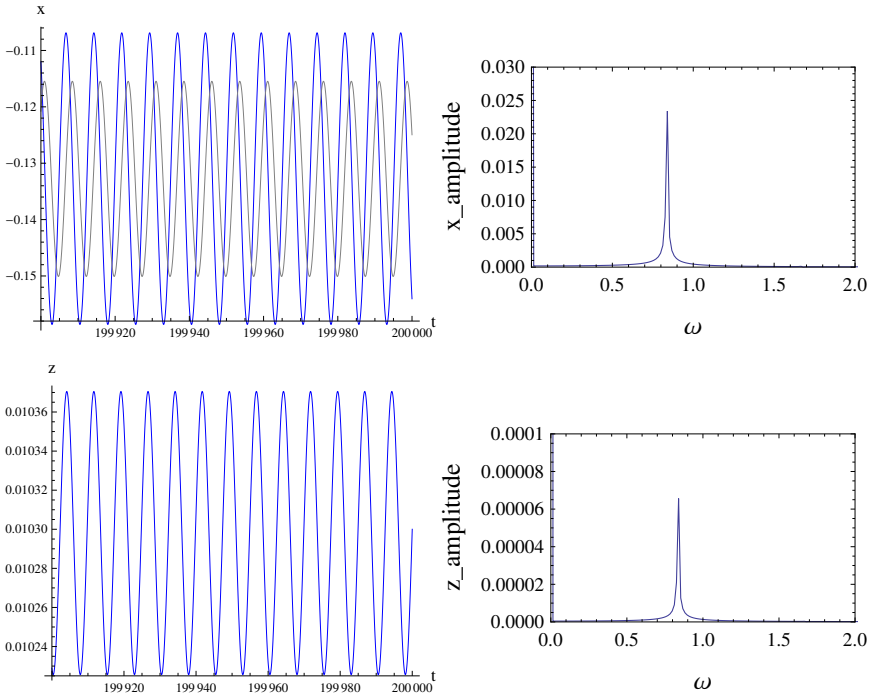

(b)

Figure 8.14: Temporary evolutions of P1′ (a) and P1″ (b) solutions at $k_g = 0.002$ for $\omega_u = 0.8358$ and $U = 0.0001$. Gray line represents the reference response evolution

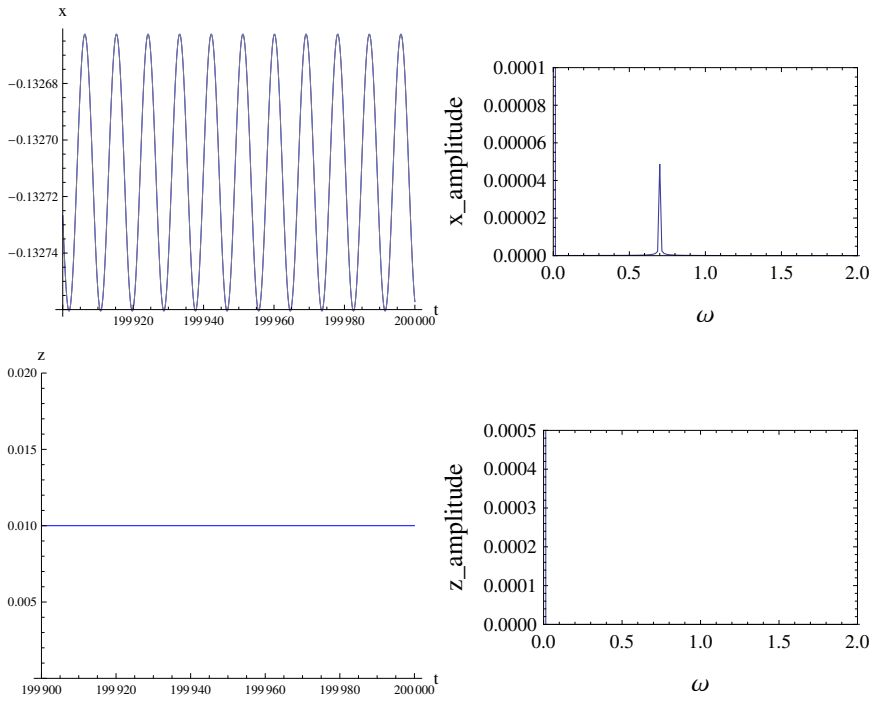

(a)

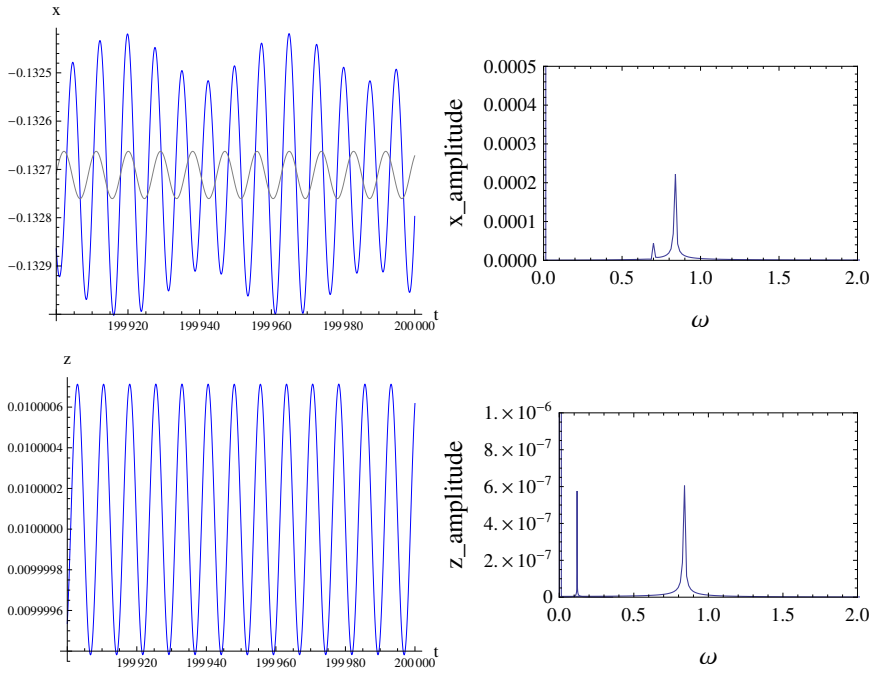

(b)

Figure 8.15: Temporary evolutions of P1 solution ($k_g = 0.0015$) (a) and of the quasiperiodic solution arisen from the torus bifurcation ($k_g = 0.00228$) (b) at $\omega_u = 0.7$. Gray line represents the reference response evolution

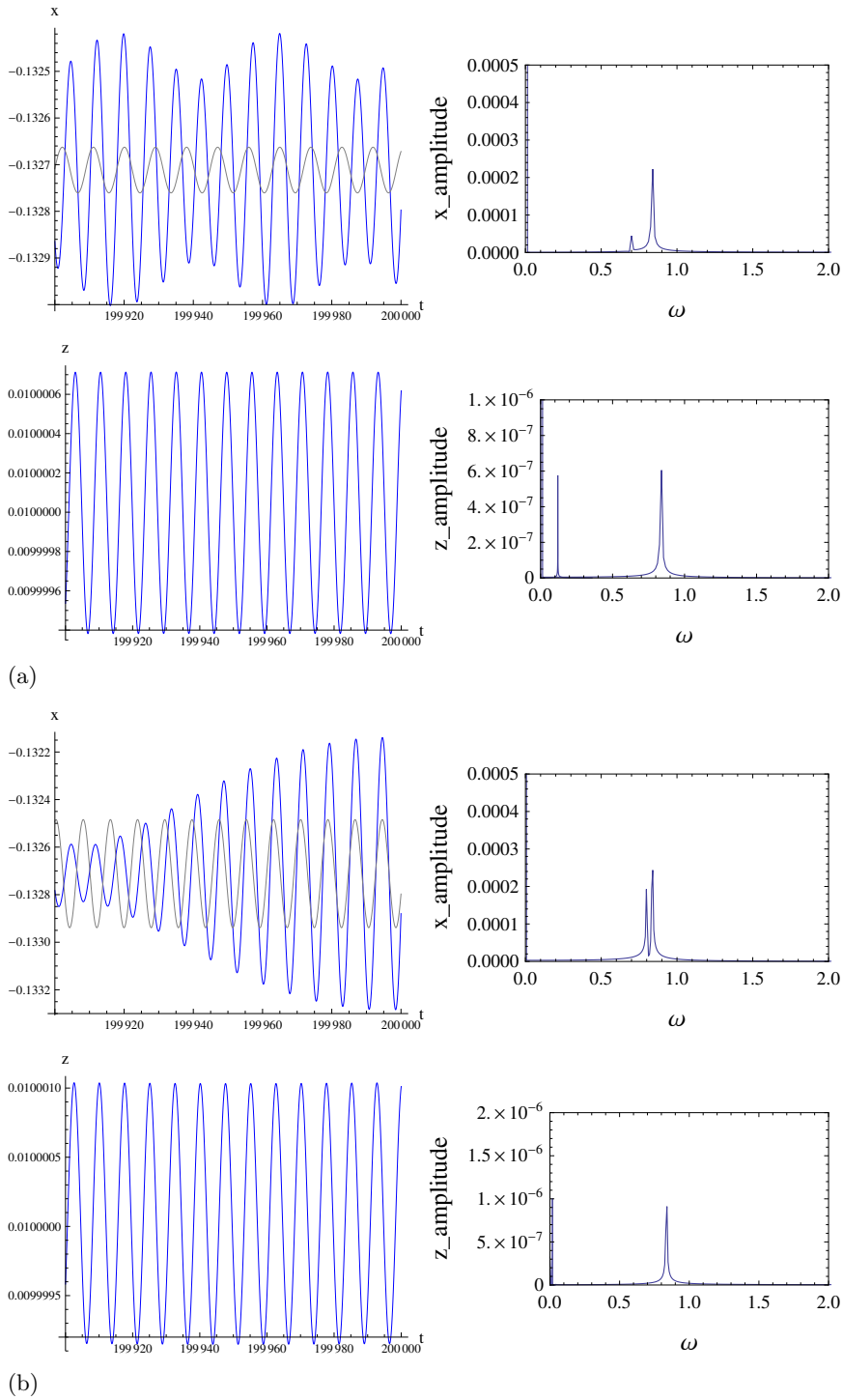

Figure 8.16: Temporary evolutions of quasiperiodic solutions at $k_g = 0.00228$ for $\omega_u = 0.7$ (a) and $\omega_u = 0.8$ (b). Gray line represents the reference response evolution

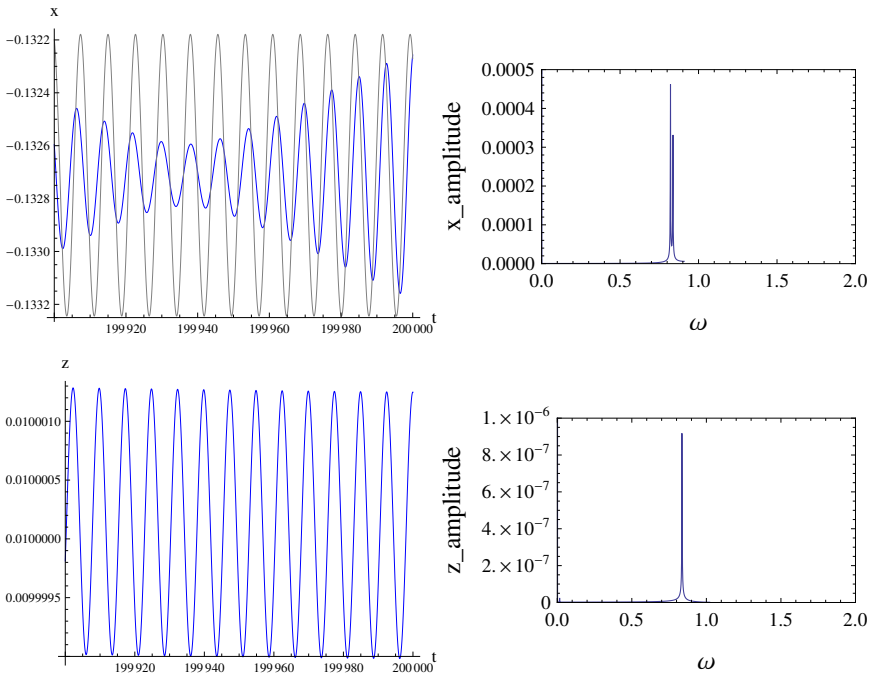

(a)

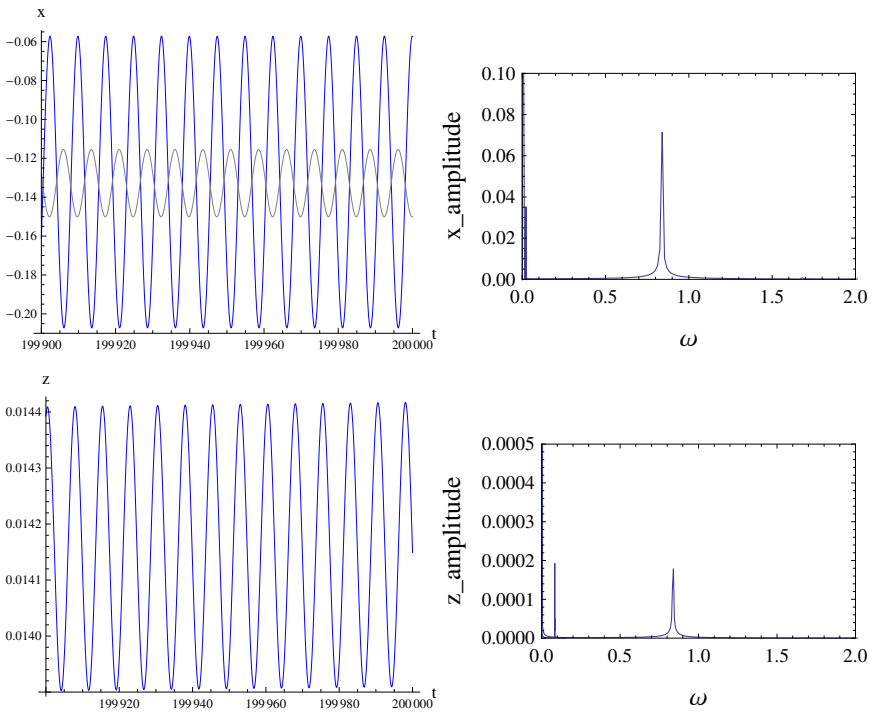

(b)

Figure 8.17: Temporary evolutions of quasiperiodic solutions at $k_g = 0.00228$ for $\omega_u = 0.82$ (a) and $\omega_u = 0.8358$ (b). Gray line represents the reference response evolution

Behavior charts of figures 8.18-8.19 in the ***k_g-U plane*** for different forcing frequencies show that some confined stable regions exist also past the disappearance of the P1L solution and for high values of the feedback control parameter; they are related to the P1H solution and are present only for rather high forcing amplitudes.

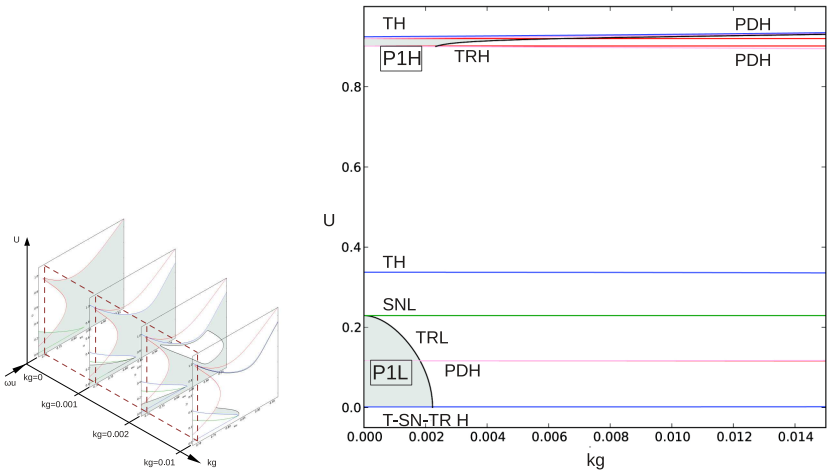

(a)

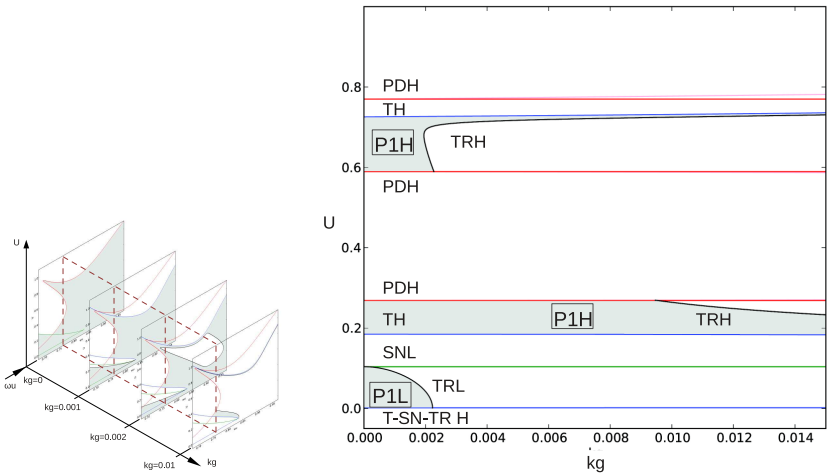

(b)

Figure 8.18: Behavior charts in the $k_g - U$ plane around primary resonance for $\omega_u = 0.7$ (a) and $\omega_u = 0.76$ (b)

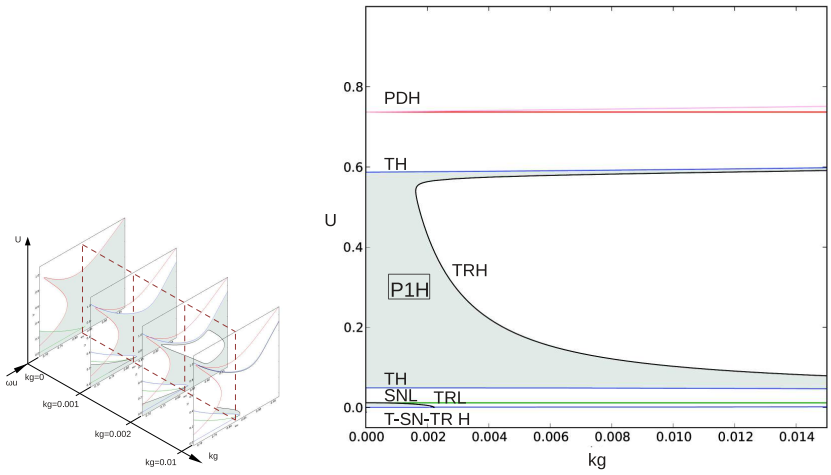

(a)

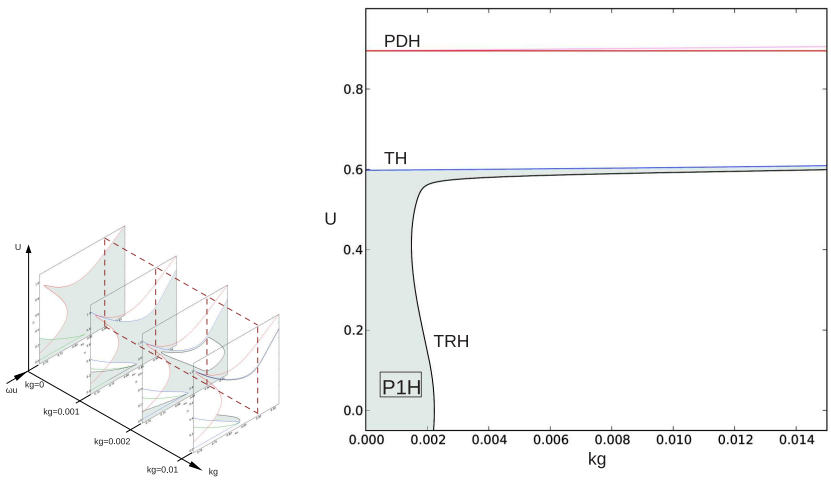

(b)

Figure 8.19: Behavior charts in the $k_g - U$ plane around primary resonance for $\omega_u = 0.82$ (a) and $\omega_u = 0.9$ (b)

Finally, changes in the dynamical response of the controlled system for varying values of the nonlinear interaction parameter Γ_1 are studied in figures 8.20-8.22 focusing at a frequency of $\omega_u = 0.7$. This value, in fact, belongs to the frequencies range which shows the presence of the lowest peak in the P1 solution of the uncontrolled system, as already explained in Sect. 3.1. A comparison with figures 3.17-3.19 permits to clearly understand the effect of the control addition on the system response to a varying atomic interaction. Also in the **Γ_1-U plane**, the region of coexistence of the P1 solutions disappears and a new torus TRL threshold lowers the escape boundary of the P1L response, formerly represented by the saddle-node SNL threshold. However, the control presence affects mostly the P1H solution, which in the uncontrolled system was confined by the period doubling threshold; the onset of a new trancritical locus (TH) and of a new torus one (TRH) significantly reduces its stability range which passes from $\Gamma_1 \in [0.127, 0.149]$ to $\Gamma_1 \in [0.1305, 0.1313]$ at a forcing amplitude of $U = 0.0005$. As expected, the escape value of the atomic interaction decreases as the forcing amplitude grows up, and the instability area consequently expands, as displayed also in the $\omega_u - \Gamma_1$ charts of figure 8.21.

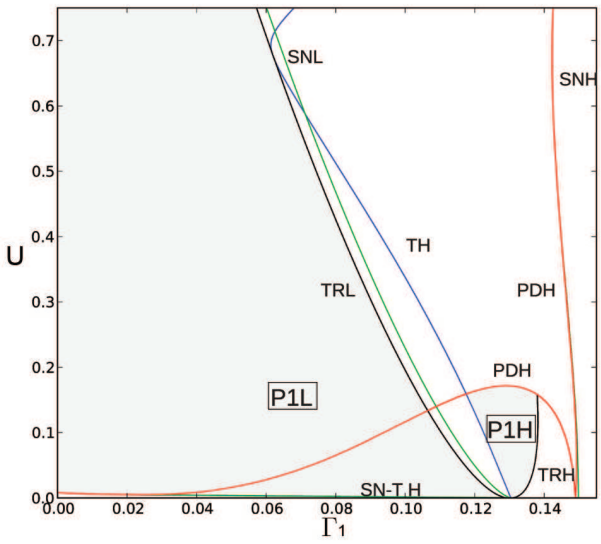

Figure 8.20: Behavior chart in the Γ_1-U plane around principal resonance for $\omega_u = 0.7$

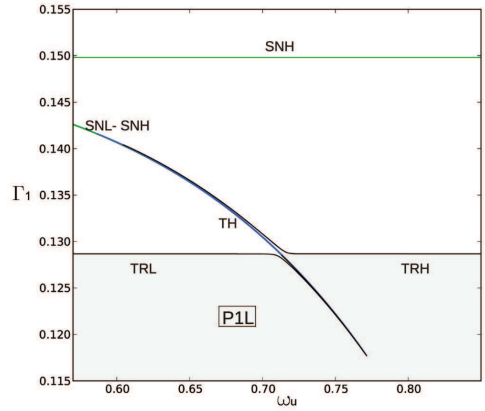

(a)

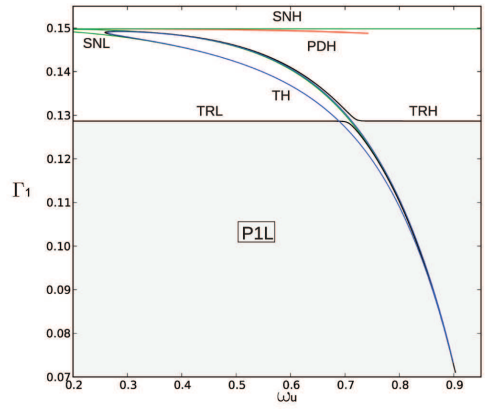

(b)

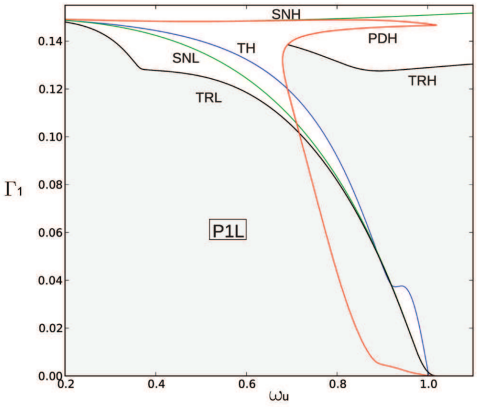

(c)

Figure 8.21: Behavior charts in the ω_u-Γ_1 plane around primary resonance for different values of the forcing amplitude: $U = 0.0001$ (a), $U = 0.0005$ (b) and $U = 0.15$ (c)

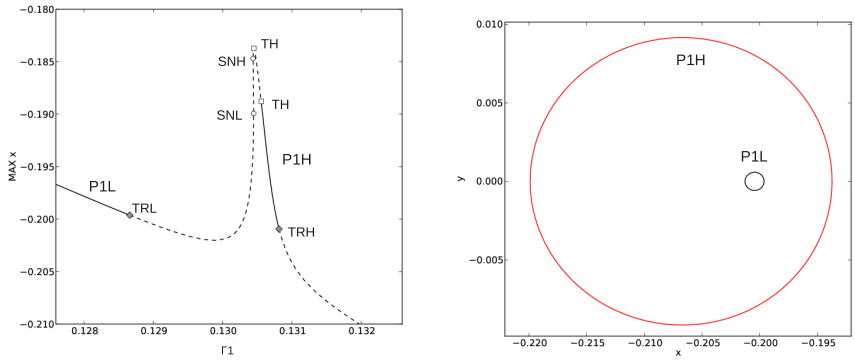

(a)

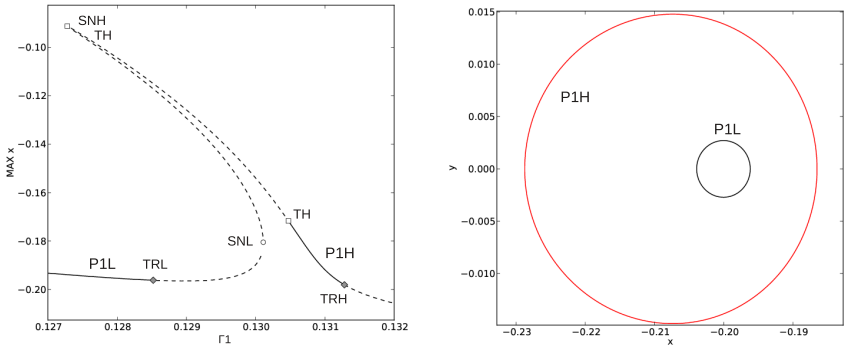

(b)

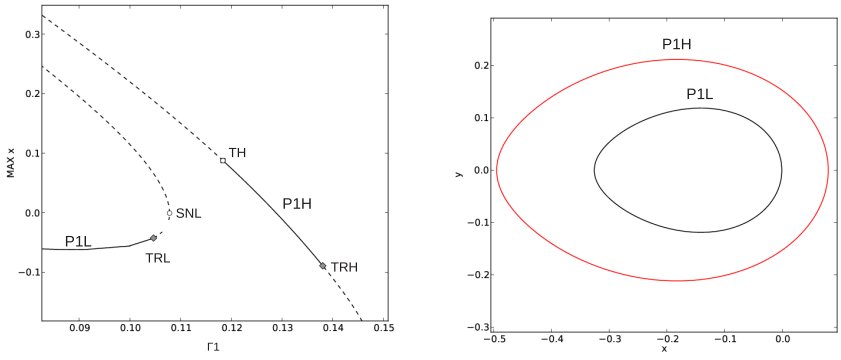

(c)

Figure 8.22: Bifurcation diagrams as function of the nonlinear interaction coefficient Γ_1 at $\omega_u = 0.7$ for $U = 0.0001$ (a), $U = 0.0005$ (b) and $U = 0.15$ (c). Periodic orbits on the phase plane refer to P1l and P1H solutions 1of the corresponding bifurcation diagrams

8.1.2 Nonlinear dynamics around the principal resonance

Moving to the neighborhood of principal resonance ($\omega_u = 1.67 = 2\omega_1$), bifurcation diagrams of figures 8.24-8.25 show the coexistence of 1-period and 2-period solutions, which is a typical feature of the system. However, with the control introduction the system displays the presence of three P2 solutions, two of them arisen from the subcritical (SbPD) and supercritical (SpPD) period doublings which occur in sequence and instabilize the P1 solution (P2$'$ (red) and P2$''$ (green) curves in figures 8.24-8.25), the third one which on the contrary is disconnected from the others (P2 (blue) solution in figures 8.24-8.25). Of these three 2-period responses, only the independent one exhibits a stable branch delimited by a saddle-node (SNP2) and a torus (TRP2) bifurcation, while the others remain unstable as the forcing amplitude increases. On the other hand, bifurcation diagrams with respect to the control variable z highlight that the feedback control works properly only on the unstable P2$'$ solution related to the subcritical period doubling, as it was reasonable to expect since it is the only 2-period solution present also in the uncontrolled system. Accordingly, in the chart of bifurcation/response scenarios in the $\boldsymbol{\omega_u}$**-**$\boldsymbol{U}$ **plane** of figure 8.23(a) the system escape threshold coincides with the subcritical period doubling curve which instabilizes the P1 solution, as in the uncontrolled case (figure 3.9). Nevertheless, it is interesting to study the dynamical evolution of the new P2 solution as the forcing amplitude increases: figure 8.23(b) is referred to its local bifurcation thresholds and some observations can be pointed out. While torus bifurcations are new events which instabilize the response, period doubling and saddle-node curves coincides with the ones related to the 2-period solution of the uncontrolled system, and thus to the bifurcations which affect the unstable P2$'$ solution arisen from the subcritical period doubling (SbPD). This entails that, differently from the other solutions typical of the controlled system (i.e. quasi-periodic responses and 1-period solutions arisen from trancritical bifurcations) which exhibit local bifurcations absent in the uncontrolled case, the P2 solution around principal resonance shows a bifurcation behavior coherent with the correctly controlled responses. However, it is qualitatively different from the original 2-period solution since its portrait in the phase plane in figure 8.24 highlights a different frequency content and an amplitude considerably lower (at $U = 0.01$ its amplitude is 0.006 versus an amplitude of 0.18 of the uncontrolled 2-period solution). A final remark

concerns the frequency range at right of the triangle region, where in the uncontrolled system P2 solution becomes stable through a supercritical period doubling (SpPD). Here the saddle-node responsible for the stability of the P2 solution gets close to the period doublings of the P1 solution but remain separated, even if the corresponding bifurcation thresholds almost coincide (see bifurcation diagram at $\omega_u = 1.75$ in figure 8.25).

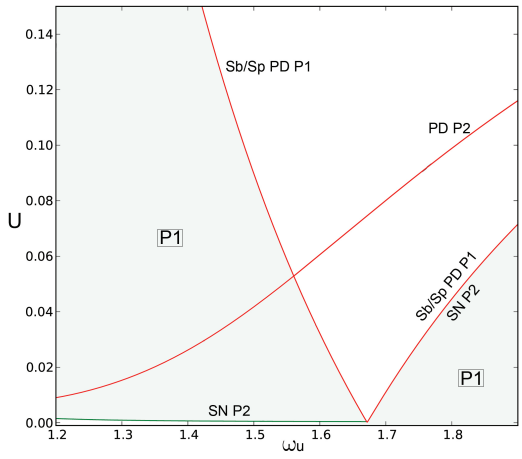

(a)

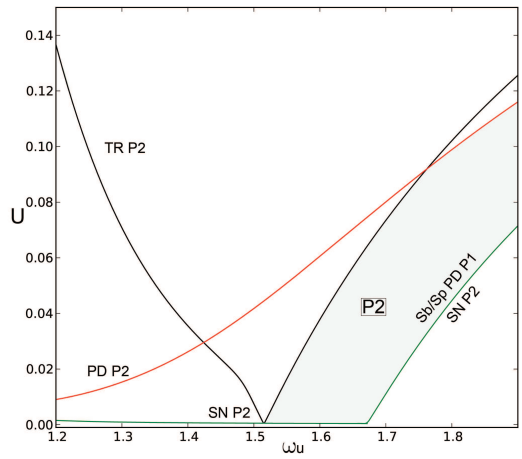

(b)

Figure 8.23: Behavior chart in the ω_u-U plane around principal resonance for $k_g = 0.001$ with detection of stability regions for the properly controlled system (i.e. P1 solution)(a) and for the P2 solution (b)

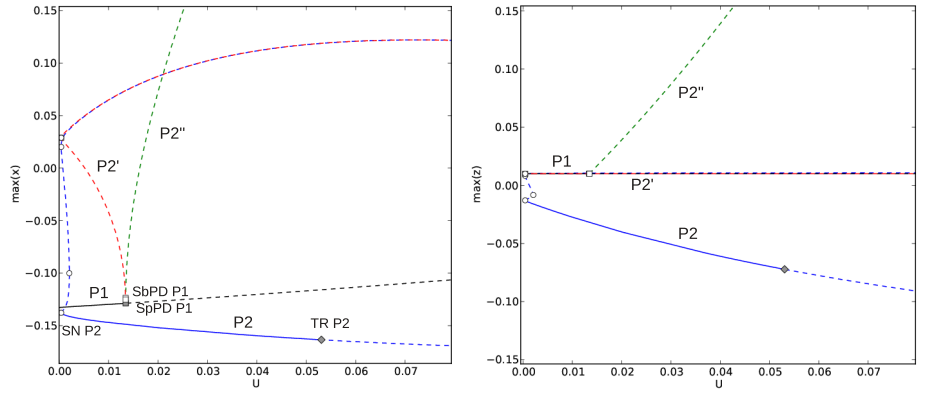

(a)

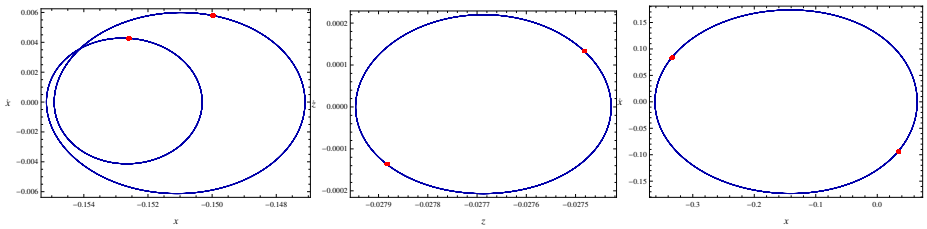

(b) (c)

Figure 8.24: Bifurcation diagrams at $\omega_u = 1.64$ with detection of the stable P1 solution (solid black line), the unstable P2′ and P2″ solutions (dashed red and green lines, respectively) and the stable P2 solution (solid blue line) (a); comparison between phase portraits of the controlled P2 solution (b) and the uncontrolled P2 one (c)

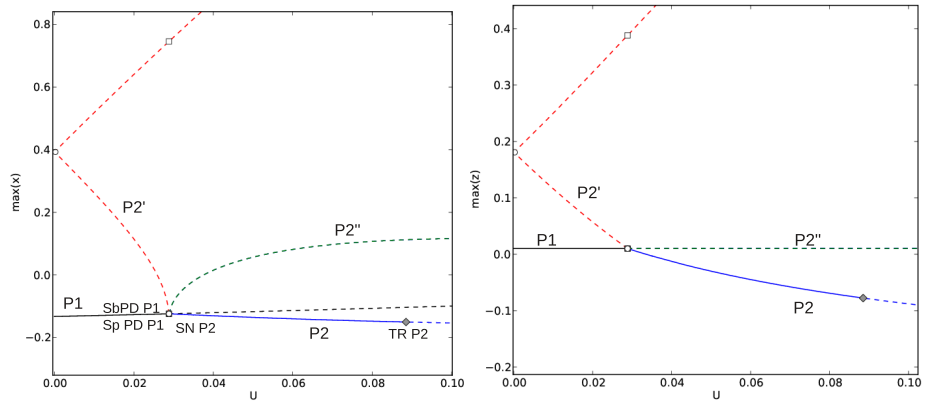

Figure 8.25: Bifurcation diagrams at $\omega_u = 1.75$ with detection of the stable P1 solution (solid black line), the unstable P2′ and P2″ solutions (dashed red and green lines, respectively) and the stable P2 solution (solid blue line)

For what concerns the system dynamical response in the ω_u-k_g **plane**, the phase locking phenomenon observed around fundamental resonance and already described in figures 8.11(a),8.13 can be detected also around principal resonance, as shown in figure 8.26(a). Here, however, the escape threshold represented by the torus bifurcation locus is interrupted by a loop of period doubling, which replaces the transcritical loop present around fundamental resonance and leads to the arise of a 2-period solution which then becomes unstable via a torus bifurcation (figure 8.26(b)). The presence of a switched 2-period solution instead of the 1-period solutions denounces the

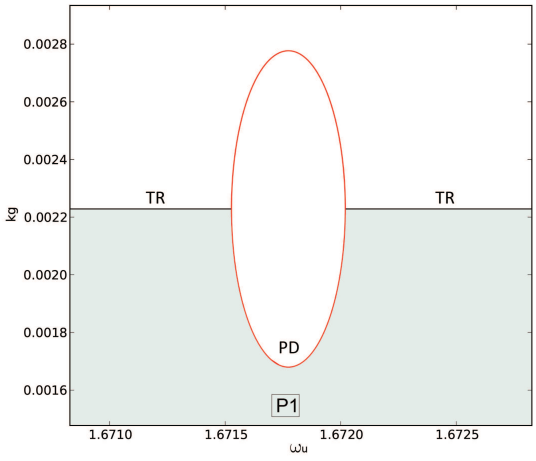

(a)

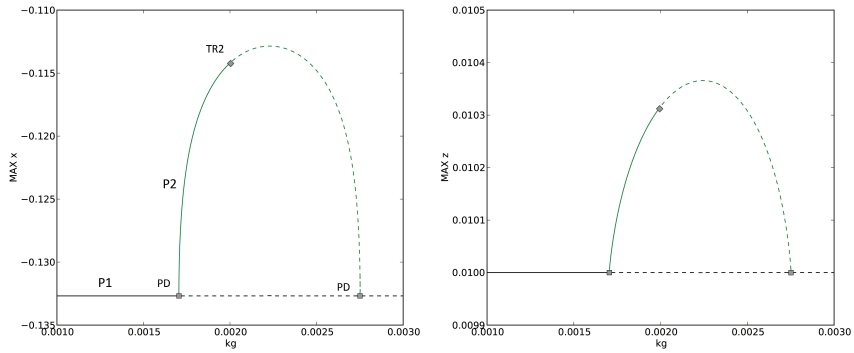

(b) (c)

Figure 8.26: Behavior chart in the $\omega_u - k_g$ plane around principal resonance for $U = 0.0001$ (a) and bifurcation diagrams at $\omega_u = 1.6717$ with respect to x variable(b) and z variable (c)

resonance region under consideration, which is characterized by the presence of period doubled responses and represents the main resonance region for a system under parametric excitation, as evident by the significantly increased loop size with respect to what obtained at $\omega_u = \omega_1$ (the period doubling threshold spans a k_g range of 1.2×10^{-3} and a ω_u range of 5×10^{-4}, while the trancritical locus exists for a k_g range of about 5×10^{-4} and for a ω_u range of about 1×10^{-4}). Finally, as for the other cases previously analyzed, the bifurcation diagram with respect to the control variable z (figure 8.26(c)) highlights the failure of the feedback control for all the solutions which are typical of the controlled system while absent in the uncontrolled one.

Still focusing around the principal resonance, analysis of the system behavior in the $\boldsymbol{k_g}$-$\boldsymbol{U}$ **plane** reported in figure 8.27 points out another feature different from what obtained in the fundamental resonance range. In the former case, in fact, escape from the stability region as function of the feedback control parameter k_g was due to the disappearance of the torus curve responsible for the instabilization of the P1 solution; around $\omega_u = 2\omega_1$, on the contrary, stability of P1 solution results to be independent of k_g since the SbPD escape threshold is not modified by the control increase. Nevertheless, around $k_g = 0.0022$ a torus bifurcation leads to the sudden annihilation of the stable P1 solution and consequently to the stability loss of the controlled system. This time the transition from stability to instability is not consequence of smooth changes in system responses, but it has to be attributed to the end of the equilibrium stability for the system (note that for $U = 0.0001$ the torus threshold appears at $k_g = 0.00223$, the same value obtained studying the equilibrium stability in Sect. 6.2), and thus to an intrinsic characteristic of the system.

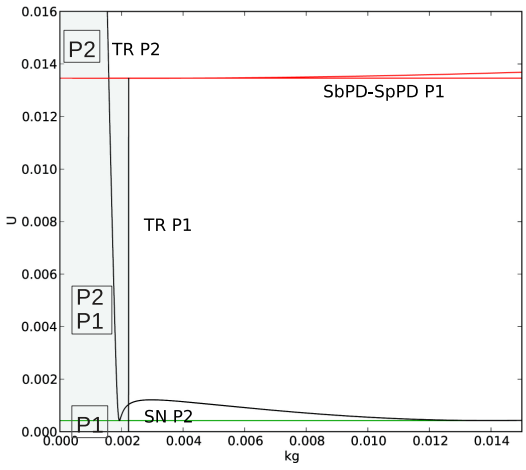

(a)

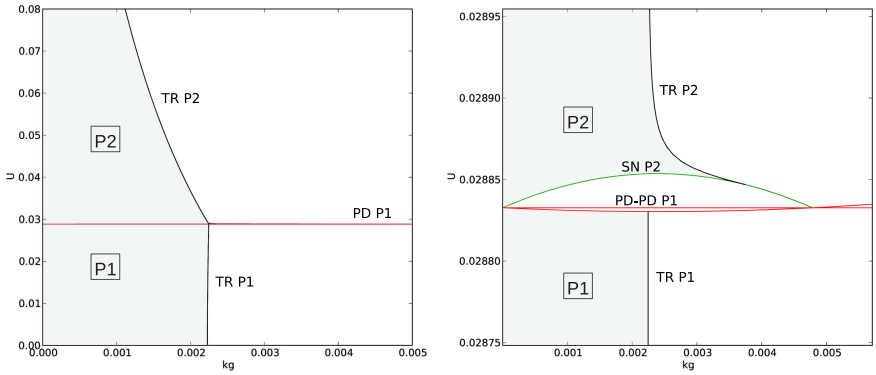

(b)

Figure 8.27: Behavior chart in the k_g-U plane around principal resonance for $\omega_u = 1.64$ (a) and $\omega_u = 1.75$ (b)

8.2 Controlled AFM system under external excitation

The analysis of the strongly nonlinear dynamics for the controlled system is completed by a summary of the outcomes obtained studying the case of sole vertical excitation, and with the parameter values (8.2). The problem is governed by the following equation:

$$\begin{aligned} \ddot{x} + \alpha_1 x + \alpha_3 x^3 = & -\frac{\Gamma_1}{\left(1 + x + V_g + z - z_s\right)^2} - \rho_1 \dot{x} \\ & - \left(\ddot{V}_g + k_g \left(\dot{x}_{ref} - \dot{x}\right) + \nu_1 \left(\dot{V}_g + k_g \left(x_{ref} - x\right)\right)\right) \nu_2 \\ \dot{z} = & \, k_g \left(x_{ref} - x\right) \end{aligned} \tag{8.3}$$

with $V_g = V \sin(\omega_v t)$ and the presented results allow one to underline similarities and differences with respect to both the uncontrolled problem and the parametrically forced system with feedback control. For what concern the system behavior as a function of the forcing amplitude V, figure 8.28 shows the bifurcation behavior in the whole range of frequencies considered previously, while charts reported in figures 8.29-8.30 focus around primary and subharmonic resonance regions.

The charts highlight that in general the vertically forced system has the same behavior of the horizontally forced one, with the maintenance of the local bifurcation thresholds present in the uncontrolled case, while new thresholds of torus and transcritical bifurcations contribute to reduce the stability region for the system. Nevertheless, some distinctions can be pointed out: around primary resonance (figure 8.29), as for the parametrically forced case (8.5(b)), the P1L solution loses stability through a torus bifurcation (TRL) which happens before the original saddle-node (SNL), while P1H solution becomes stable via a transcritical bifurcation (TH). However, the latter bifurcation occurs for amplitude values significantly higher than in the parametrically forced case, so that the presence of both the P1 solutions at the same frequency is limited to a narrow range around the triangle vertex at $\omega_v = 0.82$, and anyway without regions of coexistence, as in the horizontal case. After that, the system exhibits only one P1 solution, which disappears through a period doubling, as in the uncontrolled case (see figure 3.20). The transcritical threshold which in the case of horizontal forcing was responsible

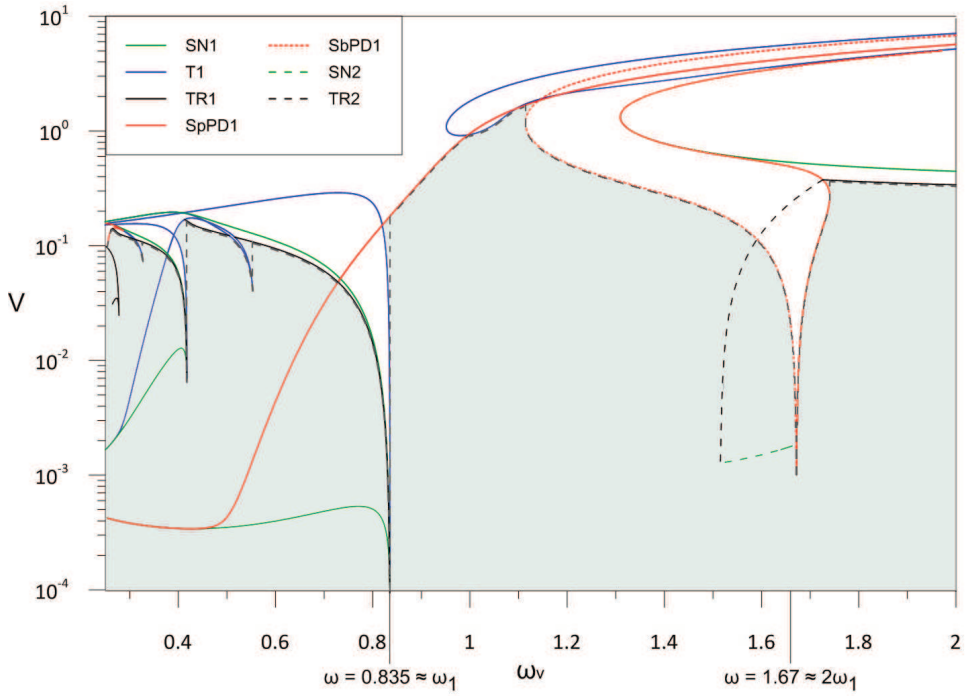

Figure 8.28: Local bifurcations map and overall escape threshold in the frequency-amplitude plane of external excitation, for $k_g = 0.001$. Gray area: region of stable reference response of the controlled system; dotted gray line: overall escape boundary; SN1: saddle-node bifurcation of P1 solution; T1: trascritical bifurcation of P1 solution; TR1: torus bifurcation of P1 solution; SpPD1: supercritical period doubling of P1 solution; SbPD1: subcritical period doubling of P1 bifurcation; SN2: saddle-node of P2 solution; TR2: torus bifurcation of P2 solution

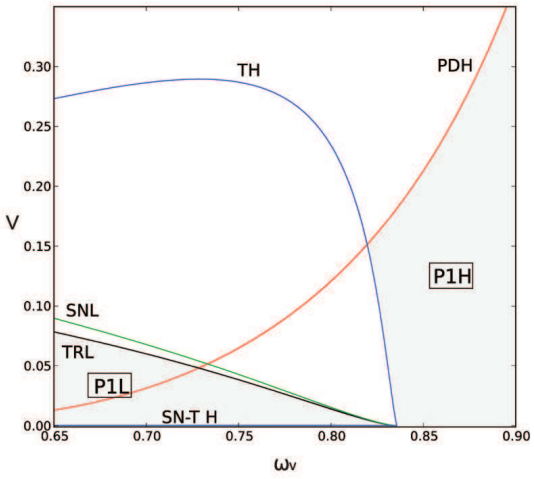

Figure 8.29: Behavior chart in the ω_v-V plane around primary resonance

for the system instability, in fact, is here shifted to high-amplitude values, and becomes escape boundary only for frequencies around $\omega_v = 1.1$.

Around subharmonic resonance in figure 8.30, the same thresholds of the uncontrolled case (see figure 3.21) can be found again, together with the reverse supercritical period doublings (RevPDP1 and RevPDP2) which confined the region of in-well instability. With the control introduction, however, the original P2 solution remains unstable as the amplitude increases, and the subcritical period doubling threshold of the P1 solution (SubPDP1) marks the stability boundary for all the properly controlled solutions. Also in the vertically forced system, as in the parametrically forced case, the presence of the disconnected P2 solution can be detected, with the associated curves of saddle-node (SNP2) and torus (TRP2) which sign its birth and death (figure 8.30(b)). Differently from what happened in the parametric case, however, the torus threshold exists also after the disappearance of the P2 solution at a frequency of about 1.74, but here pertains to the P1 solution and becomes the bifurcation event responsible for the escape from stability region in the highest frequency range, instead of the saddle-node SNP1.

Finally, the system behavior analysis as a function of the feedback control parameter k_g points out that also the vertically forced system loses stability via a torus bifurcation at a value of $k_g \cong 0.00223$ in the whole frequency range, with the exception of a loop of transcritical bifurcation around primary resonance and of a loop of period doubling bifurcation around sub-

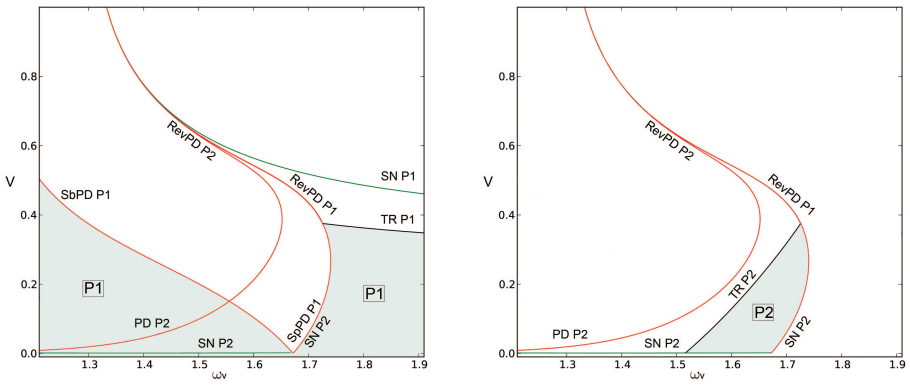

(a) (b)

Figure 8.30: Behavior charts in the ω_v-V plane around subharmonic resonance with detection of stability regions for P1 solution (a) and P2 solution (b)

harmonic resonance, as reported in figures 8.31(a)-8.31(b) and as already discussed for the parametric case (see figures 8.11(a), 8.26(a)). For the system under external excitation, however, the phase locking phenomenon is stronger around $\omega_v = \omega_1$ and involves a quite larger range of frequencies with respect to what happens at $\omega_v = 2\omega_1$. This is due to the fact that the externally forced system has its main resonance at the system natural frequency, while the parametric one at twice natural frequency.

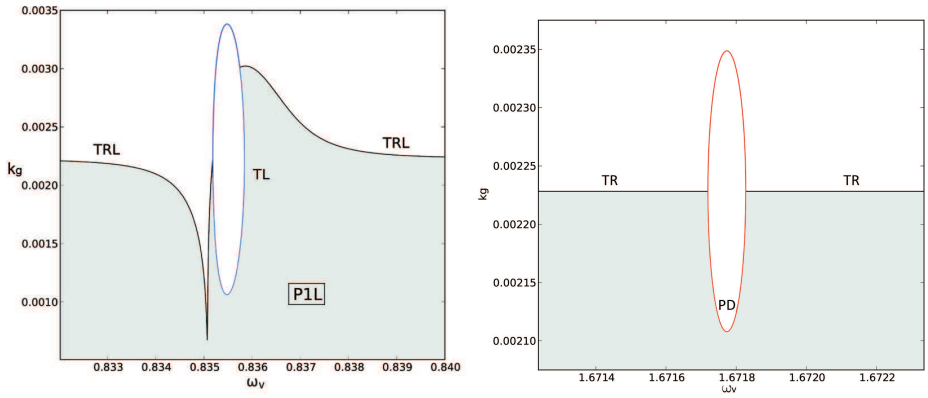

(a) (b)

Figure 8.31: Behavior chart in the ω_v-k_g plane around primary resonance (a) and around subharmonic resonance (b) for $V = 0.0001$

As a final remark, it is worth noting that the results reported in figure 8.31(a) are qualitalively similar to those presented by Yagasaki in [124], obtained from a simple model of tapping AFM subject to the same external feedback control technique and operating in the noncontact region. Figure 10 of [124], in fact, shows the stability thresholds of the externally forced system around primary resonance, with the detection of the resonance loop of transcritical bifurcation which breaks the Hopf bifurcation threshold of the main periodic orbit. Besides confirming the goodness of the obtained results, this comparison allows one to reasonably assume that the described behavior is typical of AFM systems under the presented kind of feedback control.

8.3 Stability regions with/without control

To summarize the results obtained in the previous sections concerning the controlled system, and in view of easily comparing them with what already presented for the uncontrolled system, two behavior charts in the frequency-amplitude plane are shown for both the cases of parametric and external excitations. Figures 8.32-8.33 show the overall escape thresholds of the two systems (controlled/uncontrolled) together with the detection of the corresponding stability regions, and they clearly highlight the effect of the external feedback control in reducing the dynamical stability of the system, mostly around the main resonance frequencies, i.e. ω_1, $2\omega_1$ and $\omega_1/2$.

In the close neighborhood of these values, in fact, the feedback control causes the onset of instability tongues which dramatically decrease the escape value of the forcing amplitude, with reductions of about 99,9% around the fundamental (primary) resonance, of 99,4% around the principal (subharmonic) resonance and of about 94% around the superharmonic resonance frequency. This effect can be explained, as previously mentioned, with the fact that the close proximity to the resonance frequencies leads to a substantial increase of the response amplitude of the resonant periodic solutions, that the feedback control is unable to dominate. In these regions, therefore, the escape threshold of the controlled system is governed by the nonresonant responses, which become unstable for considerably lower values of the forcing amplitude. Furthermore, the escape threshold minima of the controlled system are shifted at frequency values related to the system natural frequency ω_1 (i.e. $\omega_1/2$, ω_1, $2\omega_1$), since the nonresonant periodic solutions are not affected by the softening effect of the nonlinear resonance (as, in contrast, happened for the resonant solutions which govern the escape profile of the uncontrolled system). It is important to remember also that for the controlled system the stability region does not coincide with all the stable periodic responses, but includes only those on which the control works properly, thus causing an additional reduction of the forcing amplitude values to be taken into account. This is evident particularly around the $2\omega_1$ frequency, where the escape boundary of the uncontrolled system is governed by the 2-period response which represents the main periodic solution for the whole range of high frequency values (see figures 3.1 and 3.20 for details about the escape local bifurcations).

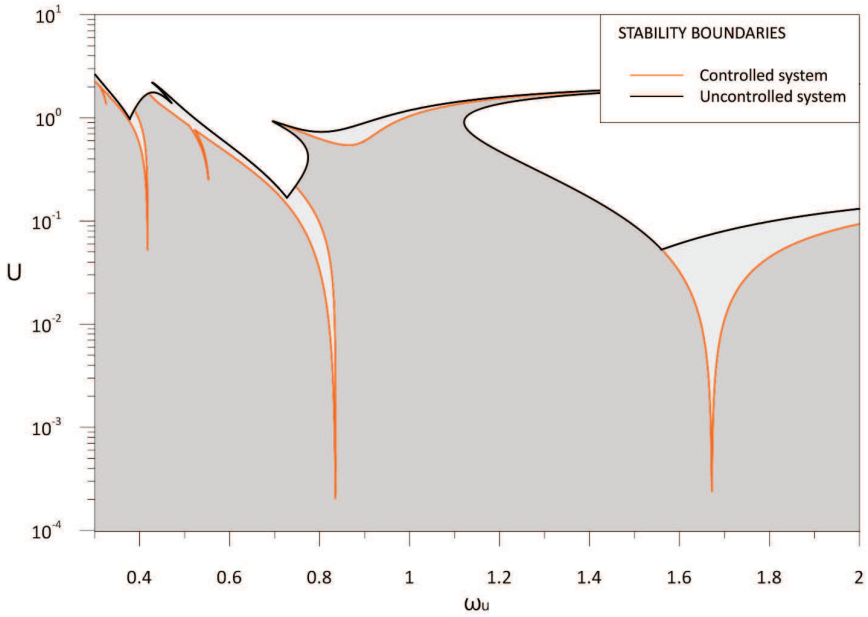

Figure 8.32: Behavior chart in the ω_u-U plane with detection of the overall escape thresholds for the controlled (orange line) and uncontrolled (black line) systems under parametric excitation. Dark gray area represents the stability region of the controlled and uncontrolled systems, light gray area represents the stability region of the sole uncontrolled system

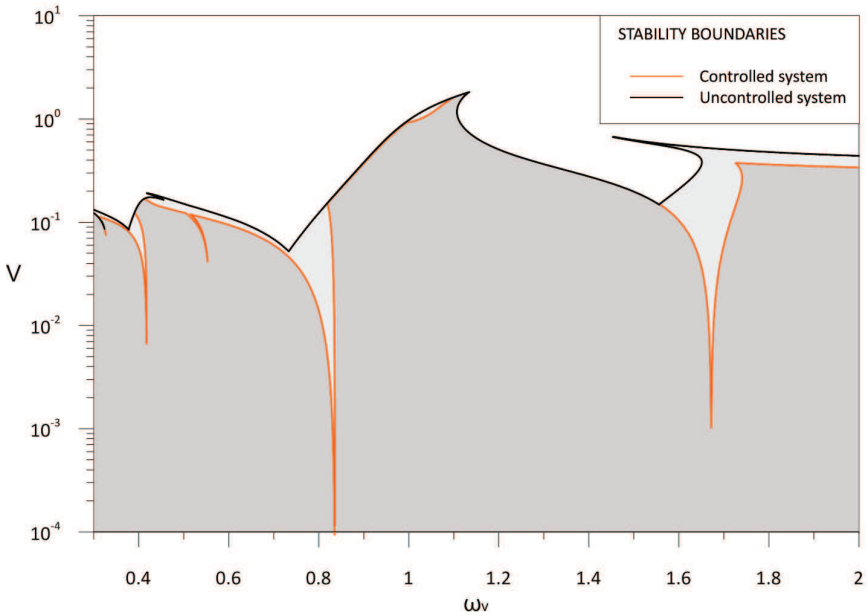

Figure 8.33: Behavior chart in the ω_v-V plane with detection of the overall escape thresholds for the controlled (orange line) and uncontrolled (black line) systems under external excitation. Dark gray area represents the stability region of the controlled and uncontrolled systems, light gray area represents the stability region of the sole uncontrolled system

Conversely, such solution cannot be considered acceptable in the controlled system, whose stability threshold settles onto the lower amplitudes values of the escape bifurcations of the 1-period solution (figures 8.1 and 8.28).

Finally, it is worth noting that the above-mentioned features are equally present both in the parametrically forced system and in the externally forced one. Furthermore, the qualitative behavior of the escape threshold is not modified by the control activation, and therefore maintains the typical features of systems under parametric (external) excitations already analyzed in the previous chapters, with V-shaped profiles around resonance regions and the absolute minimum at principal (primary) resonance, thus demonstrating that the applied control acts on the system irrespective of the forcing type.

Some concluding remarks are in order as regards the actual effectiveness of the considered control procedure. As shown in Chapter 7, it works well for the "local" purpose for which it is specifically designed, i.e. solely keeping the system dynamics to a specific 1-period response, assuming of course that this is the one actually guaranteeing reliable AFM operations. Accordingly, the control procedure cannot be discredited by the observed "globally" unfavorable effects, though they are very important in the overall system dynamics. Indeed, to possibly affect the strongly nonlinear global dynamics in a favorable way, a control procedure specifically aimed at modifying some relevant bifurcation event should be implemented as, e.g., the one controlling homoclinic bifurcations of the hilltop saddle recently shown able to increase the escape threshold for a number of dynamical systems of interest in mechanics (see, e.g., [62]). Yet, while being of no concern that a local control procedure leaves substantially unchanged the escape threshold, or even reduces it slightly, it is definitely of major concern that it strongly reduces the escape thereshold when the system works at resonance conditions, as it may happen in unexpected practical situations. As to the second issue, i.e. the occurrence of a further decrease of stability boundary at principal (subharmonic) resonance, this is actually of lower concern since, of course, control should be designed to keep the response to the dominant 2-period one where this is needed and where it plays the major response role up to the strongly nonlinear dynamic regime.

Chapter 9

Conclusions

Global dynamics of a single-mode model of noncontact AFM have been investigated with specific focus on the system dynamical response under variation of its most important parameters. Extended numerical analyses have been carried out considering the horizontal scan excitation and the vertical one separately. The obtained results have allowed to construct several bifurcation diagrams and to determine the system escape threshold in the excitation parameter space as the envelope of local bifurcation escape boundaries in a large range of forcing frequencies, which includes the primary and subharmonic resonances.

The outcomes around resonance frequencies highlight that the system has the same qualitative behavior of a number of softening oscillators, especially for what concerns the V-shaped region of escape, its limiting boundaries and the underlying triangle region with coexisting solutions. Furthermore, the system response under the two different kinds of excitation exhibits the expected position of minimum escape amplitude value, which occurs at primary (principal) resonance frequency for the external (parametrical) excitation case.

The obtained escape excitation amplitudes, corresponding to safe basin annihilation, have been then compared with those obtained via numerical integration of the system equations with fixed initial conditions, which correspond to solution divergence. By conducting a comprehensive analysis of basins of attraction evolution and by evaluating different integrity measures (GIM and IF), several erosion profiles have been obtained as a function of the increasing excitation amplitude. This kind of analysis has furnished

residual integrity levels associated with the system global dynamics. The results highlight a marked variability with respect to the stability boundary obtained via numerical integration and, mostly, a meaningful lack of homogeneous safety of the latter, as regards robustness of periodic solutions, in the excitation parameter space. In contrast, the analysis of basins of attraction evolution in state space and the construction of erosion profiles allow to detect thresholds of residual integrity able to ensure acceptable safety targets established a priori according to the required system performances.

Starting from the analyzed model, an external feedback control has been introduced with the aim of avoiding possible unstable motions of the system; the control works by keeping the cantilever vibration to the reference one which corresponds to the response obtained from the uncontrolled system with the same set of parameter values. The equilibrium stability analysis of the controlled system highlights that the control implementation does not affect the existence of equilibriun states but acts upon its stability by substantially reducing the stable range. This behavior can also be observed in the strongly nonlinear dynamical analysis, which has been systematically carried out both for the parametrically forced system and for the externally forced one. Due to the increased number of dofs, the results show a richer bifurcation scenario, characterized by the new presence of torus and transcritical bifurcations which affect the main system periodic responses and are responsible for the stability boundary reduction. Moreover, such local bifurcations lead to the onset of quasiperiodic and new periodic solutions which are absent in the uncontrolled system and for which thus the control fails to reproduce the reference response. Therefore, the escape threshold for the controlled system is no longer coincident with the limit of existence of all stable bounded solutions, but becomes dependent on the actual existence of the solutions which are the goal of the control procedure.

The comparison with the results obtained from the uncontrolled system allows one to conclude that the applied control technique works well for the "local" purpose for which it is specifically designed and from a methodological viewpoint represents a simple and efficient procedure of sample surface measurement in AFM. However, it must be supported, for its practical application, by a comprehensive analysis of its effects on the global dynamics of the system, necessary to properly define the parameters operation ranges, or even be accompained by a further control procedure specifically aimed at

modifying some relevant dynamical features of the system.

Appendix A

Integral expressions of the modal dynamical system

The integral expressions in (2.18) are:

$$
\begin{aligned}
I_1 &= \left(I_{11} - \mu I_{12}\right), \quad I_4 = \left(I_{41} - \mu I_{42}\right), \quad I_{11} = \int_0^1 \Phi_1^2 \,\mathrm{d}s = 1, \\
I_{41} &= \int_0^1 \Phi_1 \left(\Phi_{1s} \int_1^s \int_0^s {\Phi_1}_s^2 \,\mathrm{d}s \,\mathrm{d}s\right)_s \mathrm{d}s, \\
&\int_0^1 \Phi_1 \Phi_{1ssss} \,\mathrm{d}s = \omega_1^2 \int_0^1 \Phi_1^2 \,\mathrm{d}s = \omega_1^2 I_{11}, \\
I_{42} &= \int_0^1 \Phi_1 \left({\Phi_1}_s^3\right)_s \,\mathrm{d}s, \\
I_{12} &= \int_0^1 \Phi_1 \Phi_{1ss} \,\mathrm{d}s, \\
I_5 &= \int_0^1 \Phi_1 \left(\Phi_{1s}\left(s-1\right)\right)_s \,\mathrm{d}s = \int_0^1 {\Phi_1}_s^2 \left(1-s\right) \,\mathrm{d}s, \\
I_2 &= \int_0^1 \Phi_1 \,\mathrm{d}s, \\
I_6 &= \int_0^1 \Phi_1 \left({\Phi_1}_s^3 \left(s-1\right)\right)_s \,\mathrm{d}s = \int_0^1 {\Phi_1}_s^4 \left(1-s\right) \,\mathrm{d}s, \\
I_3 &= \int_0^1 \Phi_1 \left(\Phi_{1s}\left(\Phi_{1s}\Phi_{1ss}\right)_s\right)_s \,\mathrm{d}s \\
&= 2\int_0^1 \left(\Phi_{1s}\Phi_{1ss}\right)^2 \,\mathrm{d}s, \\
I_7 &= \int_0^1 \Phi_1 \left(\Phi_{1s} \int_1^s \left(\int_0^s {\Phi_1}_s^2 \,\mathrm{d}s\right)_{ss} \mathrm{d}s\right)_s \mathrm{d}s.
\end{aligned}
\tag{A.1}
$$

Appendix B

Multiple scale analysis of the uncontrolled system

The equations of motions of the uncontrolled system are analyzed around its stable point $\bar{x}_{ref}$, that is $\tilde{x}_{ref} = x - \bar{x}_{ref}$:

$$\begin{aligned}
&\ddot{\tilde{x}}_{ref} = -\frac{1}{(1+\alpha_2(\bar{x}_{ref}+\tilde{x}_{ref})^2)}\left(\alpha_1 + \alpha_2\dot{\tilde{x}}_{ref}^2 + \alpha_3(\bar{x}_{ref}+\tilde{x}_{ref})^2\right) \\
&(\bar{x}_{ref}+\tilde{x}_{ref}) + \frac{\Gamma_1}{(1+\bar{x}_{ref}+\tilde{x}_{ref})^2} \\
&+ \left(\rho_1 + \rho_2(\bar{x}_{ref}+\tilde{x}_{ref})^2\right)\dot{\tilde{x}}_{ref} + \left(\ddot{V}_g + \nu_1\dot{V}_g\right)\nu_2 \\
&- \left(\mu_1(\bar{x}_{ref}+\tilde{x}_{ref}) + \mu_2(\bar{x}_{ref}+\tilde{x}_{ref})^3\right)\left(\ddot{U}_g + \eta_1\dot{U}_g + \eta_2 U_g\right)
\end{aligned} \tag{B.1}$$

with $V_g = V\sin(\omega_v t)$, $U_g = U\sin(\omega_u t + \phi_u)$ The perturbation equations of the uncontrolled system up to the fourth order, with the same choice of variables and parameters scaling used in Sect. 7, are

order ϵ^0 :

$$\Gamma_1 + \bar{x}_{ref}(1+\bar{x}_{ref})^2(\alpha_3\bar{x}_{ref}^2 + \alpha_1) = 0 \tag{B.2a}$$

order ϵ^1 :

$$D_0^2\tilde{x}_{ref1} + \omega_1^2\tilde{x}_{ref1} = 0 \tag{B.2b}$$

order ϵ^2 :

$$\begin{aligned} D_0^2\tilde{x}_{ref2} + \omega_1^2\tilde{x}_{ref2} = &-C_{21}\tilde{x}_{ref1}^2 - C_{22}(D_0\tilde{x}_{ref1})^2 \\ &- 2D_0D_1\tilde{x}_{ref1} - C_{25}\tilde{x}_{ref1}D_0^2\tilde{x}_{ref1} \end{aligned} \tag{B.2c}$$

order ϵ^3 :

$$\begin{aligned} D_0^2\tilde{x}_{ref3} + \omega_1^2\tilde{x}_{ref3} = &-C_{25}\tilde{x}_{ref1}D_0^2\tilde{x}_{ref2} - C_{25}\tilde{x}_{ref2}D_0^2\tilde{x}_{ref1} \\ &- 2D_0D_1\tilde{x}_{ref2} - 2C_{22}D_1\tilde{x}_{ref1}D_0\tilde{x}_{ref1} - 2C_{21}\tilde{x}_{ref1}\tilde{x}_{ref2} \\ &- 2C_{25}\tilde{x}_{ref1}D_0D_1\tilde{x}_{ref1} - 2D_0D_2\tilde{x}_{ref1} - C_{37}\tilde{x}_{ref1}^2D_0^2\tilde{x}_{ref1} \\ &- 2C_{22}D_0\tilde{x}_{ref1}D_0\tilde{x}_{ref2} - C_{33}(D_0\tilde{x}_{ref1})^2\tilde{x}_{ref1} - C_{35}D_0\tilde{x}_{ref1} \\ &- D_1^2\tilde{x}_{ref1} - C_{36}\tilde{x}_{ref1}^3 - C_{cu}\cos(\omega_1T_0 + \sigma_uT_2 + \phi_u) \\ &- C_{sv}\sin(\omega_1T_0 + \sigma_vT_2) - C_{su}\sin(\omega_1T_0 + \sigma_uT_2 + \phi_u) \end{aligned} \tag{B.2d}$$

order ϵ^4 :

$$\begin{aligned} D_0^2\tilde{x}_{ref4} + \omega_1^2\tilde{x}_{ref4} = &-2C_{21}\tilde{x}_{ref3}\tilde{x}_{ref1} - C_{21}\tilde{x}_{ref2}^2 - C_{22}D_1^2\tilde{x}_{ref1}^2 \\ &- 2C_{22}D_0D_2\tilde{x}_{ref1}^2 - 4C_{22}D_0D_1\tilde{x}_{ref2}\tilde{x}_{ref1} - 2C_{22}D_0^2\tilde{x}_{ref3}\tilde{x}_{ref1} \\ &- C_{22}D_0^2\tilde{x}_{ref2}^2 - C_{25}D_1^2\tilde{x}_{ref1}^2 - 2C_{25}D_0D_2\tilde{x}_{ref1}^2 \\ &- 4C_{25}D_0D_1\tilde{x}_{ref2}\tilde{x}_{ref1} - 2C_{25}D_0^2\tilde{x}_{ref3}\tilde{x}_{ref1} - C_{25}D_0^2\tilde{x}_{ref2}^2 \\ &- 2C_{33}D_0D_1\tilde{x}_{ref1}^3 - 3C_{33}D_0^2\tilde{x}_{ref2}\tilde{x}_{ref1}^2 - C_{35}D_1\tilde{x}_{ref1} \\ &- C_{35}D_0\tilde{x}_{ref2} - 3C_{36}\tilde{x}_{ref2}\tilde{x}_{ref1}^2 - 2C_{37}D_0D_1\tilde{x}_{ref1}^3 \\ &- 3C_{37}D_0^2\tilde{x}_{ref2}\tilde{x}_{ref1}^2 - C_{400}\tilde{x}_{ref1}^4 - C_{405}D_0\tilde{x}_{ref1}^2 \\ &- C_{406}D_0^2\tilde{x}_{ref1}^4 - C_{407}D_0^2\tilde{x}_{ref1}^4 - 2D_1D_2\tilde{x}_{ref1} \\ &- 2D_0D_3\tilde{x}_{ref1} - D_1^2\tilde{x}_{ref2} - 2D_0D_2\tilde{x}_{ref2} - 2D_0D_1\tilde{x}_{ref3} \\ &- C_{cuu}\tilde{x}_{ref1}\cos(\omega_1T_0 + \sigma_uT_2 + \phi_u) \\ &- C_{suu}\tilde{x}_{ref1}\sin(\omega_1T_0 + \sigma_uT_2 + \phi_u) \\ &- \left(C_{svv}\tilde{x}_{ref1} + C_{svvv}D_0^2\tilde{x}_{ref1}\right)\sin(\omega_1T_0 + \sigma_vT_2) \end{aligned} \tag{B.2e}$$

The ϵ^0 order reports the equilibrium equation, while the homogenous equation at the first order has solution

$$\tilde{x}_{ref1} = A_{un}(T_1, T_2, T_3)e^{i\omega_1 T_0} + c.c. \tag{B.3}$$

Substitution of (B.3) into (B.2c), yields

$$\begin{aligned} D_0^2\tilde{x}_{ref2} + \omega_1^2\tilde{x}_{ref2} = &-2C_{214}A_{un}\bar{A}_{un} - C_{211}A_{un}^2 e^{2i\omega_1 T_0} \\ &- 2i\omega_1 D_1 A_{un} e^{i\omega_1 T_0} + c.c. \end{aligned} \tag{B.4}$$

The solvability condition requires that

$$D_1 A_{un} = 0 \quad \text{thus} \quad A_{un} = A_{un}(T_2, T_3) \tag{B.5}$$

and the particular solution at this order is

$$\tilde{x}_{ref2} = \frac{C_{211}}{3\omega_1^2}A_{un}^2 e^{2i\omega_1 T_0} - \frac{2C_{214}}{\omega_1^2}A_{un}\bar{A}_{un} + c.c. \tag{B.6}$$

At the third order, by means of equations (B.3) and (B.6), the perturbation equation results

$$\begin{aligned} D_0^2\tilde{x}_{ref3} + \omega_1^2\tilde{x}_{ref3} = &-\gamma_{31un}e^{i\omega_1 T_0} - \gamma_{32un}e^{2i\omega_1 T_0} \\ &- \gamma_{33un}e^{3i\omega_1 T_0} + \gamma_{37}\bar{A}_{un}D_1 A_{un} + c.c. \end{aligned} \tag{B.7}$$

where

$$\begin{aligned} \gamma_{31un} = &- D_2 A_{un} - \frac{C_{35}}{2}A_{un} + i\frac{C_{301}}{2\omega_1}\left(A_{un}^2\bar{A}_{un}\right) - \frac{D_1^2 A_{un}}{2i\omega_1} \\ &+ \frac{C_{sv}}{4\omega_1}e^{i\sigma_v T_2} + \frac{C_{su}}{4\omega_1}e^{i(\sigma_u T_2 + \phi_u)} + i\frac{C_{cu}}{4\omega_1}e^{i(\sigma_u T_2 + \phi_u)} \\ \gamma_{32un} = &C_{321}A_{un}D_1 A_{un} \\ \gamma_{33un} = &8C_{303}\omega_1^2 A_{un}^3 \end{aligned}$$

The secular terms elimination implies that

$$\begin{aligned} D_2 A_{un} = &-\frac{C_{35}}{2}A_{un} + i\frac{C_{301}}{2\omega_1}\left(A_{un}^2\bar{A}_{un}\right) \\ &+ \frac{C_{sv}}{4\omega_1}e^{i\sigma_v T_2} + \frac{C_{su}}{4\omega_1}e^{i(\sigma_u T_2 + \phi_u)} + i\frac{C_{cu}}{4\omega_1}e^{i(\sigma_u T_2 + \phi_u)} \end{aligned} \tag{B.8}$$

The particular solution at the third order is

$$\tilde{x}_{ref3} = C_{303} A_{un}^3 e^{3i\omega_1 T_0} + c.c. \tag{B.9}$$

The obtained results allow one to express the fourth order perturbation equation as

$$\begin{aligned} D_0^2 \tilde{x}_{ref4} + \omega_1^2 \tilde{x}_{ref4} = & - \gamma_{41un} e^{i\omega_1 T_0} - \gamma_{42un} e^{2i\omega_1 T_0} - \gamma_{43un} e^{3i\omega_1 T_0} \\ & - \gamma_{44un} e^{4i\omega_1 T_0} - \gamma_{47} A_{un}^2 \bar{A}_{un}^2 - \gamma_{54} A_{un} e^{-i\sigma_v T_2} \\ & - \gamma_{52} A_{un} e^{-i\sigma_u T_2 - i\phi_u} - \gamma_{56} D_2 A_{un} \bar{A}_{un} \\ & - \gamma_{57} \bar{A}_{un} D_1^2 A_{un} - \gamma_{50} D_1 A_{un} D_1 \bar{A}_{un} + c.c. \end{aligned} \tag{B.10}$$

where

$$\begin{aligned} \gamma_{41un} =& 2i\omega_1 D_3 A_{un} + C_{35} D_1 A_{un} + \gamma_{430} D_1 A_{un} A_{un} \bar{A}_{un} + \gamma_{429} A^2 D_1 \bar{A}_{un} \\ \gamma_{42un} =& \gamma_{410} A_{un}^3 \bar{A}_{un} + \gamma_{414un} A_{un}^2 + \gamma_{421} A_{un} D_1^2 A_{un} + \gamma_{420} A_{un} D_2 A_{un} \\ & + \gamma_{415} A_{un} e^{i\sigma_u T_2 + i\phi_u} + \gamma_{416} A_{un} e^{i\sigma_v T_2} + \gamma_{418} D_1 A_{un}^2 \\ \gamma_{43un} =& C_{424} A_{un}^2 D_1 A_{un} \\ \gamma_{44un} =& C_{425} A_{un}^4 \\ \gamma_{414un} =& \frac{2i C_{211} C_{35}}{3\omega_1} + i C_{405} \omega_1 \end{aligned}$$

The solvability condition requires that $\gamma_{41un} = 0$ and since $\gamma_{41un} = f(D_1 A_{un})$, from (B.5) it results

$$D_3 A_{un} = 0 \tag{B.11}$$

According to the usual reconstitution procedure [79], the amplitudes derivatives with respect to time t are obtained from (7.3) of Sect. 7

$$\dot{A}_{un} = \epsilon D_1 A_{un} + \epsilon^2 D_2 A_{un} + \epsilon^3 D_3 A_{un} \tag{B.12}$$

in which $D_1 A_{un}, D_2 A_{un}, D_3 A_{un}$ are defined in (B.5), (B.8) and (B.11). Finally, considering that $C_{35}, C_{405} = f(\hat{\rho}_1, \hat{\rho}_2)$, $C_{cu}, C_{su}, C_{cuu}, C_{suu} = f(\hat{U})$, $C_{sv}, C_{svv}, C_{svvv} = f(\hat{V})$, the ϵ parameter is completely reabsorbed through

the backward rescaling

$$\begin{aligned}
&\epsilon A_{un} \to A_{un}, \quad \epsilon^2 C_{35} \to C_{35}, \quad \epsilon^2 C_{405} \to C_{405},\\
&\epsilon^3 C_{cu} \to C_{cu}, \quad \epsilon^3 C_{su} \to C_{su}, \quad \epsilon^3 C_{cuu} \to C_{cuu},\\
&\epsilon^3 C_{suu} \to C_{suu}, \quad \epsilon^3 C_{sv} \to C_{sv}, \quad \epsilon^3 C_{svv} \to C_{svv},\\
&\epsilon^3 C_{svvv} \to C_{svvv}, \quad \epsilon^2 \sigma_u \to \sigma_u, \quad \epsilon^2 \sigma_v \to \sigma_v.
\end{aligned} \tag{B.13}$$

The obtained complex modulation equation (or bifurcation equation) is

$$\begin{aligned}
\dot{A}_{un} = &-\frac{C_{35}}{2} A_{un} + \frac{C_{sv}}{4\omega_1}\cos(\sigma_v t)\\
&+ \frac{C_{su}}{4\omega_1}\cos(\sigma_u t + \phi_u) - \frac{C_{cu}}{4\omega_1}\sin(\sigma_u t + \phi_u)\\
&+ i\left(\frac{C_{301}}{2\omega_1} A_{un}^2 \bar{A}_{un} + \frac{C_{sv}}{4\omega_1}\sin(\sigma_v t)\right.\\
&\left.+\frac{C_{su}}{4\omega_1}\sin(\sigma_u t + \phi_u) + \frac{C_{cu}}{4\omega_1}\cos(\sigma_u t + \phi_u)\right)
\end{aligned} \tag{B.14}$$

To express equation (B.14) in the Cartesian coordinates, it has to be transformed in an autonomous system, so that the horizontally forced system (U_g) and the vertically forced one (U_g) have to be considered separately. Here, the system under horizontal parametric excitation is analyzed, i.e. $V_g = 0$. Equation (B.14) in exponential form hence becomes

$$\begin{aligned}
\dot{A}_{un} = &-\frac{C_{35}}{2} A_{un} + \frac{C_{su}}{4\omega_1} e^{i\sigma_u t + i\phi_u}\\
&+ i\left(\frac{C_{301}}{2\omega_1} A_{un}^2 \bar{A}_{un} + \frac{C_{cu}}{4\omega_1} e^{i\sigma_u t + i\phi_u}\right)
\end{aligned} \tag{B.15}$$

Pre-multiplication of both sides of (B.15) by $e^{-i\sigma_u t - i\phi_u}$, and transformation of variables as follows

$$G_{un} = A_{un} e^{-i\phi_u - (\Omega_u - 1)\omega_1 t}, \quad \bar{G}_{un} = \bar{A}_{un} e^{-i\phi_u - (\Omega_u - 1)\omega_1 t}, \quad \sigma_u = (\Omega_u - 1)\,\omega_1$$

yields

$$\begin{aligned}
\dot{G}_{un} = &-\frac{C_{35}}{2} G_{un} + \frac{C_{su}}{4\omega_1}\\
&+ i\left(\frac{C_{301}}{2\omega_1} G_{un}^2 \bar{G}_{un} + \frac{C_{cu}}{4\omega_1} + \omega_1 G_{un}(1 - \Omega_u)\right)
\end{aligned} \tag{B.16}$$

Finally, using the following coordinates transformations

$$G_{un} = \frac{1}{2}(j_{un}(t) + i\, n_{un}(t)), \quad \bar{G}_{un} = \frac{1}{2}(j_{un}(t) - i\, n_{un}(t))$$

system (B.16) results

$$\begin{aligned}
\dot{j}_{un}(t) = &+ \frac{C_{su}}{4\omega_1} - \frac{C_{35}}{4} j_{un}(t) - \frac{C_{301}}{16\omega_1}\left(j_{un}(t)^2 n_{un}(t) + n_{un}(t)^3\right) \\
&+ \frac{\omega_1}{2} n_{un}(t)\,(\Omega_u - 1) \\
\dot{n}_{un}(t) = &+ \frac{C_{cu}}{4\omega_1} - \frac{C_{35}}{4} n_{un}(t) + \frac{C_{301}}{16\omega_1}\left(n_{un}(t)^2 j_{un}(t) + j_{un}(t)^3\right) \\
&- \frac{\omega_1}{2} j_{un}(t)\,(\Omega_u - 1)
\end{aligned} \tag{B.17}$$

Expressions of the introduced coefficients not defined here are reported in Appendix C.

Appendix C

Expressions of the Multiple Scale analysis coefficients

C.1 Expressions of N_{ij} terms in the order equations

Terms of order (ϵ^2) equations (7.6c):

$$N_{21} = -C_{21}y_1^2 - C_{22}(D_0y_1)^2 - 2D_0D_1y_1 - C_{25}y_1D_0^2y_1$$
$$N_{22} = -C_{21}\tilde{x}_{ref1}^2 - C_{25}(D_0\tilde{x}_{ref1})^2 - 2D_0D_1\tilde{x}_{ref1} - C_{25}\tilde{x}_{ref1}D_0^2\tilde{x}_{ref1}$$
$$N_{23} = -C_{26}p_1^2$$
$$N_{24} = -2C_{22}D_0y_1D_0\tilde{x}_{ref1} - C_{25}\tilde{x}_{ref1}D_0^2y_1 - C_{25}y_1D_0^2\tilde{x}_{ref1} - 2C_{21}\tilde{x}_{ref1}y_1$$
$$N_{25} = -C_{23}p_1D_0^2y_1 - C_{24}p_1y_1$$
$$N_{26} = -C_{23}p_1D_0^2\tilde{x}_{ref1} - C_{24}p_1\tilde{x}_{ref1}$$

Terms of order (ϵ^3) equations (7.6d):

$$
\begin{aligned}
N_{31} = &- C_{25}y_1D_0^2y_2 - C_{25}y_2D_0^2y_1 \\
&- 2D_0D_1y_2 - 2C_{22}D_1y_1D_0y_1 - 2C_{21}y_1y_2 \\
&- 2C_{25}y_1D_0D_1y_1 - 2D_0D_2y_1 - C_{37}y_1^2D_0^2y_1 \\
&- 2C_{22}D_0y_1D_0y_2 - C_{33}(D_0y_1)^2y_1 - C_{35}D_0y_1 \\
&- D_1^2y_1 - C_{36}y_1^3 \\
N_{32} = &- C_{25}\tilde{x}_{ref1}D_0^2\tilde{x}_{ref2} - C_{25}\tilde{x}_{ref2}D_0^2\tilde{x}_{ref1} \\
&- 2D_0D_1\tilde{x}_{ref2} - 2C_{22}D_1\tilde{x}_{ref1}D_0\tilde{x}_{ref1} - 2C_{21}\tilde{x}_{ref1}\tilde{x}_{ref2} \\
&- 2C_{25}\tilde{x}_{ref1}D_0D_1\tilde{x}_{ref1} - 2D_0D_2\tilde{x}_{ref1} - C_{37}\tilde{x}_{ref1}^2D_0^2\tilde{x}_{ref1} \\
&- 2C_{22}D_0\tilde{x}_{ref1}D_0\tilde{x}_{ref2} - C_{33}(D_0\tilde{x}_{ref1})^2\tilde{x}_{ref1} - C_{35}D_0\tilde{x}_{ref1} \\
&- D_1^2\tilde{x}_{ref1} - C_{36}\tilde{x}_{ref1}^3 \\
N_{33} = &- C_{41}p_1p_2 \\
N_{34} = &- 3C_{36}y_1^2\tilde{x}_{ref1} - C_{36}y_1\tilde{x}_{ref1}^2 \\
&- 2C_{21}y_2\tilde{x}_{ref1} - 2C_{21}y_1\tilde{x}_{ref2} - 2C_{22}D_1\tilde{x}_{ref1}D_0y_1 \\
&- 2C_{22}D_1y_1D_0\tilde{x}_{ref1} - C_{33}\tilde{x}_{ref1}(D_0y_1)^2 - C_{33}y_1(D_0\tilde{x}_{ref1})^2 \\
&- 2C_{33}y_1D_0y_1D_0\tilde{x}_{ref1} - 2C_{33}\tilde{x}_{ref1}D_0y_1D_0\tilde{x}_{ref1} \\
&- 2C_{22}D_0y_2D_0\tilde{x}_{ref1} - 2C_{22}D_0y_1D_0\tilde{x}_{ref2} - 2C_{25}\tilde{x}_{ref1}D_0D_1y_1 \\
&- 2C_{25}y_1D_0D_1\tilde{x}_{ref1} - 2C_{37}y_1\tilde{x}_{ref1}D_0^2y_1 - 2C_{37}y_1\tilde{x}_{ref1}D_0^2\tilde{x}_{ref1} \\
&- C_{37}\tilde{x}_{ref1}^2D_0^2y_1 - C_{37}y_1^2D_0^2\tilde{x}_{ref1} - C_{25}\tilde{x}_{ref2}D_0^2y_1 \\
&- C_{25}\tilde{x}_{ref1}D_0^2y_2 - C_{25}y_2D_0^2\tilde{x}_{ref1} - C_{25}y_1D_0^2\tilde{x}_{ref2} \\
N_{35} = &- C_{43}y_1^2p_1 - C_{48}y_1p_1^2 \\
&- C_{24}y_2p_1 - C_{24}y_1p_2 - C_{42}p_1(D_0y_1)^2 \\
&- 2C_{23}p_1D_0D_1y_1 - C_{30}y_1p_1D_0^2y_1 - C_{49}p_1^2D_0^2y_1 \\
&- C_{23}p_2D_0^2y_1 - C_{23}p_1D_0^2y_2 \\
N_{36} = &- C_{43}\tilde{x}_{ref1}^2p_1 - C_{48}\tilde{x}_{ref1}p_1^2 \\
&- C_{24}\tilde{x}_{ref2}p_1 - C_{24}\tilde{x}_{ref1}p_2 - C_{42}p_1(D_0\tilde{x}_{ref1})^2 \\
&- 2C_{23}p_1D_0D_1\tilde{x}_{ref1} - C_{30}\tilde{x}_{ref1}p_1D_0^2\tilde{x}_{ref1} - C_{49}p_1^2D_0^2\tilde{x}_{ref1} \\
&- C_{23}p_2D_0^2\tilde{x}_{ref1} - C_{23}p_1D_0^2\tilde{x}_{ref2} \\
N_{37} = &- 2C_{43}y_1p_1\tilde{x}_{ref1} - 2C_{42}p_1D_0y_1D_0\tilde{x}_{ref1} \\
&- C_{30}\tilde{x}_{ref1}p_1D_0^2y_1 - C_{30}y_1p_1D_0^2\tilde{x}_{ref1}
\end{aligned}
$$

Terms of order (ϵ^4) equations (7.6e):

$$
\begin{aligned}
N_{41} = &- 2C_{21}y_3y_1 - C_{21}y_2^2 - C_{22}(D_1y_1)^2 - 2C_{22}D_0y_1D_2y_1 \\
&- 2C_{22}D_0y_2D_1y_1 - 2C_{22}D_0y_1D_1y_2 - 2C_{22}D_0y_3D_0y_1 \\
&- C_{22}(D_0y_2)^2 - C_{25}y_1D_1^2y_1 - 2C_{25}y_1D_0D_2y_1 \\
&- 2C_{25}y_1D_0D_1y_2 - 2C_{25}y_2D_0D_1y_1 - C_{25}y_3D_0^2y_1 \\
&- C_{25}y_1D_0^2y_3 - C_{25}y_2D_0^2y_2 \\
&- 2C_{33}y_1D_0y_1D_1y_1 - 3C_{33}y_2(D_0y_1)^2 - C_{35}D_1y_1 \\
&- C_{35}D_0y_2 - 3C_{36}y_2y_1^2 - 2C_{37}y_1^2D_0D_1y_1 \\
&- 2C_{37}y_1y_2D_0^2y_1 - C_{37}y_1^2D_0^2y_2 - C_{400}y_1^4 - C_{405}y_1D_0y_1 \\
&- C_{406}y_1^2(D_0y_1)^2 - C_{407}y_1^3D_0^2y_1 - 2D_1D_2y_1 \\
&- 2D_0D_3y_1 - D_1^2y_2 - 2D_0D_2y_2 - 2D_0D_1y_3 \\
&- C_{cuu}y_1\cos(\omega_1T_0 + \sigma_uT_2 + \phi_u) \\
&- C_{suu}y_1\sin(\omega_1T_0 + \sigma_uT_2 + \phi_u) \\
&- \left(C_{svv}y_1 + C_{svvv}D_0^2y_1\right)\sin(\omega_1T_0 + \sigma_vT_2) \\
N_{42} = &- 2C_{21}\tilde{x}_{ref3}\tilde{x}_{ref1} - C_{21}\tilde{x}_{ref2}^2 - C_{22}(D_1\tilde{x}_{ref1})^2 \\
&- 2C_{22}D_0\tilde{x}_{ref1}D_2\tilde{x}_{ref1} - 2C_{22}D_0\tilde{x}_{ref2}D_1\tilde{x}_{ref1} \\
&- 2C_{22}D_0\tilde{x}_{ref1}D_1\tilde{x}_{ref2} - 2C_{22}D_0\tilde{x}_{ref3}D_0\tilde{x}_{ref1} \\
&- C_{22}(D_0\tilde{x}_{ref2})^2 - C_{25}\tilde{x}_{ref1}D_1^2\tilde{x}_{ref1} - 2C_{25}\tilde{x}_{ref1}D_0D_2\tilde{x}_{ref1} \\
&- 2C_{25}\tilde{x}_{ref1}D_0D_1\tilde{x}_{ref2} - 2C_{25}\tilde{x}_{ref2}D_0D_1\tilde{x}_{ref1} \\
&- C_{25}\tilde{x}_{ref3}D_0^2\tilde{x}_{ref1} - C_{25}\tilde{x}_{ref1}D_0^2\tilde{x}_{ref3} \\
&- C_{25}\tilde{x}_{ref2}D_0^2\tilde{x}_{ref2} - 2C_{33}\tilde{x}_{ref1}D_0\tilde{x}_{ref1}D_1\tilde{x}_{ref1} \\
&- 3C_{33}\tilde{x}_{ref2}(D_0\tilde{x}_{ref1})^2 - C_{35}D_1\tilde{x}_{ref1} - C_{35}D_0\tilde{x}_{ref2} \\
&- 3C_{36}\tilde{x}_{ref2}\tilde{x}_{ref1}^2 - 2C_{37}\tilde{x}_{ref1}^2D_0D_1\tilde{x}_{ref1} \\
&- 2C_{37}\tilde{x}_{ref1}\tilde{x}_{ref2}D_0^2\tilde{x}_{ref1} - C_{37}\tilde{x}_{ref1}^2D_0^2\tilde{x}_{ref2} \\
&- C_{400}\tilde{x}_{ref1}^4 - C_{405}\tilde{x}_{ref1}D_0\tilde{x}_{ref1} - C_{406}\tilde{x}_{ref1}^2(D_0\tilde{x}_{ref1})^2 \\
&- C_{407}\tilde{x}_{ref1}^3D_0^2\tilde{x}_{ref1} - 2D_1D_2\tilde{x}_{ref1} \\
&- 2D_0D_3\tilde{x}_{ref1} - D_1^2\tilde{x}_{ref2} - 2D_0D_2\tilde{x}_{ref2} - 2D_0D_1\tilde{x}_{ref3} \\
&- C_{cuu}\tilde{x}_{ref1}\cos(\omega_1T_0 + \sigma_uT_2 + \phi_u) \\
&- C_{suu}\tilde{x}_{ref1}\sin(\omega_1T_0 + \sigma_uT_2 + \phi_u) \\
&- \left(C_{svv}\tilde{x}_{ref1} + C_{svvv}D_0^2\tilde{x}_{ref1}\right)\sin(\omega_1T_0 + \sigma_vT_2)
\end{aligned}
$$

$$
\begin{aligned}
N_{43} = & - C_{26}p_2^2 - C_{41}p_1p_3 - C_{411}p_1\cos\left(\omega_1T_0 + \sigma_uT_2 + \phi_u\right) \\
& - C_{412}p_1\sin\left(\omega_1T_0 + \sigma_vT_2\right) - C_{413}p_1\sin\left(\omega_1T_0 + \sigma_uT_2 + \phi_u\right) \\
N_{44} = & - 2C_{406}y_1\tilde{x}_{ref1}(D_0\tilde{x}_{ref1})^2 - 3C_{407}y_1\tilde{x}_{ref1}^2D_0^2\tilde{x}_{ref1} \\
& - C_{407}D_0^2y_1\tilde{x}_{ref1}^3 - 4C_{400}y_1\tilde{x}_{ref1}^3 - 2C_{406}\tilde{x}_{ref1}^2D_0y_1D_0\tilde{x}_{ref1} \\
& - C_{406}\tilde{x}_{ref1}^2(D_0y_1)^2 - 3C_{407}y_1^2(D_0\tilde{x}_{ref1})^2 - C_{406}y_1^2(D_0\tilde{x}_{ref1})^2 \\
& - 3C_{407}y_1\tilde{x}_{ref1}^2D_0^2y_1 - 6C_{400}y_1^2\tilde{x}_{ref1}^2 - 4C_{406}y_1\tilde{x}_{ref1}D_0y_1D_0\tilde{x}_{ref1} \\
& - 4C_{37}y_1\tilde{x}_{ref1}D_0D_1\tilde{x}_{ref1} - C_{46}\tilde{x}_{ref1}D_0y_1D_1\tilde{x}_{ref1} \\
& - C_{46}y_1D_1\tilde{x}_{ref1}D_0\tilde{x}_{ref1} - 2C_{33}\tilde{x}_{ref1}D_0\tilde{x}_{ref1}D_1y_1 \\
& - 2C_{37}\tilde{x}_{ref1}^2D_0D_1y_1 - C_{33}y_2(D_0\tilde{x}_{ref1})^2 \\
& - 2C_{37}y_2\tilde{x}_{ref1}D_0^2\tilde{x}_{ref1} - C_{37}\tilde{x}_{ref1}^2D_0^2y_2 - 3C_{36}y_2\tilde{x}_{ref1}^2 \\
& - 2C_{33}\tilde{x}_{ref1}D_0y_2D_0\tilde{x}_{ref1} - C_{407}y_1^3D_0^2\tilde{x}_{ref1} - 2C_{406}y_1^2D_0y_1D_0\tilde{x}_{ref1} \\
& - 3C_{407}y_1^2\tilde{x}_{ref1}D_0^2y_1 - 4C_{400}y_1^3\tilde{x}_{ref1} - 2C_{406}y_1\tilde{x}_{ref1}(D_0y_1)^2 \\
& - 2C_{37}y_1^2D_0D_1\tilde{x}_{ref1} - 2C_{33}y_1D_1\tilde{x}_{ref1}D_0y_1 - C_{46}\tilde{x}_{ref1}D_0y_1D_1y_1 \\
& - 4C_{37}y_1\tilde{x}_{ref1}D_0D_1y_1 - C_{46}y_1D_0\tilde{x}_{ref1}D_1y_1 - C_{25}y_1D_1^2\tilde{x}_{ref1} \\
& - C_{25}\tilde{x}_{ref1}D_1^2y_1 - C_{405}y_1D_0\tilde{x}_{ref1} - 2C_{25}y_1D_0D_2\tilde{x}_{ref1} \\
& - C_{405}\tilde{x}_{ref1}D_0y_1 - 2C_{22}D_2\tilde{x}_{ref1}D_0y_1 - 2C_{22}D_1y_1D_1\tilde{x}_{ref1} \\
& - 2C_{22}D_0\tilde{x}_{ref1}D_2y_1 - 2C_{25}\tilde{x}_{ref1}D_0D_2y_1 - 2C_{37}y_1\tilde{x}_{ref2}D_0^2\tilde{x}_{ref1} \\
& - 2C_{37}y_1\tilde{x}_{ref1}D_0^2\tilde{x}_{ref2} - C_{46}y_1D_0\tilde{x}_{ref2}D_0\tilde{x}_{ref1} \\
& - 2C_{37}\tilde{x}_{ref2}\tilde{x}_{ref1}D_0^2y_1 - 6C_{36}\tilde{x}_{ref2}y_1\tilde{x}_{ref1} \\
& - 2C_{33}\tilde{x}_{ref2}D_0y_1D_0\tilde{x}_{ref1} - C_{46}\tilde{x}_{ref1}D_0y_1D_0\tilde{x}_{ref2} \\
& - 2C_{25}y_2D_0D_1\tilde{x}_{ref1} - 2C_{22}D_1y_2D_0\tilde{x}_{ref1} - 2C_{22}D_0y_2D_1\tilde{x}_{ref1} \\
& - 2C_{25}\tilde{x}_{ref1}D_0D_1y_2 - 2C_{37}y_1\tilde{x}_{ref1}D_0^2y_2 - 2C_{37}\tilde{x}_{ref1}y_2D_0^2y_1 \\
& - 2C_{37}y_1y_2D_0^2\tilde{x}_{ref1} - C_{46}y_1D_0\tilde{x}_{ref1}D_0y_2 - 6C_{36}y_1y_2\tilde{x}_{ref1} \\
& - 2C_{33}y_2D_0y_1D_0\tilde{x}_{ref1} - C_{46}\tilde{x}_{ref1}D_0y_1D_0y_2 \\
& - C_{25}y_3D_0^2\tilde{x}_{ref1} - C_{25}\tilde{x}_{ref1}D_0^2y_3 - 2C_{21}y_3\tilde{x}_{ref1} \\
& - 2C_{22}D_0y_3D_0\tilde{x}_{ref1} - C_{37}y_1^2D_0^2\tilde{x}_{ref2} - C_{33}\tilde{x}_{ref2}(D_0y_1)^2 \\
& - 2C_{37}y_1\tilde{x}_{ref2}D_0^2y_1 - 3C_{36}\tilde{x}_{ref2}y_1^2 - 2C_{33}y_1D_0\tilde{x}_{ref2}D_0y_1 \\
& - 2C_{25}\tilde{x}_{ref2}D_0D_1y_1 - 2C_{22}D_1y_1D_0\tilde{x}_{ref2} - 2C_{22}D_0y_1D_1\tilde{x}_{ref2} \\
& - 2C_{25}y_1D_0D_1\tilde{x}_{ref2} - C_{25}\tilde{x}_{ref3}D_0^2y_1 - C_{25}y_1D_0^2\tilde{x}_{ref3} \\
& - 2C_{21}\tilde{x}_{ref3}y_1 - 2C_{22}D_0\tilde{x}_{ref3}D_0y_1 - C_{25}\tilde{x}_{ref2}D_0^2y_2 \\
& - C_{25}y_2D_0^2\tilde{x}_{ref2} - 2C_{21}\tilde{x}_{ref2}y_2 - 2C_{22}D_0\tilde{x}_{ref2}D_0y_2
\end{aligned}
$$

$$
\begin{aligned}
N_{45} = &- C_{23}p_1D_1^2y_1 - 2C_{23}p_1D_0D_2y_1 \\
&- 2C_{23}p_2D_0D_1y_1 - C_{23}p_3D_0^2y_1 - 2C_{23}p_1D_0D_1y_2 \\
&- C_{23}p_2D_0^2y_2 - C_{23}p_1D_0^2y_3 - C_{24}p_3y_1 - C_{24}p_2y_2 \\
&- C_{24}p_1y_3 - C_{30}p_2y_1D_0^2y_1 - C_{30}p_1y_2D_0^2y_1 \\
&- C_{30}p_1y_1D_0^2y_2 - C_{407}p_1y_1D_0^2y_1 - 2C_{42}p_1D_0y_1D_1y_1 \\
&- C_{42}p_2(D_0y_1)^2 - 2C_{42}p_1D_0y_1D_0y_2 - C_{420}p_1y_1^3 \\
&- C_{421}p_1^2y_1^2 - C_{422}p_1p_2y_1 - C_{423}p_1D_0y_1 \\
&- C_{424}p_1y_1D_0D_1y_1 - C_{425}p_1^2D_0D_1y_1 - C_{425}p_1p_2D_0^2y_1 \\
&- C_{426}p_1y_1^2D_0^2y_1 - C_{427}p_1^2(D_0y_1)^2 - 2C_{427}p_1^2y_1D_0^2y_1 \\
&- C_{43}p_2y_1^2 - 2C_{43}p_1y_2y_1 - C_{48}p_1^2y_2 - C_{49}p_1^2D_0^2y_2 \\
N_{46} = &- C_{23}p_1D_1^2\tilde{x}_{ref1} - 2C_{23}p_1D_0D_2\tilde{x}_{ref1} - 2C_{23}p_2D_0D_1\tilde{x}_{ref1} \\
&- C_{23}p_3D_0^2\tilde{x}_{ref1} - 2C_{23}p_1D_0D_1\tilde{x}_{ref2} - C_{23}p_2D_0^2\tilde{x}_{ref2} \\
&- C_{23}p_1D_0^2\tilde{x}_{ref3} - C_{24}p_3\tilde{x}_{ref1} - C_{24}p_2\tilde{x}_{ref2} \\
&- C_{24}p_1\tilde{x}_{ref3} - C_{30}p_2\tilde{x}_{ref1}D_0^2\tilde{x}_{ref1} - C_{30}p_1\tilde{x}_{ref2}D_0^2\tilde{x}_{ref1} \\
&- C_{30}p_1\tilde{x}_{ref1}D_0^2\tilde{x}_{ref2} - C_{407}p_1\tilde{x}_{ref1}D_0^2\tilde{x}_{ref1} \\
&- 2C_{42}p_1D_0\tilde{x}_{ref1}D_1\tilde{x}_{ref1} - C_{42}p_2(D_0\tilde{x}_{ref1})^2 \\
&- 2C_{42}p_1D_0\tilde{x}_{ref1}D_0\tilde{x}_{ref2} - C_{420}p_1\tilde{x}_{ref1}^3 - C_{421}p_1^2\tilde{x}_{ref1}^2 \\
&- C_{422}p_1p_2\tilde{x}_{ref1} - C_{423}p_1D_0\tilde{x}_{ref1} - C_{424}p_1\tilde{x}_{ref1}D_0D_1\tilde{x}_{ref1} \\
&- C_{425}p_1^2D_0D_1\tilde{x}_{ref1} - C_{425}p_1p_2D_0^2\tilde{x}_{ref1} \\
&- C_{426}p_1\tilde{x}_{ref1}^2D_0^2\tilde{x}_{ref1} - C_{427}p_1^2(D_0\tilde{x}_{ref1})^2 \\
&- 2C_{427}p_1^2\tilde{x}_{ref1}D_0^2\tilde{x}_{ref1} - C_{43}p_2\tilde{x}_{ref1}^2 - 2C_{43}p_1\tilde{x}_{ref2}\tilde{x}_{ref1} \\
&- C_{48}p_1^2\tilde{x}_{ref2} - C_{49}p_1^2D_0^2\tilde{x}_{ref2}
\end{aligned}
$$

$$
\begin{aligned}
N_{47} = & - C_{30}p_2\tilde{x}_{ref1}D_0^2y_1 - C_{30}p_1\tilde{x}_{ref2}D_0^2y_1 - C_{30}p_1\tilde{x}_{ref1}D_0^2y_2 \\
& - C_{30}p_2y_1D_0^2\tilde{x}_{ref1} - C_{30}p_1y_1D_0^2\tilde{x}_{ref2} - C_{30}p_1y_2D_0^2\tilde{x}_{ref1} \\
& - 2C_{407}p_1y_1D_0\tilde{x}_{ref1}D_0y_1 - 2C_{407}p_1\tilde{x}_{ref1}D_0\tilde{x}_{ref1}D_0y_1 \\
& - C_{407}p_1y_1(D_0\tilde{x}_{ref1})^2 - C_{407}p_1\tilde{x}_{ref1}(D_0y_1)^2 \\
& - 2C_{42}p_1D_1\tilde{x}_{ref1}D_0y_1 - 2C_{42}p_2D_0\tilde{x}_{ref1}D_0y_1 \\
& - 2C_{42}p_1D_0\tilde{x}_{ref2}D_0y_1 - 2C_{42}p_1D_0\tilde{x}_{ref1}D_0y_2 \\
& - 2C_{42}p_1D_0\tilde{x}_{ref1}D_1y_1 - 3C_{420}p_1\tilde{x}_{ref1}y_1^2 \\
& - 3C_{420}p_1\tilde{x}_{ref1}^2y_1 - 2C_{421}p_1^2\tilde{x}_{ref1}y_1 \\
& - C_{424}p_1\tilde{x}_{ref1}D_1D_0y_1 - C_{424}p_1y_1D_0D_1\tilde{x}_{ref1} \\
& - C_{426}p_1y_1^2D_0^2\tilde{x}_{ref1} - 2C_{426}p_1\tilde{x}_{ref1}y_1D_0^2\tilde{x}_{ref1} \\
& - 2C_{426}p_1\tilde{x}_{ref1}y_1D_0^2y_1 - C_{426}p_1\tilde{x}_{ref1}^2D_0^2y_1 \\
& - 2C_{427}p_1^2D_0\tilde{x}_{ref1}D_0y_1 - 2C_{427}p_1^2y_1D_0^2\tilde{x}_{ref1} \\
& - 2C_{427}p_1^2\tilde{x}_{ref1}D_0^2y_1 - 2C_{43}p_2\tilde{x}_{ref1}y_1 \\
& - 2C_{43}p_1\tilde{x}_{ref2}y_1 - 2C_{43}p_1\tilde{x}_{ref1}y_2
\end{aligned}
$$

C.2 Expressions of MSM coefficients

Expressions of the coefficients introduced in the formulation of the asymptotic problem described in Chapter 7.

Coefficients of order (ϵ^1) equations:

$$\omega_1^2 = \frac{\alpha_1 + 5\alpha_3\bar{x}_{ref}^3 + 3\alpha_3\bar{x}_{ref}^2 + 3\alpha_1\bar{x}_{ref}}{(\bar{x}_{ref}+1)\left(\alpha_2\bar{x}_{ref}^2+1\right)}$$

$$C_{11} = \frac{2\bar{x}_{ref}\left(\alpha_1 + \alpha_3\bar{x}_{ref}^2\right)}{(\bar{x}_{ref}+1)\left(\alpha_2\bar{x}_{ref}^2+1\right)}$$

Coefficients of order (ϵ^2) equations:

$$C_{21} = \frac{2\alpha_1 + 10\alpha_3\bar{x}_{ref}^3 + 12\alpha_3\bar{x}_{ref}^2 + 3\alpha_1\bar{x}_{ref} + 3\alpha_3\bar{x}_{ref}}{(\bar{x}_{ref}+1)^2\left(\alpha_2\bar{x}_{ref}^2+1\right)}$$

$$C_{22} = \frac{\alpha_2\bar{x}_{ref}}{\alpha_2\bar{x}_{ref}^2+1}$$

$$C_{23} = \frac{2}{\bar{x}_{ref}+1}$$

$$C_{24} = \frac{2\left(\alpha_1 + 4\alpha_3\bar{x}_{ref}^3 + 3\alpha_3\bar{x}_{ref}^2 + 2\alpha_1\bar{x}_{ref}\right)}{(\bar{x}_{ref}+1)^2\left(\alpha_2\bar{x}_{ref}^2+1\right)}$$

$$C_{25} = \frac{2\left(2\alpha_2\bar{x}_{ref}^2 + \alpha_2\bar{x}_{ref} + 1\right)}{(\bar{x}_{ref}+1)\left(\alpha_2\bar{x}_{ref}^2+1\right)}$$

$$C_{26} = \frac{\bar{x}_{ref}\left(\alpha_1 + \alpha_3\bar{x}_{ref}^2\right)}{(\bar{x}_{ref}+1)^2\left(\alpha_2\bar{x}_{ref}^2+1\right)}$$

$$C_{211} = C_{21} - \omega_1^2(C_{22} + C_{25})$$

$$C_{212} = \frac{C_{11}\left(C_{11}C_{21} - C_{24}\omega_1^2\right)}{\omega_1^4} + C_{26}$$

$$C_{213} = C_{11}\left(C_{25} - \frac{2C_{21}}{\omega_1^2}\right) - C_{23}\omega_1^2 + C_{24}$$

$$C_{214} = C_{21} + \omega_1^2(C_{22} - C_{25})$$

Coefficients of order (ϵ^3) equations:

$$
\begin{aligned}
C_{30} =& \frac{2\left(3\alpha_2\bar{x}_{ref}^2 + 2\alpha_2\bar{x}_{ref} + 1\right)}{(\bar{x}_{ref}+1)^2\left(\alpha_2\bar{x}_{ref}^2+1\right)} \\
C_{33} =& \frac{\alpha_2(3\bar{x}_{ref}+1)}{(\bar{x}_{ref}+1)\left(\alpha_2\bar{x}_{ref}^2+1\right)} \\
C_{35} =& \frac{\rho_1 + \rho_2\bar{x}_{ref}^2}{\alpha_2\bar{x}_{ref}^2+1} \\
C_{36} =& \frac{\alpha_1 + \alpha_3 + 10\alpha_3\bar{x}_{ref}^2 + 8\alpha_3\bar{x}_{ref}}{(\bar{x}_{ref}+1)^2\left(\alpha_2\bar{x}_{ref}^2+1\right)} \\
C_{37} =& \frac{\alpha_2 + 6\alpha_2\bar{x}_{ref}^2 + 6\alpha_2\bar{x}_{ref} + 1}{(\bar{x}_{ref}+1)^2\left(\alpha_2\bar{x}_{ref}^2+1\right)} \\
C_{41} =& \frac{2\bar{x}_{ref}\left(\alpha_1 + \alpha_3\bar{x}_{ref}^2\right)}{(\bar{x}_{ref}+1)^2\left(\alpha_2\bar{x}_{ref}^2+1\right)} \\
C_{42} =& \frac{2\alpha_2\bar{x}_{ref}}{(\bar{x}_{ref}+1)\left(\alpha_2\bar{x}_{ref}^2+1\right)} \\
C_{43} =& \frac{2\left(\alpha_1 + 6\alpha_3\bar{x}_{ref}^2 + 3\alpha_3\bar{x}_{ref}\right)}{(\bar{x}_{ref}+1)^2\left(\alpha_2\bar{x}_{ref}^2+1\right)} \\
C_{48} =& \frac{\alpha_1 + 3\alpha_3\bar{x}_{ref}^2}{(\bar{x}_{ref}+1)^2\left(\alpha_2\bar{x}_{ref}^2+1\right)} \\
C_{49} =& \frac{1}{(\bar{x}_{ref}+1)^2} \\
C_{cu} =& -\frac{\eta_1 U\bar{x}_{ref}\omega_1\left(\mu_1 + \mu_2\bar{x}_{ref}^2\right)}{\alpha_2\bar{x}_{ref}^2+1} \\
C_{sv} =& \frac{2V\bar{x}_{ref}\left(\alpha_1 + \alpha_3\bar{x}_{ref}^2\right)}{(\bar{x}_{ref}+1)\left(\alpha_2\bar{x}_{ref}^2+1\right)} \\
C_{su} =& -\frac{U\bar{x}_{ref}\left(\eta_2 - \omega - 1^2\right)\left(\mu_1 + \mu_2\bar{x}_{ref}^2\right)}{\alpha_2\bar{x}_{ref}^2+1}
\end{aligned}
$$

$$
\begin{aligned}
C_{301} =& \frac{1}{3}\Bigg(\frac{2C_{21}(C_{211}-6C_{214})}{\omega_1^2}+4C_{211}C_{22}-5C_{211}C_{25}\\
&+6C_{214}C_{25}+3\omega_1^2(C_{33}-3C_{37})+9C_{36}\Bigg)\\
C_{302} =& -\frac{4C_{11}^2C_{37}-4C_{11}C_{213}C_{25}+8C_{11}C_{43}+8C_{21}C_{212}+C_{213}^2}{4\omega_1^2}\\
&+\frac{3C_{11}^2C_{36}}{\omega_1^4}+C_{11}C_{30}+C_{212}C_{25}-C_{213}C_{23}+C_{48}-C_{49}\omega_1^2\\
C_{303} =& \frac{2C_{21}C_{211}+\omega_1^2\left(-4C_{211}C_{22}-5C_{211}C_{25}-3\omega_1^2(C_{33}+C_{37})+3C_{36}\right)}{24\omega_1^4}\\
C_{304} =& \frac{1}{9\omega_1^6}\Bigg(-2C_{11}C_{21}C_{211}+\omega_1^4(3(C_{11}C_{33}+2C_{11}C_{37}+C_{43}))\\
&+\omega_1^4(-4C_{211}C_{23}-3C_{213}(C_{22}+C_{25}))+\omega_1^2(C_{211}(4C_{11}C_{25}-4C_{213}+C_{24})\\
&-9\omega_1^2C_{11}C_{36})-3\omega_1^6(C_{30}+C_{42})\Bigg)\\
C_{305} =& 2\Bigg(\frac{1}{\omega_1^6}\left(-2C_{11}C_{21}C_{214}+\omega_1^2(3C_{11}C_{36}+C_{214}C_{24})\right.\\
&\left.+\omega_1^4(-(-C_{11}C_{33}+2C_{11}C_{37}+C_{213}C_{22}-C_{213}C_{25}+C_{43}))\right)+C_{30}-C_{42}\Bigg)\\
C_{306} =& \frac{C_{11}^3C_{36}-C_{11}\omega_1^2(C_{11}C_{43}+2C_{21}C_{212})+\omega_1^4(C_{11}C_{48}+C_{212}C_{24})}{\omega_1^8}\\
C_{307} =& -\frac{C_{11}^2C_{37}+2C_{11}C_{43}+2C_{21}C_{212}}{\omega_1^2}\\
&+C_{11}\left(\frac{3C_{11}C_{36}}{\omega_1^4}+C_{30}\right)+C_{212}C_{25}+C_{48}-C_{49}\omega_1^2\\
C_{308} =& \frac{2}{3}\Bigg(\frac{2C_{21}(C_{211}-6C_{214})}{\omega_1^2}+4C_{211}C_{22}\\
&-5C_{211}C_{25}+6C_{214}C_{25}+3\omega_1^2(C_{33}-3C_{37})+9C_{36}\Bigg)\\
C_{309} =& \frac{1}{3}\Bigg(\frac{2C_{21}(C_{211}-6C_{214})}{\omega_1^2}+4C_{211}C_{22}\\
&-5C_{211}C_{25}+6C_{214}C_{25}+3\omega_1^2(C_{33}-3C_{37})+9C_{36}\Bigg)\\
C_{310} =& -\frac{2iC_{11}C_{22}}{\omega_1}\\
C_{311} =& 2iC_{23}\omega_1-\frac{2iC_{11}C_{25}}{\omega_1}\\
C_{312} =& \frac{i\left(C_{11}k_g+C_{35}\omega_1^2\right)}{\omega_1}\\
C_{320} =& \frac{1}{3}\Bigg(-\frac{2C_{11}C_{21}C_{211}}{\omega_1^4}+\frac{4C_{11}C_{211}C_{25}-9C_{11}C_{36}+C_{211}C_{24}}{\omega_1^2}\\
&+3C_{11}C_{33}+6C_{11}C_{37}-4C_{211}C_{23}-3\omega_1^2(C_{30}+C_{42})+3C_{43}\Bigg)\\
C_{321} =& \frac{8iC_{211}}{3\omega_1}+2i\omega_1(C_{22}+C_{25})
\end{aligned}
$$

$$
\begin{aligned}
\gamma_{31} =& C_{309}A^2\bar{A} + C_{309}A^2\bar{A}_{un} + C_{308}A\bar{A}A_{un} \\
&+ C_{308}AA_{un}\bar{A}_{un} + C_{307}AB^2 + A(C_{310}D_1B + C_{312}) \\
&+ C_{309}\bar{A}A_{un}^2 + C_{307}A_{un}B^2 + C_{310}A_{un}D_1B \\
&+ B(C_{311}D_1A + C_{311}D_1A_{un}) + D_1^2A + 2iD_2A\omega_1 \\
\gamma_{32} =& (A + A_{un})(BC_{320}(A + A_{un}) + C_{321}D_1A) + AC_{321}D_1A_{un} \\
\gamma_{33} =& 8AC_{303}\omega_1^2\left(A^2 + 3AA_{un} + 3A_{un}^2\right) \\
\gamma_{35} =& \frac{-C_{11}^3C_{36} + C_{11}\omega_1^2(C_{11}C_{43} + 2C_{21}C_{212}) + \omega_1^4(-(C_{11}C_{48} + C_{212}C_{24}))}{\omega_1^6} \\
\gamma_{36} =& \frac{4C_{11}C_{21}C_{214}}{\omega_1^4} - \frac{6C_{11}C_{36} + C_{214}C_{24}}{\omega_1^2} \\
&+ 2\left(-C_{11}C_{33} + 2C_{11}C_{37} + \omega_1^2(C_{42} - C_{30}) + C_{43}\right) \\
\gamma_{37} =& -2i\omega_1(C_{22} - C_{25})
\end{aligned}
$$

Coefficients of order (ϵ^4) equations:

$$
\begin{aligned}
C_{400} =& \frac{\alpha_3(5\bar{x}_{ref}+2)}{(\bar{x}_{ref}+1)^2\left(\alpha_2\bar{x}_{ref}^2+1\right)}\\
C_{405} =& \frac{2\left(\rho_1+2\rho_2\bar{x}_{ref}^2+\rho_2\bar{x}_{ref}\right)}{(\bar{x}_{ref}+1)\left(\alpha_2\bar{x}_{ref}^2+1\right)}\\
C_{406} =& \frac{\alpha_2(3\bar{x}_{ref}+2)}{(\bar{x}_{ref}+1)^2\left(\alpha_2\bar{x}_{ref}^2+1\right)}\\
C_{407} =& \frac{2\alpha_2(2\bar{x}_{ref}+1)}{(\bar{x}_{ref}+1)^2\left(\alpha_2\bar{x}_{ref}^2+1\right)}\\
C_{cuu} =& -\frac{\eta_1 U\omega_1\left(\mu_1+5\mu_2\bar{x}_{ref}^3+3\mu_2\bar{x}_{ref}^2+3\mu_1\bar{x}_{ref}\right)}{(\bar{x}_{ref}+1)\left(\alpha_2\bar{x}_{ref}^2+1\right)}\\
C_{suu} =& -\frac{U\left(\eta_2-\omega_1^2\right)\left(\mu_1+5\mu_2\bar{x}_{ref}^3+3\mu_2\bar{x}_{ref}^2+3\mu_1\bar{x}_{ref}\right)}{(\bar{x}_{ref}+1)\left(\alpha_2\bar{x}_{ref}^2+1\right)}\\
C_{svv} =& \frac{2V\left(\alpha_1+4\alpha_3\bar{x}_{ref}^3+3\alpha_3\bar{x}_{ref}^2+2\alpha_1\bar{x}_{ref}\right)}{(\bar{x}_{ref}+1)^2\left(\alpha_2\bar{x}_{ref}^2+1\right)}\\
C_{svvv} =& \frac{2V}{\bar{x}_{ref}+1}\\
C_{411} =& -\frac{2\eta_1 U\bar{x}_{ref}\omega_1\left(\mu_1+\mu_2\bar{x}_{ref}^2\right)}{(\bar{x}_{ref}+1)\left(\alpha_2\bar{x}_{ref}^2+1\right)}\\
C_{412} =& \frac{2V\bar{x}_{ref}\left(\alpha_1+\alpha_3\bar{x}_{ref}^2\right)}{(\bar{x}_{ref}+1)^2\left(\alpha_2\bar{x}_{ref}^2+1\right)}\\
C_{413} =& -\frac{2U\bar{x}_{ref}\left(\eta_2-\omega_1^2\right)\left(\mu_1+\mu_2\bar{x}_{ref}^2\right)}{(\bar{x}_{ref}+1)\left(\alpha_2\bar{x}_{ref}^2+1\right)}\\
C_{420} =& \frac{2\alpha_3(4\bar{x}_{ref}+1)}{(\bar{x}_{ref}+1)^2\left(\alpha_2\bar{x}_{ref}^2+1\right)}\\
C_{421} =& \frac{3\alpha_3\bar{x}_{ref}}{(\bar{x}_{ref}+1)^2\left(\alpha_2\bar{x}_{ref}^2+1\right)}\\
C_{422} =& \frac{2\left(\alpha_1+3\alpha_3\bar{x}_{ref}^2\right)}{(\bar{x}_{ref}+1)^2\left(\alpha_2\bar{x}_{ref}^2+1\right)}\\
C_{423} =& \frac{2\left(\rho_1+\rho_2\bar{x}_{ref}^2\right)}{(\bar{x}_{ref}+1)\left(\alpha_2\bar{x}_{ref}^2+1\right)}\\
C_{424} =& \frac{4\left(3\alpha_2\bar{x}_{ref}^2+2\alpha_2\bar{x}_{ref}+1\right)}{(\bar{x}_{ref}+1)^2\left(\alpha_2\bar{x}_{ref}^2+1\right)}\\
C_{425} =& \frac{2}{(\bar{x}_{ref}+1)^2}
\end{aligned}
$$

$$C_{426} = \frac{2\alpha_2(3\bar{x}_{ref}+1)}{(\bar{x}_{ref}+1)^2\left(\alpha_2\bar{x}_{ref}^2+1\right)}$$
$$C_{427} = \frac{\alpha_2\bar{x}_{ref}}{(\bar{x}_{ref}+1)^2\left(\alpha_2\bar{x}_{ref}^2+1\right)}$$

$$\begin{aligned}
\gamma_{41} =& {}^2\gamma_{426}\bar{A}B + \gamma_{426}A^2\bar{A}_{un}B + A^2(\gamma_{429}D_1\bar{A} + \gamma_{429}D_1\bar{A}_{un}) \\
&+ \gamma_{428}A\bar{A}A_{un}B + A\bar{A}(\gamma_{430}D_1A + \gamma_{430}D_1A_{un}) \\
&+ \gamma_{428}AA_{un}\bar{A}_{un}B + AA_{un}(2\gamma_{429}D_1\bar{A} + 2\gamma_{429}D_1\bar{A}_{un}) \\
&+ A\bar{A}_{un}(\gamma_{430}D_1A + \gamma_{430}D_1A_{un}) + \gamma_{427}AB^3 \\
&+ AB(\gamma_{432}D_1B + \gamma_{433}) + A(\gamma_{440}D_1^2B + \gamma_{436}D_2B) \\
&+ \gamma_{426}\bar{A}A_{un}^2B + \bar{A}A_{un}(\gamma_{430}D_1A + \gamma_{430}D_1A_{un}) \\
&+ \gamma_{426}A_{un}^2\bar{A}_{un}B + \gamma_{429}A_{un}^2D_1\bar{A} + \gamma_{430}A_{un}\bar{A}_{un}D_1A \\
&+ \gamma_{427}A_{un}B^3 + A_{un}B(\gamma_{432}D_1B + \gamma_{434}) + A_{un}(\gamma_{440}D_1^2B + D_2B\gamma_{436}) \\
&+ B^2(\gamma_{431}D_1A + \gamma_{431}D_1A_{un}) + B\big(\gamma_{438}D_1^2A + \gamma_{438}D_1^2A_{un} \\
&- 2i\omega_1\gamma_{438}D_2A - 2i\omega_1\gamma_{438}D_2A_{un} + \gamma_{437}e^{i\sigma_uT_2+ic} \\
&+ \gamma_{439}e^{i\sigma_vT_2}\big) + C_{35}D_1A + 2D_1D_2A + \gamma_{435}D_1AD_1B \\
&+ \gamma_{435}D_1A_{un}D_1B + 2i\omega_1D_3A \\
\gamma_{42} =& \gamma_{410}A^3\bar{A} + \gamma_{410}A^3\bar{A}_{un} + \gamma_{408}A^2\bar{A}A_{un} + \gamma_{408}A^2A_{un}\bar{A}_{un} + \gamma_{407}A^2B^2 \\
&+ \gamma_{411}A^2D_1B + \gamma_{414}A^2 + \gamma_{408}A\bar{A}A_{un}^2 + \gamma_{408}AA_{un}^2\bar{A}_{un} + \gamma_{409}AA_{un}B^2 \\
&+ D_1A(\gamma_{412}AB + \gamma_{412}A_{un}B) + 2\gamma_{411}AA_{un}D_1B + \gamma_{413}AA_{un} \\
&+ \gamma_{412}ABD_1A_{un} + \gamma_{421}AD_1^2A + \gamma_{419}AD_1^2A_{un} + \gamma_{420}AD_2A \\
&+ \gamma_{417}AD_2A_{un} + \gamma_{415}Ae^{i\sigma_uT_2+i\phi_u} + \gamma_{416}Ae^{i\sigma_vT_2} + \gamma_{410}\bar{A}A_{un}^3 \\
&+ \gamma_{407}A_{un}^2B^2 + \gamma_{411}A_{un}^2D_1B + \gamma_{412}A_{un}BD_1A_{un} + \gamma_{421}A_{un}D_1^2A \\
&+ \gamma_{420}A_{un}D_2A + \gamma_{418}D_1A^2 + 2\gamma_{418}D_1AD_1A_{un} \\
\gamma_{43} =& \gamma_{422}A^3B + \gamma_{423}A^2A_{un}B + A^2(\gamma_{424}D_1A + \gamma_{425}D_1A_{un}) \\
&+ \gamma_{423}AA_{un}^2B + AA_{un}(2\gamma_{424}D_1A + 2\gamma_{424}D_1A_{un}) \\
&+ \gamma_{422}A_{un}^3B + \gamma_{424}A_{un}^2D_1A \\
\gamma_{44} =& \gamma_{425}A^4 + 4\gamma_{425}A^3A_{un} + 6\gamma_{425}A^2A_{un}^2 + 4\gamma_{425}AA_{un}^3 \\
\gamma_{45} =& \frac{1}{\omega_1^6}\Big(-6C_{11}^2C_{214}C_{36} - 2\omega_1^4(C_{11}(-C_{11}C_{406} + 3C_{11}C_{407} + C_{21}C_{305} + 3C_{420}) \\
&+ 3C_{212}C_{36} + C_{214}C_{48}) + 4\omega_1^2(C_{11}(3C_{11}C_{400} + C_{214}C_{43}) + C_{21}C_{212}C_{214}) \\
&+ \omega_1^6(-2C_{11}C_{407} + 4C_{11}C_{426} - 2C_{212}C_{33} + 4C_{212}C_{37} + C_{24}C_{305} + 2C_{421}) \\
&- 2C_{427}\omega_1^8\Big)
\end{aligned}$$

$$
\begin{aligned}
\gamma_{46} =& \frac{1}{\omega_1^8}\Big(C_{11}^4 C_{400} - C_{11}^2\omega_1^2(C_{11}C_{420} + 3C_{212}C_{36}) \\
&+ \omega_1^4\left(C_{11}(C_{11}C_{421} + 2C_{212}C_{43}) + C_{21}C_{212}^2\right) \\
&- \omega_1^6(2C_{11}C_{21}C_{306} + C_{212}C_{48}) + C_{24}C_{306}\omega_1^8\Big) \\
\gamma_{47} =& \frac{2}{9\omega_1^4}\Big(C_{21}\left(C_{211}^2 + 18C_{214}^2\right) \\
&+ \omega_1^2\left(4C_{211}^2(C_{22} - C_{25}) + 9C_{36}(C_{211} - 6C_{214})\right) \\
&+ 9\omega_1^4((C_{211} - 2C_{214})(C_{33} - 2C_{37}) + 3C_{400}) \\
&+ 9\omega_1^6(C_{406} - 3C_{407})\Big) \\
\gamma_{48} =& -\frac{i\left(C_{11}(4C_{37} - C_{46}) + \omega_1^2(2C_{42} - C_{424})\right)}{\omega_1} \\
\gamma_{49} =& \frac{ik_g\left(C_{24} - C_{23}\omega_1^2\right)}{\omega_1} \\
\gamma_{50} =& 2C_{22} - \frac{4C_{214}}{\omega_1^2} \\
\gamma_{51} =& \frac{C_{11}^2 C_{22} - 2C_{212}\omega_1^2}{\omega_1^4} \\
\gamma_{52} =& -\frac{2C_{11}}{\omega_1^2} \\
\gamma_{53} =& -\frac{C_{11}C_{35}}{\omega_1^2} \\
\gamma_{54} =& \frac{1}{2}i\left(C_{svv} - C_{svvv}\omega_1^2\right) \\
\gamma_{55} =& \frac{1}{2}(C_{cuu} + iC_{suu}) \\
\gamma_{56} =& 2i\omega_1(C_{22} + C_{25}) \\
\gamma_{57} =& C_{25} - \frac{2C_{214}}{\omega_1^2} \\
\gamma_{58} =& \frac{C_{11}^2 C_{25} - \omega_1^2(C_{11}C_{23} + 2C_{212})}{\omega_1^4}
\end{aligned}
$$

$$
\begin{aligned}
\gamma_{401} =& -\frac{i}{12\omega_1^5}\Big(6(-4C_{22}C_{304}+C_{25}(5C_{304}+C_{305})-C_{407}+3C_{426})\omega_1^6\\
&+2(C_{211}(5C_{30}-4C_{42})-3(2C_{214}C_{30}-C_{23}C_{301}+2C_{21}(C_{304}+C_{305})\\
&+C_{213}C_{33}-3C_{213}C_{37}-2C_{11}C_{406}+9C_{11}C_{407}+3C_{420}))\omega_1^4\\
&+(3(-2C_{11}C_{25}C_{301}+C_{213}(C_{301}-4C_{214}C_{25})+8C_{11}C_{214}C_{37}\\
&+24C_{11}C_{400}+8C_{214}C_{43})-2C_{211}(4C_{213}C_{22}-5C_{213}C_{25}\\
&+10C_{11}C_{37}+2C_{43}-2C_{11}C_{46}))\omega_1^2+12C_{11}(C_{211}-6C_{214})C_{36}\Big)\\
\gamma_{402} =& -\frac{i}{8\omega_1^7}\Big(4C_{25}C_{306}\omega_1^8+2(-2C_{212}C_{30}+2C_{23}C_{302}-4C_{21}C_{306}\\
&+C_{213}C_{425}-4C_{11}C_{427})\omega_1^6+(C_{23}C_{213}^2+2(-2C_{212}C_{25}+C_{302}\\
&-C_{11}C_{424})C_{213}+4C_{11}(-C_{25}C_{302}+2C_{212}C_{37}+2C_{421}+C_{11}C_{426})\\
&+8C_{212}C_{43})\omega_1^4-C_{11}(C_{25}C_{213}^2-4C_{11}C_{37}C_{213}+24C_{212}C_{36}\\
&+4C_{11}(C_{11}C_{407}+3C_{420}))\omega_1^2+16C_{11}^3C_{400}\Big)\\
\gamma_{403} =& \frac{1}{8\omega_1^4}\Big(4(C_{23}C_{35}-C_{423})\omega_1^4+4C_{11}(C_{405}-C_{25}C_{35})\omega_1^2\\
&+C_{11}(C_{213}+8C_{11}C_{22})k_g\Big)\\
\gamma_{404} =& \frac{1}{4\omega_1^4}\Big(2(C_{23}C_{35}-C_{423})\omega_1^4+2(C_{11}(-C_{25}C_{35}+C_{405}+C_{23}k_g)-C_{41}k_g)\omega_1^2\\
&+C_{11}(C_{213}+4C_{11}C_{22}+2C_{24}-2C_{11}C_{25})k_g\Big)\\
\gamma_{405} =& \frac{1}{16\omega_1^3}\Big(4(iC_{411}+C_{413}-iC_{23}C_{cu}-C_{23}C_{su})\omega_1^2\\
&+C_{213}(-iC_{cu}-C_{su})+4C_{11}(iC_{25}C_{cu}-iC_{cuu}+C_{25}C_{su}-C_{suu})\Big)\\
\gamma_{406} =& \frac{1}{16\omega_1^3}\left(4(C_{412}-C_{23}C_{sv})\omega_1^2-C_{213}C_{sv}+4C_{11}C_{25}C_{sv}-4C_{11}C_{svv}\right)
\end{aligned}
$$

$$
\begin{aligned}
\gamma_{407} =& \frac{1}{3\omega_1^6}\Big(3C_{11}^2C_{211}C_{36} + \omega_1^4(C_{211}(4C_{11}C_{30} + 4C_{212}C_{25} + C_{48}) \\
& - 3(C_{11}(C_{11}C_{406} + 3C_{11}C_{407} + 2C_{21}C_{304} + 3C_{420}) \\
& + 3C_{212}C_{36})) - 2\omega_1^2(C_{11}(2C_{11}C_{211}C_{37} \\
& - 9C_{11}C_{400} + C_{211}C_{43}) + C_{21}C_{211}C_{212}) \\
& + \omega_1^6(3(C_{11}(4C_{25}C_{304} + C_{407} + 2C_{426}) + C_{212}C_{33} \\
& + 2C_{212}C_{37} + C_{24}C_{304} + C_{421}) - 4C_{211}C_{49}) \\
& - 3\omega_1^8(4C_{23}C_{304} + 3C_{427})\Big) \\
\gamma_{408} =& 2\Big(-\frac{2C_{21}C_{211}C_{214}}{\omega_1^4} + 3C_{21}C_{303} \\
& + \frac{4C_{211}C_{214}C_{25} + 3C_{211}C_{36} - 9C_{214}C_{36}}{\omega_1^2} + C_{211}C_{33} \\
& - 6C_{211}C_{37} + 3C_{214}C_{33} + 6C_{214}C_{37} \\
& + 3\omega_1^2(3C_{22}C_{303} - 5C_{25}C_{303} - 2C_{407}) + 6C_{400}\Big) \\
\gamma_{409} =& \frac{1}{3\omega_1^6}\Big(6C_{11}^2C_{211}C_{36} + 2\omega_1^4(C_{211}(4C_{11}C_{30} + 4C_{212}C_{25} + C_{48}) \\
& - 3(C_{11}(C_{11}C_{406} + 3C_{11}C_{407} + 2C_{21}C_{304} + 3C_{420}) + 3C_{212}C_{36})) \\
& - 4\omega_1^2(C_{11}(2C_{11}C_{211}C_{37} - 9C_{11}C_{400} + C_{211}C_{43}) \\
& + C_{21}C_{211}C_{212}) + 2\omega_1^6(3(C_{11}(4C_{25}C_{304} + C_{407} + 2C_{426}) \\
& + C_{212}C_{33} + 2C_{212}C_{37} + C_{24}C_{304} + C_{421}) - 4C_{211}C_{49}) \\
& - 6\omega_1^8(4C_{23}C_{304} + 3C_{427})\Big) \\
\gamma_{410} =& \frac{1}{3\omega_1^4}\Big(2\omega_1^4(3C_{21}C_{303} + C_{211}(C_{33} - 6C_{37}) \\
& + 3C_{214}C_{33} + 6C_{214}C_{37} + 6C_{400}) - 4C_{21}C_{211}C_{214} \\
& + 2\omega_1^2(4C_{211}C_{214}C_{25} + 3C_{211}C_{36} - 9C_{214}C_{36}) \\
& + 6\omega_1^6(3C_{22}C_{303} - 5C_{25}C_{303} - 2C_{407})\Big) \\
\gamma_{411} =& -\frac{2i\left(2C_{11}C_{211}C_{22} + 3C_{11}C_{33}\omega_1^2 - 6C_{304}\omega_1^4\right)}{3\omega_1^3} \\
\gamma_{412} =& \frac{i}{3\omega_1^3}\Big(-8C_{11}C_{211}C_{25} - 6C_{11}\omega_1^2(C_{33} + 2C_{37}) \\
& + 8C_{211}C_{23}\omega_1^2 + 3\omega_1^4(8C_{304} + 2C_{42} + C_{424})\Big) \\
\gamma_{413} =& \frac{i\left(C_{11}C_{211}k_g + \omega_1^2\left(4C_{211}C_{35} - 3C_{23}k_g\omega_1^2 + 3C_{24}k_g + 6C_{405}\omega_1^2\right)\right)}{3\omega_1^3} \\
\gamma_{414} =& \frac{i\left(C_{11}C_{211}k_g + 2\omega_1^2\left(2C_{211}C_{35} + 3\omega_1^2(C_{405} - C_{23}k_g) + 3C_{24}k_g\right)\right)}{6\omega_1^3}
\end{aligned}
$$

$$
\begin{aligned}
\gamma_{415} =& \frac{1}{2}(C_{cuu} - iC_{suu}) \\
\gamma_{416} =& -\frac{1}{2}i\left(C_{svv} - C_{svvv}\omega_1^2\right) \\
\gamma_{417} =& \frac{8iC_{211}}{3\omega_1} + 2i\omega_1(C_{22} + C_{25}) \\
\gamma_{418} =& \frac{2C_{211}}{3\omega_1^2} + C_{22} \\
\gamma_{419} =& \frac{2C_{211}}{3\omega_1^2} + C_{25} \\
\gamma_{420} =& \frac{8iC_{211}}{3\omega_1} + 2i\omega_1(C_{22} + C_{25}) \\
\gamma_{421} =& \frac{2C_{211}}{3\omega_1^2} + C_{25} \\
\gamma_{422} =& \frac{1}{3\omega_1^4}\Big(\omega_1^4(3(9C_{11}C_{25}C_{303} + 2C_{11}C_{406} + 3C_{11}C_{407} \\
&+ 2C_{21}C_{304} + C_{24}C_{303} + C_{420}) - C_{211}(5C_{30} + 4C_{42})) \\
&+ 2\omega_1^2(C_{11}(-3C_{21}C_{303} + 2C_{211}C_{33} + 5C_{211}C_{37} - 6C_{400}) + C_{211}C_{43}) \\
&- 6C_{11}C_{211}C_{36} - 3\omega_1^6(4C_{22}C_{304} + 9C_{23}C_{303} + 5C_{25}C_{304} + C_{407} + C_{426})\Big) \\
\gamma_{423} =& 3\Big(C_{11}\big(-\frac{2(C_{21}C_{303} + 2C_{400})}{\omega_1^2} + 9C_{25}C_{303} + 2C_{406} + 3C_{407}\big) \\
&+ 2C_{21}C_{304} + \omega_1^2(-(4C_{22}C_{304} + 9C_{23}C_{303} + 5C_{25}C_{304} + C_{407} + C_{426})) \\
&+ C_{24}C_{303} + C_{420}\Big) + C_{211}\big(\frac{2(2C_{11}C_{33} + 5C_{11}C_{37} + C_{43})}{\omega_1^2} \\
&- \frac{6C_{11}C_{36}}{\omega_1^4} - 5C_{30} - 4C_{42}\big) \\
\gamma_{424} =& \frac{2iC_{211}(4C_{22} + 5C_{25})}{3\omega_1} + 2i\omega_1(9C_{303} + C_{33} + C_{37}) \\
\gamma_{425} =& \frac{1}{9\omega_1^4}\Big(C_{21}C_{211}^2 \\
&+ 3\omega_1^4(6C_{21}C_{303} - 5C_{211}C_{33} - 6C_{211}C_{37} + 3C_{400}) \\
&+ C_{211}\omega_1^2(9C_{36} - 4C_{211}(C_{22} + C_{25})) \\
&- 9\omega_1^6(6C_{22}C_{303} + 10C_{25}C_{303} + C_{406} + C_{407})\Big) \\
\gamma_{426} =& \frac{1}{3\omega_1^4}\Big(\omega_1^4(-6C_{11}C_{406} + 27C_{11}C_{407} + 6C_{21}(C_{304} + C_{305}) \\
&- 5C_{211}C_{30} + 4C_{211}C_{42} + 6C_{214}C_{30} + 9C_{420}) \\
&- 2\omega_1^2(C_{11}(2C_{211}C_{33} - 5C_{211}C_{37} + 6C_{214}C_{37} + 18C_{400}) - C_{43}(C_{211} - 6C_{214})) \\
&- 6C_{11}C_{36}(C_{211} - 6C_{214}) \\
&+ 3\omega_1^6(4C_{22}C_{304} - C_{25}(5C_{304} + C_{305}) + C_{407} - 3C_{426})\Big)
\end{aligned}
$$

$$
\begin{aligned}
\gamma_{427} =& \frac{1}{\omega_1^6}\Big(-4C_{11}^3C_{400} - \omega_1^4\big(C_{11}^2C_{426} + 2C_{11}(C_{212}C_{37} + C_{421}) + 2C_{212}C_{43}\big) \\
&+ \omega_1^6(2C_{11}C_{427} + 2C_{21}C_{306} + C_{212}C_{30}) \\
&+ C_{11}\omega_1^2(C_{11}(C_{11}C_{407} + 3C_{420}) + 6C_{212}C_{36}) - C_{25}C_{306}\omega_1^8\Big) \\
\gamma_{428} =& \frac{1}{3\omega_1^4}\Big(2\omega_1^4(-6C_{11}C_{406} + 27C_{11}C_{407} + 6C_{21}(C_{304} + C_{305}) \\
&- 5C_{211}C_{30} + 4C_{211}C_{42} + 6C_{214}C_{30} + 9C_{420}) \\
&- 4\omega_1^2(C_{11}(2C_{211}C_{33} - 5C_{211}C_{37} + 6C_{214}C_{37} + 18C_{400}) \\
&- C_{43}(C_{211} - 6C_{214})) - 12C_{11}C_{36}(C_{211} - 6C_{214}) \\
&+ 6\omega_1^6(4C_{22}C_{304} - C_{25}(5C_{304} + C_{305}) + C_{407} - 3C_{426})\Big) \\
\gamma_{429} =& -\frac{2i\left(C_{211}(C_{25} - 2C_{22}) + 6C_{214}C_{22} + 3\omega_1^2(C_{37} - C_{33})\right)}{3\omega_1} \\
\gamma_{430} =& -\frac{4i\left(C_{211}(C_{22} - 2C_{25}) + 3C_{214}(C_{22} + C_{25}) - 3C_{37}\omega_1^2\right)}{3\omega_1} \\
\gamma_{431} =& \frac{i\left(2C_{11}^2C_{37} - \omega_1^2(C_{11}C_{424} + 2C_{212}C_{25}) + C_{425}\omega_1^4\right)}{\omega_1^3} \\
\gamma_{432} =& \frac{2i\left(C_{11}^2C_{33} - \omega_1^2(C_{11}C_{42} + 2C_{212}C_{22})\right)}{\omega_1^3} \\
\gamma_{433} =& -\frac{i\left(C_{11}k_g(C_{213} + 2C_{24}) + 2\omega_1^2(C_{11}C_{405} - C_{41}k_g) - 2C_{423}\omega_1^4\right)}{2\omega_1^3} \\
\gamma_{434} =& -\frac{i\left(C_{11}C_{213}k_g + 2C_{11}C_{405}\omega_1^2 - 2C_{423}\omega_1^4\right)}{2\omega_1^3} \\
\gamma_{435} =& -\frac{2C_{11}C_{22}}{\omega_1^2} \\
\gamma_{436} =& -\frac{2iC_{11}C_{22}}{\omega_1} \\
\gamma_{437} =& \frac{1}{2}\left(-\frac{C_{11}(C_{cuu} - iC_{suu})}{\omega_1^2} + C_{411} - iC_{413}\right) \\
\gamma_{438} =& C_{23} - \frac{C_{11}C_{25}}{\omega_1^2} \\
\gamma_{439} =& -\frac{1}{2}i\left(C_{412} - \frac{C_{11}C_{svv}}{\omega_1^2}\right) \\
\gamma_{440} =& -\frac{C_{11}C_{25}}{\omega_1^2}
\end{aligned}
$$

$$
\begin{aligned}
\beta_1 =& \frac{1}{12\omega_1^5}\Big(6(4C_{22}C_{304} - C_{25}(5C_{304} + C_{305}) + C_{407} - 3C_{426})\omega_1^6 \\
& - 2(C_{211}(5C_{30} - 4C_{42}) - 3(2C_{214}C_{30} - C_{23}C_{301} + 2C_{21}(C_{304} + C_{305}) \\
& + C_{213}C_{33} - 3C_{213}C_{37} - 2C_{11}C_{406} + 9C_{11}C_{407} + 3C_{420}))\omega_1^4 \\
& + (2C_{211}(4C_{213}C_{22} - 5C_{213}C_{25} + 10C_{11}C_{37} + 2C_{43} - 2C_{11}C_{46}) \\
& - 3(-2C_{11}C_{25}C_{301} + C_{213}(C_{301} - 4C_{214}C_{25}) + 8C_{11}C_{214}C_{37} \\
& + 24C_{11}C_{400} + 8C_{214}C_{43}))\omega_1^2 - 12C_{11}(C_{211} - 6C_{214})C_{36}\Big) \\
\beta_2 =& \frac{1}{8\omega_1^7}\Big(-4C_{25}C_{306}\omega_1^8 + 2(2C_{212}C_{30} - 2C_{23}C_{302} + 4C_{21}C_{306} \\
& - C_{213}C_{425} + 4C_{11}C_{427})\omega_1^6 - (C_{23}C_{213}^2 + 2 \\
& (-2C_{212}C_{25} + C_{302} - C_{11}C_{424})C_{213} + 4C_{11}(-C_{25}C_{302} \\
& + 2C_{212}C_{37} + 2C_{421} + C_{11}C_{426}) + 8C_{212}C_{43})\omega_1^4 \\
& + C_{11}(C_{25}C_{213}^2 - 4C_{11}C_{37}C_{213} \\
& + 24C_{212}C_{36} + 4C_{11}(C_{11}C_{407} + 3C_{420}))\omega_1^2 - 16C_{11}^3C_{400}\Big) \\
\beta_3 =& \frac{C_{302}}{2\omega_1} \\
\beta_4 =& \frac{C_{301}}{2\omega_1} \\
\beta_5 =& \frac{4(C_{23}C_{35} - C_{423})\omega_1^4 + 4C_{11}(C_{405} - C_{25}C_{35})\omega_1^2 + C_{11}(C_{213} + 8C_{11}C_{22})k_g}{8\omega_1^4} \\
\beta_6 =& \frac{1}{4\omega_1^4}\Big(2(C_{23}C_{35} - C_{423})\omega_1^4 \\
& + 2(C_{11}(-C_{25}C_{35} + C_{405} + C_{23}k_g) - C_{41}k_g)\omega_1^2 \\
& + C_{11}(C_{213} + 4C_{11}C_{22} + 2C_{24} - 2C_{11}C_{25})k_g\Big) \\
\beta_7 =& \frac{C_{213}}{2\omega_1} \\
\beta_8 =& \frac{4(C_{413} - C_{23}C_{su})\omega_1^2 - C_{213}C_{su} + 4C_{11}C_{25}C_{su} - 4C_{11}C_{suu}}{16\omega_1^3} \\
\beta_9 =& -\frac{C_{35}\omega_1^2 + C_{11}k_g}{2\omega_1^2} \\
\beta_{10} =& \frac{4(C_{411} - C_{23}C_{cu})\omega_1^2 - C_{213}C_{cu} + 4C_{11}C_{25}C_{cu} - 4C_{11}C_{cuu}}{16\omega_1^3} \\
\beta_{11} =& \frac{4(C_{411} - C_{23}C_{sv})\omega_1^2 - C_{213}C_{sv} + 4C_{11}C_{25}C_{sv} - 4C_{11}C_{svv}}{16\omega_1^3}
\end{aligned}
$$

Appendix D

Local bifurcations of periodic orbits

The determination of the asymptotic stability and bifurcation behavior of the periodic orbits, solutions of the system under analysis, is carried out by means of the continuation software AUTO, which refers to the well known Floquet theory [41],[79] to compute the Floquet multipliers having modulus nearly 1 and the number of multipliers lying well inside or well outside the unit circle [30]. For this purpose, the system equations have to be expressed in the form of a system of n autonomous first-order ordinary differential equations

$$\dot{\mathbf{y}}(t) = \mathbf{f}(\mathbf{y}(t), \boldsymbol{\zeta}) \tag{D.1}$$

with $\boldsymbol{\zeta}$ being the bifurcation parameter vector and with T-periodic solution $\mathbf{p}(t, \boldsymbol{\zeta_0})$. To analyze the stability of such solution, a small variation of $\mathbf{p}(t, \boldsymbol{\zeta}_0)$ is applied:

$$\mathbf{y}(t, \boldsymbol{\zeta_0}) = \mathbf{p}(t, \boldsymbol{\zeta_0}) + \mathbf{v}(t)$$

and equation (D.1), after carrying out a first order Taylor expansion, becomes

$$\begin{aligned} \dot{\mathbf{p}}(t, \boldsymbol{\zeta_0}) + \dot{\mathbf{v}}(t) =& \mathbf{f}(\mathbf{p}(t, \boldsymbol{\zeta_0}) + \mathbf{v}(t)) \\ =& \mathbf{f}(\mathbf{p}(t, \boldsymbol{\zeta_0})) + \mathbf{f}_{\mathbf{v}}(\mathbf{p}(t, \boldsymbol{\zeta_0}), \boldsymbol{\zeta_0})\mathbf{v}(t) + o(\mathbf{v}(t)) \end{aligned} \tag{D.2}$$

where $\mathbf{f_v}$ is the Jacobian matrix, so that

$$\begin{aligned} \dot{\mathbf{v}}(t) &= \mathbf{f_v}(\mathbf{p}(t, \boldsymbol{\zeta_0}), \boldsymbol{\zeta_0})\mathbf{v}(t) \\ \mathbf{v}(0) &= \mathbf{v_0} \end{aligned} \tag{D.3}$$

represents the first-order variational equation with associated set of initial conditions. Equations (D.3) are linear in $\mathbf{v}(t)$ and thus have solution

$$\mathbf{v}(t) = \mathbf{M}(t, 0)\mathbf{v_0} \tag{D.4}$$

where $\mathbf{M}(t, 0)$ is the fundamental matrix for (D.3), so that $\mathbf{M}(0, 0) = \mathbf{I}$. Since $\mathbf{f_v}(\mathbf{p}(t, \boldsymbol{\zeta_0}), \boldsymbol{\zeta_0})$ has period T (due to the T-periodicity of $\mathbf{p}(t, \boldsymbol{\zeta_0})$), one of Floquet's theorems allows one to express the fundamental matrix as

$$\mathbf{M}(t, 0) = \mathbf{R}(t)e^{\mathbf{Q}t} \tag{D.5}$$

where $\mathbf{R}(t) \in \mathbb{R}^{n\times n}$ has period T, $\mathbf{R}(0) = \mathbf{R}(T) = \mathbf{I}$, and $\mathbf{Q} \in \mathbb{R}^{n\times n}$. Since $\mathbf{M}(t, 0)$ and $\mathbf{R}(t)$ are T-periodic matrices, after a period T equation (D.5) becomes

$$\begin{aligned} \mathbf{M}(t + T, 0) &= \mathbf{R}(t + T)e^{\mathbf{Q}(t+T)} \\ &= \mathbf{R}(t)e^{\mathbf{Q}t}e^{\mathbf{Q}T} \\ &= \mathbf{R}(t)e^{\mathbf{Q}t}\mathbf{R}(T)e^{\mathbf{Q}T} \\ &= \mathbf{M}(t, 0)\mathbf{M}(T, 0) \end{aligned} \tag{D.6}$$

and after n periods

$$\mathbf{M}(t + nT, 0) = \mathbf{M}(t, 0)\mathbf{M}(T, 0)^n \tag{D.7}$$

so that , from (D.4),

$$\mathbf{v}(t + nT) = \mathbf{M}(t, 0)\mathbf{M}(T, 0)^n\mathbf{v_0}, \qquad t \in [0, T), \quad n \in \mathbb{N} \tag{D.8}$$

The matrix $\mathbf{M}(T, 0)$ is called monodromy matrix of the periodic orbit $\mathbf{p}(t, \boldsymbol{\zeta_0})$ and has eigenvalues

$$1, \lambda_1, \lambda_2, ..., \lambda_{n-1}$$

where λ_i are known as Floquet multipliers (or characteristic multipliers), while eigenvalues γ_i of the matrix $\mathbf{Q}$ are known as Floquet exponents (or

characteristic exponents). They are related via

$$\lambda_i = e^{\gamma_i t} \tag{D.9}$$

and their values determine the asymptotic stability of the periodic solution $\mathbf{p}(t, \boldsymbol{\zeta_0})$. In particular, the periodic orbit $\mathbf{p}$ is asymptotically stable if all Floquet multipliers satisfy $|\lambda_i| < 1$ (respectively all Floquet exponents satisfy $\mathrm{Re}(\gamma_i) < 0$), while it is asymptotically unstable if at least one Floquet multiplier satisfyes $|\lambda_i| > 1$ (respectively one Floquet exponent satisfyes $\mathrm{Re}(\gamma_i) > 0$). If for some multiplier (exponent) it occurs that $|\lambda_i| = 1$ ($\mathrm{Re}(\gamma_i) = 0$), while for the others is $|\lambda_i| < 1$ ($\mathrm{Re}(\gamma_i) < 0$), the stability evaluation requires the anaysis of the higher order terms of the linearized equation (D.3). Note that λ_i correspond to the multipliers of the linearized Poincaré map associated with the periodic orbit $\mathbf{p}$.

In order to evaluate the Floquet multipliers, it is necessary to calculate a fundamental set of solutions of (D.3); it can be done by numerically integrating (D.3) during a period of oscillation, using alternatively as initial conditions $\mathbf{v_0}$ the columns of the identity matrix $\mathbf{I}$ and evaluating it at $t = T$. Each solution provides one column of the monodromy matrix $\mathbf{M}(T, 0)$, whose characteristic equation produces the wanted multipliers.

The values of the Floquet multipliers can also be used to ascertain the bifurcation behavior of the branches of periodic orbits traced out when the parameter ζ is varied [55].

A bifurcation occurs when a single real, or complex conjugate pair of Floquet multipliers pass through the unit circle in the complex plane, and a Floquet multiplier lying precisely on the unit circle defines the bifurcation point. The type of ensuing bifurcation is determined by the point at which the Floquet multiplier passes through the unit circle and the direction in which it is moving. As in the case of bifurcations of fixed points, bifurcations of periodic orbits can be classified into continuous and discontinuous or catastrophic bifurcations. In the case of continuous bifurcations, the motion of the system evolves continuously onto another motion as a control parameter is varied in a quasi-stationary manner. As in the case of fixed points, discontinuous or catastrophic bifurcations may be dangerous or explosive. In a dangerous bifurcation, the system response jumps to a remote attractor which may be infinity, as a control parameter is varied in a quasi-stationary

manner. In an explosive bifurcation, the old attractor explodes into a larger attractor, with the old attractor being a proper subset of the new attractor. Periodic orbits can exhibit three kinds of codimension-1 local bifurcations:

Divergence Bifurcation: It is a local bifurcation which occurs when a real Floquet multiplier, increasing its values, passes through the unit circle on the positive side of the real axis of the complex plane; the Floquet multiplier defining the bifurcation point is thus $\lambda = 1$. Depending on the nature of the periodic solution prior to the bifurcation, transcritical bifurcation, symmetry-breaking bifurcation or cyclic-fold (saddle-node) bifurcation can occur.

If the periodic solution possesses a symmetry property, the bifurcation which breaks such symmetry is called a *symmetry-breaking bifurcation*; in the case of a supercritical bifurcation, locally stable asymmetric periodic solutions coexist with unstable symmetric periodic solutions on one side of the bifurcation point. In the case of a subcritical bifurcation, locally unstable asymmetric periodic solutions coexist with stable symmetric periodic solutions on one side of the bifurcation point.

Conversely, if a branch of stable periodic solutions and a branch of unstable periodic solutions coalesce and obliterate each other at the bifurcation point, the local bifurcation is called *saddle-node (cyclic-fold) bifurcation.* Saddle-node bifurcations are discontinuous or catastrophic bifurcations.

Finally, if branches of stable and unstable periodic solutions exchange thier stability after the bifurcation point, the so called *transcritical bifurcation* occurs.

Period Doubling (flip) Bifurcation: It is a local bifurcation which occurs when a real Floquet multiplier passes through the unit circle on the negative side of the real axis of the complex plane; the Floquet multiplier defining the bifurcation point is thus $\lambda = -1$. This entails that a periodic orbit reverses its stability, and in addition, a new periodic solution with doubled period appears in its immediate neighborhood.

There are two types of period-doubling bifurcations, namely supercritical and subcritical. In the supercritical form the original stable periodic orbit loses stability by emanating a stable period-doubled orbit whereas in the subcritical form an unstable orbit gains stability by absorbing an unstable period-doubled orbit. Both these forms occur when a real Floquet multiplier

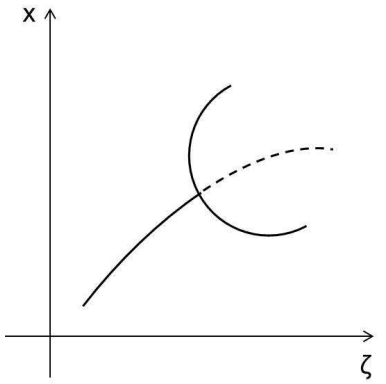

(a) Supercritical symmetry-breaking bifurcation

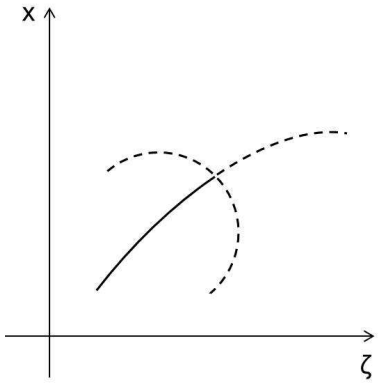

(b) Subcritical symmetry-breaking bifurcation

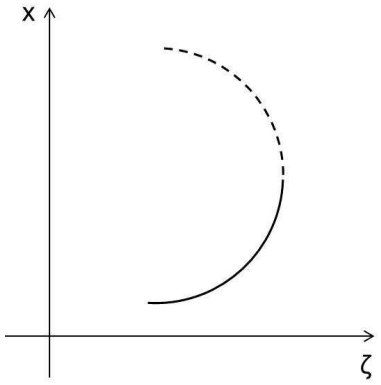

(c) Saddle-node bifurcation

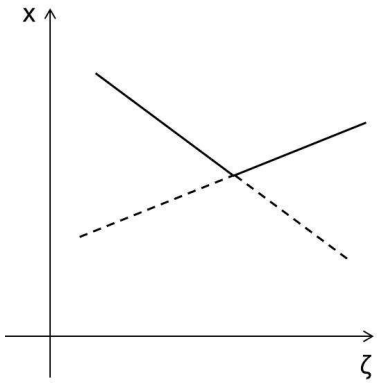

(d) Transcritical bifurcation

Figure D.1: Different kinds of divergence bifurcation

decreases through the point $\lambda = -1$ on the complex plane.

Period doubling bifurcations can also occur in reverse, when an unstable periodic solution changes its stability, by absorbing a stable period-doubled orbit (supercritical case) or by emanating an unstable period-doubled orbit (subcritical case). Reverse period-doubling bifurcations occur when a real Floquet multiplier increases through the point $\lambda = -1$ on the complex plane.

TORUS (SECONDARY HOPF) BIFURCATION: It is a local bifurcation occurring when a complex conjugate pair of Floquet multipliers with nonzero imaginary part $\lambda_{1,2} = e^{\pm i\theta_0}$ crosses the unit circle. In a torus bifurcation, a spiral limit cycle reverses its stability and spawns a zero-amplitude torus in its immediate neighborhood, to which trajectories in the system are asymp-

totically attracted or repelled. The amplitude of the torus grows as the bifurcation parameter ζ is pushed further beyond the bifurcation point. Also in this case, supercritical and subcritical forms can occur, corresponding to the arise of a stable or unstable torus, respectively.

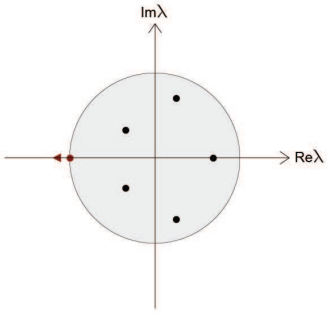

(a) Period Doubling bifurcation

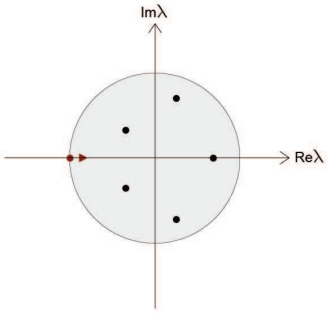

(b) Reverse Period Doubling bifurcation

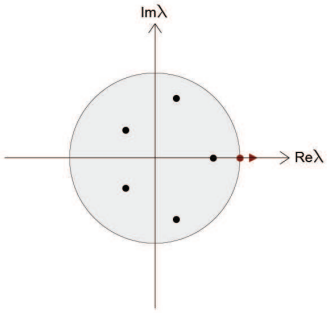

(c) Divergence bifurcation

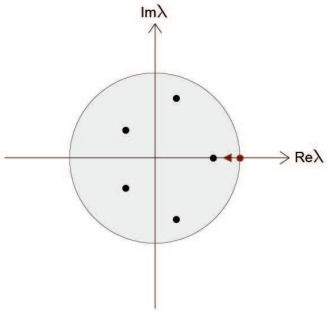

(d) Reverse Divergence bifurcation

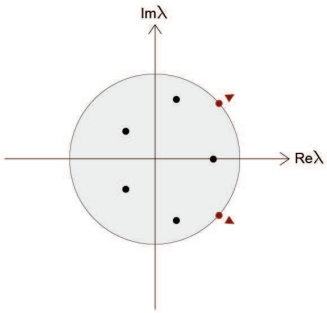

(e) Torus or Neimark-Sacher bifurcation

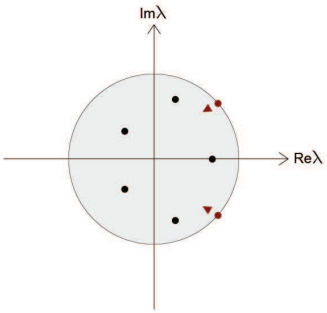

(f) Reverse Torus bifurcation

Figure D.2: Critical and stable Floquet multipliers in the complex plane for codimension-1 bifurcations of periodic orbits

Bibliography

[1] T.R. Albrecht, P. Grutter, D. Horne, and D. Rugar. Frequency modulation detection using high q cantilevers for enhanced force microscope sensitivity. *J. Appl. Phys.*, 69(2):668–673, 1991.

[2] F.M. Alsaleem, M.I. Younis, and L. Ruzziconi. An experimental and theoretical investigation of dynamic pull-in in mems resonators actuated electrostatically. *J. Microelectromech. Syst.*, 19(4):794–806, 2010.

[3] U. Andreaus, L. Placidi, and G. Rega. Microcantilever dynamics in tapping mode atomic force microscopy via higher eigenmodes analysis. *J. Appl. Phys.*, to appear.

[4] H.N. Arafat, A.H. Nayfeh, and E.M. Abdel-Rahman. Modal interactions in contact-mode atomic force microscopes. *Nonlinear Dyn.*, 54: 151–166, 2008.

[5] T. Arecchi, S. Boccaletti, M. Ciofini, C. Grebogi, and R. Meucci. Control of chaos: new perspectives in experimental and theoretical nonlinear science. *Int. J. Bif. Chaos*, 8(8), 1998.

[6] M.T. Arjmand, H. Sadeghian, H. Salarieh, and A. Alasty. Chaos control in afm systems using nonlinear delayed feedback via sliding mode control. *Nonlinear Anal. Hybrid Syst.*, 2:993–1001, 2008.

[7] M. Ashhab, M.V. Salapaka, M. Dahlec, and I. Mezic. Melnikov-based dynamical analysis of microcantilevers in scanning probe microscopy. *Nonlinear Dyn.*, 20:197–220, 1999.

[8] M. Ashhab, M.V. Salapaka, M. Dahleh, and I. Mezic. Dynamical analysis and control of microcantilevers. *Automatica*, 35:1663–1670, 1999.

[9] A. Bahrami and A.H. Nayfeh. On the dynamics of tapping mode atomic force microscope probes. *Nonlinear Dyn.*, 70:1605–1617, 2012.

[10] V. Bellitto. *Atomic Force Microscopy - Imaging, Measuring and Manipulating Surfaces at the Atomic Scale*. InTech: Open Access Publisher, Croatia, 2012.

[11] G. Binning, C.F. Quate, and C. Gerber. Atomic force microscope. *Phys. Rev. Lett.*, 56(9):930–936, 1986.

[12] B. Blazejczyk, T. Kapitaniak, J. Wojewoda, and J. Brindley. Controlling chaos in mechanical systems. *Applied Mechanics Review*, 46(7): 385–391, 1993.

[13] S. Boccaletti, C. Grebogi, Y.-C. Lai, H. Mancini, and D. Maza. The control of chaos: theory and applications. *Physics Reports*, 329:103–197, 2000.

[14] R. Boisgard, D. Michel, and J.P. Aimé. Hysteresis generated by attractive interaction: oscillating behavior of a vibrating tipmicrolever system near a surface. *Surf. Sci.*, 401(2):199–205, 1998.

[15] H. J. Butt, K. Graf, and M. Kappl. *Physics and chemistry of interfaces*. Wiley, VCH, 2003.

[16] R. Chacon. *Control of homoclinic chaosv by weak periodic perturbations*, volume 55 of *Series on nonlinear science. Series A*. World Scientific, Singapore, 2005.

[17] I. Chakraborty and B. Balachandran. Noise influenced elastic cantilever dynamics with nonlinear tip interaction forces. *Nonlinear Dyn.*, 66:427–439, 2011.

[18] G.R. Chen. *Controlling chaos and bifurcations in engineering systems*. CRC press, Boca Raton, 1999.

[19] G.R. Chen and X. Dong. *From chaos to order: methodologies, perspectives and applications*. World Scientific, Singapore, 1998.

[20] G. Couturier and R.J.-P. Boisgard. Noncontact atomic force microscopy: Stability criterion and dynamical responses of the shift of

frequency and damping signal. *Rev. Sci. Instrum.*, 74(5):2726–2734, 2003.

[21] G. Couturier, L. Nony, R. Boisgard, and J.P. Aim. Stability of an oscillating tip in noncontact atomic force microscopy: theoretical and numerical investigations. *J. Appl. Phys.*, 91(4):2537–2543, 2002.

[22] M.R.M. Crespo da Silva and C.C. Glynn. Nonlinear flexural-flexural-torsional dynamics of inextensional beams. i. equations of motion. *Mech. Based Des. Struct. Mach.*, 6(4):437–448, 1978.

[23] H. Dankowicz, X. Zhao, and S. Misra. Near-grazing dynamics in tapping-mode atomic-force microscopy. *International Journal of Non-Linear Mechanics*, 42(4):697–709, 2007.

[24] M.S.T. de Freitas, R.L. Viana, and C. Grebogi. Erosion of the safe basin for the transversal oscillations of a suspension bridge. *Chaos Solitons Fractals*, 18:829–841, 2003.

[25] E.J. Doedel and B.E. Oldeman. *AUTO-07p: Continuation and bifurcation software for ordinary differential equations*. Concordia University, Montreal, 2012.

[26] U. Durig, O. Zuger, and A. Stalder. Interaction force detection in scanning probe microscopy: methods and applications. *J. Appl. Phys.*, 72(5):1778–1798, 1992.

[27] P. Eaton and P. West. *Atomic Force Microscopy*. Oxford University Press, Oxford, 2010.

[28] B. Epureanu, S.T. Trickey, and E. Dowell. Stabilization of unstable limit cycles in systems with limited controllability: expanding the basin of convergence of ogy-type controllers. *Nonlin. Dyn.*, 15:191–205, 1998.

[29] R. Erlandsson and L Olsson. Force interaction in low amplitude ac-mode atomic force microscopy:cantilever simulation and comparison with data from si(111)7 x 7. *Appl. Phys. A*, 66:S879–S883, 1998.

[30] T.F. Fairgrieve and A.D. Jepson. O.k. floquet multipliers. *SIAM J. Numer. Anal.*, 28(5):1446–1462, 1991.

[31] A.L. Fradkov. Chaos control bibliography (1997-2000). *Russian systems and control archive (RUSYCON)*, 2000. http://www.rusycon.ru/chaos-control.html.

[32] A.L. Fradkov and R.J. Evans. Control of chaos: Methods and applications in engineering. *Annual Reviews in Control*, 29:33–56, 2005.

[33] A.L. Fradkov and A.Yu. Pogromsky. *Introduction to control of oscillations and chaos*. World Scientific, Singapore, 1998.

[34] A.L. Fradkov, R.L. Evans, and B.R. Andrievski. Control of chaos: methods and applications in mechanics. *Phil. trans. Roy. Soc. A*, 364: 2279–2307, 2006.

[35] C. Gan, Q. Lu, and K. Huang. Nonstationary effects on safe basins of a forced softening duffing oscillator. *Acta Mech. Sin.*, 11:253–260, 1998.

[36] R. García and R. Pérez. Dynamic atomic force microscopy methods. *Surf. Sci. Rep.*, 47:197–301, 2002.

[37] M.H. Ghayesh, M. Amabili, and H. Farokhi. Coupled global dynamics of an axially moving viscoelastic beam. *International Journal of Non-Linear Mechanics*, 51:54–74, 2013.

[38] F.J. Giessibl. Advances in atomic force microscopy. *Rev. Mod. Phys.*, 75(3):949–983, 2003.

[39] P.B. Gonçalves, F.M.A. Silva, and Z.J.G.N. Del Prado. Global stability analysis of parametrically excited cylindrical shells through the evolution of basin boundaries. *Nonlinear Dyn.*, 50:121–145, 2007.

[40] P.B. Gonçalves, F.M.A. Silva, G. Rega, and S. Lenci. Global dynamics and integrity of two-dof model of parametrically excited cylindrical shell. *Nonlinear Dyn.*, 63:61–82, 2011.

[41] B.P. Hartman. *Ordinary differential equations*. Wiley, New York, 1964.

[42] D.L. Hill. On the control of chaotic dynamical systems using nonlinear approximations. *Int. J. Bif. Chaos*, 11(1):207–213, 2001.

[43] S. Hornstein. *Nonlinear spatio-temporal dynamics of the scan process in atomic force microscopy*. PhD thesis, Technion, Haifa, 2012.

[44] S. Hornstein and O. Gottlieb. Nonlinear dynamics, stability and control of the scan process in noncontacting atomic force microscopy. *Nonlinear Dynamics*, 54:93–122, 2008.

[45] S. Hornstein and O. Gottlieb. Nonlinear multimode dynamics and internal resonances of the scan process in noncontacting atomic force microscopy. *J. Appl. Phys.*, 112:074314, 2012.

[46] A.D.L. Humphris, J. Tamayo, and M.J. Miles. Active quality factor control in liquids for force spectroscopy. *Langmuir*, 16:7891–7894, 2000.

[47] A. Isidori. *Nonlinear Control Systems*. Springer-Verlag, Secaucus, 3rd edition, 1995.

[48] A. Isidori. *Nonlinear Control Systems II*. Springer-Verlag, London, 2000.

[49] J. Israelachvili. *Intermolecolar and surface forces*. Academic Press, London, 1992.

[50] F. Jamitzky, M. Stark, W. Bunk, W.M. Heckl, and R.M. Stark. Chaos in dynamic atomic force microscopy. *Nanotechnology*, 17:S213, 2006.

[51] K. Judd, A.I. Mees, K.L. Teo, and T. Vincent. *Control of chaos*. Birkhauser, Boston, 1997.

[52] T. Kapitaniak. *Controlling chaos*. Academic Press, Lodz, 1996.

[53] D. Kiracofe and A. Raman. Microcantilever dynamics in liquid environment dynamic atomic force microscopy when using higher-order cantilever eigenmodes. *J. Appl. Phys.*, 108:034320, 2010.

[54] M.H. Korayem, S. Zafari, A. Amanati, M. Damircheli, and N. Ebrahimi. Analysis and control of micro-cantilever in dynamic mode afm. *Int. J. Adv. Manuf. Technol.*, 50(9-12):979–990, 2010.

[55] Y.A. Kuznetsov. *Elements of applied bifurcation theory*. Number 112 in Applied Mathematical Sciences. Springer, New York, 2004.

[56] A.N. Lansbury, J.M.T. Thompson, and H.B. Stewart. Basin erosion in the twin-well duffing oscillator: two distinct bifurcation scenarios. *Int. J. Bifurc. Chaos*, 2:505–532, 1992.

[57] M. Larkshmanan and K. Murali. *Chaos in nonlinear oscillators: controlling and synchronization.* World Scientific, Singapore, 1996.

[58] S.I. Lee and S.A.R. Howell. Nonlinear dynamic perspectives on dynamic force microscopy. *Ultramicroscopy*, 97:185–198, 2003.

[59] S.I. Lee, S.W. Howell, A. Raman, and R. Reifenberger. Nonlinear dynamics of microcantilevers in tapping mode atomic force microscopy: A comparison between theory and experiment. *Phys. Rev. B*, 66: 115409, 2002.

[60] S. Lenci and G. Rega. Optimal control of homoclinic bifurcation: theoretical treatment and practical reduction of safe basin erosion in the helmholtz oscillator. *J. Vibr. Control*, 9:281–315, 2003.

[61] S. Lenci and G. Rega. Optimal control of nonregular dynamics in a duffing oscillator. *Nonlinear Dyn.*, 33:71–86, 2003.

[62] S. Lenci and G. Rega. A unified control framework of the nonregular dynamics of mechanical oscillators. *J. Sound Vibr.*, 278:1051–1080, 2004.

[63] S. Lenci and G. Rega. Control of pull-in dynamics in a nonlinear thermoelastic electrically actuated microbeam. *J. Micromech. Microeng.*, 16:390–401, 2006.

[64] S. Lenci and G. Rega. *Exploiting chaotic properties of dynamical systems for their control: suppressing, enhancing, using chaos.* Philosophical transactions: Mathematical, physical, and engineering sciences. Royal Society, 2006.

[65] S. Lenci and G. Rega. Competing dynamic solutions in a parametrically excited pendulum : Attractor robustness and basin integrity. *J. Comput. Nonlinear Dynam.*, 3(4):041010, 2008.

[66] S. Lenci and G. Rega. Experimental vs theoretical robustness of rotating solutions in a parametrically excited pendulum: a dynamical integrity perspective. *Physica D*, 240:814–824, 2011.

[67] S. Lenci and G. Rega. Load carrying capacity of systems within a global safety perspective. part ii. attractor/basin integrity under dynamic excitations. *Int. J. Non-Linear Mech.*, 46:1240–1251, 2011.

[68] S. Lenci and L. Ruzziconi. Nonlinear phenomena in the single-mode dynamics of a cable-supported beam. *I. J. Bif. Chaos*, 19(3):923–945, 2009.

[69] S. Lenci, W. Luzi, E. Venturi, and G. Rega. Practical stability of rotating solutions in a parametrically excited experimental pendulum via dynamical integrity concepts. In M. Wiercigroch and G. Rega, editors, *IUTAM Symposium on Nonlinear Dynamics for Advanced Technologies and Engineering Design*, volume 32 of *IUTAM Bookseries (closed)*, pages 173–184. Springer Netherlands, 2013. doi: 10.1007/978-94-007-5742-4{_}14.

[70] S. Lenci, G. Rega, and L. Ruzziconi. The dynamical integrity concept for interpreting/predicting experimental behaviour: from macro- to nano-mechanics. *Phil. Trans. R. Soc. A*, 371:20120423, 2013.

[71] R. Lima and M. Pettini. Suppression of chaos by resonant parametric perturbations. *Phys. Rev. A*, 41:726, 1990.

[72] J.T. Liu, D. Yang, and L.Q. Chen. Bifurcations and chaos of an axially moving plate under external and parametric excitations. *J. Str. Stab. Dyn.*, 12:1250023, 2012.

[73] J. H. Masliyah and S. Bhattacharjee. *Electrokinetic and Colloid Transport Phenomena*. Wiley, 2006.

[74] R. Merry, M. Uyanik, R. van de Molengraft, R. Koops, M. van Veghel, and M. Steinbuch. Identification, control and hysteresis compensation of a 3 dof metrological afm. *Asian Journal of Control*, 11(2):130–143, 2009.

[75] S. Misra and H.M.R. Dankowicz. Degenerate discontinuity-induced bifurcations in tapping-mode atomic-force microscopy. *Physica D*, 239: 33–43, 2010.

[76] S. Morita, R. Wiesendanger, and E.A. Meyer. *Noncontact atomic force microscopy*, volume 1. Springer, Berlin, 2002.

[77] S. Morita, F.J. Giessibl, and R. Wiesendanger. *Noncontact atomic force microscopy*, volume 2. Springer, Berlin, 2009.

[78] N. Mullin, C. Vasilev, J.D. Tucker, C. N. Hunter, C.H.M. Weber, and J.K. Hobbs. Torsional tapping atomic force microscopy using t-shaped cantilevers. *Appl. Phys. Lett.*, 94:173109, 2009.

[79] A.H. Nayfeh and D.T. Mook. *Nonlinear oscillations*. Wiley, New York, 1979.

[80] L. Nony and R.J.-P. Boisgard. Stability criterions of an oscillating tip-cantilever system in dynamic force microscopy. *Eur. Phys. J. B*, 24:221–229, 2001.

[81] R. Nozaki, J.M. Balthazar, A.M. Tusset, Jr. Pontes, B.R., and Á.M. Bueno. Nonlinear control system applied to atomic force microscope including parametric errors. *Journal of Control, Automation and Electrical Systems*, pages 1–9, 2013.

[82] D. Orlando, P.B. Gonçalves, G. Rega, and S. Lenci. Nonlinear dynamics and sensitivity to imperfections in augusti's model. *J. Mech. Mater. Struct.*, 6(7-8):1065–1078, 2011.

[83] D. Orlando, P.B. Gonalves, G. Rega, and S. Lenci. Nonlinear dynamics and instability as important design concerns for a guyed mast. In M. Wiercigroch and G. Rega, editors, *IUTAM Symposium on Nonlinear Dynamics for Advanced Technologies and Engineering Design*, volume 32 of *IUTAM Bookseries (closed)*, pages 223–234. Springer Netherlands, 2013.

[84] E. Ott, C. Grebogi, and J.A. Yorke. Controlling chaos. *Phys. Rev. Lett.*, 64(11):1196, 1990.

[85] A.S. Paulo and R. García. Unifying theory of tapping-mode atomic-force microscopy. *Phys. Rev. B*, 66:041406(R), 2002.

[86] O. Pfeiffer, C. Loppacher, C. Wattinger, M. Bammerlin, U. Gysin, M. Guggisberg, S. Rast, R. Bennewitz, E. Meyer, and H.J. Guntherodt. Using higher flexural modes in non-contact force microscopy. *Appl. Surf. Sci.*, 157:337–342, 2000.

[87] K. Pyragas. Continuous control of chaos by self-controlling feedback. *Phys. Lett. A*, 170:421–428, 1992.

[88] G. Rega and S. Lenci. Bifurcations and chaos in single-d.o.f. mechanical systems: exploiting nonlinear dynamics properties for their control. In A. Luongo, editor, *Recent research developments in structural dynamics*, pages 331–369. Transworld research network, 2003.

[89] G. Rega and S. Lenci. Identifying, evaluating and controlling dynamical integrity measures in non-linear mechanical oscillators. *Nonlinear Anal.*, 63:902–914, 2005.

[90] G. Rega and S. Lenci. Dynamical integrity and control of nonlinear mechanical oscillators. *J. Vibr. Control*, 14(1-2):159–179, 2008.

[91] G. Rega and A. Salvatori. Bifurcation structure at 1/3-subharmonic resonance in an asymmetric nonlinear elastic oscillator. *Int. J. Bif. Chaos*, 6:1529–1546, 1996.

[92] G. Rega, A. Salvatori, and F. Benedettini. Numerical and geometrical analysis of bifurcation and chaos for an asymmetric elastic nonlinear oscillator. *Nonlinear Dyn.*, 7:249–272, 1995.

[93] T.R. Rodriguez and R. García. Tip motion in amplitude modulation (tapping-mode) atomic-force microscopy: Comparison between continuous and point-mass models. *Appl. Phys. Lett.*, 80(9):1646–1648, 2002.

[94] T.R. Rodriguez and R. García. Compositional mapping of surfaces in atomic force microscopy by excitation of the second normal mode of the microcantilever. *Appl. Phys. Lett.*, 84(3):449, 2004.

[95] L. Ruzziconi, S. Lenci, and M.I. Younis. An imperfect microbeam under an axial load and electric excitation: nonlinear phenomena and dynamical integrity. *I. J. Bif. Chaos*, 23(2), 2013.

[96] L. Ruzziconi, M.I. Younis, and S. Lenci. An electrically actuated imperfect microbeam: Dynamical integrity for interpreting and predicting the device response. *Meccanica*, pages 1–15, 2013. doi: 10.1007/s11012-013-9707-x.

[97] O. Sahin, C.F. Quate, O. Solgaard, and A. Atalar. Resonant harmonic response in tapping-mode atomic force microscopy. *Phys. Rev. B*, 69: 165416, 2004.

[98] H. Salarieh and A. Alasty. Control of chaos in atomic force microscopes using delayed feedback based on entropy minimization. *Commun. Nonlinear Sci. Numer. Simul.*, 14:637–644, 2009.

[99] M.A.F. Sanjuán and C. Grebogi. *Recent progress in controlling chaos.* Series on stability, vibration, and control of systems. Series B. World Scientific, 2010. ISBN 9789814291705.

[100] D. Sarid. *Scanning Force Microscopy: With Applications to Electric, Magnetic, and Atomic Forces.* Oxford University Press, New York, 1991.

[101] D. Sarid, T.G. Ruskell, R.K. Workman, and D. Chen. Driven nonlinear atomic force microscopy cantilevers: from noncontact to tapping modes of operation. *J. Vac. Sci. Technol. B*, 14(2):864–867, 1996.

[102] E. Schöll and H.G. Schuster. *Handbook of Chaos Control; 2nd ed.* Wiley, Weinheim, 2008.

[103] M.K. Sifakis and S.J. Elliott. Strategies for the control of chaos in a Duffing-Holmes oscillator. *Mech. Syst. Sign. Process.*, 14:987–1002, 2000.

[104] M.S. Soliman and P.B. Gonçalves. Chaotic behavior resulting in transient and steady state instabilities of pressure-loaded shallow spherical shells. *J. Sound Vib.*, 259:497–512, 2003.

[105] M.S. Soliman and J.M.T. Thompson. Integrity measures quantifying the erosion of smooth and fractal basins of attraction. *J. Sound Vib.*, 135:453–475, 1989.

[106] M.S. Soliman and J.M.T. Thompson. Global dynamics underlying sharp basin erosion in nonlinear driven oscillators. *Phys. Rev. A*, 45: 3425–3431, 1992.

[107] Y. Song and B. Bhushan. Coupling of cantilever lateral bending and torsion in torsional resonance and lateral excitation modes of atomic force microscopy. *J. Appl. Phys.*, 99:094911, 2006.

[108] Y. Song and B. Bhushan. Atomic force microscopy dynamic modes: modeling and applications. *J. Phys. Condens. Matt.*, 20:225012, 2008.

[109] J.R. Jr. Souza and M.L. Rodrigues. An investigation into mechanisms of loss of safe basins in a 2 d. o. f. nonlinear oscillator. *J. Braz. Soc. Mech. Sci. Eng.*, 24:93–98, 2002.

[110] R.W. Stark and W.M. Heckl. Fourier transformed atomic force microscopy: tapping mode atomic force microscopy beyond the hookian approximation. *Surf. Sci.*, 457:219–228, 2000.

[111] R.W. Stark, T. Drobek, and W.M. Heckl. Tapping-mode atomic force microscopy and phase-imaging in higher eigenmodes. *Appl. Phys. Lett.*, 74(22), 1999.

[112] W. Szemplinska-Stupnicka. Cross-well chaos and escape phenomena in driven oscillators. *Nonlinear Dyn.*, 3:225–243, 1992.

[113] W. Szemplinska-Stupnicka and E. Tyrkiel. Effects of multi global bifurcations on basin organization, catastrophes and final outcomes in a driven nonlinear oscillator at the 2t-subharmonic resonance. *Nonlinear Dyn.*, 17:41–59, 1998.

[114] W. Szemplinska-Stupnicka and E. Tyrkiel. Sequencies of global bifurcations and the related outcomes after crisis of the resonant attractor in a nonlinear oscillator. *Int. J. Bif. Chaos*, 12:159–168, 2002.

[115] J.M.T. Thompson. Chaotic phenomena triggering the escape from a potential well. *Proc. R. Soc. Lond. A*, 421:195–225, 1989.

[116] J.M.T. Thompson. *Nonlinear dynamics and chaos.* Wiley, New York, 2002.

[117] J.A. Turner. Non-linear vibrations of a beam with cantilever- hertzian contact boundary conditions. *J. Sound Vibr.*, 275:177–191, 2004.

[118] J.A. Turner, S. Hirsekorn, U. Rabe, and W. Arnold. High-frequency response of atomic-force microscope cantilevers. *J. Appl. Phys.*, 82(3): 966–979, 1997.

[119] C.C. Wang, N.S. Pai, and H.T. Yau. Chaos control in afm system using sliding mode control by backstepping design. *Commun. Nonlinear Sci. Numer. Simulat.*, 15:741–751, 2010.

[120] K. Wolf and O. Gottlieb. Nonlinear dynamics of a noncontacting atomic force microscope cantilever actuated by a piezoelectric layer. *J. Appl. Phys.*, 91(7):4701–4709, 2002.

[121] J. Xu, Q. Lu, and K. Huang. Controlling erosion of safe basin in nonlinear parametrically excited systems. *Acta Mech. Sin.*, 12:281–288, 1996.

[122] K. Yagasaki. Nonlinear dynamics of vibrating microcantilevers in tapping-mode atomic force microscopy. *Phys. Rev. B*, 70:245419, 2004.

[123] K. Yagasaki. New control methodology of microcantilevers in atomic force microscopy. *Phys. Lett. A*, 375:23–28, 2010.

[124] K. Yagasaki. Nonlinear dynamics and bifurcations in external feedback control of microcantilevers in atomic force microscopy. *Commun Nonlinear Sci. Numer. Simul.*, 18(10):2926–2943, 2013.

[125] K. Yagasaki and T. Uozumi. Controlling chaos using nonlinear approximations and delay coordiante embedding. *Phys. Lett. A*, 247: 129–139, 1998.

[126] K. Yamasue and T. Hikihara. Control of microcantilevers in dynamic force microscopy using time delayed feedback. *Rev. Sci. Instrum.*, 77: 053703, 2006.

[127] G. Zavala. Atomic force microscopy, a tool for characterization, synthesis and chemical processes. *Colloid and Polymer Science*, 286(1): 85–95, 2008.

[128] Y. Zhang and Y.P. Zhao. Nonlinear dynamics of atomic force microscopy with intermittent contact. *Chaos, Solitons and Fractals*, 34, 2007.

[129] Q. Zou, K.K. Leang, E. Sadoun, M.J. Reed, and S. Devasia. Control issues in high-speed afm for biological applications: collagen imaging sample. *Asian Journal of Control*, 6(2):164–178, 2004.